

Circumferential Groove Casing Treatments in Centrifugal Compressor Aerodynamics

Von der Fakultät Energie-, Verfahrens- und Biotechnik der
Universität Stuttgart zur Erlangung der Würde eines Doktors der
Ingenieurwissenschaften (Dr.-Ing.) genehmigte Abhandlung

Vorgelegt von
Simon Bareiß
aus Schorndorf

Hauptberichter: Prof. Dr. Techn. Damian M. Vogt
Mitberichter: Prof. Dr.-Ing. Heinz-Peter Schiffer

Tag der mündlichen Prüfung: 30. November 2020

Institut für Thermische Strömungsmaschinen
und Maschinenlaboratorium der Universität Stuttgart

2021

Preface

The work described in the present thesis has been carried out during my employment as a research associate at the Institute of Thermal Turbomachinery (ITSM) at the University of Stuttgart between March 2014 and August 2019.

First of all, I am especially grateful to my supervisor Professor Tekn. Dr. Damian M. Vogt for placing his trust in me and for enabling this project. This work would not have been accomplished without his guidance, wide knowledge and thought provoking discussions. I would also like to thank Prof. Dr.-Ing. Heinz-Peter Schiffer for co-examining this thesis.

Many thanks are owed to all colleagues who shared my time at the institute and helped and supported me in various different ways. I always enjoyed the friendly relationships and the inspiring talks. In particular, though, I would like to thank Patrick Buchwald for the outstanding work atmosphere in our office, the helpful discussions and for proof-reading the manuscript.

Furthermore, I am extremely thankful to all of the technical staff for their work and support that helped in so many ways. In this context, the contribution of Martin Brausewetter must be emphasized. The experimental part of this work would not have been possible without his great commitment and knowledge. Moreover, I would like to thank all students that contributed to this dissertation during the course of their studies.

On a more personal note I would like to thank my wife Kerstin for her love and the unwavering support and encouragement, which has made all the difference.

Abstract

In this work, the applicability of circumferential groove casing treatments in centrifugal compressors is investigated. So far these treatments proved to be effective in axial aero-engine compressors, whereby their specific advantages are highly desirable for a wide range of centrifugal machines as well. However, no thorough studies are available yet and the transferability of the present knowledge is questionable. As the typical flow fields of axial and centrifugal compressors are significantly different, the present study is focused on the effectiveness, the respective design and the understanding of the underlying mechanisms of such grooves, when applied to a centrifugal compressor.

The study has been conceived to involve computational methods as well as experimental testing. A representative compressor design and the corresponding test facility were developed to allow for a modular testing of different groove designs. Firstly, a numerical study has been performed to assess the impact of different groove design parameters on the compressor flow field. Clear trends were identified, whereby the groove location was found to be the most influential parameter. Improvements in terms of pressure rise and efficiency were observed for groove locations towards the inducer. Moreover, high inclination angles and a normalized width at the casing of 4 % to 10 % of the meridional blade length were found to be most effective for all locations. The results obtained with multiple groove configurations suggested that the respective single groove effects can be superimposed and do not degenerate the performance by interference. Furthermore, a smoothing of the near tip flow distortions was identified, which suggested possibly improved stability. Thereupon, design guidelines were derived and the two most promising variants were selected and manufactured for testing and validation. Two different diffusers, a vaned and a vaneless configuration, were used for the following studies to clearly identify the groove impact on the impeller flow field.

In general, the measured results showed a significant improvement of the overall compressor characteristics for both selected configurations. The range of stable operation is extended by several percentage points depending on the configuration and the specific speedline. On top of that, the efficiency and the overall pressure ratio are considerably increased, whereby typical improvements of about half of a percentage point in overall efficiency were found.

Experimental and numerical analyses both traced back these results to an alteration of the near tip flow field in consequence of the groove application. Thereby, a reduction of blockage is found to be the major mechanism that enables the stall margin improvement and the increased performance. Essentially, effective grooves lead to a redistribution of the local tip leakage shares, which weakens the tip jet strength and thus reduces and smoothens the distorted flow regions near the casing. However, significant differences have been determined for the different effective groove locations in terms of stall margin improvement (*SMI*). Inducer grooves directly affect the early development of the tip vortex, which results in a weakening and a deflection that delays the flow spillage causing the initial instability at subsonic speeds. Grooves in the bend region relieve the highly blocked areas near the splitter blade leading edges by preventing leakage backflows and reducing the accumulation of low momentum fluid that destabilizes the impeller flow field at transonic conditions.

Kurzfassung

Die vorliegende Arbeit untersucht die Anwendbarkeit von gehäuseseitigen Umfangsnuten in Radialverdichtern. Für Axialverdichter konnten mithilfe dieser Art von *casing treatment* bereits vielversprechende Verbesserungen erzielt werden, die auch für viele Anwendungsgebiete von radialen Maschinen sehr vorteilhaft wären. Allerdings fehlte es bisher an entsprechenden Studien und die Frage der Übertragbarkeit blieb ebenfalls noch ungeklärt. Aufgrund der stark unterschiedlichen Charakteristik der Strömungsfelder liegt das Hauptaugenmerk dieser Untersuchung einerseits auf der generellen Wirksamkeit dieser Nuten in Radialverdichtern. Andererseits befasst sich die Arbeit mit der zugehörigen Auslegung und den aerodynamischen Wirkmechanismen.

Hierfür wurde eine kombinierte Studie konzipiert, bei der sowohl numerische als auch experimentelle Methoden zum Einsatz kommen. Zur Untersuchung verschiedener Nutvarianten wurde ein repräsentativer Radialverdichter samt dem zugehörigen Versuchsstand und den numerischen Modellen entwickelt und aufgebaut. Anschließend wurde im ersten Schritt eine Parameterstudie bezüglich des Einflusses verschiedener Designparameter der Nuten auf die Verdichterströmung durchgeführt. Dabei konnten eindeutige Trends identifiziert werden. Der größte Einfluss wurde für die Lage der Nut beobachtet, wobei sich eine Platzierung in Richtung des Verdichtereintritts als vorteilhaft für Wirkungsgrad und Druckverhältnis erwies. Außerdem erzielten große Anstellwinkel und normalisierte Öffnungsbreiten zwischen 4 und 10 % der abgewickelten Schaufellänge die besten Ergebnisse, unabhängig von der Lage. Die Ergebnisse bei Verwendung mehrerer Nuten lassen darauf schließen, dass die Einzeleffekte überlagert werden können, ohne dass es zu einer negativen gegenseitigen Beeinflussung kommt. Darüberhinaus konnte ein vergleichmäßiger Effekt auf die gehäusenaher Strömung festgestellt werden, der Grund zur Annahme einer Stabilitätsweiterung darstellt.

Basierend auf den Ergebnissen konnten entsprechende Auslegungsrichtlinien abgeleitet werden. Zusätzlich wurden zwei vielversprechende Varianten für weitere Tests und genauere Untersuchungen ausgewählt und gefertigt. Hierfür wurden zwei verschiedene Diffusoren, mit und ohne Beschaukelung, eingesetzt, um eine klare Abgrenzung der Effekte zu ermöglichen.

Im Großen und Ganzen zeigten die Messungen eine deutliche Verbesserung des Verdichterkennfelds für beide Varianten. Der stabile Betriebsbereich

konnte, abhängig von der jeweiligen Konfiguration und der entsprechenden Drehzahlkennlinie, um mehrere Prozentpunkte erweitert werden. Zusätzlich wurde eine Verbesserung der Wirkungsgrades und des Gesamtdruckverhältnisses beobachtet, wobei typische Verbesserungen von etwa einem halben Prozentpunkt im Gesamtwirkungsgrad erreicht werden.

Sowohl die experimentellen Daten als auch die numerischen Resultate führen diese Effekte auf eine Beeinflussung der gehäusenahen Strömung zurück. Als Hauptmechanismus kann dabei die Verminderung von aerodynamischen Versperrungen identifiziert werden, die zu einer Erweiterung des Betriebsbereichs und zur verbesserten Verdichterleistung führt.

Im Wesentlichen ermöglichen wirksame Nuten eine Umverteilung der lokalen Schaufelspaltströmungsanteile, was zu einer Abschwächung der saugseitigen Beeinflussung der Hauptströmung, und damit zu einer Abschwächung der Versperrungen, führt. Allerdings wurden Unterschiede bezüglich der Nutlage in Bezug auf die Verdichterstabilität ausgemacht. Nuten im unmittelbaren Eintrittsbereich beeinflussen direkt die Entstehung des Spitzenspaltwirbels, was zu einer entsprechenden Ablenkung und Abschwächung führt. Dies wiederum verzögert das Überströmen in benachbarte Passagen, was die Instabilität der Strömung im subsonischen Bereich initiiert. Nuten im gekrümmten Bereich des Verdichters hingegen entlasten die stark versperren Bereiche nahe der Zwischenschaufeln durch die Vermeidung von Rückströmungen und Überströmeffekten, welche für die Destabilisierung bei transonischen Bedingungen verantwortlich sind.

Contents

| | |
|---|-------------|
| Preface | iii |
| Abstract | v |
| Kurzfassung | vii |
| Contents | ix |
| Nomenclature | xiii |
| 1 Introduction | 1 |
| 2 Background | 5 |
| 2.1 Centrifugal Compressor Flow | 5 |
| 2.2 Compressor Stall and Surge | 10 |
| 2.2.1 Impeller Stall | 13 |
| 2.2.2 Diffuser Stall | 17 |
| 2.3 Casing Treatments | 19 |
| 2.3.1 Centrifugal Compressors | 20 |
| 2.3.2 Circumferential Grooves | 24 |
| 2.4 Discussion | 30 |
| 3 Test Object and Experimental Methods | 33 |
| 3.1 Centrifugal Compressor Stage | 33 |
| 3.2 Compressor Test Rig | 36 |
| 3.2.1 Flow Measurement Section | 36 |
| 3.2.2 Stage Pressure Measurements | 43 |
| 3.2.3 Experimental Approach | 48 |
| 3.2.4 Reproducibility | 51 |

| | |
|--|-----------|
| 4 Numerical Models | 55 |
| 4.1 Discretization | 56 |
| 4.1.1 Impeller | 57 |
| 4.1.2 Diffuser | 59 |
| 4.1.3 Volute and Pipe System | 60 |
| 4.1.4 Casing Grooves | 61 |
| 4.2 CFD Modeling | 63 |
| 4.2.1 Steady-State Models | 64 |
| 4.2.2 Time-Resolved Models | 66 |
| 4.3 Verification | 70 |
| 4.4 Validation | 75 |
| 4.4.1 Vaned Diffuser Configuration | 75 |
| 4.4.2 Vaneless Diffuser Configuration | 81 |
| 4.4.3 Discussion | 84 |
| 5 Numerical Groove Design Study | 87 |
| 5.1 Investigation Approach | 88 |
| 5.1.1 Parametrization of the Groove Geometry | 88 |
| 5.1.2 Methodology of the Design Study | 89 |
| 5.2 Performance Impact of Groove Parameters | 92 |
| 5.2.1 Groove Location | 92 |
| 5.2.2 Groove Inclination | 93 |
| 5.2.3 Groove Dimension | 96 |
| 5.2.4 Multiple Groove Interaction | 99 |
| 5.3 Flow Mechanisms | 101 |
| 5.3.1 Inducer Grooves | 105 |
| 5.3.2 Bend Region Grooves | 108 |
| 5.3.3 Outlet Region Grooves | 109 |
| 5.4 Findings and Discussion | 112 |

| | | |
|----------|--|------------|
| 5.4.1 | Design Guidelines | 112 |
| 5.4.2 | Selection of Final Groove Configurations | 114 |
| 6 | Stability with Casing Grooves | 119 |
| 6.1 | Stability of the Baseline Compressor Stage | 119 |
| 6.2 | Influence on Operating Range | 123 |
| 6.2.1 | Vaned Diffuser Measurements | 123 |
| 6.2.2 | Vaneless Diffuser Measurements | 125 |
| 6.3 | Discussion of Measured Results | 126 |
| 6.4 | Analysis at Transonic Operating Conditions | 128 |
| 6.4.1 | Influence at Near-Stall Operation | 128 |
| 6.4.2 | Numerical Simulation of Stall Inception | 134 |
| 6.4.3 | Discussion | 143 |
| 6.5 | Analysis at Subsonic Operating Conditions | 144 |
| 6.6 | Summary on Stability | 148 |
| 7 | Performance with Casing Grooves | 151 |
| 7.1 | Vaned Diffuser Measurements | 151 |
| 7.2 | Vaneless Diffuser Measurements | 154 |
| 7.3 | Mechanisms and Discussion | 157 |
| 7.3.1 | Influence on Efficiency and Work Input | 157 |
| 7.3.2 | Influence on Choke Margin | 165 |
| 8 | Summary and Conclusion | 167 |
| | Bibliography | 173 |
| | Appendix | 187 |

Nomenclature

Latin

| | | |
|-------------------|--|--------------------------------|
| a | speed of sound | m/s |
| A | area of cross section | mm ² |
| b | height of flow channel | mm |
| b | groove width | mm |
| c | velocity | m/s |
| C | Sutherland constant | K |
| c_p | specific heat capacity at constant pressure | J/(kg K) |
| d | pipe diameter | mm |
| D | diameter | mm |
| f | frequency | Hz |
| g | groove number | |
| h | specific enthalpy | J/kg |
| k | turbulent kinetic energy | m ² /s ² |
| \dot{m} | massflow | kg/s |
| m' | normalized meridional coordinate | |
| M | Mach number | |
| M_u | tip speed Mach number | |
| n | normal direction | |
| n | rotational speed | rpm |
| p | pressure | Pa |
| r | radius | mm |
| R | specific gas constant | J/(kg K) |
| r, ϑ, z | cylindrical coordinates - radial, circumferential, axial | |
| s | specific entropy | J/(kg K) |

| | | |
|-------------------|--|-----|
| s, ϑ, m | compressor coordinates - spanwise, circumferential, meridional | |
| t | time | s |
| t | groove depth | mm |
| T | temperature | K |
| T | timestep | |
| u | circumferential velocity | m/s |
| v | velocity | m/s |
| x, y, z | Cartesian coordinates | |
| y^+ | dimensionless wall distance | |
| Z | blade number | |

Greek

| | | |
|------------|---|-------------------|
| α | absolute flow angle | ° |
| β | relative flow angle | ° |
| γ | groove inclination angle | ° |
| δ | tip clearance | mm |
| Δ | throttle parameter | mm |
| ϵ | blockage ratio | |
| η_s | isentropic efficiency | |
| η_p | polytropic efficiency | |
| κ | heat capacity ratio | |
| λ | thermal conductivity | W/(m K) |
| λ | work coefficient - $\lambda = \Delta h_t / u_2^2$ | |
| μ | dynamic viscosity | Pa s |
| π | pressure ratio | |
| ρ | density | kg/m ³ |
| σ | standard deviation – root-mean-square | |

| | | |
|-----------|--|-----|
| τ | temperature ratio | |
| φ | vortex cone expansion angle | ° |
| Φ | flow coefficient - $\Phi = \dot{m} / (\rho A u^2)$ | |
| ω | specific turbulent dissipation rate | 1/s |

Subscripts

| | |
|--------|---------------------------------|
| a | axial vector component |
| amb | ambient condition |
| area | area averaged |
| choke | choke operating point |
| CT | casing treatment |
| diff | diffuser |
| gc | grooved casing |
| h | hub |
| imp | impeller |
| in | inlet |
| mass | massflow averaged |
| m | meridional vector component |
| n | counter |
| nozzle | bellmouth nozzle |
| out | outlet |
| peak | peak efficiency operating point |
| red | reduced to reference state |
| ref | reference state |
| r | radial vector component |
| sc | smooth casing |
| s | shroud |
| s | static condition |

| | |
|-------|-------------------------------|
| stall | stall operating point |
| t | stagnation or total condition |
| 1-22 | pressure tap locations |
| 1 | impeller inlet location |
| 2 | impeller outlet location |
| 3 | diffuser outlet location |

Operators, Functions and Symbols

| | |
|------------|---|
| Δ | difference or change of specific quantity |
| ∂ | partial derivative |
| — | averaged value |
| \square | placeholder for groove shape values |

Abbreviations

| | |
|------------|--|
| <i>sc</i> | smooth casing |
| <i>g2</i> | groove configuration with 2 inducer grooves |
| <i>g4</i> | groove configuration with 2 inducer and 2 bend grooves |
| <i>SMI</i> | stall margin improvement |
| <i>SM</i> | stall margin |

Acronyms

| | |
|-------|---|
| BPF | Blade Passing Frequency |
| CFD | Computational Fluid Dynamics |
| CT | casing treatment |
| DES | Detached Eddy Simulation |
| DFT | discrete Fourier transform |
| EXP | experiment |
| FFT | fast Fourier transform |
| HLRS | High Performance Computing Center, Stuttgart |
| ITSM | Institute for Thermal Turbomachinery and Machinery Laboratory |
| LE | leading edge |
| PIV | particle image velocimetry |
| PS | pressure side |
| RANS | Reynolds Averaged Navier-Stokes |
| RMS | root-mean-square |
| SS | suction side |
| TE | trailing edge |
| URANS | Unsteady Reynolds Averaged Navier-Stokes |

1 Introduction

Centrifugal compressors are the major compression device in the industry when it comes to the constant and robust delivery of high pressure gases. Relatively speaking, they offer high durability, cheap manufacturing and low maintenance costs while achieving an unmatched power density with acceptable efficiency. One field of application includes the classic, rather stationary usage in pipeline applications, chemical plants, process industry or refrigeration cycles. Another field are more dynamic applications with varying operating conditions, such as helicopter aero-engines, hand-held devices and turbochargers, where flexible operation and thus wide operating ranges are required. The latter alone stands for hundreds of millions of produced units in operation, which emphasizes the importance of further optimization, even if only small improvements might be realizable. However, not only operating range, but also efficiency, power output for a given size and obviously costs have to comply with the specific requirements and future optimization goals. In general, these goals show contradictory trends, which is why tradeoffs are made in many applications. In particular, this affects the operating range, which is limited by aerodynamic phenomena and instabilities.

An exemplary compressor performance map showing the pressure rise over the massflow rate for different speeds is depicted in figure 1.1. The maximum massflow rate for each single speedline is limited by choke, which is typically determined by the throat area in either the impeller or the downstream diffuser. Therefore, it is for the most part defined by the geometric design of the different components. Towards low flow rates, the speedlines are limited by the occurrence of aerodynamic flow instabilities, such as surge or stall. The point of their occurrence is strongly depending on the aerodynamic design of the compressor. However, for a given design the onset of such phenomena can often be traced back to spatially limited flow disturbances.

Casing treatments (CT) have proven to be an effective method to delay the onset of such disturbances and thus are widely applied to shift the stability line towards lower flow rates. In general, they mainly aim at extending the stall margin (SM), which is defined as

$$SM = 1 - \left(\frac{\dot{m}_{\text{stall}}}{\dot{m}_{\text{choke}}} \right), \quad (1.1)$$

following the definition of Houghton [83]. The stall margin improvement (SMI) is then used to quantify a certain gain with respect to the untreated baseline design, also referred to as smooth casing (sc), whereby

$$SMI = SM_{CT} - SM_{sc}. \quad (1.2)$$

The definition of the stall margin and the SMI are schematically shown for a single speedline in figure 1.2. In this example the shape of the treated speedline remains almost unchanged but is extended to lower flow rates by the application of a CT. However, this improvement normally comes at the cost of a deterioration of the efficiency and also the pressure rise characteristics.

At present, inducer recirculation casing treatments are almost exclusively used in centrifugal compressors due to their large gain in stall margin, despite imposing several considerable disadvantages. These include a significant deterioration of the aerodynamic efficiency and the pressure rise, an increased size and complex manufacturing that results in high costs. Alternative treatments have been investigated mostly for axial compressors due to the demands and huge funding of large aero-engine development.

Thereby, circumferential groove casing treatments that were applied over the rotor tips led to a considerable SMI , while maintaining or even improving efficiency and pressure rise (Müller et al. [123]). Moreover, these grooves are much cheaper to manufacture and do not require additional space and weight.

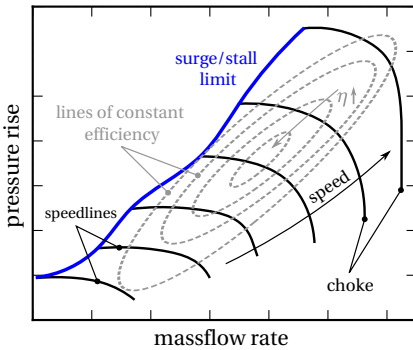


Figure 1.1 – Schematic compressor performance map showing different speedlines, the stability limit, choke and contours of efficiency

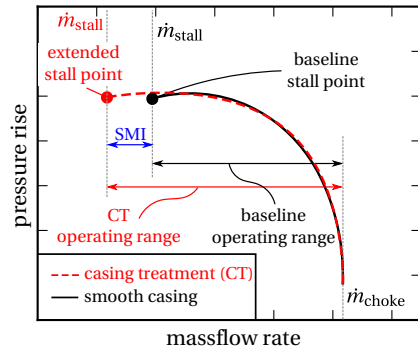


Figure 1.2 – Schematic compressor speedline showing a stall margin improvement (SMI) due to the application of casing treatment (CT)

Objective and Scope of Present Study

Increasing the operating range and the efficiency with such a simple treatment would naturally be highly beneficial for a wide field of centrifugal compressor applications as well. However, a thorough investigation on the applicability in centrifugal compressors is not available in the open literature. Consequently, this thesis studies the application of such rotor casing grooves to a state-of-the-art centrifugal compressor. Thereby, the main aim of the present work is to investigate the following key issues.

- Can such grooves be applied to the centrifugal flow field to effectively increase the compressor operating range?
- How to design optimized groove geometries in terms of *SMI*, efficiency and compressor performance?
- What are the corresponding flow mechanisms that are responsible for the respective effects?

To shed light on these points, numerical simulations as well as experimental tests are carried out. Accordingly, this thesis is structured as follows. Firstly, the background chapter discusses the necessary fundamentals of centrifugal compressor flow and the available literature that is related to the topic. Thereupon, some conclusions for the approach of this work are derived. Chapter 3 then introduces the test object and describes the experimental methods and the test rig setup that is used for the measurements. A typical high-pressure ratio compressor stage is selected and developed to represent the current state-of-the-art. Thereby, two different diffuser configurations are employed to cover a broad range of typical applications and to gain diffuser independent knowledge on the groove effects.

The corresponding numerical methods are presented in chapter 4 alongside their validation with the measured data for the baseline, smooth casing design. Chapter 5 deals with the question on how to design the casing grooves. For this purpose, a parametrized study is performed to investigate the impact and importance of the various design parameters on the impeller flow field and performance. Building on this, the major flow mechanisms that are triggered by the respective groove parameters are discussed. As a result, design guidelines are derived and two high potential groove configurations are identified for testing and further numerical investigation, whereby various speedlines are considered to cover subsonic as well as transonic operating conditions.

Three different impeller casings (baseline smooth casing and 2 groove configurations) combined with two diffusers are tested, which yields a total of six configurations. The respective results are presented and assessed in the final chapters.

Chapter 6 is focused on the influence on the compressor stability line. The measured results in terms of *SMI* are presented and the mechanisms that are believed to be responsible are analyzed in detail. In addition to the test rig data, high fidelity simulations are evaluated to understand the governing mechanisms. Subsequently, the impact on the compressor performance, more precisely the impact on the efficiency and the work input, is evaluated in chapter 7. Again, experimental data as well as CFD results are presented and compared. Finally, a summary of the work and the main conclusions is given in chapter 8. In addition, some recommendations on future work are derived.

2 Background

This chapter introduces the background and discusses the published work, which is relevant for the present thesis. The chapter is subdivided into three main sections. Firstly, the fundamentals of the flow in centrifugal compressors are addressed. The governing flow mechanisms and their impact on the resulting flow field are reviewed with respect to an application of circumferential grooves. The subsequent section focuses on the field of compressor instability. The fundamental flow processes which limit the stable operating range are described. Thereafter, the present knowledge of the corresponding flow mechanisms are reviewed to create a fundamental understanding for potential improvements of casing treatment (CT) applications. The third section then focuses on published studies that involve casing treatments to increase the stable range of operation. The different concepts that are applied in axial as well as in centrifugal compressors are reviewed with specific focus on circumferential casing grooves. Extensive research was performed in this particular field for axial compressors, which is therefore discussed with respect to the centrifugal compressor flow field. Finally, the literature findings are reviewed and the relevant key messages are extracted. Thereupon, the approach of the present study is elucidated.

More basic information on compressors can be found in the books by Cumpsty [23] and Japikse [96]. The fundamentals of the numerical methods that are used within this thesis are not covered here but can be reviewed in Ferziger and Peric [44], Versteeg and Malalasekera [157] or Blazek [10] for example.

2.1 Centrifugal Compressor Flow

This section covers the fundamental mechanisms that characterize the flow in centrifugal compressors. In general, the impeller flow is strongly dominated by the typical shape of the flow channels. On the one hand, this includes the flow turning from the axial inflow to the radially directed outflow. On the other hand, a circumferential velocity component is added as the flow is turned in circumferential direction. In addition, the deceleration due to the increasing cross section area and the opposing acceleration caused by the centrifugal effect are of relevance. The corresponding presence of high centrifugal and

Coriolis forces leads to the development of secondary flows, which strongly affect the resulting impeller flow field.

In general, these secondary flows are considered as deviations from the main flow direction. Typically, they occur as a result of the reduced velocity levels in the boundary layers that are exposed to the pressure gradients of the core flow. Equation (2.1) describes the simple equilibrium of normal pressure force and acceleration for an arbitrary curved streamline, where n is the direction normal to the flow, c is the flow velocity, r denotes the radius of the curvature and p the pressure.

$$\partial p / \partial n = \rho c^2 / r \quad (2.1)$$

As the corresponding pressure gradient is imposed to the respective boundary layers, the curvature radius decreases there to account for the decreased flow velocities. Consequently, the flow near the walls is deflected in direction of the positive pressure gradient, see Greitzer et al. [66] or Cumpsty [23] for example.

The corresponding effects in the rear part of a typical impeller passage are depicted in figure 2.1. Secondary flows from the blade pressure side (PS) to the suction side (SS) emerge as a result of the flow turning in circumferential direction ϑ . Moreover, additional secondary flows are directed in spanwise direction s from hub to shroud at the blade endwalls, due to the flow turning in radial direction.

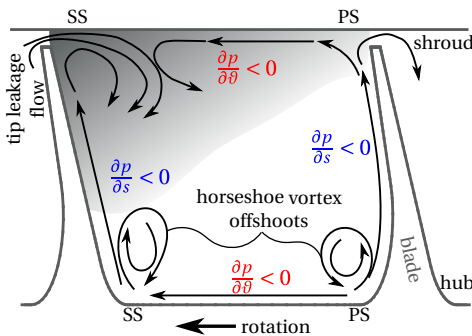


Figure 2.1 – Typical secondary flow mechanisms in a centrifugal compressor passage interacting with the tip leakage flow

As a consequence, low momentum fluid is transported from the boundary layers towards the shroud-SS corner, where they accumulate towards the impeller outlet. This also involves other secondary flows, such as the horseshoe vortices that emerge at the hub leading edges. The respective offshoots are indicated in figure 2.1 as well. These are washed up on the blades and thus contribute to this accumulation. Accordingly, a region of sound flow develops

towards the hub-PS corner. This phenomenon is well known as the so-called jet-wake pattern, which was first introduced by Dean and Senoo [28] as a 2D-model based on experimental observations going back as far as the 30's (Fischer and Thoma [46]).

For unshrouded impellers, a further interaction with the tip leakage flow takes place. Detailed measurements by Eckardt [36, 37] and later Krain [105] significantly improved the understanding of the flow pattern evolution and the associated mechanisms. The shroud and suction side secondary flows deflect the leakage flow, which results in a roll up and a growth of the wake region. Several studies, including Farge et al. [43], Casey et al. [18] and Hah and Krain [70], have shown that the presence of leakage flow moves the wake region away from the blade suction side, depending on its strength, which in turn is influenced by the tip clearance and the blade loading. Moreover, the extent and location of the wake region are depending on the operating point, as shown by the investigations of Johnson and Moore [97, 98].

The increasing pressure levels additionally intensify this effect. A strong pressure gradient develops due to the flow deceleration, particularly at the shroud in the impeller outlet section. Thus, the flow is prone to separation in this region, especially towards lower flow rates where the specific work load increases. Figure 2.2 presents a corresponding sketch, which visualizes this effect in the meridional plane. The location and the extent of such separations is again strongly depending on the compressor design and the operating conditions.

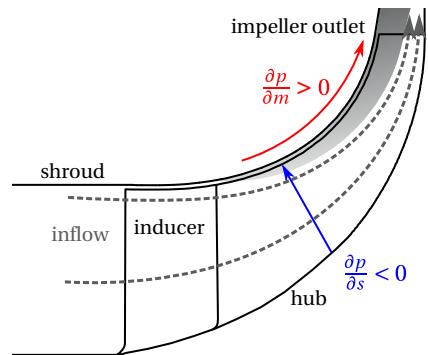


Figure 2.2 – Meridional cross section showing the typical evolution of the near tip flow field in a centrifugal compressor

Another important mechanism that contributes to the highly three-dimensional impeller flow field is the formation of the tip vortex, starting in the inducer. It results from the gap between casing and unshrouded impellers and is driven by the blade loading. A leakage flow from pressure to suction side develops and interacts with the incoming mainflow and the suction side secondary flows. As a result, the leakage flow rolls up and forms a vortex that is transported downstream on its specific trajectory. The direction of

this trajectory is also depending on the operating point as it moves towards the circumferential direction for lower flow rates. Schleer et al. [140] experimentally confirmed a similarity to axial compressor characteristics, which is plausible as there is no flow turning in radial direction in the inducer yet. Shrouded impellers eliminate these leakage flows but for many applications such geometries are unsuitable due to the mechanical integrity aspects.

In contrast to axial machines, most centrifugal impellers feature splitter blades. Usually, these are cut back main blades to increase the impeller throat area. Obviously, they strongly affect the impeller flow field as the main passage is subdivided into two parts. Moreover, the flow to those blades is defined by the incoming flow field, which is strongly affected by the tip vortex in the near shroud region. Figure 2.3 exemplifies the evolution of the tip vortex in a typical centrifugal impeller inducer section with splitter blades. The different colors denote different flow rates from high to low. Additionally, it illustrates the importance of the vortex trajectories for the resulting flow fields. At high flow rates most of the vortex enters the channel near the main blade suction side, whereas at low flow rates the main blade pressure side channel is more strongly affected. At medium flow, the vortex impinges onto the splitter blade leading edge near the shroud, possibly affecting both channels in this example. As a result, increasing blockage regions develop alongside increased mixing effects between the tip and the core flow that subsequently results in higher losses.

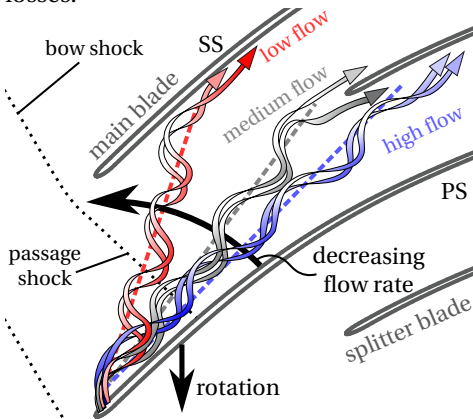


Figure 2.3 – Exemplary tip vortex trajectory evolution in a centrifugal impeller inducer section with splitter blades

The existence of shocks in high speed, transonic impellers is another mechanism that strongly affects the development of the impeller flow field. The structure of these shocks is comparable to those of axial compressors for axially aligned inducers. According to Cumpsty [23], a detached bow shock and a passage shock are formed in front of the main blade leading edge in the transonic region near the tip, see sketch in figure 2.3. The experiments and calculations of Eisenlohr et al. [38] showed a compa-

rable shock pattern for a centrifugal impeller with a pressure ratio of up to 6. Again, the shape and direction of these shocks is strongly depending on the specific operating conditions. Furthermore, they significantly affect the tip vortex formation as well as the growth of the boundary layers and the secondary flows, as shown for example by Ibaraki and Iwakiri [88], Ibaraki et al. [89] and Yamada et al. [167]. In particular the passage shock, which impinges on the neighboring blade suction side, slices the vortex trajectory and interferes with the local blade boundary layer. Subsequently, the thickness of the boundary layer increases and it becomes more prone to separation. Similar to the vortex trajectory, the shock orientation changes for different inflow angles. A reduction in flow rate results in incidence on the main blade leading edge which moves the passage shock impingement location upstream in the flow channel. To conclude, the interaction of the governing flow mechanisms leads to complex, highly 3-dimensional flow fields, which are typical for unshrouded centrifugal impellers. Moreover, the level of complexity is strongly influenced by the flow rates, leading to extremely distorted flows towards lower massflows. It is obvious that the generation of losses and thus impeller efficiency is closely connected to the governing flow mechanisms, which are mentioned above.

According to Denton [30] and also Greitzer et al. [66], the generation of losses in turbomachinery flows and thus a rise in entropy is caused by the following processes: viscous effects in boundary layers, mixing processes, shocks and heat transfer across temperature differences. To maintain, or even improve efficiency, an application of circumferential groove casing treatments thus needs to reduce or at least maintain the entropy production of those processes. Therefore, the prevention of non-uniform distortions which result in mixing losses, such as the tip flow field formation, is of particular interest as the other mechanisms can be only influenced to a certain degree.

The resulting non-uniform discharge flow of the impeller subsequently affects the flow in the diffuser. Additionally, the sensitivity of the diffuser performance is strongly depending on the diffuser configuration (vaned or vaneless type). Inoue and Cumpsty [90] performed experiments with different diffusers and reported that the distorted inflow is rapidly mixed out in vaned diffusers, whereas the distortion was clearly visible at large radii in a vaneless diffuser. The rapid mixing in vaned diffusers was confirmed later by Filipenco et al. [45] and Deniz et al. [29], who performed studies on different types of vaned diffusers (cascade and straight channel). They report that the diffuser performance directly correlates with the momentum averaged flow angle of the impeller discharge flow. Consistent to that, Everitt et al. [40] also conclude

from their studies on radial vaned diffusers that the flow angle, or more specifically the incidence at the diffuser vanes, has the highest impact on diffuser performance. However, they also present a ranking where the latter is followed by the inflow Mach number, the circumferential non-uniformity and the spanwise non-uniformity.

The performance of vaneless diffusers is as well mostly governed by the inflow angles, which determine the flow path through the diffuser. High flow angles result in an extended length of the flow paths, which increases the frictional losses. When exceeding critical flow angles, flow reversal on the diffuser endwalls may occur (Inoue and Cumpsty [90], Japikse [96]), leading to separation and reduced pressure recovery. In contrast to vaned diffusers however, circumferential and spanwise non-uniformity is more important as the distorted flow remains present in the diffuser and thus also affects the subsequent components.

In conclusion, diffuser performance, independently of the type of diffuser, seems to be mostly defined by the impeller discharge flow angles, the inflow Mach number and the circumferential distortion levels. Therefore efficient casing treatments, which do not degenerate stage performance or efficiency, should be designed with respect to those findings.

2.2 Compressor Stall and Surge

The operating range of compressors is limited towards low flow rates due to the occurrence of unstable flow phenomena that deteriorate the compressor pressure rise by a breakdown of the sound flow through the compressor. These phenomena are commonly known as stall and surge, where the latter is a large scale instability involving the whole compression system. Surge is characterized by large massflow and pressure fluctuations in the flow direction, up to completely reversed flows that affect the whole system. Stall however is of smaller scale and can reach sizes from only parts of a single flow passage up to large parts of the circumference of the respective component. Its disturbance is of circumferential nature at a local streamwise location and it is also accompanied by pressure and massflow fluctuations, but at a much smaller scale, see Greitzer [62, 64]. If stall occurs in a single or in multiple passages, the corresponding blockage leads to increased incidence on the adjacent blade, resulting in a propagation of the stall cell along the circumference. Therefore, it is often referred to as rotating stall and it often precedes surge. Nevertheless,

abrupt onset of surge has been observed as well, in particular for centrifugal compressors (Emmons et al. [39]). For engine type compressors, Day [25] concluded that surge is not only always preceded by at least a brief period of stall but also caused by it. Besides the deterioration of the performance, the periodic characteristic of both can lead to mechanical excitations of the blades, which may exceed the stress limits of the highly loaded structures and thus lead to vibration induced failure (Haupt et al. [75], Japikse [96]). However, it is noteworthy that the drop in outlet pressure is much less pronounced in centrifugal compressors as a substantial part of the pressure rise is performed by the centrifugal effect (Cumpsty [23]). Therefore, an operation on the positive slope of the characteristic sometimes is still stable and in contrast to axial compressors, the occurrence of stall does not always impose a hard limit for the operating range.

Extensive research has been undertaken to understand and prevent the occurrence of stall, mostly driven by jet engine developments beginning after world war II, which is summarized by Day [27]. Up to now, major advances have been made, but the complex unsteady mechanisms that are responsible for the inception of stall are still not yet fully understood. Based on early experimental investigations and theories (Emmons et al. [39], Marble [114]), analytical models were developed to describe the stall characteristics and behavior (Greitzer [62, 63], Moore and Greitzer [120]). Moreover, indications on the existence of circumferential perturbations prior to stall were made. Experimental proof of these modal perturbations was provided by McDougall et al. [115] and also later by Day [24]. Small amplitude disturbances steadily grow into a fully developed rotating stall over tens to hundreds of rotor revolutions and is consequently referred to as modal stall. The initial stage of this evolution is well described by linear stability analysis [120], whereby various attempts were made to detect and actively suppress these modal perturbations (Day [26], Garnier et al. [60], Haynes et al. [76], Paduano et al. [127, 128]).

Another stall inception mechanism was identified by Day [24] as well. He observed short length-scale, spike-type disturbances in the tip region which appeared abruptly in contrast to the long length-scale modal type disturbances. Figure 2.4 depicts the typical nature of both of those disturbances by means of near tip velocity measurements from Day's work. Camp and Day [15] found that modes can only develop in axial compressors if no spikes are formed due to localized overload or excessive incidence first. They conclude that the main difference between the two is that modes are a phenomenon of the whole compression system flow, whereas spike stall inception is localized

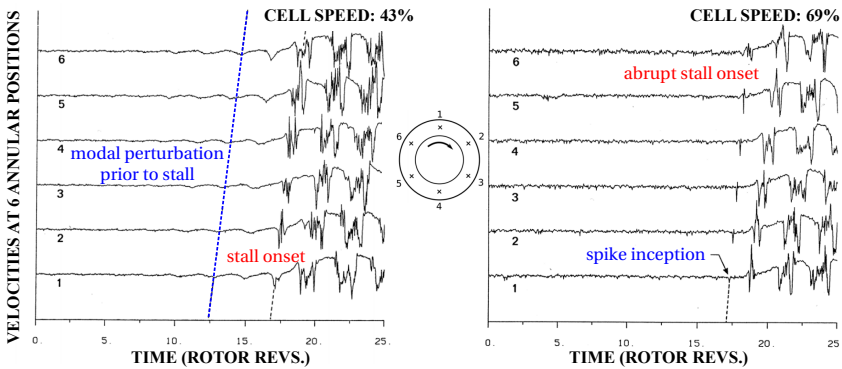


Figure 2.4 – Velocity measurements during modal (left) and spike-type stall inception (right), reprinted from Day [24]

to an individual blade row and a local flow disturbance. Normally, less than 10 rotor revolutions elapse before the stall is fully developed and by contrast with modal waves, the occurrence of spikes does not simply follow linear analysis.

Somewhat later, similar observations were made in centrifugal compressor testing. Modal waves were detected in the Purdue Low Speed Centrifugal Research Compressor for both vaned and vaneless diffuser configurations by Lawless and Fleeter [106, 107], as a precursor to fully developed stall. Spakovszky and Roduner [147] performed experimental studies for a high pressure ratio centrifugal compressor with a vaned diffuser. They showed that both, spikes and also modal perturbations, can lead to the onset of stall in the vaneless space between impeller and diffuser by varying the endwall leakage at the impeller exit. A loss in surge margin of about 50% was measured for the modal type inception with opened bleed valve. Moreover a significant change in the shape of the speedline was observed. Similar to the conclusions of Camp and Day [15], a spike emerges in the horizontal part of the speedline at low massflows, whereas the formation of modal waves at the peak of the characteristic results in a negative slope of the total pressure rise towards stall.

In general, every sub-component, namely the impeller, the vaned diffuser and also the vaneless diffuser, can be involved in the stall inception process in centrifugal compressors. Apart from that, the asymmetric shape of the volute imposes pressure perturbations that also can influence the stall behavior of

a specific stage. Therefore, the interaction of the complete system is of vital importance as the individual components are closely coupled [96].

Different types of stall have been identified, which can be triggered by either spike or modal type stall inception mechanisms. Frigne and Van Den Braembussche [48] for example, experimentally identified different groups of stall in a centrifugal compressor with different vaneless diffuser configurations. They distinguished between rotating stall in the diffuser and mild, abrupt and progressive impeller stall. The distinction was made by different stall cell propagation speeds, which were increasing in the same sequence. Moreover, the relative pressure amplitude levels increased as well, corresponding with a reduction of the stall cell number. Kämmer and Rautenberg [99] tested a 2.7 pressure ratio centrifugal compressor with vaneless diffuser and observed a dependency of the stall location for different rotational speeds. At low speeds inducer stall was present, whereas at high speeds, stall in the vaneless diffuser limited the operating range. Hunziker and Gyarmathy [87] also found different types of stall for various rotational speeds in tests with vaned diffusers (15° to 30° inflow angle). Moreover they showed that a change in the diffuser blade angle can also affect the stall patterns.

In contrast to modal perturbations as a result of system instability, the events that lead to the emergence of spikes are much smaller in scale and less well understood. Different processes, that are nonlinear, three-dimensional and unsteady are believed to be involved, depending on the flow fields in the specific components.

2.2.1 Impeller Stall

There are substantial indications which link the path to stall in impellers to the flow behavior in the tip region. This has been investigated more extensively for axial compressors but some of the principles are believed to be applicable to the centrifugal inducer as well. Early on, Camp and Day [15] suggested that the spike origination is linked to a flow separation at the blade suction side near the rotor tip. Hoying et al. [84] numerically investigated an isolated rotor and identified the spillage of the tip vortex flow to an adjacent passage to be a cause for spike-type stall inception. They concluded that a circumferential orientation of the tip vortex trajectory can be used as a criterion for spike stall inception in tip critical rotors. This was also observed earlier in the numerical work of Adamczyk et al. [3] who also observed an increase in blockage due

to the accumulation of low energy fluid near the tip, until the calculations diverged.

Several studies suggest that the breakdown of the near tip flow field, that is accompanied by the onset of stall, is connected to a breakdown of the tip vortex [54, 55, 138, 166, 168]. This breakdown occurs if the vortex is subjected to a certain pressure gradient, for example caused by shocks or other flow resistances and results in an increased blockage of the passage. The type of breakdown is likely to be of a spiral type and leads to strong fluctuations and eventually to flow separations, see Furukawa et al. [54, 55]. Hazby and Xu [77] presented a numerical study for a centrifugal compressor in which similar observations were made. They associated the vortex breakdown with the interaction of the tip vortex with the following splitter blade, which was accompanied by a flow separation at the splitter blade tip leading edge. Yamada et al. [167] used detached eddy simulations (DES) to investigate two different centrifugal impellers. They found that one of the impellers experienced a similar vortex breakdown of the main blade tip vortex, which led to blockage growth and ultimately to flow spillage at the main blade leading edge. The second impeller showed a different type of disturbance. The increased blockage results from tornado shaped vortices, which are shed from a main blade suction side separation. These tornado-like vortices were first introduced by Inoue et al. [91] who experimentally studied the characteristics of small stall cells at low speeds, which were argued to be similar to the disturbances involved in the spike inception process.

Vo et al. [158] presented a criterion for spike formation in axial compressors according to which spillage of the tip vortex flow, accompanied by a trailing edge back-flow, needs to be present in the near tip region. They also reported that a sudden increase in blockage gives rise to unsteadiness in their computations. This was confirmed experimentally in the studies of Deppe et al. [31]. Hah et al. [69] described the same path to stall in their investigations of a transonic axial compressor. Wu et al. [164, 165] performed experimental and numerical studies for an axial flow compressor. They also confirmed the criterion of Vo et al. [158] and linked the occurrence of the back-flow and the forward spillage to the blockage induced by the unsteady tip vortex breakdown. Figure 2.5, reprinted from Tan et al. [154], visualizes this criterion alongside the typical pressure rise characteristics for spike inception in contrast to the modal inception type. It shows that spike inception occurs abruptly due to local unsteady flow effects, whereas modal type stall results from a system instability as the peak of the pressure rise characteristic is reached.

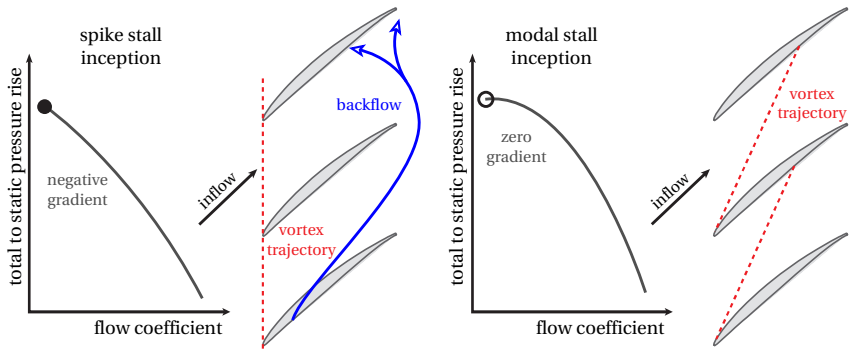


Figure 2.5 – Stall inception mechanisms in axial compressors according to Tan et al. [154]

The work of Pullan et al. [131] focuses on the mechanisms and flow structures that lead to the onset of spike-type stall. They propose that vorticity, shed from a leading edge separation, rolls up to a discrete vortex that stretches from the suction side to the casing and subsequently forms the spike disturbance. They compared their numerical calculations to several sets of experimental data, whereby a good agreement was observed. They also stress that the tip leakage flow influences the spike formation but its existence is not a requirement, as seen from zero clearance calculations. Moreover, they conclude that the formation can also be triggered by a downstream separation that leads to increased blockage and thus incidence. Hewkin-Smith et al. [79] extend this and show that depending on the clearance, either blockage due to a downstream separation, or the tip leakage jet causes the spillage. The same criterion is reported to be valid for a fan stage investigated by Kim et al. [103].

The work of Yamada et al. [170] reports the same path to spike stall inception. They performed experiments and DES for a low speed axial compressor and showed that in their case, the blockage that leads to flow spillage is resulting from the shedding of tornado-like vortices at the blade suction sides. A corresponding sketch of the mechanisms is given in figure 2.6, also visualizing the findings of Pullan et al. [131]. The detailed measurements of the pre-stall spike inception behavior by Weichert and Day [159], as well as the investigation by Dodds and Vahdati [32, 33], also indicate the existence of such vortices. However, a recent study of Yamada et al. [169] reports that these vortices are not

solely restricted to the tip region as they observed the spikes being initiated by hub-corner stall in a multistage axial compressor.

Similar observations have been made for the stall originating in centrifugal impellers as well. Early on, measurements linked the inception processes to the inducer tip region [96, 119]. Schleer et al. [140] performed high resolution measurements of the pressure distribution at the casing of a centrifugal compressor towards unstable operation at subsonic operating conditions. Just like for axial compressors, the tip vortex trajectory is aligned in circumferential direction just before the onset of stall.

A further reduction of the flow rate then triggers a rotating stall in the vaneless diffuser. This suggests that despite observing the stall cells in the diffuser, the flow in the inducer can be responsible for the inception. Lou et al. [111] tested the stability of a high speed centrifugal compressor with a vaned diffuser during speed transients. Time-resolved static pressure measurements at different meridional locations identified a spike at the impeller leading edge triggering the stall, which is localized in the impeller in their tests.

Recently, sophisticated numerical studies on the stall inception processes were performed in centrifugal compressors as a result of increasing computational resources. Guo et al. [68] investigated a centrifugal compressor with a vaned diffuser, where leading edge spillage at the main blade initiated the stall. The results indicate that the circumferential location of the stall onset is defined by the volute tongue position. Similarly, the investigations of Yang et al. [171, 172] and Zhang et al. [174] also concluded that up- and downstream distortions, induced by the volute or an inlet bend, influence the location of the spike formation due to spillage.

Bousquet et al. [12, 13] investigated the flow field in a high speed centrifugal compressor with a vaned diffuser and a return channel instead of a volute. They also report a similar path to stall as for axial compressor cases. The vortex trajectory at the main blade becomes perpendicular to the axis of rotation

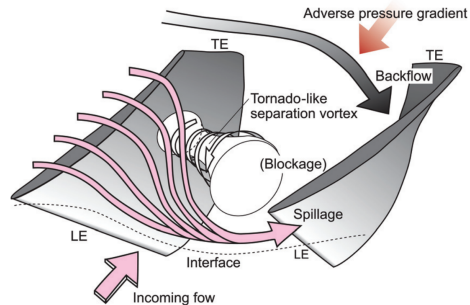


Figure 2.6 – Illustration of tip flow spillage as a result of tornado-like vortex shedding in an axial compressor from Yamada et al. [170]

towards smaller flow rates. Moreover, tornado-type vortices are shed from the main blade leading edge and travel to the adjacent blade pressure sides. Nevertheless, additional modal waves are observed in the vaneless space of the diffuser, which they suggest to trigger diffuser stall despite the occurrence of spikes in the inducer, see also Buffaz and Trébinjac [14].

Summing this up, impeller stall is for the most part connected to the inducer tip region. Flow disturbances arise due to increased blockage and unsteadiness, which destabilize the local flow field. At subsonic conditions, the tip vortex becomes perpendicular and the flow spills in front of the main blades. At transonic operating conditions, the breakdown is furthermore associated with increasing blockage due to the interaction of the tip vortex with the splitter blade and the passage shock. Moreover, inducer stall does not necessarily lead to full instability of the complete stage in centrifugal compressors. Especially at low rotational speeds, spillage and stall can lead to the formation of a quasi-stable recirculation zone before surge occurs.

The criterion proposed by Vo et al. [158] might be similarly applicable to centrifugal compressors, whereby a different flow phenomenon replaces the trailing edge back-flow requirement, that contributes to the blockage in the tip region. However, the exact details of the mechanisms vary for different types of stages and the individual path to stall is not yet fully understood, nor sufficiently predictable.

2.2.2 Diffuser Stall

Stall occurring in diffusers is always strongly depending on the discharge flow of the impeller. For vaned diffusers, the incidence of the incoming flow with respect to the blade inlet angle is of paramount importance for the emergence of separations. Both modal wave and also spike-type inception are reported to emerge in the vaneless space between impeller and vaned diffuser, especially for highly loaded stages at high speeds [145, 147, 160, 178]. However, modal wave stall inception is well described by linear compression system modeling [120].

Substantial evidence exists, that locates the stall inception mechanisms to the diffuser inlet region, namely the vaneless and semi-vaneless space in front of the blade channels. To the knowledge of the author, no publications that report otherwise are available. After early experimental observations, summarized for example in [96], recent studies focused on the detailed mechanisms

that lead to the inception of stall. Everitt and Spakovszky [41] performed isolated diffuser calculations to obtain insight into the mechanisms of spike initiated stall in vaned diffusers. They suggest that the inception is triggered by a diffuser leading edge separation in the tip region. Two different effects contribute to the separation and define its location. Firstly, the flow becomes oriented in circumferential direction due to the swirl and the decreasing flow rate. Secondly, the jet-wake discharge pattern leads to a momentum deficit near the shroud, whereby the separation occurs near the tip. This resembles the criteria of Vo et al. [158] in axial compressor spike inception, though different flow effects are involved. Similar to axial compressor spike inception, vortical structures arise, which are transported radially inwards into the vaneless space and propagate in circumferential direction as a result of near casing back-flows that emerge towards stall. These structures form low stagnation pressure regions, then accumulate and ultimately lead to flow breakdown and the onset of rotating stall.

Similar observations were made in the studies of Bousquet et al. [12, 13] and also Zhao et al. [175], where a separation at the diffuser tip leading edge is observed and suggested to contribute to the onset of stall as well. Further experimental and numerical investigations are performed by Fujisawa et al. [50, 51, 52], who analyze the behavior of a centrifugal compressor with a vaned diffuser towards unstable operation. They conclude that the characteristic of the emerging disturbances are again tornado-type vortices that introduce further flow blockage in the diffuser. In their case an additional leading edge vortex forms and merges with the tornado-vortices, resulting in large blockage regions that then develop into stall cells. Furthermore, they stress the importance of the impeller flow field for the vaneless space spike inception. Despite initially occurring at the diffuser inlet, the flow perturbations due to rising blockage and unsteadiness in the impeller play a major role in the stall inception process.

The behavior of vaneless diffusers is somewhat different from vaned ones. Jansen [94] performed fundamental studies on vaneless diffuser stability and was the first to conclude that the stall could be triggered by a local return flow. Large absolute flow angles resulting from the swirl of the flow lead to almost circumferential streamlines. Therefore, the flowpaths become even longer towards decreasing flow rates and viscous friction increases. The onset of stall is then likely to occur in the boundary layers. The streamlines are curved more inwardly than in the core flow and at some point the adverse pressure gradient causes a radial flow reversal. Several studies [2, 49, 141]

confirmed and extended those theories and correlations and showed that a critical flow angle exists, in which flow reversal takes place and initiates a flow separation. This flow separation becomes unsteady, rotates and develops into stall cells with further throttling, depending on the specific flow conditions. This is also valid for steady, uniform inflow conditions and thus the process is independent of the interaction with the impeller [96]. However, the variation of the flow angle due to circumferential inhomogeneities of the impeller discharge flow, can affect the point of stall inception. Schleer and Abhari [139] for example, present detailed measurements of the flow in a vaneless diffuser and report strong velocity and flow angle variations in circumferential direction. Moreover, they investigated different tip clearances and showed that regions of reversed flow near the shroud are existing for a larger clearance ratio, which results in earlier stall inception. The characteristic of the flow reversal can be complex, whereby the flow separation sometimes starts at the shroud, reattaches and switches to the hub endwall, see Inoue and Cumpsty [90] and Senoo et al. [142] for example. Furthermore, the critical flow angle is strongly depending on the shape of the diffuser, in particular the width to radius ratio, see Abdelhamid [1]. Narrow channels in general offer a wider stable range than wide channels. More recent publications focus on the use of CFD to either study the mechanisms of the stall evolution in detail or to predict the critical inflow angles [72, 149]. Despite reporting different stall patterns, the inception of rotating stall in vaneless diffuser channels is always linked to an initial flow reversal or separation at one of the endwalls.

2.3 Casing Treatments

Influencing the flow to achieve an extension of the stable operating range has been under investigation ever since aerodynamic instabilities in compressor flows have been discovered. Casing treatments came into focus after the causes, or rather some of the inception mechanisms of stall and surge were linked to the near tip flow field. This is obvious as most treatments, in particular passive ones, can only influence the flow in their immediate vicinity. Based on experiments with an axial compressor, Greitzer et al. [65] postulated that only tip-critical rotors in which the stall originates in the tip region can be positively influenced. In other words, and also transferable to centrifugal compressors, the impact of the casing treatment on the flow field needs to affect the dominant stall origination processes. According to Vo et al. [158],

any technique that delays these processes eventually leads to an improved stall point.

Passive treatments, such as circumferential grooves, affect the entire operating range from choke to stall. Therefore, a sound understanding of the corresponding mechanisms is required in order to assess their effectiveness and transferability to other compressor designs. In general, the major aims of such treatments are to stabilize the flow towards stall, in such a way that no deterioration of the efficiency takes place. Moreover, an accurate prediction of the performance is required to enable optimized designs for the respective applications.

The following sections provide an overview of the studies that have been published in the past to establish an understanding of the related mechanisms. Firstly, existing investigations and applications of casing treatments concerned with centrifugal compressors are reviewed to provide an integration of the present work into the overall picture. Subsequently, the existing findings on circumferential grooves, almost exclusively found for axial compressors, are discussed alongside other relevant studies. Due to its relevance for this work, statements on the design and on the governing flow mechanisms, that could be transferable to centrifugal compressors, are of particular interest.

It's worth mentioning that a great variety of further casing treatments has been investigated for axial compressors, driven by the aero-engine development. A corresponding overview of the historic development of passive casing treatments up until the year 2006 can be found in the report of Hathaway [74].

2.3.1 Centrifugal Compressors

Casing treatments in centrifugal compressors have gained much less attention than in their axial counterparts. The most common ones are illustrated in figure 2.7. Publicly available research is very limited except for the so-called ported shrouds, which is presently the only casing treatment of industrial relevance in centrifugal compressors. These consist of an inducer internal bleed system that allows for a recirculation of fluid between the inducer (some distance downstream of the main blade leading edge) and the inlet upstream of the impeller. A conceptual sketch including the flow mechanism of such a treatment is given in figure 2.7a. Towards surge, flow from the inducer is transported to the inlet tip region due to the adverse pressure gradient. This artificially increases the inducer tip flow-rate, which therefore reduces incidence.

Thus, the inducer is less prone to separation and less likely to become unstable. Moreover, the low momentum fluid regions that form near the shroud are sucked in and thus are partially removed. Both effects contribute to a delay of the inducer stall inception as mentioned by Ishida et al. [93] and also Tamaki [153]. Considerable improvements in surge margin are reported for a variety of different stages, in particular for high rotational speeds [42, 47, 86, 144].

Furthermore, the treatment can also offer an increase in the choke flow-rate. If the impeller is choking and the bleed slot is located downstream of the throat, the pressure gradient is inverted and the inlet flow can bypass the throat. Thus, a larger flow-rate can pass the compressor and the range is extended. However, choking in highly loaded compressors often happens in the vaned diffuser, in particular at high speeds, which thus wipes out the advantages of the treatment near choke. However, as a part of the flow recirculates, the specific work input decreases, which results in lower pressure ratios and inferior efficiencies. If mentioned at all, drops of several percentage points in peak efficiency are reported (mostly in the range of 2 % to 4 %), see Sivagnanasundaram et al. [144] and Hunziker et al. [86]. Moreover, substantial differences in the performance maps occur and subsequently have to be anticipated during the design process. As a consequence, extensive effort has been made to reduce the losses that are associated with the recirculation devices by optimizing their geometrical design [92, 148]. Chen and Lei [19] and also Sivagnanasundaram et al. [144] showed that introducing cavity guide vanes can significantly reduce those losses. Nevertheless, the high costs prevent an economically attractive application, which is why only simple designs are found in high volume applications such as turbochargers. In general, the range extension in these devices comes with a substantial decrease in overall

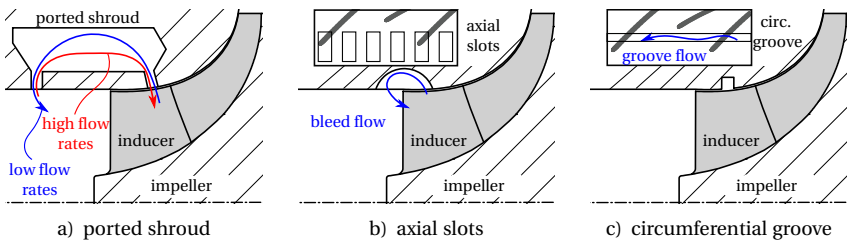


Figure 2.7 – Conceptual drawings of different forms of centrifugal compressor casing treatments

efficiency and pressure ratio. Moreover, as the inclusion of such treatments in the design process becomes mandatory, the costs for the stage development increase.

Research on other treatments and also examples of applications are scarce. A very limited number of publications deals with casing treatments in centrifugal compressors aside from recirculation systems. Most of them are inspired by work on axial compressors thought to be extendable to the centrifugal flow field. One of the earliest reports on centrifugal compressors comes from Amann et al. [4]. It deals with the experimental investigation of a circumferential casing slot located at the impeller trailing edge that is connected to a chamber. They report an increase in range as the vaned diffuser tip loading is reduced, though no statements are made regarding the impact on the efficiency. Jansen et al. [95] somewhat later tested a high number of different casing treatments, such as axial slots in the impeller inducer and rotating slots at the hub of the vaned diffuser inlet. Their early experiments showed considerable range extensions for a few of the treatments. However, those were accompanied by a strong deterioration of the performance.

More recently, Yang et al. [173] numerically investigated an inlet duct treatment consisting of circumferentially arranged holes in front of the impeller leading edges, which add a certain pre-swirl to the flow in the tip region. The treatment acts like an inlet guide vane specifically designed for the near tip region. They applied it to a turbocharger compressor with a vaneless diffuser and predicted a range extension, which is accompanied by a decrease in efficiency and pressure rise.

Axial slots in the inducer region, inspired by axial compressor applications ([53, 130, 146]), are another treatment that has been under investigation to stabilize the inducer flow field. Figure 2.7b illustrates the concept of such a treatment offering axial bleed flow recirculation. Harley et al. [73] recently applied and tested such slots for a typical automotive turbocharger compressor with a vaneless diffuser. They showed that this kind of treatment can offer a similar range extension and performance as a ported shroud treatment. However, they limit the applicability to high trim compressors, where typically large recirculation zones emerge in the inducer towards low flow rates. Furthermore, they conclude that axial slots could decrease the required axial length of the stage with comparable costs as for a ported shroud system. Similar conclusions are drawn by Koyyalamudi and Nagpurwala [104] from their numerical work. Early experimental studies of Jansen et al. [95] and Fisher [47] also report an increase in surge margin, which is associated with a

drop in efficiency of several percentage points. Another study on the design of such slots for a mixed flow compressor is published by Du and Seume [35]. Based on numerical design optimizations they state that the *SMI* for axial inducer slots directly correlates with the deterioration of the peak efficiency. Axial compressor research confirms this and it is generally accepted that the considerable *SMIs* of axial slots come at the cost of higher losses, compared to circumferential grooves, shown for example by Hembera et al. [78], Lu et al. [112] and Du and Seume [35]. This is mostly attributed to the increasing work input that is required for a certain enthalpy rise due to the axial recirculation in the slots, similar to ported shroud treatments.

A further treatment that was also inspired by axial compressor research [8, 155] is introduced by Taghavi-Zenouz et al. [151], who experimentally and numerically investigated various configurations of a stepped tip gap casing treatment at the impeller exit. The treatment is comparable to a very wide and shallow circumferential groove, stretching from about 70 % to 105 % of the blade chord length. Their results show an increase in surge margin of up to 10 % for the shallow configurations which reverses for deeper gaps. Efficiency is also maintained for the shallow gaps but the pressure ratio is reduced by about 2 %. However, due to the rather low peak efficiency of the tested impeller of only 60 % it remains unclear if their findings are transferable to modern, more efficient impeller designs. As the onset of stall often originates in the vaned diffuser, treatments that stabilize the diffuser flow are under investigation as well. Galloway et al. [56, 57] report the application of a diffuser channel recirculation duct as well as a circumferential cavity at the diffuser shroud. Both treatments offer an increase in surge margin for most of the performance map, while almost retaining the efficiency. Chen et al. [20, 21] performed numerical studies with a rectangular groove applied in a vaned diffuser compressor. The steady-state calculations predicted an increase in range of up to 10 % but it remains unclear if those results are transferable to real applications.

Common for all studies that have been published with regard to centrifugal compressor casing treatments is the localization of the target region near the blade tips, to either influence the emergence of stall in the impeller or in the following diffuser. The same applies for circumferential grooves in the rotor, that are the focus of the present study. Figure 2.7c presents an exemplary single groove configuration alongside the different treatments mentioned above.

2.3.2 Circumferential Grooves

Until now, only very limited reports are available on the application of circumferential grooves in centrifugal compressors. A single shallow groove near the impeller outlet has been tested among some other treatments by Jansen et al. [95]. They report an increase in range for all considered speedlines when tested in a vaneless diffuser configuration. However, the *SMI* compared to axial slots was rather small but the efficiency was found to remain almost unchanged from the smooth wall configuration. Fisher [47] also presents two variants of grooves that were applied in an automotive turbocharger compressor. A single rectangular groove directly above the leading edge was found to be ineffective, as both range and efficiency were considerably reduced. In contrast to that, a rounded groove near the outlet proved to be effective for an individual speedline where a large improvement was observed, whereas the remaining performance map was unaffected. A similar effect is reported in the work of Bareiss et al. [6] who tested 3 configurations of multiple grooves at the outlet of a truck turbocharger impeller. A large *SMI* is observed in their experiments for a single speedline. The responsible mechanisms could not be identified, as the steady-state CFD calculations did not capture this trend of *SMI*. Nevertheless, it was shown that the application of grooves enables a circumferential transport of the tip leakage flow in such a way, that it reduces the accumulation of low momentum fluid in the wake region. Moreover, the experiments also showed an increase in pressure rise towards stall for high speeds while the changes in efficiency were negligible. Gao et al. [58, 59] present some limited numerical results for multiple inducer grooves applied to Krain's impeller [105], with and without additional bleed holes. The steady-state calculations suggest an increase in surge margin for the only untreated groove configuration, while retaining pressure rise and efficiency. They attribute this to blockage reduction and removal of low momentum fluid near the tip, but no further evidence is presented.

In contrast to centrifugal compressors, circumferential grooves are among the most common applications of casing treatments in axial compressors. On the one hand, this is due to their effectiveness in relation to the efficiency losses compared to other treatments, such as axial slots [53, 78, 109, 112]. On the other this is caused by their simplicity and modest size, which allows for simple and cost effective manufacturing and integration.

Some of the first reports of circumferential groove casing treatments to extend the stable operating range of compressors are based on the work at

NASA Lewis Research Center in the 1970s. After it was found that those could provide beneficial effects, numerous different configurations were tested for jet engine compressors. The main questions that came up were concerned with the optimum design and the understanding of the corresponding flow mechanisms that lead to an extension of the stall margin.

Groove Design

Based on previously published work of Bailey [5], Prince et al. [130] and others, Wisler and Hilvers [162] summarized rules-of-thumb for an optimized design. According to those, the grooves should be placed in the mid 60 % of the chord as treating either the leading or the trailing edges is ineffective. They propose a groove aspect ratio of greater than 3 and a depth which is greater than 15 % of the blade spacing. Moreover, they summarize that the most effective treatments have a groove number that leads to an opened area of 65 % to 75 % with a ratio of cavity to land width greater than 2.

Increasing experimental efforts and advancing measurement techniques, combined with the development of numerical methods, led to advancements in the design of optimized grooves. Based on today's knowledge and the present database, the suggestions for the design of efficient casing grooves in axial compressors are discussed below. The most important values and conclusions that are drawn from several different sources for axial compressors are additionally summarized in figure 2.8.

- *axial location*

Experience to date shows that grooves should be placed completely above the blades in any case, as efficiency and effectiveness decrease substantially if placed upstream of the leading or downstream the trailing edges, see Kim et al. [101] and Mirzabozorg et al. [118] for example. In general, a placement near mid-chord or near the leading edges is found to be most efficient in terms of a range extension. Houghton and Day [81, 82] experimentally and numerically investigated different groove locations and found two maxima for the *SMI* at 8 % and 50 % axial chord. Tests with a second compressor confirmed these results. Numerous other studies, namely the ones of Huang et al. [85], Nezym [125], Perrot et al. [129], Rabe and Hah [133], Wu et al. [163] and Zhao et al. [176], also suggest that grooves in the front area seem to be most efficient in their respective cases. The studies of Du et al. [34]

and Mirzabozorg et al. [118] however, revealed optimum locations near mid-chord. Grooves towards the trailing edges are often found to be ineffective [53, 117, 133, 143]. As a consequence, Nezym [125] and Hembera et al. [78] suggest to reduce the depth of those grooves.

- *groove width*

No detailed studies focusing on the optimized width of a single circumferential groove are presently available. However, most treatments reported to be effective have a width of about 10 % of the axial chord length [81, 82, 143]. Wu et al. [163], for example, experimentally investigated three different groove width configurations and the smallest values of about 10 % chord provided the highest *SMIs*. Anyway, the effectiveness and the impact on performance and efficiency depends on the specific compressor design. Choi et al. [22] presents a design of experiment (DOE) optimization that yields a larger optimized value of 16 %, whereas Ross et al. [135] and Rolfes et al. [134] even use widths of 20 % and 26 %. In contrast to that, considerably smaller values of 5.8 % and 7 % are used in the cases of Mao et al. [113] and Sakuma et al. [136] for example.

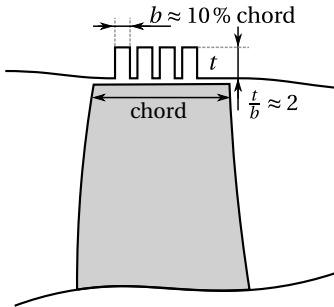
- *groove depth*

The statements regarding optimized groove depth are somewhat inconsistent throughout the published investigations. Most studies that present effective casing treatments use a groove depth that is at least double the groove width, up to an aspect ratio of 4. Comparative studies [123, 136, 176] suggest that such deep grooves are superior to shallow ones in terms of a range extension. Nevertheless, considerable *SMIs* are reported for shallower grooves with an aspect ratio below one as well. The results of Rabe and Hah [133] show that such shallow grooves can yield the same *SMI* as deep ones with even less reduction of the efficiency. Perrot et al. [129] and also Choi et al. [22] and Kim et al. [102] use almost square-shaped geometries in their studies and demonstrate their effectiveness.

- *groove number*

Most applications consist of multiple groove treatments and the published results suggest that the effectiveness of several grooves, in terms of *SMI*, is superior to single groove configurations. The experiments of Müller et al. [123] and Ross et al. [135] for example, who tested different groove numbers, both show an increase of the *SMI* for higher groove numbers. Nevertheless, these trends are not valid in general. The work of Houghton and Day [82]

for example, clearly shows that individual groove effectiveness does not sum up in multi-groove arrangements. Based on single groove effectiveness, they studied both, a double and a triple groove configuration and found that two grooves yield superior results compared to the triple groove configuration. In terms of efficiency, they conclude that the overall net value can indeed be obtained by summing up the individual single groove values. Both trends are supported by various different studies, both experimentally [53, 123] and numerically [129, 161].



| | |
|---------------|---|
| location | more effective towards the front section |
| width | $b \approx 10\%$ axial chord length |
| depth | $t \approx 2b$ |
| groove number | multiple grooves seem favorable for <i>SMI</i> depending on single groove effectiveness |

Figure 2.8 – Summary of optimized casing groove design parameters from published axial compressor studies

Groove Mechanisms

Aside from the optimized design, research in this field is mainly focused on the flow mechanisms that lead to a delay of aerodynamic instabilities and moreover affect the performance. Major advances have been made in understanding the corresponding effects but no general understanding is available yet, due to the different flow characteristics and operating conditions of different designs and types of compressors.

Prince et al. [130] already tried to find hypotheses for the working mechanisms in the 1970's but their experimental attempts were unsuccessful. Nevertheless, they assumed that the *SMI* is connected to a suppression of incipient flow separations near the treatment locations. Similar observations are reported by Takata and Tsukuda [152], who experimentally investigated a treatment consisting of 5 circumferential grooves above the rotor among others. They

concluded that the tangential momentum introduced by the flow that exits the grooves resulted in an increased stall margin.

More sophisticated measurement techniques and the use of CFD then facilitated a deeper insight into the changes in the flow structures. Several different mechanisms were identified to be responsible or at least closely linked to the delay of the stall onset. A generally valid analytical approach for analyzing the effect of circumferential groove CTs in tip critical stages is published by Shabbir and Adamczyk [143]. They performed numerical calculations of a subsonic axial compressor with and without circumferential grooves and evaluated the axial momentum equation and its individual components in a near tip control volume. For the smooth casing, the axial pressure force resulting from the pressure gradient is only balanced by the axial viscous shear forces at the casing wall. Towards stall, the axial pressure force increases until it cannot be balanced anymore and thus the flow becomes unstable. The study shows that circumferential grooves enable a transport of axial momentum in radial direction over the groove/casing interface which contributes to the axial momentum balance. The share of this component increases towards smaller flow rates and maintains the balance beyond the former stall point despite lower levels of axial shear forces. The authors attribute this to a substantial reduction of blockage towards smaller flow rates, which they believe to be the dominating flow mechanism. Legras et al. [108, 109] and also Ross et al. [135] confirmed the validity of this approach in their studies. Nan et al. [124] additionally proposed a further segmentation of the control volume to localize the individual contributions to the balance of momentum. Furthermore, Legras et al. [108] state that the temporal fluctuation of the radial transport of axial momentum attenuates the pressure gradient fluctuations and thus, leads to a reduction of unsteadiness in the near tip region.

This effect is also found to be present in other research studies. The numerical work of Zhao et al. [176] showed a reduction of the tip clearance flow unsteadiness as the flow is able to migrate circumferentially inside the grooves. The detailed, unsteady casing measurements by Van de Wyer et al. [156] also proved a reduction of the pressure fluctuations for the grooved configurations, despite not leading to a range extension due to their hub critical rotor. Hah et al. [71] emphasize that the unsteady flow injection from the groove into the core flow region is the major flow mechanism that improves stability.

As already discussed in section 2.2.1, impeller stall is often triggered by a rise in blockage, accumulation of low momentum fluid near the tip region and ultimately a flow spillage in front of the leading edges. Almost all studies,

which examine the groove mechanisms, conclude that this process is affected either in an immediate or indirect manner. Depending on the specific flow conditions near stall, different mechanisms induced by the CT are believed to be involved. For transonic flow conditions, Sakuma et al. [136], for example, attribute the *SMI* to a delay of the tip vortex breakdown that generates a high blockage region. Mirzabozorg et al. [118] also highlight the importance of the vortex breakdown but furthermore stress that suction side flow separation and the vortex shock interaction play an important role. Choi et al. [22] conclude that the reduction of blockage downstream of the passage shock is responsible for the *SMI*. According to their results, a blade suction side separation, which is induced by an interaction of the shock with the leakage vortex, is suppressed by the CT as it enables circumferential flow transport over the blades. Qiang et al. [132] also report a weakening of the interaction of the passage shock with the leakage vortex to be responsible for the *SMI*.

Numerous studies, see [16, 34, 35, 109, 112, 113, 121, 122, 133], trace the *SMI* back to a deflection of the tip vortex trajectory towards the flow direction. This deflection often causes a reduction in blockage and subsequently delays the spillage of flow in front of the leading edges. It is observed for subsonic as well as for transonic operating conditions. Du et al. [34] for example performed extensive experimental and numerical studies for a low speed axial compressor with grooves placed at different axial locations. Their results clearly demonstrate that the effectiveness in terms of *SMI* is coupled to a shift of the vortex trajectory. A groove located very close to the leading edge proved to be ineffective, as the vortex trajectory was not deflected but rather intersected. In contrast to that, downstream grooves, which shifted the trajectory, led to a *SMI*. Further studies also document a deflection of the tip vortex induced by the casing grooves, both experimentally and numerically [123, 129, 156].

Summing this up, the reduction of blockage and unsteadiness seems to be the major mechanism that causes the *SMI* in axial compressor applications. These effects are closely coupled to the near tip flow field and thus especially to the evolution of the tip vortex in almost all of the available studies.

2.4 Discussion

Today's most utilized casing treatment in centrifugal compressors is the ported shroud recirculation system. However, the *SMI* comes at the cost of a deterioration of the efficiency, comparatively high manufacturing and design costs and increased compressor housing dimensions, resulting from the necessarily complex geometrical shapes. Circumferential grooves are much simpler, presumably less disadvantageous for the efficiency and thus, could be more cost effective. The few available studies that applied circumferential grooves indicate that these could also provide range extensions, despite only using arbitrary test designs. These are commonly adopted from axial compressors. However, it has been shown that the centrifugal impeller flow field is strongly dominated by the Coriolis and centrifugal forces and thus significantly varies from axial compressor flows. Furthermore, the existence of splitter blades directly influences the near tip flow field, which is of great importance for the compressor stability. The question as to whether those designs can be equally used for the centrifugal compressor flow field remains yet unanswered. Therefore, this work will investigate the design of circumferential grooves and provide design guidelines for optimized configurations in a typical centrifugal impeller.

The effectiveness of casing treatments is not only measured by an increase in surge margin. From an aerodynamic point of view, efficiency and also the pressure rise characteristics are equally important. The near casing flow field, dominated by leakage and secondary flows, has one of the highest shares in the impellers entropy generation and furthermore directly affects the diffuser inflow. This region is particularly affected by the CT. Therefore, the present work on the one hand analyzes the impact of casing grooves on the overall performance map. On the other hand, the mechanisms that are responsible for changes in efficiency and pressure rise, assumingly attributable to the near tip flow, are covered in detail.

It has been shown that centrifugal compressor instability can originate in different subcomponents, namely the impeller or the vaned and vaneless diffusers. In comparison with axial compressor flows, the stall inception mechanisms are less well understood. Impeller stall is most likely initiated in the inducer tip region and is directly affected by the near tip flow. Similar inception mechanisms as in tip-critical axial compressors have been observed, where casing grooves are effectively applied. Flow spillage, as well as vortex breakdown phenomena, mostly observed in transonic cases, are reported

to initiate the stall. Diffuser stall is mostly linked to the impeller discharge flow field. The stall is initiated by excessive incidence on the blades in vaned diffusers or by the surpassing of a critical flow angle in vaneless configurations. Hence, not only the impact of circumferential grooves on the impeller flow field has to be considered, but also the consequences for the diffuser flow. More uniform outlet profiles and reduced unsteadiness could lead to increased diffuser stability, for example shown by Galloway et al. [57].

Two different routes to stall, namely modal and spike-type stall inception, have been identified, whereof only the latter can be effectively delayed by casing treatments according to the work of Greitzer et al. [65]. Since predictions of the stall mechanisms and the corresponding onset locations in the design process of a specific machine are not yet reliable, it remains unknown which mechanisms will occur in a newly designed compressor. Consequently, the present study analyzes a typical high pressure compressor stage, operated at sub- and transonic speeds, with both, a vaned and a vaneless diffuser. Thereby, the investigation covers a wide range of different states of operations, which are typical for most centrifugal compressor applications.

Substantial evidence has been discussed, which links the *SMI* of casing grooves in axial compressors to changes in the near casing flow field. Specifically, a reduction of blockage that is generated by a tip vortex deflection, a delay of a vortex breakdown or a suppression of flow separations is mentioned in almost all studies. Similar mechanisms might occur in centrifugal compressors as well. Thus, the near casing flow fields are analyzed in detail to understand the underlying mechanisms and to evaluate if the knowledge gained from axial compressor studies is transferable to the centrifugal flow field.

3 Test Object and Experimental Methods

This chapter describes the centrifugal compressor stage which acts as a baseline design and the corresponding experimental methods that are applied for the investigations. In the first section 3.1, the stage design and its key parameters are presented. Thereafter, the compressor test rig is described in section 3.2. This includes the general structure, the measuring points, the measurement equipment and the different systems and components which are used to run and control the rig. Furthermore, the data acquisition, the corresponding data processing and the experimental approach for the recording of the operating maps are described. Finally, reproducibility measurements are shown to assess the measurement uncertainty.

3.1 Centrifugal Compressor Stage

As part of this study a new centrifugal compressor stage was developed at the ITSM in collaboration with PCA Engineers Limited. The aerodynamic design in terms of blade and channel shape has been designed for the application at the ITSM test rig with the intention to reflect a state of the art, high-pressure centrifugal compressor, as for example used in large scale turbocharges. The design goals are summarized in table 3.1. Due to restrictions imposed by the engine and the gearbox that are used to drive the compressor, limiting parameters for the maximum speed and the power supply had to be taken into account. Therefore, the design targets were defined for the maximum speed of 90 000 rpm. Typical moderate values, well within the range known to achieve best efficiencies, are chosen for the flow coefficient $\Phi_{t,1}$ and the work coefficient λ .

Figure 3.1 shows a photo of the manufactured impeller alongside the CAD model of the compressor stage assembly. The impeller has 14 blades and is milled from aluminum alloy Al2618-T61. Every second blade is cut back to a splitter blade. The stage design features a vaned diffuser comprising 17 vanes and a constant channel height. Additionally, a simple vaneless diffuser is used in this study with the same constant channel height. The channel height and the mechanical integrity of the part is maintained by three circumferentially distributed pins. The pins have a diameter of 4 mm and are placed far off the impeller exit at $D = 170$ mm. Thanks to this, it is ensured that the impeller flow

Table 3.1 – Design point parameters of the ITSM centrifugal compressor stage

| parameter | symbol | value | unit |
|-----------------------|--------------|--------|------|
| massflow | \dot{m} | 0.6 | kg/s |
| pressure ratio | π | 4.5 | – |
| flow coefficient | $\Phi_{t,1}$ | 0.073 | – |
| work coefficient | λ | 0.72 | – |
| speed | n | 90 000 | rpm |
| tip speed Mach number | M_u | 1.55 | – |

is not disturbed and that the blockage in the diffuser is minimized. However, it has to be noted that the volute flow area is matched to the vaned diffuser outflow conditions. Moreover, this vaneless diffuser is not matched to the impeller. As a result, lower efficiencies have to be expected compared to the typically achievable values with such configurations.

A numerical stress analysis was performed with 5 % overspeed to check the maximum stresses in the impeller. Additional modal analysis showed that there is sufficient clearance from any intersection points with the dominant engine orders. To verify the stress analysis and to rule out any material defects, an overspeed test of the impeller at 100 000 rpm was performed. To prevent inadmissible vibrations, the impeller is balanced with grade 1 according to DIN ISO 21940 before being mounted to the shaft. Shaft and hub are connected using a press fit, which is enforced by a aerodynamically designed spinner screw nut which is screwed onto the shaft.

A modular construction has been developed to enable interchangeability of the different stage parts. The different casing parts are split up so that the impeller casing, the diffuser and the volute can be replaced individually. The casing parts of impeller and diffuser are turned and milled from aluminum alloy AlCuMgPb and the volute is lost-wax casted and milling finished from AlSi7Mg0.6. The impeller casing is attached to the diffuser and the volute with screws and thus can be replaced without dismantling the other components. Moreover, this ensures reduced tolerances for the different tested groove configurations as all other parts remain unchanged. The casing parts used within the study are all manufactured with utmost care on the same machinery, whereby minimized geometric differences are ensured. Therefore, the variation of the tip gap, which is of particular interest for the efficiency measurements, is minimized. A flange is then used upstream of the impeller

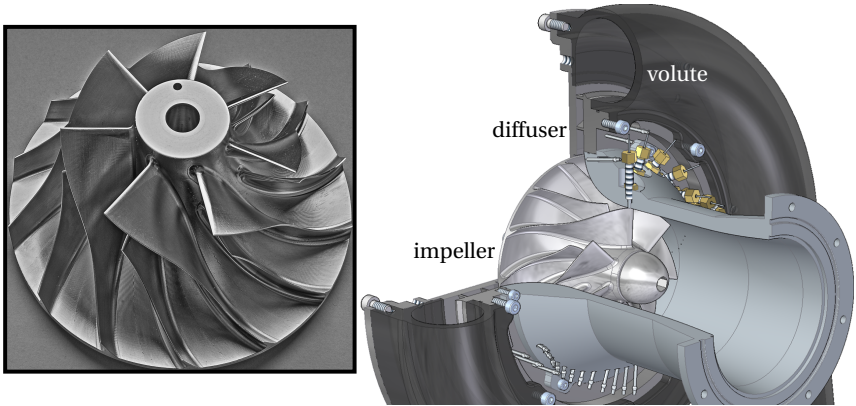


Figure 3.1 – Photo of the centrifugal compressor impeller and CAD model of the compressor stage assembly

to apply the stage to the test rig piping system. Some of the key dimensions of the stage components are summarized in table 3.2.

Table 3.2 – Key dimensions of the ITSM compressor stage

| parameter | symbol | value | unit |
|--|----------------|-------|------|
| diameter at impeller inlet hub | $D_{1,h}$ | 29 | mm |
| diameter at impeller inlet shroud | $D_{1,s}$ | 73.2 | mm |
| diameter at impeller outlet | D_2 | 113 | mm |
| impeller outlet height | b_2 | 6.1 | mm |
| impeller inlet tip clearance | δ_1 | 0.4 | mm |
| impeller outlet tip clearance | δ_2 | 0.3 | mm |
| impeller blade number | Z_{imp} | 7+7 | – |
| diameter at vaned diffuser leading edge | $D_{diff, LE}$ | 130 | mm |
| diameter at vaned diffuser trailing edge | $D_{diff, TE}$ | 180.8 | mm |
| vaned diffuser blade number | Z_{diff} | 17 | – |
| diffuser height | b_{diff} | 5.39 | mm |
| diffuser outlet diameter | D_3 | 184 | mm |

3.2 Compressor Test Rig

The test rig used for the experimental investigations is described in this section. Firstly, the general structure of the rig and the different components which are required for the operation and the testing of the compressor are shown. Moreover, the different measurement systems, the acquisition and the post processing of the test data are presented in detail. The rig has been purpose-rebuilt within the scope of the current thesis, based on an existing version having the goal to enable reliable and accurate measurements of different centrifugal compressor components. Therefore, a modular construction approach was chosen to reduce the costs and the effort of changing individual components, while maintaining comparable test conditions.

A functional drawing of the compressor test rig is given in figure 3.2. It includes all major components that are required for the operation. A DC motor with a power output of up to 90 kW and a maximum speed of 3000 rpm is used to drive the compressor. A timing belt drive with a transmission ratio of 40/19 is used to increase the rotational speed of the gearbox entry shaft. The planetary gearbox has an additional transmission ratio of 15, which results in a maximum compressor speed of almost 95 000 rpm. An oil loop is required at the test rig to ensure lubrication and cooling of the gearbox. A pump is used to deliver a constant supply of oil from the reservoir. The oil inlet temperature is set to 80 °C, which is controlled by a mixing valve that accordingly mixes cold oil from the water cooled heat exchanger and hot oil from the preheated oil reservoir.

Different measurement systems are used to log and process the data, depending on the required measurement frequency and accuracy. These are described in subsection 3.2.1. The acquired data is then recorded, processed and evaluated with a LabView based program. The values and commands that are required for the control of the rig are fed to a PLC control system which ensures a safe and reliable operation.

3.2.1 Flow Measurement Section

This section focuses on the description of the flow measurement section of the test rig in figure 3.2 and the acquisition of the experimental data. A more detailed schematic sketch of the flow section concept is depicted in figure 3.3. It contains all measurement and control devices directly used in the

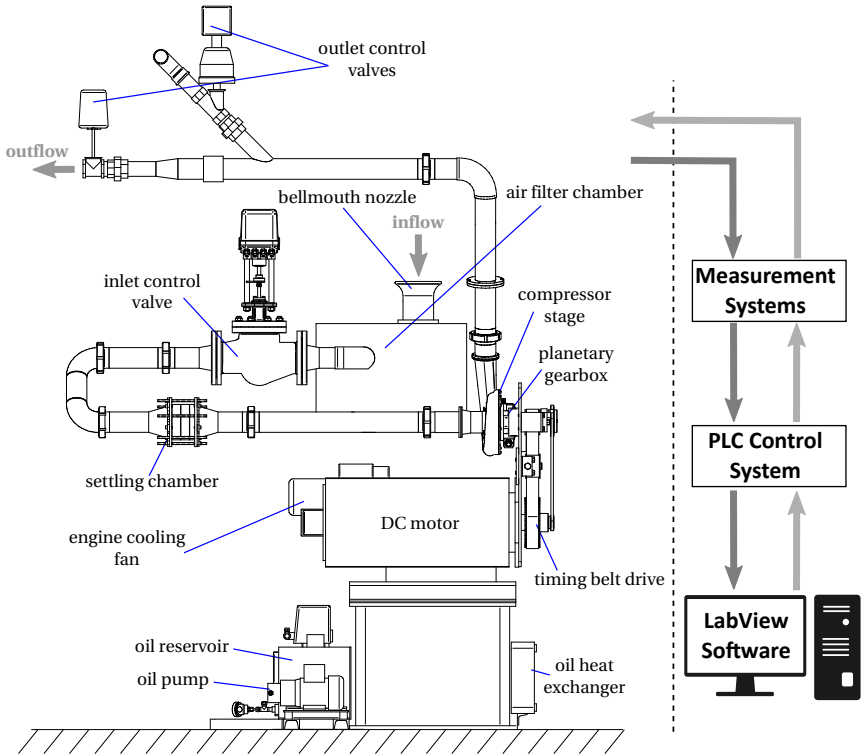


Figure 3.2 – Functional sketch of the ITSM centrifugal compressor test rig - support structures not shown

gas path, except for the ones within the compressor stage, which are presented in detail in the following section 3.2.2. The test rig is designed as an open loop, whereby stainless steel pipes with a nominal diameter of 80 mm are used to guide the flow. The air is sucked in at ambient conditions through a bellmouth nozzle, which is followed by an air filter to prevent particles, such as dust, from entering the system. The nozzle is equipped with static pressure taps to measure the differential pressure which is used to determine the air massflow through the stage. The flow is then guided to a pressure control valve, which is used to control the static pressure at the inlet of the compressor. Hence, it is possible to reduce the compressor inlet pressure below ambient conditions.

Consequently, the inlet density can be varied, which results in a controllable massflow through the compressor at each operating point.

For the present compressor stage, it is necessary to reduce the inlet pressure levels to meet the maximum power output of the electrical motor. To ensure comparable test conditions for the different compressor configurations, the inlet pressure is set according to table 3.3 for all tests. For this purpose, an automated PID controller is used to adjust the inlet pressure, whereby typical deviations from the target value of well below 300 Pa are obtained. This pressure reduction affects the inlet Reynolds numbers, which can lead to a deterioration of the overall efficiency, see Casey [17]. However, only relative comparisons between different casing configurations at constant Reynolds numbers are used in this work. Thus, there is no need to take this into account.

Table 3.3 – Inlet pressure levels used for the recording of the operating maps

| | 50 000 rpm | 60 000 rpm | 70 000 rpm | 80 000 rpm | 90 000 rpm |
|-------------------|------------|------------|------------|------------|------------|
| vaned diffuser | 85 kPa | 80 kPa | 75 kPa | 70 kPa | 65 kPa |
| vaneless diffuser | 80 kPa | 75 kPa | 70 kPa | 65 kPa | 60 kPa |

A settling chamber, featuring several wire meshes ensures a circumferentially uniform flow profile to enter the compressor inlet pipe. The average inlet static pressure p_{in} is measured 5 pipe diameters in front of the stage inlet, followed by a temperature measurement location representing T_{in} . The pipe diameter is $d = 80\text{ mm}$ for the whole facility. Four equally distributed wall pressure taps are used for the determination of the inlet pressure. A single PT100 temperature sensor is employed for measuring the inlet temperature.

The outlet static pressure is measured using the same methodology in the pipe behind the compressor stage. To improve the accuracy of the outlet temperature measurement, a flow straightener of VORTAB VIP type is used to remove the swirl of the flow in front of the measuring point. Four PT100 probes are used at this location to provide an averaged value of the outlet temperature field. Each probe is rotated by 90° in circumferential direction, whereas every second probe is moved 35 mm in axial direction to reduce the blockage of the flow cross section. Mineral wool insulation is used for all hot components, including the complete outlet pipe and most of the volute, to reduce the heat losses to the surrounding air.

Downstream the measurement pipe, the piping system is split up and two adjustable valves are installed at the exit of the gas path. These are used

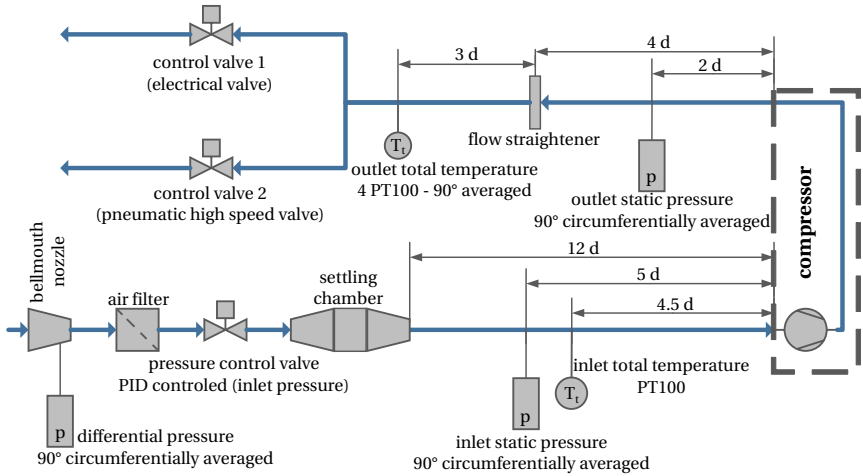


Figure 3.3 – Schematic sketch of the ITSM centrifugal compressor test rig flow measurement section

to control the flow through the system and thus the operating point of the compressor. One is a conventional, electrically controlled slider, whereas the second valve is controlled pneumatically. This enables fast adjustments in the case of system instability as well as a fine control resolution as the valve position can be adjusted in steps of 0.1 %. Subsequently, the flow discharges to ambient conditions.

Data Acquisition and Processing

The acquisition of the measured test data and the subsequent processing of the data is described in this section. The recording of the data is realized in the same LabView program that is used for the control of the test rig. The pressure transducers that are used at the different pressure measurement locations are listed in table 3.4. The accuracy, specified by the manufacturer, refers to the full-scale range. Each transducer is selected and adjusted based on the required measurement range. Inlet and nozzle pressure are measured in differential mode, whereas an absolute sensor is used for the outlet pressure measurement. All sensors are in-house calibrated in their specific operating range to compensate zero point shifting and sensitivity deviations of the trans-

ducers. For this purpose, a 2-point calibration using a Mensor APC600 pressure calibrator is performed. This calibrator has a total uncertainty of 0.01% of each of its different channels that range from 0 bar to 5 bar, ± 500 mbar and ± 35 mbar. Accordingly, this further reduces the uncertainties of the different sensors, whereby the theoretically obtained accuracy is also listed in table 3.4.

Table 3.4 – Pressure transducers for the flow measurements at the ITSM centrifugal compressor test rig – manufactured by Siemens

| model | range | manufacturer accuracy | calibration accuracy | mode | location |
|-----------|--------------|-----------------------|----------------------|--------------|---------------------|
| SITRANS P | 0.04 – 4 bar | $\leq 0.074\%$ | 0.0125% | absolute | p_{out} |
| TELEPERM | -400 – 0mbar | $\leq 0.3\%$ | 0.0125% | differential | p_{in} |
| SITRANS P | -20 – 0 mbar | $\leq 0.074\%$ | 0.0175% | differential | p_{nozzle} |

The massflow \dot{m} is obtained from the differential pressure measurement of the bellmouth, which has been calibrated for the expected massflow range. The required density of the surrounding air is calculated from the ambient values of pressure, temperature and humidity. These are measured centrally in the ITSM experimental hall and updated every 30 seconds in the measurement software. Using the calibration coefficient of 0.992, the massflow is calculated by

$$\dot{m} = 0.992 \frac{\pi D_{\text{nozzle}}^2}{4} \sqrt{2 \rho_{\text{amb}} p_{\text{nozzle}}}. \quad (3.1)$$

All temperatures are measured using PT100 sensors with an accuracy of 0.1 K. Smaller sensors with a diameter of 3 mm are used at the outlet measurement location due to the blockage that is generated by the higher number of sensors. The inlet sensor has a diameter of 6 mm. The compressor rotational speed is measured indirectly using the speed of the engine and gearbox by taking advantage of the fixed gear ratios. An opto-electronical sensor, type Braun AIS30, is used to record the impulses of a reflecting marker foil that is glued onto the gearbox driving wheel.

The data logging of the sensor output data is performed using a Delphin Expert Key data logger system, which also stores the calibration curves of the respective sensors.

Performance Map Data

Performance maps are commonly used to evaluate and compare the performance of different compressors. They correlate the total pressure ratio and the respective efficiency with the corresponding operating conditions, such as rotational speed and massflow rate. As the ambient conditions for experimental tests are not constant, this has to be accounted for when evaluating the data. For instance, quantities like temperature, density, humidity and pressure are depending on weather conditions during the tests. Moreover, the inlet pressure p_{in} is controlled during the experiments. As a result, the test data has to be corrected or reduced to obtain comparable quantities, according to the theory of similarity. For more details see Cumpsty [23] or Grieb [67]. A reference state of $p_{ref} = 100 \text{ kPa}$ and $T_{ref} = 293.15 \text{ K}$ is used for the correction. Including humid air conditions following Berdanier et al. [9], this results in

$$n_{red} = n \frac{a_{ref}}{a_{t,in}} \quad (3.2)$$

for the reduced speed of the compressor and

$$\dot{m}_{red} = \dot{m} \frac{\rho_{ref}}{\rho_{t,in}} \frac{a_{ref}}{a_{t,in}} \quad (3.3)$$

for the reduced massflow, using the speed of sound $a = \sqrt{\kappa RT_t}$ and the density ρ of the humid, ambient air. The heat capacity ratio κ and the specific gas constant R are determined based on material values from REFPROP [110]. The total-to-total and static-to-static pressure ratios π_{tt} and π_{ss} are then calculated with the respective pressures from

$$\pi_{tt} = \frac{p_{t,out}}{p_{t,in}} \quad \text{and} \quad \pi_{ss} = \frac{p_{out}}{p_{in}}, \quad (3.4)$$

whereas the isentropic efficiency is calculated from

$$\eta_{s,tt} = \frac{\pi_{tt}^{\frac{\kappa}{\kappa-1}} - 1}{\left(T_{t,out}/T_{t,in}\right) - 1} \quad \text{and} \quad \eta_s = \frac{\pi^{\frac{\kappa}{\kappa-1}} - 1}{\left(T_{out}/T_{in}\right) - 1}. \quad (3.5)$$

As the test rig only features static wall pressure measurements, the stagnation values are calculated using the continuity equation to determine the kinetic component of the flow.

$$p_t = p + \frac{\rho}{2} \left(\frac{\dot{m}}{\rho A} \right)^2 \quad (3.6)$$

Accordingly, the local Mach numbers are calculated with

$$M = \frac{\dot{m}}{\rho A \sqrt{\kappa R T}}. \quad (3.7)$$

The static and total temperatures are obtained from

$$T = \frac{T_{\text{EXP}}}{\left(1 + r \frac{\kappa - 1}{2} M^2\right)} \quad \text{and} \quad T_t = T \left(1 + \frac{\kappa - 1}{2} M^2\right), \quad (3.8)$$

with T_{EXP} being the measured value of the respective PT100 sensor and a recovery factor for turbulent air flows of $r = 0.9$ according to Nitsche and Brunn [126]. Moreover, as the density is a function of temperature, the calculation of the density dependent variables is performed iteratively in the post processing of the measured data to get the best fit.

As the continuity equation only takes the axial component of the pipe flows into account, the share of swirl in the dynamic pressure evaluation is neglected. However, this is only relevant for the outlet pressure measurement location. After exiting the volute, the flow is likely to have a swirling component, which thus is not included in the total pressure values of the measurements. To reduce uncertainties in the total temperature measurement, the flow is straightened before the temperature measurement location. However, since the Mach numbers in the pipes are well below 0.3 for the whole compressor operating range, the errors in the estimation of the kinetic components in the stagnation values are almost negligible compared to other measurement uncertainties. Moreover, this also justifies the assumption of incompressible flow in equation (3.6).

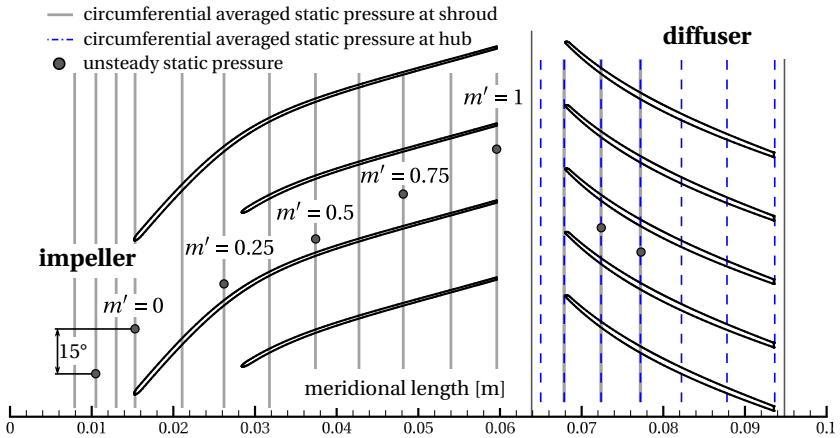


Figure 3.4 – Unsteady and steady static pressure measurement locations in the m - ϑ -plane at the shroud of the compressor impeller and in the diffuser for the smooth casing configuration

3.2.2 Stage Pressure Measurements

Additional pressure measurement locations are applied in the tests of the different configurations for a detailed examination of the compressor pressure rise and flow field characteristics. Both steady and unsteady sensors are used to obtain data for the validation of the CFD results and to evaluate different configurations and operating points. Eight unsteady Kulite XCE-062-60A sensors are deployed to measure the time resolved pressure fluctuations at the casing of the stage. Figure 3.4 presents the locations of the pressure sensors in the unwrapped $m - \vartheta$ - plane for the smooth casing configuration. Due to installation space limitations, each unsteady sensor is shifted by 15° in circumferential direction. Six sensors are used above the impeller and two are deployed in the diffuser. Five sensors in the impeller are equally distributed from the leading to the trailing edge. This equals to normalized meridional locations of $m' = 0, 0.25, 0.5, 0.75$ and 1 . One additional sensor is deployed 5 mm upstream of the main blade leading edges.

The meridional positions of the static pressure taps are also plotted in figure 3.4. Each location, indicated by the gray lines, represents three pressure taps at the shroud which are equally distributed over the circumference at the impeller casing. Thus, twelve different circumferential averaged static

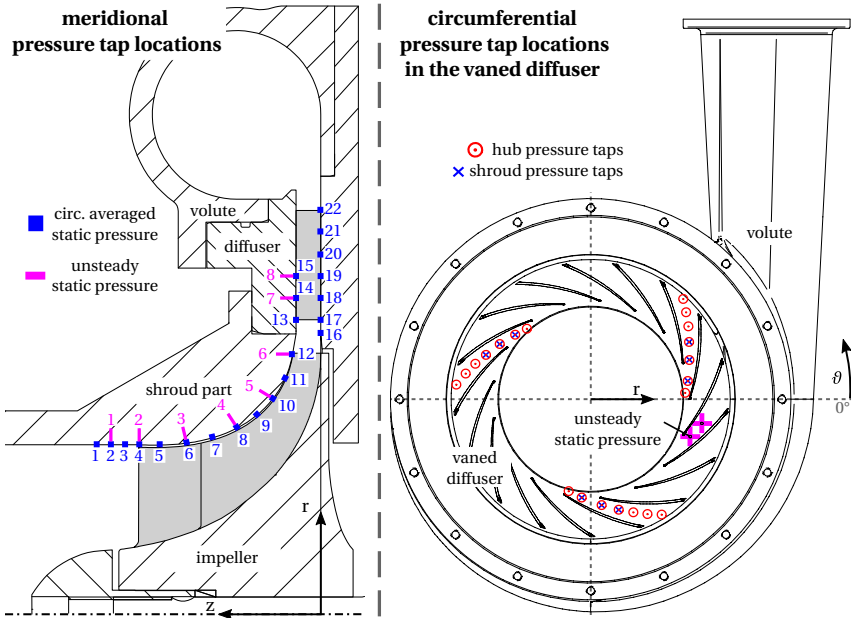


Figure 3.5 – Compressor measurement locations - meridional and circumferential distribution of the pressure taps of the *sc* configuration with the vaned diffuser (equivalent locations used in the vaneless diffuser)

pressure values are obtained. Additional pressure tap locations are applied in the diffuser. Again, three locations in the circumferential direction are used.

Figure 3.5 depicts the locations in the z - r -plane on the left and the r - θ -plane on the right. The locations are sequentially numbered from inlet to outlet. Both the diffuser shroud and the hub are equipped with static pressure taps at the specified locations. All taps are aligned with the blades of the vaned diffuser. As the diffuser flow field is certainly nonuniform in circumferential direction due to the asymmetric volute, this provides at least an average value to compare the results to the steady-state simulations, where periodicity is assumed. Each tap is located exactly in the center of the respective diffuser channel. The circumferential positions are shown on the right of figure 3.5 with respect to the position of the volute. Restricted access limits the shroud locations in the diffuser. Thus, only three measuring points are used here near the diffuser LE. A total of seven taps are applied at the hub to cover the com-

plete diffuser. The same radial locations are also used for the measurements with the vaneless diffuser.

For the grooved configurations that were tested, some positions of the sensors had to be adjusted due the change in the casing geometry. The respective locations are given in section 5.4.2, where the investigated configurations are presented. The pictures in figure 3.6 show the implementation of the static pressure measurements in the impeller casing and the diffuser. Moreover, a sketch of the stage cross section is given on the right side of the figure, where the implementation of both measurement systems is exemplified. The locations are kept constant for both diffuser configurations, namely the vaned and the vaneless case. Scanivalve pipes are used for the pressure taps, which are glued into the casing parts using a high temperature resistant two component adhesive. To minimize the size of the taps, holes with a diameter of 0.5 mm are used for the last part at the shroud. The taps are connected to respective manifolds using temperature resistant tubes which are secured against movement and leakage by springs over the Scanivalve tubes. The averaged pressures are then measured using a pressure transducer.

The unsteady Kulite sensors have a diameter of 1.7 mm and are flush mounted to the shroud surfaces. The sensors are glued into a special sleeve with an offset to allow for flexible usage in different parts. A fine-pitch thread is used to adjust the position of the sensor sleeve in the stepped bore. A corresponding screw nut is used to fix the location of the sensor. Leakage is prohibited by using a liquid high temperature thread sealant.

Data Acquisition

All averaged static wall pressures are measured using a single pressure transducer. The specifications are listed in table 3.5. Once more, a calibration for the required operating range was performed. A rotatory stepping system is used to change between the different channels. Each tube system is individually connected to the respective stepper channels and sequentially queried to log the pressure data. A holding time of 1 s is implemented after the switch of a channel to allow for a steady state pressure level in the respective tube system. A measurement period of 3 s with a measurement frequency of 10 Hz is used to calculate the mean values and the respective standard deviations, which are then logged for each channel.

A separate system is required for the supply, the amplification and the acquisition of the unsteady pressure transducer data. GEPA MOM-DMSi amplifier

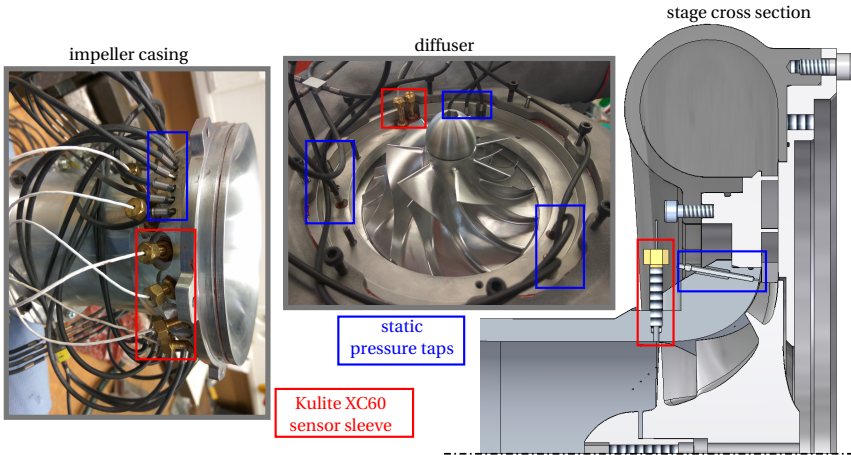


Figure 3.6 – Steady and unsteady static shroud pressure measurement setup

Table 3.5 – Stepping system pressure transducer specifications

| model | range | manufacturer accuracy | calibration accuracy | mode | location |
|--------------|----------------|-----------------------|----------------------|----------|----------------|
| SITRANS P200 | 0 bar to 4 bar | $\leq 0.25\%$ | 0.0125% | absolute | $p_1 - p_{22}$ |

cards are used to supply each sensor and to amplify the sensor output signal. This analog signal is then converted to a digital signal using a NI 6356 Multi-function DAQ system. Again, LabView is used to monitor and log these signals simultaneously for the respective operating points. A sampling rate of 400 kHz is used, which results in a resolution of unsteady phenomena of up to 200 kHz, according to the Nyquist criterion. This covers at least nine harmonics of the blade passing frequency for the maximum rotational frequency of 1.5 kHz. The observation time for the measurements is set to 250 ms. Therefore a frequency resolution of $\Delta f = 4$ Hz is obtained, which is found to be sufficient for the present investigations. Moreover, a sufficient number of rotor revolutions has to be recorded to allow for an adequate number of data points for the following averaging process. The chosen observation time results in more than 200 full rotor revolutions for the minimum speed of 50 000 rpm, that is considered in this study.

It has to be noted, that the eigenfrequencies of the Kulite sensor screens, which are typically in the range of 100 kHz for the types used in this study, need to be considered in the analysis of the unsteady data.

Data Processing - Ensemble Averaging

The time resolved signals of the impeller Kulite pressure transducers are processed with the following methodology in order to resolve the periodic pressure signal. An ensemble averaging is applied, which is frequently used in turbomachinery analysis of time resolved data, see Schleer et al. [140] for example. Hence, the deterministic share of the signal can be obtained by removing the turbulent and stochastic fluctuations of the flow, as well as measuring fluctuations of the sensors. This averaged signal can then be used for comparisons with the numerical calculations as well as for an evaluation of the different groove configurations.

The recorded pressure signals are processed as follows. Normally, a trigger signal, which is fixed to a specific point on the rotor is used to detect the exact starting time of each revolution. As no such measurement system is available in the test rig, this starting time is calculated from the respective blade passing frequencies. To account for possible speed variations during the measurements, each signal is split into individual blocks of about 15 rotor revolutions to determine the respective rotational frequencies. However, it has to be noted that the speed remains generally constant during the short measurement time. Nevertheless, the real speed varies for different operating points as the reduced speed is controlled during the tests to ensure similarity in terms of Mach numbers. The actual blade passing frequency and thus the rotational speed is then determined by an evaluation of the signal in the frequency domain, applying a Fast Fourier Transformation (FFT). For this, the frequency of the peak pressure amplitude in the range of 200 Hz around the known speed is determined.

The signal is then cut into single pitches and interpolated onto a linearly spaced sampling vector. These are averaged to obtain the periodic pressure signal of a single pitch for the respective block. The procedure for an exemplarily chosen block for a sensor located at $m' = 25\%$ is illustrated in figure 3.7. It depicts the shifted raw data and the obtained mean signal, as well as the corresponding standard deviation σ . Thereafter, the block signals are linearly interpolated and again averaged. By shifting the respective frequencies of each block, even small speed variations are removed. Figure 3.8 shows the final

ensemble averaged mean signal of one impeller pitch at $m' = 25\%$, based on the individual block averaged signals. The respective standard deviations are averaged as well (σ_{mean}) and included in the figure. Moreover, the maximum RMS values of the method are plotted (σ_{max}). These can be used as a measure for flow unsteadiness at a certain circumferential position.

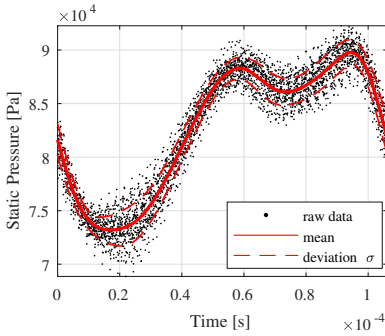


Figure 3.7 – Example of the ensemble averaging procedure at sensor position 3 from the raw pressure data of an exemplary block – operating point of $n = 80000$ rpm and $\dot{m}_{\text{red}} = 0.5$ kg/s

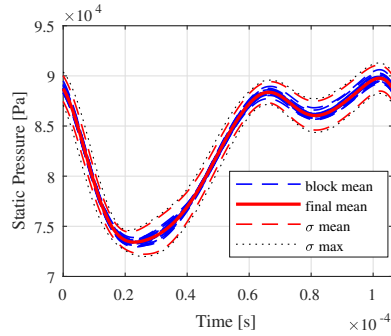


Figure 3.8 – Final pressure signal at position 3, including the mean and the maximum standard deviation (RMS) of all blocks – operating point of $n = 80000$ rpm and $\dot{m}_{\text{red}} = 0.5$ kg/s

Despite a calibration of the Kulite transducers, the steady component of the unsteady signals is replaced by the respective static pressure tap value in the post processing, as the sensors are subjected to drifts of their absolute values over time. Moreover, higher accuracy is achieved for the static pressure tap measurements. Therefore, only the fluctuating share of the recorded signal is considered in the evaluation. To evaluate and compare the determined periodic pressure signals to other operating points or numerical data, their phases have to be matched. For this purpose, a FFT is performed and the signals are shifted based on the phase of their most dominant frequency, typically the first or second harmonic of the blade passing frequency (BPF).

3.2.3 Experimental Approach

This section describes the approach of the performance map measurements. To eliminate errors due to flow fluctuations and measurement noise, all steady-state values presented in this thesis are mean values over a certain period

of time. A measurement period of 15 s is selected and the measurement frequency is set to 2 Hz.

To identify and ensure quasi steady-state operating points, these mean values are monitored during the rig operation. This means that all relevant values have sufficiently approached their asymptotic end value for a specific operating point before starting the data logging. In general, the compressor outlet temperature requires the most time to reach this condition. Typically, an averaged fluctuation below 0.3 K is reached, before the data logging is started by the rig operator. Normally, a holding time of 2 min to 5 min is sufficient to obtain such conditions. To additionally assess the steadiness of any averaged values, the standard deviation is calculated and stored for the entire measurement period.

A consistent approach for the performance map recording is chosen to ensure comparability between the different configurations. Accordingly, the reduced speed n_{red} , the reduced massflow \dot{m}_{red} and the static inlet pressure are controlled during the rig operation. In general, the recording is started at choke and then the flow rate is reduced stepwise until the compressor enters unstable operation. The following procedure is used for the determination of the last stable operating point.

Near the stall point, the throttle valve position is adjusted gradually by steps of 0.5 %. Simultaneously, the unsteady pressure signals are monitored in both the time and frequency domain to identify the onset of unstable operation. Once the compressor becomes unstable, the previous throttle condition is defining the last stable operating point. Figure 3.9 illustrates examples of the waveform and frequency content of the pressure signals for different operating points when the compressor is throttled into stall and then surge. Sensor position 1, upstream of the impeller LE, is selected here as this also allows for a detection of inducer instabilities. The upper plot shows the pressure fluctuations whereas the lower part shows the discrete Fourier transform (DFT). The signal is dominated by the blade passing frequency but the onset of stall and then surge can be clearly detected. For the chosen example, the instability is of progressive type. Firstly, a low amplitude perturbation or stall cell emerges and gradually becomes stronger until the whole circumference is affected and the stall cells merge into an inducer recirculation region. This behavior is well known in centrifugal compressors at low tip speed Mach numbers, see Schleer et al. [140] or Kämmer and Rautenberg [99] for example. In the DFT this is indicated by the shift from a clear stall frequency emerging near stall (figure 3.9b) to a broadband hump around the stall frequency (figure 3.9c).

Further throttling of the compressor initiates surge which is shown in an mild form in figure 3.9d.

The stall frequency and amplitudes depend on the operating conditions and may change for different speeds and operating points. Surge can occur in different forms, whereby the surge frequencies are fixed by the system geometry. For the present compressor mild surge occurs at ≈ 21 Hz with moderate pressure fluctuations. Deep surge is characterized by violent pressure fluctuations and flow reversal. Typically, even lower frequencies are found depending on the test rig volume – approximately 4 Hz in the present case. Therefore, surge can be clearly determined during the rig operation as significant changes are observed in the waveform and DFT signals at the characteristic surge frequency. Moreover, the onset of compressor surge is clearly audible during the rig operation which helps in identifying the last stable point. As the onset of rotating stall is difficult to determine during operation, this study detects its presence in the post processing of the unsteady data by evaluating the DFT signal at position 1 for dominant frequencies or high broadband pressure fluctuations below the blade passing frequency, following the methodology of Schleer et al. [140]. The pressure amplitudes are normalized with the pressure amplitude at the blade passing frequency and the first stall point is then defined if any frequency content below the BPF exceeds an empirical value of 0.25. This is only relevant for low rotational speeds as the compressor experiences an abrupt type surge at speeds starting from 70 krpm, which simplifies the determination of the surge line at these speeds.

For the vaneless diffuser configuration, sensor position 8 in the diffuser is additionally evaluated, as a distinct diffuser stall is found for low speed operation at 50 krpm. As the BPF amplitudes are less pronounced here, the criterion that has to be exceeded is empirically set to 1, meaning the stall amplitude is more dominant than the BPF. This was not applicable for the vaned diffuser configuration, as no rotating instabilities could be identified in the present investigations. However, significant indications on vortical structures (broadband hump) were detected in the diffuser at position 8 for all speedlines, whereby the pattern did not change with rotational speed.

The main drawback of the stall point determination in the post processing is the dependence on the number of measurement points, which defines the resolution of the speedline. Hence the method is rather used for pointing out trends than for determining the exact stalling flow rates at low speeds.

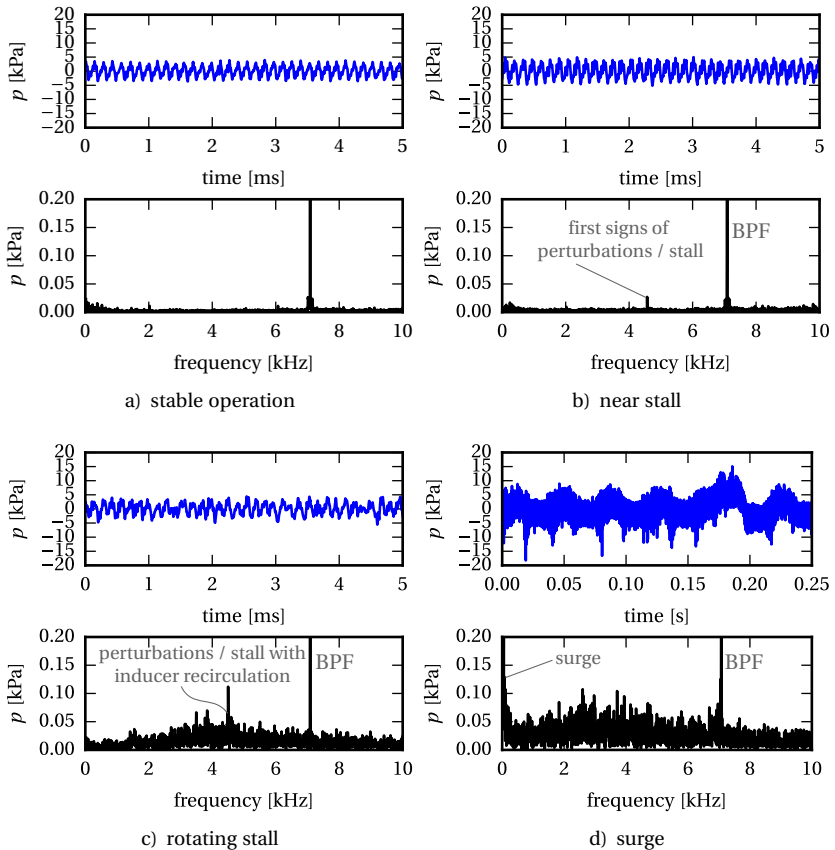


Figure 3.9 – Example of time resolved pressure monitoring at impeller inlet (position 1) for different operating points at 60 000 rpm

3.2.4 Reproducibility

Reproducibility measurements are performed to demonstrate the capability of the test rig to generate reliable results for the various measuring points. The measurements were carried out on different days to account for typical changes in the ambient conditions that are present at the experimental facility. Moreover, the procedure of the operating point setting is changed as greater

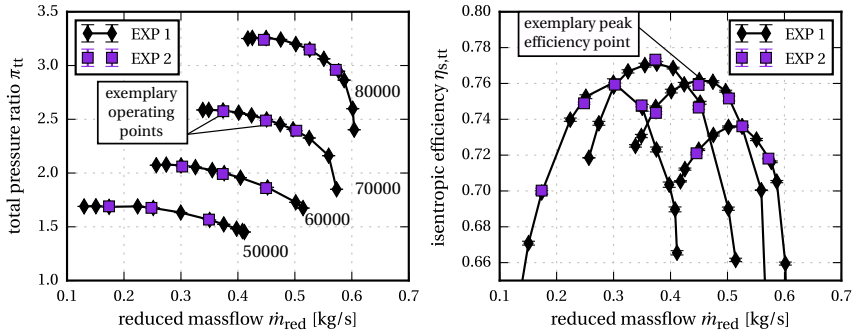


Figure 3.10 – Reproducibility measurements for the *sc* configuration with the vaneless diffuser - measurements performed on different days - errorbars showing the standard deviation σ of the averaged values

flow changes are realized between the different points. The measurement devices and the procedure for the data acquisition and logging remained unchanged. Therefore, systematic errors, such as calibration errors are removed. The baseline configuration with the vaneless diffuser and selected operating points, representing the whole performance map, are used for this study. Figure 3.10 depicts the performance map (left) and the isentropic efficiencies (right) for the two measurement campaigns. The results of the second experiment match well with the first for pressure ratio and efficiency. For the performance map, the maximum relative differences are below 0.5 %. The maximum efficiency difference of 0.3 % is found for low speeds, whereas even smaller differences are observed for the higher speedlines. This is caused by the low outlet temperature levels at low speeds, where small differences in the measured values result in significant changes of the efficiency.

Additionally, errorbars indicating the respective standard deviation σ of the underlying measured values are included in the plots. In general, the results show that these are negligible for higher speeds. For 50 000 rpm a maximum range of $\pm 0.2\%$ in efficiency is found, whereas the standard deviation is typically below $\pm 0.05\%$ for higher speeds.

The measured static pressures at the casing and diffuser hub for the two measurement campaigns are compared in figure 3.11 for the peak efficiency operating point marked in figure 3.10. Similar results are obtained for all other operating points as well. Again, a good agreement is reached between

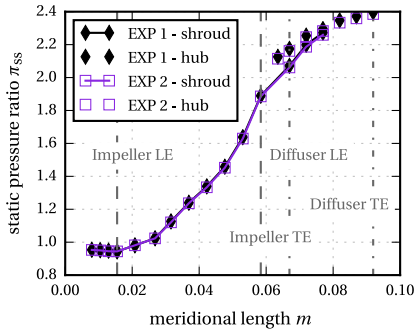


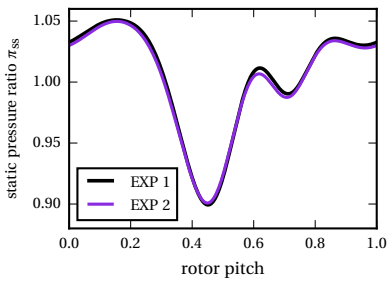
Figure 3.11 – Reproducibility measurements for the static casing pressures for 70 000 rpm and $\dot{m}_{red} = 0.45 \text{ kg/s}$

encies in the pitch-averaged signals and the amplitudes of the dominant frequencies are observed for all locations. This indicates that the main features of the near tip pressure fields can be reproduced with sufficient accuracy. For example the circumferential location of the tip vortex core, indicated by the pressure drop marked in figure 3.12c is precisely reproduced by the second experiment.

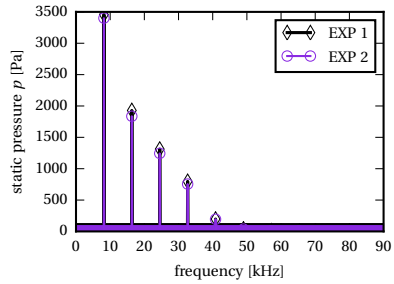
All in all this demonstrates that the measurements of a certain configuration are reproducible within a certain range of uncertainty. In conclusion, relative comparisons between the different configurations that are used in this work are permissible, in particular if the results show clear trends for not only single operating points but large regions of the map.

both cases which demonstrates that the test rig instrumentation allows for reproducible measurements. This also applies for the unsteady measurement techniques that are used in the test rig.

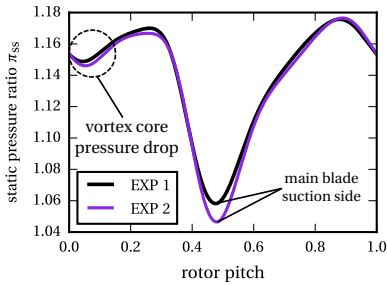
Figure 3.12 shows selected ensemble averaged signals of the Kulite pressure transducers alongside the corresponding frequency spectrum for the considered near stall operating point at $\dot{m}_{red} = 0.375 \text{ kg/s}$. The respective locations are given in figure 3.6. Only marginal discrepancies



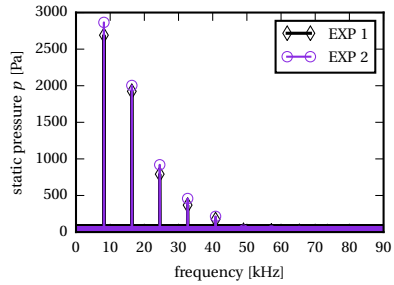
a) position 1 - pressure signal



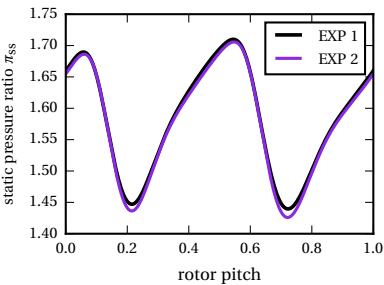
b) position 1 - spectrum



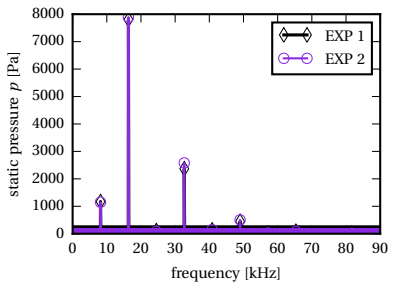
c) position 3 - pressure signal



d) position 3 - spectrum



e) position 5 - pressure signal



f) position 5 - spectrum

Figure 3.12 – Reproducibility measurements for the ensemble averaged unsteady casing pressures for 70 000 rpm and $\dot{m}_{red} = 0.375$ kg/s

4 Numerical Models

This chapter introduces the numerical models that are used in this work to investigate the different flow fields in detail. Firstly, the transformation from the actual geometry to the numerical domain is shown. Section 4.1 addresses the discretization of the different fluid volumes that are used in the numerical models. Moreover, the meshing strategy for the application of casing grooves to the baseline geometry is covered. The following section 4.2 introduces the different modeling approaches and the corresponding boundary conditions, which are applied to the respective models. Thereafter, section 4.3 demonstrates the suitability of the chosen models in terms of discretization and furthermore presents the applied criteria for convergence. Finally, section 4.4 presents the validation of the selected models. Therefore, the numerical results are compared to the test data for the baseline, smooth casing configuration.

Figure 4.1 presents a cross section view of a simplified technical drawing of the compressor stage. The simplifications that are made in the numerical models compared to the actual geometry are marked in red. The gap between the spinner screw nut and the impeller is closed and the hex bolt opening at the spinner front is neglected. Furthermore, the backspace behind the impeller is neglected as well and the corresponding gap is closed with a straight radial line. The boundaries of the different CFD domains are marked in blue. To comply with the experimental setup, the numerical model consists of up to five domains. The inlet pipe is followed by the impeller, the diffuser, the volute and the outlet pipe. The size of the model is chosen to include all measurement locations of the test rig. The planes of these locations are shown in gray. The inlet and outlet boundaries of the computational domain are placed in sufficient distance up- and downstream the respective measurement planes. Inlet and outlet plane 1 and 2 represent the respective locations of the temperature and pressure measuring locations, see also figure 3.3.

Additional planes, such as the stage inlet, the stage outlet and the impeller outlet plane are defined. These are used for the reduced models, where only selected domains are used to reduce the computational costs, see section 4.2.

The impeller inlet interface, which connects the inlet pipe and the impeller domain, is placed well inside of the converging part of the impeller but sufficiently distanced from the blades. For reasons of numerical robustness, the impeller diffuser interface is located directly at the physical connection be-

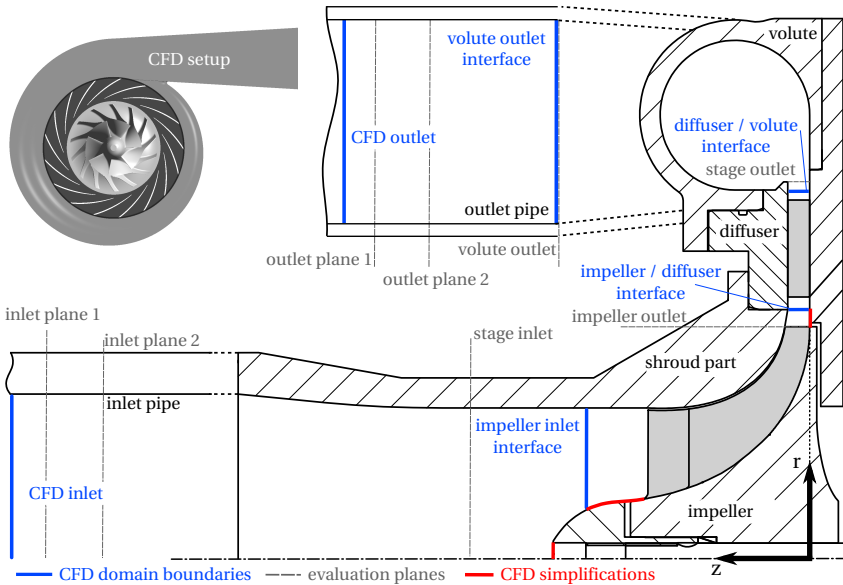


Figure 4.1 – Simplified compressor cross section view including CFD domains, boundaries, evaluation planes and simplifications according to the experimental setup

tween both casing parts, in the center between impeller TE and diffuser LE. The diffuser-to-volute interface is placed slightly inside the diffuser to enable a structured meshing approach of the volute. The volute outlet interface is placed in agreement to the experimental setup at the end of the diverging cross section. A sketch of the resulting model is shown in the left top of figure 4.1 to illustrate the different domains.

4.1 Discretization

This section presents the discretization that is used for the investigations within this study. As numerical investigations of centrifugal compressors are of great interest in industrial research, several software programs for automated mesh generation are commercially available. These deliver high-quality

meshes for standard geometries such as the baseline configuration of the ITSM compressor stage. However, the automated meshing of additional geometric shapes, such as the herein investigated casing grooves, is not possible within these programs. Many publications in the open literature therefore use interfaces to connect the grooves to an automatically generated mesh [22, 101, 102, 108, 117].

However, the usage of interfaces requires interpolation between the different meshes. Unlike circumferential grooves, automatically generated meshes are generally aligned towards the blade normal vector to improve the cell quality. This leads to different mesh orientation and different cell sizes that may result in significant interpolation errors. Very fine impeller meshes are required to reduce these errors to an acceptable level when casing grooves are applied, see Kempter [100].

Hence, in this thesis, a different approach for the discretization of the impeller fluid volume is used. To prevent the need of any interfaces to connect the groove volumes to the impeller, manually generated meshes are applied. Furthermore, this also prevents the necessity of tip gap interfaces, which are also commonly used in automated meshing tools.

To ensure comparability, the baseline mesh is prepared to allow for the addition of different circumferential grooves. The approach and the respective blocking strategy are described in the following sections. Moreover, the rather conventional discretization of the remaining fluid volumes is presented.

4.1.1 Impeller

To account for the circumferential alignment of the casing groove mesh, the impeller block structured mesh is accordingly prepared at the shroud. The corresponding blocking strategy is depicted schematically in figure 4.2. A streamwise view of the blocking orientation is shown on the left. Separated blocks are used to cover the boundary layers at the walls. The hub and the blade boundary layers are connected in such a way that this blocking layer covers the whole impeller surface. As a result, it is possible to use a so-called butterfly meshing approach for the blade fillets. Another layer is used at the shroud endwall. As can be seen from the sketch on the right, the respective blocks are aligned towards the circumferential direction. Thus, the casing groove blocks, which are discussed in section 4.1.4, can easily be applied to the baseline blocking. O-grids around the blade and in the tip gap are used

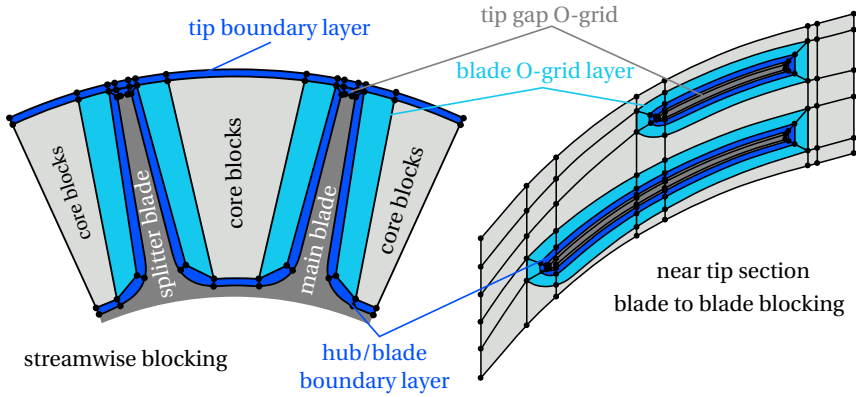


Figure 4.2 – Hexa blocking strategy for the impeller domain

to align the mesh to the shape of the blades. Ansys ICEM CFD is used for the blocking and the mesh generation of the impeller. Making use of the symmetrical geometry, only one passage including a main and a splitter blade is meshed.

An illustration of the final impeller mesh is given in figure 4.3. The surface mesh of the impeller passage is shown on the right, whereas a cross section view according to the sketch in figure 4.2 is presented on the left. The number of cells is adopted from a grid independency study. The corresponding results are discussed in section 4.3. The final mesh consists of approx-

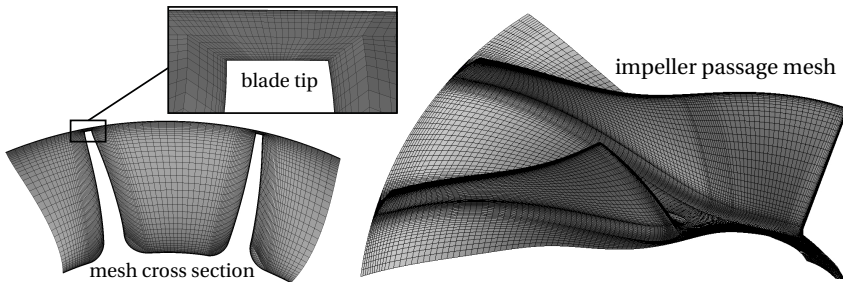


Figure 4.3 – ICEM CFD Mesh of the baseline compressor impeller with circumferential mesh alignment at the shroud

imately 1.16×10^6 cells per impeller passage for the baseline configuration. The amount and spacing of the cells in the boundary layers is selected to obtain $y^+ \approx 1$. Hence, the viscous sublayer is fully resolved without using wall functions. This is of paramount importance for the study, as the sufficient resolution of the near tip flows is required to correctly assess the impact of the grooves on the compressor flow fields. Accordingly, each boundary layer consists of 14 cells, which results in 28 cells for the spanwise resolution of the tip gap. The corresponding spacing is exemplified in the close-up view in figure 4.3.

4.1.2 Diffuser

An automated meshing strategy using Numeca AutoGrid is applied for the vaned diffuser. A single passage including one diffuser blade is meshed with periodic interfaces in circumferential direction. Figure 4.4 presents the final hexahedral structured mesh. Again, the boundary layer resolution is made to fit $y^+ \approx 1$ on all surfaces. In total, the mesh consists of approximately 2.6×10^5 cells per passage. The results for the corresponding grid independence study are presented in section 4.3. A second variant is meshed due to the requirements of the reduced stage model, where the computational domain ends after the diffuser. For numerical stability the diffuser is extended in this case, to move the outlet boundary to a higher radius. This extension is simply added to the final selected mesh shown in figure 4.4. Thus, the actual diffuser region is kept identical. The second part of this extension is nozzle shaped to prevent inadmissible diffusion, which could lead to numerical instabilities and thus deteriorate convergence.

The mesh of the vaneless diffuser is generated in conformity with the final vaned diffuser mesh. Therefore, equal node numbers are used in circumferential and streamwise direction. The spanwise node distribution is preserved as well, to maintain a comparable boundary layer resolution. Again, a second variant with an extension is necessary to apply with the reduced stage model, which is described in section 4.2.1. The pins that are used in the tests to maintain the mechanical integrity of the diffuser part are neglected for reasons of computational cost, as no significant impact is expected.

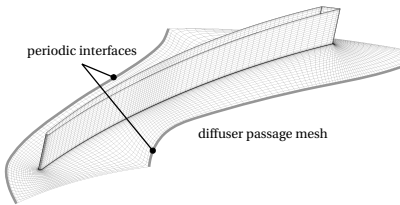


Figure 4.4 – Passage mesh of the vaned diffuser generated with Numeca AutoGrid

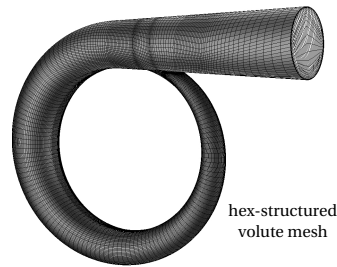


Figure 4.5 – Ansys ICEM CFD generated hex-structured mesh of the volute flow domain

4.1.3 Volute and Pipe System

Once again, hexahedral elements are used for the volute and the pipe system to obtain robust and computationally cost efficient models for the simulations. Consequently, a block structured approach is chosen for the meshing of these domains as well. The resulting mesh for the volute is presented in figure 4.5. Simple O-grid approaches are used for the pipes. To reduce the computational effort, the volute and the outlet pipe are generated with a y^+ value of around 20. Thus, the viscous sublayer near the wall is approximated using wall functions here. This approach is sufficient for the present work as no major effects, such as flow separations or extreme gradients, which could affect the casing groove investigations, are expected to occur in these domains.

In total, the volute mesh comprises 6.42×10^5 cells and 7.6×10^4 cells are used for the outlet pipe mesh. The inlet pipe mesh is matched to the downstream impeller mesh to account for a sufficient resolution of eventual backflows into the inlet pipe at certain operating conditions. As the flow profile is assumed to be uniform in circumferential direction, a passage of $360/7^\circ$ according to the impeller is used. The mesh consists of approximately 5.2×10^4 cells for the inlet pipe passage.

The cell sizes of all meshes are controlled by respective functions to prevent inadmissible expansion factors and to allow for a smooth transition between the blocks and the domains. To prevent any influences of numerical reflections at the interfaces and flow boundaries in the unsteady calculations, the grids near the respective locations are coarsened in the main flow direction to act as buffer layers towards the boundaries of the computational domain.

4.1.4 Casing Grooves

The blocking strategy of the baseline impeller, see section 4.1.1, allows for a high quality insertion of additional circumferential shapes, such as grooves. To include one or multiple grooves to the existing baseline mesh of the impeller, an additional circumferential row of blocks has to be included for each individual groove. For this purpose, the baseline blocking is split at the respective meridional locations. Once more, ICEM CFD is used to modify the blocking and to generate the meshes of the grooved configurations. The newly generated blocks are extended to fit the groove geometry. Furthermore, the tip boundary layer is adapted to the new surface. Figure 4.6 illustrates the blocking concept for a single groove and moreover shows an example of the corresponding mesh.

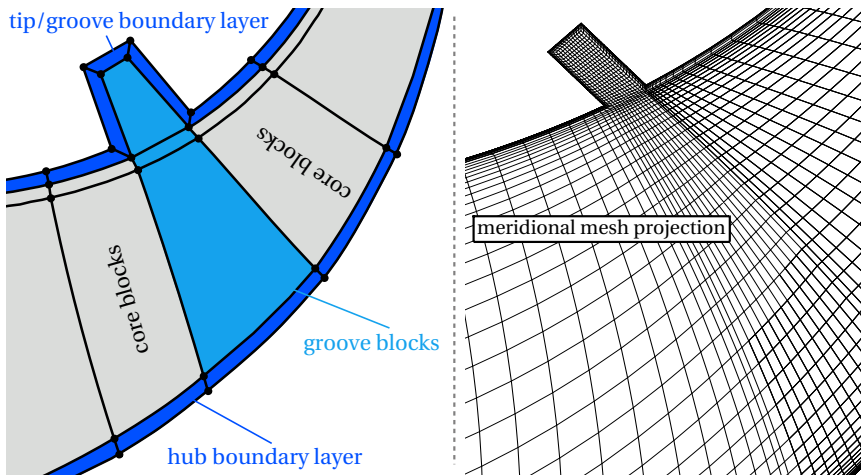


Figure 4.6 – Sketch of the blocking approach for the casing groove insertion (left) and corresponding final meridional mesh projection for an exemplary groove configuration (right)

The core blocks are split and several additional groove blocks are included. Additional groove boundary layer blocks are required to align the boundary layer to the groove endwall shape. This imposes additional effort for the mesh generation but increases the mesh quality as no high aspect ratio boundary layer cells remain in the fluid region of high interest where the groove is connected to the impeller mesh.

An example of the resulting mesh of a grooved configuration is given on the right side of figure 4.6. The mesh lines are shown as a meridional projection on the periodic surface of the impeller domain. To ensure comparability between different configurations and the baseline mesh, the cell distributions in the fluid core regions are preserved for all cases. However, with every additional groove, more cells are required to ensure a sufficient resolution of the individual grooves. Thus, the overall number of cells in the domain changes. As the geometric parameters of the grooves are varied within the studies, the groove cell numbers are varied as well. A uniform cell distribution is chosen for the groove block. Based on the results in section 4.3, a resolution of 10 cells per millimeter of depth and width for the inner groove block is selected. As the boundary layer resolution is preserved, the respective number of cells is consequently added to the overall meridional and spanwise values inside the grooves. The number of nodes in circumferential direction remains constant.

To preserve the overall meridional cell distribution in the impeller flow channel at best, the node numbers in the core blocks are reduced for each groove that is included. To maintain a smooth transition between the blocks, the node distributions are coupled by expansion laws, as can be seen in the picture. Nevertheless, the total number of nodes in streamwise direction increases with more grooves applied, as additional cells are required to allow for these smooth transitions. However, the impact on the results of the computations is assumed to be negligible as the final grid is almost independent from further refinement.

The presented concept is independent of the geometrical parameters of the groove. However, it has to be noted that the quality of the mesh in terms of skewness can decrease for very high and very low groove angles, as the angles between the groove and the shroud become small. Consequently, the approach is used for all investigations in this work, whereby the smallest angles near the transition from main flow channel to the groove are kept above approximately 10° .

A Python-based tool is used for an automation of the meshing process. The required parameters are calculated based on the user-specified groove geometry. Thereafter, the tool automatically adjusts the blocking and the meshing setup in ICEM CFD. Several quality criteria, in particular the minimum angles and cell determinants, are checked afterwards for each case to ensure a constant level of mesh quality. If this is found to be insufficient, manual adjustments are made until the minimum quality criteria are met.

4.2 CFD Modeling

Different computational models are used within this study, depending on the purpose of the simulations. Steady-state RANS (Reynolds Averaged Navier-Stokes), as well as time resolved URANS (Unsteady RANS) models are applied. Moreover, the computational domains and the respective boundary conditions are varied to account for certain flow features, such as circumferential non-uniformity, or to reduce the computational costs. The corresponding models are described in this section.

All CFD simulations are performed with the commercial solver Ansys CFX 19.0. The fluid properties of air are calculated using the ideal gas equation. Table 4.1 presents the specific fluid properties for air. The temperature dependent dynamic viscosity μ is modeled according to Sutherlands equation, see [150]

$$\mu = \mu_{\text{ref}} \frac{T_{\text{ref}} + C}{T + C} \left(\frac{T}{T_{\text{ref}}} \right)^{\frac{3}{2}}, \quad (4.1)$$

where C is the Sutherland constant, which for air comes to $C = 120\text{K}$. The reference values are $T_{\text{ref}} = 291.15\text{K}$ and $\mu_{\text{ref}} = 18.27 \times 10^{-6}\text{Pas}$.

Table 4.1 – Fluid property settings for air as ideal gas

| property | setting |
|--------------------------------|--------------------------|
| molar mass M | 28.96 kg/kmol |
| thermal conductivity λ | 0.0261 W/(m K) |
| dynamic viscosity μ | Sutherland model: $f(T)$ |
| specific heat capacity c_p | polynomial fit: $f(T)$ |

Likewise, the specific heat capacity c_p is also modeled as a function of the temperature for the expected range, as the impact of the corresponding pressure variation is negligible. A fifth degree polynomial fit, based on data from the NIST software REFPROP [110], is applied for the considered temperature range of 250 K to 700 K.

Menters SST- $k-\omega$ turbulence model [116] is applied to close the RANS equations for its well known suitability and robustness in flows with adverse pressure gradients. Bourgeois et al. [11] recommend this model for centrifugal compressors as it shows the best results compared to experimental data over a

wide operating range for their case. This is also confirmed by Gibson et al. [61] who specifically investigated different turbulence models for a centrifugal compressor with a vaned diffuser.

4.2.1 Steady-State Models

Two different steady-state models are used within this study. Rotational periodicity is assumed for both and thus only one periodic passage of the geometry has to be modeled, which drastically reduces the overall mesh size. To validate and compare the numerical results with the measured data, it is paramount to accurately model the corresponding test section. Thus, a so-called full stage model is used for this purpose, which models all relevant parts of the test rig setup, see figure 4.1.

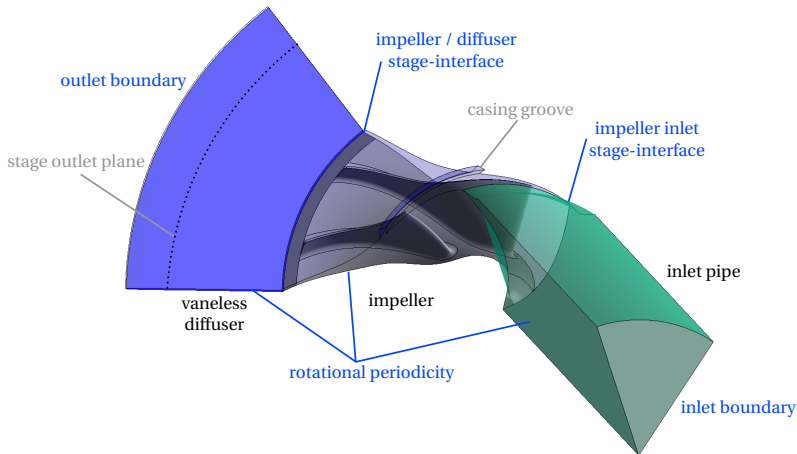


Figure 4.7 – Numerical stage model with the vaneless diffuser configuration using periodic boundary conditions

To assess the basic impacts of different groove shapes and configurations in the design study, a reduced model is deployed to decrease the computational costs. It comprises only the impeller domain, an inlet region and a diffuser region downstream of the impeller. The volute and the additional pipes are neglected. Figure 4.7 depicts the numerical domains of this reduced stage model

with a vaneless diffuser and the corresponding boundaries and interfaces. A converging extension of the diffuser domain is used in this model to ensure numerical stability and to prevent any repercussion of the outlet boundary conditions on the evaluation planes.

All boundary conditions are applied according to the experimental setup for both models. The walls are modeled as adiabatic no slip walls, whereas counter rotating walls are used for fixed walls within the rotating impeller domain. Depending on the operating point, either the massflow or the pressure at the exit of the computational domain is fixed. Total pressure and temperature boundary conditions are used at the inlet, whereas the pressure is set according to the inlet pressure levels of the respective experiments. Mixing plane interfaces are used to model the transition from stationary to moving reference frames and vice versa.

Data Extraction

In general, the data extraction for the subsequent evaluation of the results is performed in accordance to the measurements. If not stated otherwise, all comparisons are based on the same evaluation positions. Averaged values are used to calculate the overall performance values, whereby area-averages are used for static quantities and massflow-averages for flow dependent variables.

A different approach is required for the comparison of the steady-state CFD to the measured casing pressures and the ensemble-averaged Kulite data in the rotating impeller domain. Circumferential lines at the casing are used at each pressure tap position for the data extraction. The line-averaged pressure represents the measured value from the experiments, whereas the pressure distribution along these lines can be compared to the time resolved pressure signal of the ensemble averaged sensor data.

For the measuring locations in the diffuser the representative value at the same location is used from the calculations. As the steady-state calculations represent an averaged flow solution, this is comparable to the averaged measured data.

Speedline Calculation Approach

Steady-state performance maps are calculated to compare to the measured speedlines. Therefore, a similar approach is chosen for the calculations of the

different operating points. Starting at choke, the flow rate is automatically decreased in specified steps until the solution does not converge anymore. The flow rate is then increased in smaller steps to identify the last converging operating point. This method is applied for all the different configurations to ensure comparability.

4.2.2 Time-Resolved Models

To evaluate the impact of the grooves on the compressor stability and to obtain further insight into the corresponding flow mechanisms, transient calculations are required to capture the inherently unsteady effects towards unstable operation. Furthermore, transient effects, such as uneven flow distributions induced by the volute asymmetry or rotor stator interaction, are present at all operating points. To account for those, a full 360° model is deployed.

A sketch of the flow domains is depicted in figure 4.8. Both, the vanned and the vaneless configurations are used. In contrast to the steady-state full stage model, the pipes up- and downstream of the stage are shortened. Thereby, the computational costs in terms of simulation time can be drastically reduced. This is necessary as the convection of information through the long pipes would lead to an excessive increase of the required timesteps until convergence is obtained. To improve the robustness of the outlet boundary condition, a volute extension nozzle is used at the domain outlet. Moreover, the element sizes of the extension mesh increase significantly towards the outlet to damp numerical reflections, which can emerge at the outlet due to the formulation of the boundary conditions in Ansys CFX.

The number of physical timesteps to discretize a full impeller rotation is set to 700. This equals 100 steps per impeller main blade passing period and approximately 41 steps per diffuser passage. These values are selected on the basis of a corresponding study for a comparable setup [137]. For the vaneless diffuser configuration, 80 steps per impeller main blade passing period were found to be sufficient. Five sub-iterations are performed within the inner loop for each physical timestep, generally reducing the residuals by 1.5 orders of magnitude.

At the inlet of the flow domain, the total pressure, the total temperature, axial flow and a medium turbulence intensity of 5% are prescribed. Regarding the outlet boundary condition, several problems arise for a physically correct implementation towards the occurrence of flow instabilities at low massflow

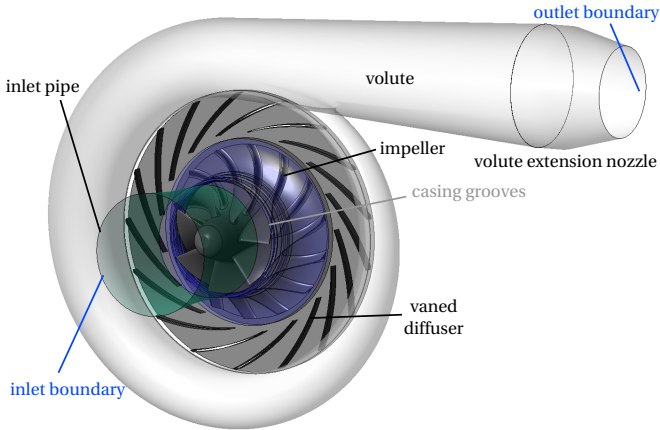


Figure 4.8 – Sketch of the numerical model used for the unsteady calculations (URANS) with the vaned diffuser configuration

rates. Using a massflow boundary condition is inappropriate due to the large expected massflow fluctuations when driving the compressor into unstable operation. A standard pressure boundary condition is also not applicable as the slope of the characteristic becomes positive for operating points close to stall. Therefore, a throttle like boundary condition similar to the work of Bousquet et al. [12] is applied. The outlet pressure p_{out} is adjusted in each timestep T_n , depending on the current massflow rate \dot{m} at the volute outlet, according to the following equation

$$p_{\text{out}}(T_{n+1}) = p_{\text{in}} + \Delta (\dot{m}(T_n))^2, \quad (4.2)$$

where p_{in} is the inlet pressure and Δ denotes the throttle parameter. This formulation permits to model the whole operating characteristic from choke to stall as the outlet pressure is a function of the current massflow rate. A constant throttle parameter thus enables the calculation of static operating points.

Dynamic simulations towards stall are realized by simply increasing the throttle parameter. The left part of figure 4.9 illustrates this concept and moreover introduces the methodology of the calculations towards stall. Solutions of

stable operating points are calculated with a constant throttle parameter Δ , based on a previously conducted steady-state solution of the full 360° model. These calculations are run for 10 full rotor revolutions, which was found to be sufficient to obtain converged solutions. Subsequently, one additional revolution is simulated while the data is logged and the flow variables are averaged. This mean solution can then be compared to the experimental and the steady-state data.

To capture the dynamic processes towards compressor instability, this throttle parameter is sequentially increased. Starting from a stable, near stall operating point, the throttle parameter is increased to force the operating point to lower massflow rates. The corresponding methodology is depicted in the sketch on the right side of figure 4.9. The initial throttle parameter Δ_{start} is obtained from a steady-state calculation. Thereafter, the transient simulation is run for 15 full rotor revolutions to obtain a converged solution for the still stable operating point. Subsequently, the throttle parameter is increased in steps of 1% of the start value after each 2 full rotor revolutions until the onset of flow instabilities. These are normally followed by a substantial drop in the massflow rate. Consequently, the simulations are stopped if the inlet massflow falls below an arbitrary value of 50% of the initial steady-state flow rate.

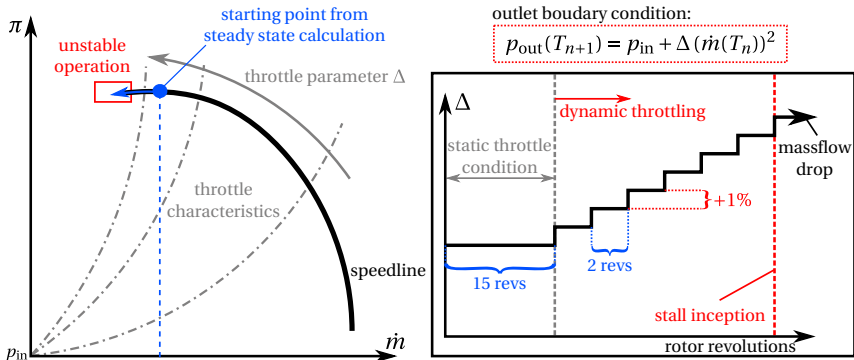


Figure 4.9 – Methodology of unsteady calculations towards compressor instability using a throttle-like boundary condition

Due to the high computational cost of the dynamic computations, only a very limited number of runs is feasible. Thus, only the smooth casing and the final groove configurations, that are also tested experimentally, are investigated

using this methodology. The simulations are performed on the Cray XC40 type supercomputer Hazel Hen of the HLRS at the University of Stuttgart, see [80]. Table 4.2 summarizes the required computational resources for the distinct configurations up until the prescribed stop criterion is reached. The number of revolutions given in the table refers to the running time of the simulations and does not necessarily coincide with the onset of stall, as the initial drop in massflow might not reach the prescribed criterion.

Table 4.2 – Computational resources for the dynamic URANS simulations towards compressor instability

| case | diffuser | total mesh size | revolutions | CPU hours |
|-----------|----------|----------------------------------|---------------|-----------|
| <i>sc</i> | vaned | $\approx 13.9 \times 10^6$ cells | ≈ 58 | 168 635 |
| <i>g2</i> | vaned | $\approx 16.7 \times 10^6$ cells | ≈ 57 | 180 390 |
| <i>g4</i> | vaned | $\approx 21 \times 10^6$ cells | ≈ 52 | 227 690 |
| <i>sc</i> | vaneless | $\approx 9.8 \times 10^6$ cells | ≈ 80 | 129 694 |
| <i>g2</i> | vaneless | $\approx 12.5 \times 10^6$ cells | ≈ 86 | 163 500 |
| <i>g4</i> | vaneless | $\approx 15.1 \times 10^6$ cells | ≈ 101 | 224 389 |

Data Extraction

Once more, the data extraction for the subsequent evaluation of the results is performed in accordance to the measurements. All averaged values are calculated in accordance to the steady-state calculations. However, the respective values are extracted from a time-averaged flow field of the full computational domain. Therefore, the time-averaged solution of the last full rotor revolution of the simulation is stored.

Not all evaluation planes are available for the data extraction, as the extend of the domains is reduced in the URANS models. If necessary, different locations are used for comparisons to the experimental data. However, this is emphasized in the specific text description. The data at the Kulite sensor locations is recorded over the course of the complete simulations and thus can be treated according to the measured data.

4.3 Verification

A verification of the previously described numerical model is required to assess the suitability for the present study. This includes numerical errors as well as errors due to insufficient discretization. To minimize these, or at least to evaluate the sensitivity on the results, grid independency studies are carried out for the domains of interest. This means that the impact of the discretization of the flow domains on the numerical results is checked. Moreover, the convergence of the numerical results is an issue as the solutions are obtained iteratively. An evaluation of the software itself is not required here, as the commercial solver Ansys CFX is used for the simulations, which is verified for a wide range of different flow problems, including centrifugal compressor flows [61].

Impact of Discretization

A grid independency study has been carried out to select appropriate mesh resolutions for the main components of the study, more specifically the impeller and the diffuser. The mesh sizes of the remaining domains are selected from experience as no significant impact on the results is expected here. Moreover, the focus of the study is on the impact of circumferential grooves on the flow field in the impeller and its interaction with the diffuser, which are for the most part responsible for the performance and the stability of the system.

Five different meshes are generated for the impeller domain. The changes are applied in each direction of the blocking, more precisely in spanwise, streamwise and circumferential direction. However, the boundary layer resolution, more precisely the cell number and distribution in normal direction of the walls, is maintained to ensure comparability. The cell numbers are varied between 3×10^5 and 1.65×10^6 cells, which is well within the range of recent investigations available in the open literature, see [13, 61] for example. Finer meshes are not considered in this study as there is also a demand for low computational costs, which has to be met.

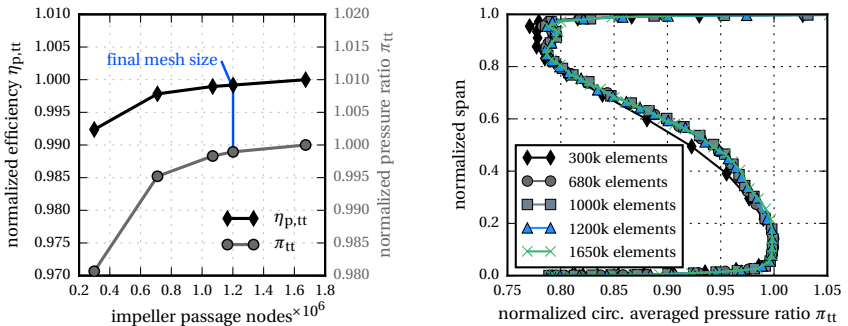
The simulations are performed with the reduced stage model, described in 4.2.1, using an identical setup for the remaining domains. Figure 4.10 presents the results for the five different simulations. An operating point at the highest speed of 90 000 rpm and a reduced massflow of 0.59 kg/s is chosen as the loading of the blades is high and the flow patterns are complex due to shocks and

strong secondary flows. Figure 4.10a shows the normalized overall results for the pressure ratio and the efficiency of the stage. The results are normalized with the respective results of the finest mesh. A typical asymptotic trend is observed for both variables. The changes between the four finest meshes are below 0.25%. Figure 4.10b presents the normalized circumferential averaged pressure ratio profile at the impeller exit. Except for the coarsest mesh, the results are almost identical, which complies with the results of the stage performance.

In this case the mesh with 1.16×10^6 cells is selected to be used for the study as the differences to the finest mesh are below 0.1%. Moreover, selecting a finer mesh makes it easier to generate smooth meshes when casing grooves are applied.

After selecting the final impeller mesh size, the diffuser is varied as well. Once more, five different mesh sizes are investigated, while retaining the boundary layer resolution. All calculations are performed using the final impeller mesh. A variation between 70 000 and 370 000 cells is studied for a single diffuser passage. The corresponding results are plotted in figure 4.11.

The trend of efficiency and total pressure ratio in figure 4.11a is again asymptotic. In this case, the mesh with approximately 300 000 cells yields almost the same results as the finest mesh. As the differences are negligible, it is not necessary to study even finer meshes. Actually, this is also shown by the



a) Normalized stage efficiency and total pressure ratio

b) Normalized circumferential averaged total pressure ratio at the impeller exit

Figure 4.10 – Impeller grid study results for the smooth casing configuration

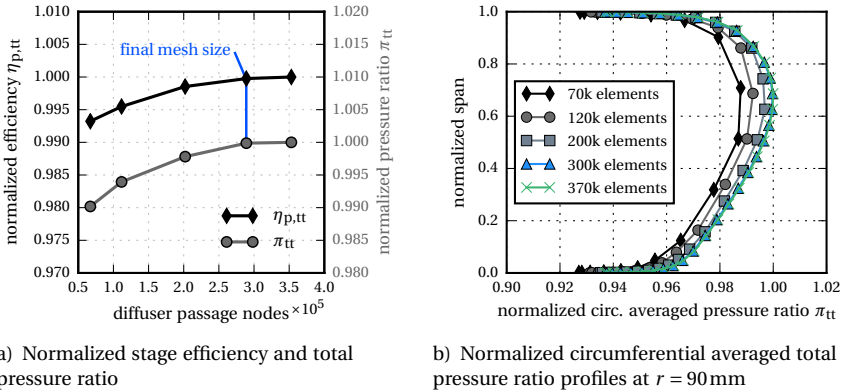


Figure 4.11 – Diffuser grid study results generated with the final impeller mesh

normalized circumferential averaged pressure ratio profiles in figure 4.11b. Distinct differences are visible for all mesh sizes despite for the two finest ones.

As a result, the diffuser mesh with approximately 300 000 elements is sufficient for the present study and thus selected. Because the calculations of the grid studies are performed with the extended diffuser, this results in a mesh size for the actual diffuser domain of 2.6×10^5 cells, which is already given in 4.1.2.

To fully resolve the turbulent boundary layer as well as the laminar sublayer with a sufficient amount of cells, a dimensionless wall distance y^+ of around

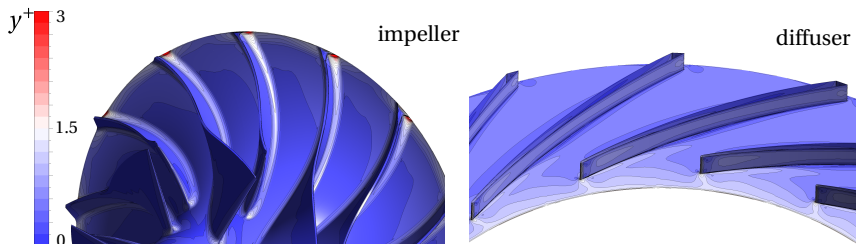


Figure 4.12 – y^+ distribution for the hub and blade surfaces of the impeller and the diffuser of the final meshes for $n = 90$ krpm and $\dot{m}_{red} = 0.59$ kg/s

1 is aimed for [44]. Moreover, a cell expansion ratio below 1.4 is ensured. The distribution of the y^+ values on the hub and the blades of the final impeller and diffuser meshes are shown in figure 4.12. As intended, the dimensionless wall distance is in the range of 1 throughout the domains. In fact the values are below 1 for most of the surfaces, resulting in mean values of 0.701 on all impeller surfaces and 0.753 in the diffuser. The highest values are located at the impeller trailing edge where values of up to almost 5 are observed at this operating point. Based on these results, the meshes are suited for the present study.

An additional grid study is carried out to assess the number of cells required to sufficiently discretize the casing grooves, which are added to the baseline mesh. One representative groove configuration, namely $g1\ m'50\ t3\ b1.5\ \gamma45$ is selected for this study. The groove parametrization and the respective nomenclature is given in section 5.1.1. It is assumed that the results are transferable to other geometric shapes and locations as well. The circumferential node distribution is adopted from the core mesh and thus is not varied. Moreover, the grid preferences of the boundary layer blocks remain constant.

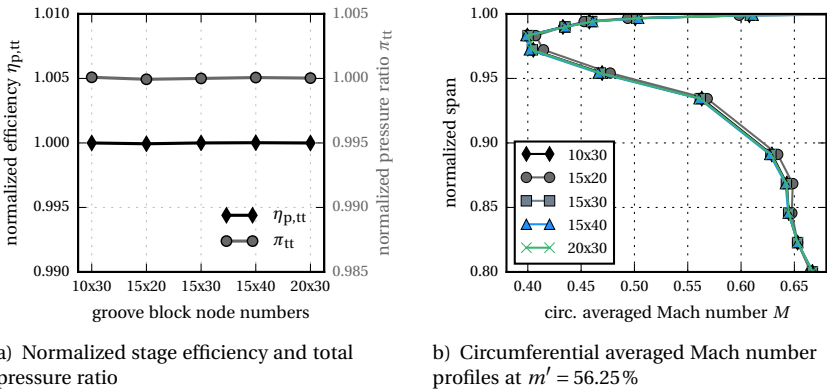


Figure 4.13 – Groove discretization study results with the final impeller mesh

The meridional and spanwise node numbers of the inner groove mesh are varied to assess the impact on the numerical solution and to select a sufficient resolution. An initial value of 10 nodes per millimeter of depth and width is chosen, which results in similar cell sizes compared to the core mesh of the

impeller. In the present configuration this results in 15 meridional nodes and 30 nodes in spanwise direction. Both parameters are varied by increasing and decreasing the node number in each direction by one third.

The corresponding results are plotted in figure 4.13. The overall results in terms of efficiency and pressure ratio are shown in figure 4.13a. The normalization is performed with respect to the initial grid spacing 15x30. The results suggest that the impact on integral values is negligible for the considered range. Figure 4.13b shows the circumferential averaged Mach number profile near the tip, directly downstream of the groove location at $m' = 56.25\%$. Again the impact is negligible, except for the 15x20 case, which shows a slightly altered profile. Nevertheless, the impact of the groove grid resolution is small within the considered range. Therefore, the initial spacing is used for all further investigations with 10 nodes per millimeter for each direction. An example of the final grid resolution of the casing grooves is given in figure 4.6 for a similar configuration.

Convergence

Achieving and ensuring convergence of the simulations is always a key objective in any numerical work. To ensure comparability between different configurations with potentially only marginal differences, a precise formulation is required when a simulation is considered to be converged. The present study utilizes a residual based approach. During each simulation, the isentropic efficiency, the stage pressure ratio and the imbalance of the massflow at the in- and outlet are monitored. The values of the last 100 iterations are considered for the evaluation. Subsequently, the steady-state simulations are defined to be converged if the corresponding variance is below 0.02%. Thus numerical fluctuations, resulting from the iterative calculation process are minimized. This enables comparisons of even small differences between configurations.

Due to the throttle-like boundary condition specification in the URANS calculations (see section 4.2.2), no classical convergence with completely periodic solutions is obtainable. Hence, convergence is defined by the user if the mean values reach a steady level and the fluctuations are close to being fully periodic.

4.4 Validation

The results of the numerical models are compared to the available experimental data to assess if and to what extent these models are capable of predicting the measured compressor characteristics and flow fields. Equivalent reduced speeds n_{red} are used for all comparisons. The validation is carried out for the smooth casing configuration acting as a baseline. Both diffuser configurations (vaned and vaneless type) are considered and the results are presented in the following sections. Thereafter, the results are discussed with respect to the suitability of the models for the present work.

4.4.1 Vaned Diffuser Configuration

This section compares the numerical results to the experimentally obtained ones for the vaned diffuser configuration, which was initially designed for the investigated compressor stage. Figure 4.14 summarizes the results for the global compressor characteristics and some distinguished operating points. In addition to the steady-state model described in section 4.2.1, time-resolved simulations (URANS) have been performed for selected operating points. The presented results for these calculations are based on the averaged flow variables of one full rotor revolution. Furthermore, steady-state calculations where the diffuser is extended to the full circumference (RANS - 360°) are used to study if the circumferential nonuniformity imposed by the volute needs to be considered in the following studies.

The performance map in figure 4.14a shows a good agreement for the speed-lines up to 70 000 rpm. The slope of the characteristic and the maximum flow rate are matching well for the complete operating range. However, the pressure rise is over-predicted by the RANS calculations, in particular for high rotational speeds. A good agreement with differences below 2 % is found for 50 000 rpm and 60 000 rpm, whereas the experimental results are over-predicted by up to 9 % for the maximum speed at 90 000 rpm. The 360°-diffuser calculations show that these discrepancies are not resulting from the volute asymmetry, as very similar results are obtained for pressure rise and efficiency for the high rotational speeds.

As the total temperature ratio τ_{tt} in figure 4.14c matches very well for the complete map, the isentropic efficiency in figure 4.14b shows the same trends as the pressure rise. A constant offset of about 4 points in maximum efficiency

is observed up to 70 000 rpm, whereas this increases for the higher speeds. Nevertheless, the slope of the speedline and the flow rate of maximum efficiency is predicted accurately. The unsteady calculations support the general results of the steady-state calculations for the mid speedline, whereby only small differences are observed for the pressure rise and the efficiency. Further physical effects, such as for example wakes, circumferential nonuniformity in the rotor and flow unsteadiness in general are included in this model. These are suppressed by the mixing plane and the periodic boundary conditions in the steady-state models. Consequently, the results become more accurate compared to the experiments, in particular for the maximum speedline where the prediction is significantly closer to the experiments. This indicates that the steady-state models are not able to capture some of the dominant flow features, which are present at high rotational speeds.

Figures 4.14d to 4.14f present comparisons of the impeller and diffuser pressure tap data along the meridional coordinate for selected operating points. All pressure ratio values are based on the respective inlet pressures. Both numerical models (RANS and URANS) yield very similar results for the pressure rise up until the impeller TE, even for the maximum speed of 90 000 rpm. Again, an over-prediction of the experimentally obtained results is observed. However, at 90 krpm in figure 4.14f these deviations are much smaller compared to the overall pressure ratio deviations shown in figure 4.14a. The discrepancies increase drastically in the diffuser, where the RANS model predicts a much larger pressure rise and thus a stronger diffusion of the flow, in particular in the rear part of the diffuser. The unsteady model however, remains much closer to the measured values. This indicates severe blockage zones covering large areas of the flow channels in the vaned diffuser, as almost no pressure rise is generated in the rear part.

Figure 4.15 depicts a comparison of the Mach number distribution on midspan in the diffuser for the URANS and the RANS - 360° calculations. The URANS results are obtained and averaged with the method described in section 4.2.2. The circumferential mixing in the RANS model at the diffuser inlet leads to a very homogeneous flow field for all diffuser channels, whereby only a small flow separation is predicted on the blade pressure sides. These separations are much larger for the unsteady case, where large parts of the flow area are blocked. Several fully blocked channels develop that lead to an unstable behavior of the flow in the diffuser. This affects the convergence of the solutions for this operating point. The flow variables remain on similar levels but no clear periodicity in time is reached, even after a rather long simula-

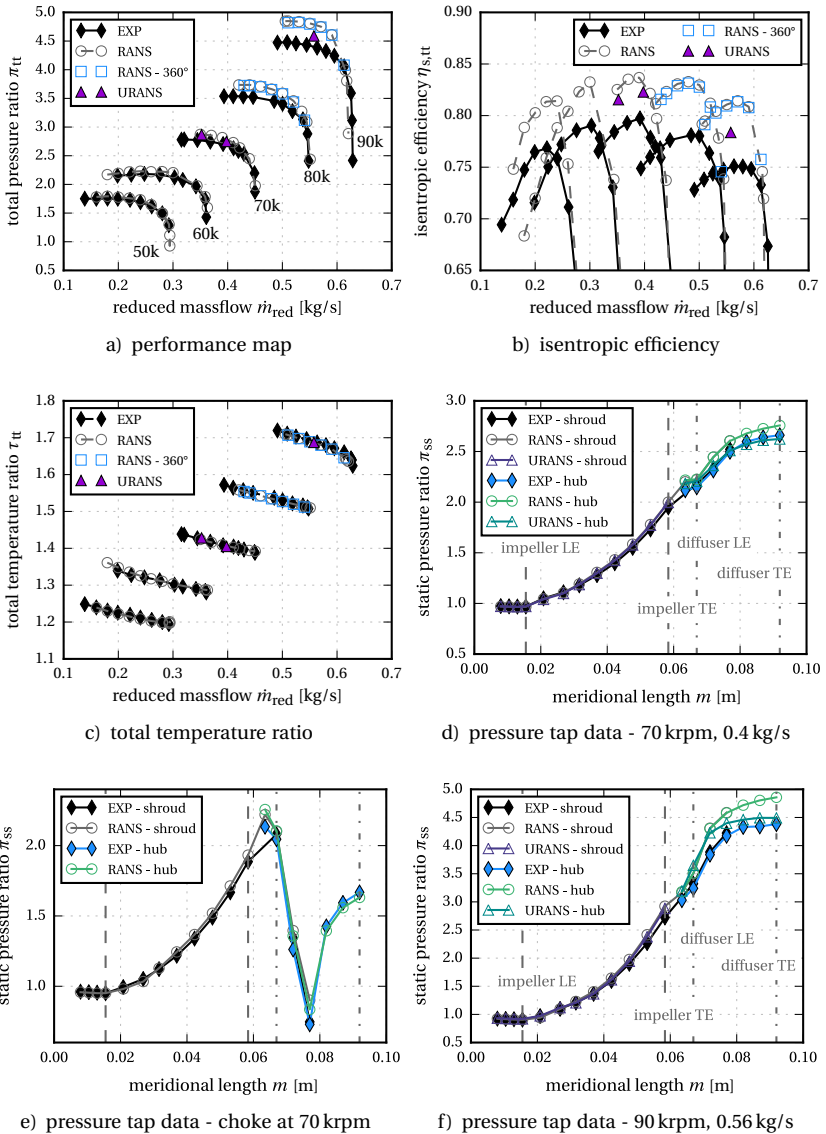


Figure 4.14 – CFD validation with experimental data for the smooth casing and the vaned diffuser setup, URANS pressure tap locations equal the experiments, RANS pressure tap data represents circumferential average

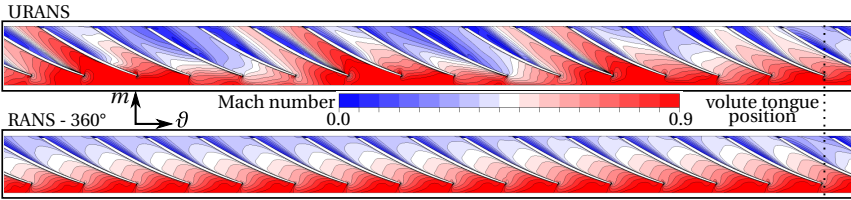


Figure 4.15 – Comparison of midspan Mach number distribution in the diffuser for the URANS and the RANS - 360° calculations at $n = 90\,000$ rpm and $\dot{m}_{\text{red}} = 0.56$ kg/s, URANS results averaged over one full rotor revolution

tion time of 10 full rotor revolutions. Nevertheless, this explains the increased discrepancies as the diffusion of the flow decreases and losses are increased.

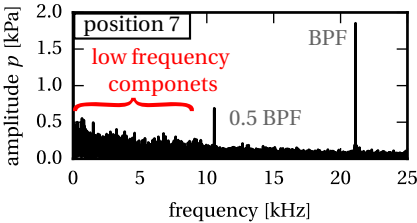


Figure 4.16 – Measured frequency spectrum in the vaned diffuser (position 7) at 90 000 rpm and 0.56 kg/s

These indicate strong unsteadiness of the flow, which most likely stems from unsteady flow separations, similar to the URANS results. As the mixing plane model leads to an underestimation of these effects, it is not capable of predicting the diffuser flow field accurately towards higher speeds in the studied compressor stage.

Nevertheless, the model still captures most of the global flow phenomena correctly. The averaged pressure rise characteristic and the pressure drop location at choke matches very well with the experiments, see figure 4.14e. The unsteady impeller casing pressures also show a close resemblance. The pressure amplitude results for an exemplary operating point are summarized in figure 4.17 for the different sensor positions in the time and also the frequency domain. The RANS and the URANS pressure signals and temporal decompositions match very well for the whole impeller. This indicates that no

In conclusion, the results suggest that the diffuser experiences high unsteadiness and presumably large scale flow separations in the experiments at high diffuser inlet Mach numbers that are present at high rotational speeds. This is supported by the frequency spectrum derived at the diffuser inlet (sensor position 7) in figure 4.16, where large broadband amplitudes are observed below the blade passing frequencies. These

major differences in the impeller flow field prediction are present, in contrast to the diffuser.

Comparing the CFD results with the ensemble averaged test data, the following observations are made. The general overall characteristic and the pressure gradient in the middle of the blade channels matches well at all sensor positions. This also resembles in the amplitudes of the frequency components which show similar trends. However, the sharp pressure gradients and the peaks in the immediate vicinity of the blades are much more pronounced in the computed curves. The signal in front of the impeller at position 1 for example, which is dominated by the potential field of the main blade, is almost identically reproduced by the computations. Other striking phenomena are at least reproduced to some extent. For example the tip-vortex core location, marked by the pressure drop at position 3, or the kinks in the pressure curves at positions 5 and 6 are similarly predicted. In contrast to that, the signals at position 2 directly above the LE match poorly as the pressure to suction side drop near the blade is not resolved accurately in the experimental data. The signal shape is very similar to position 1, which indicates that the measured signal represents a location in front of the blades. This might result from the extent of the sensor which stretches throughout the LE of the main blades, where the pressure gradient is much lower. However, the exact reasons could not be identified but the measuring location directly above the LE should be reconsidered in future applications. An error in the ensemble averaging algorithm can be ruled out, as the raw data is resembled very well by the averaged values, see appendix figure A.1.

The other positions match quite well but in general it seems that the computations include a significant share of higher frequency components, which are not resolved in the ensemble averaged signals, despite a sufficiently high sampling rate, see section 3.2.2.

Summarizing this, the steady-state models are in general capable of predicting the global performance trends and the dominant flow features. An exception is observed for high diffuser inlet Mach numbers, where the results indicate that large scale separations develop in the vaned diffuser. These are suppressed in the steady-state CFD models, which therefore over-predicts the pressure rise and efficiency. Nevertheless, the impeller flow fields are predicted well by the RANS models, particularly for this works primary aim of demonstrating trends and understanding the physical mechanisms.

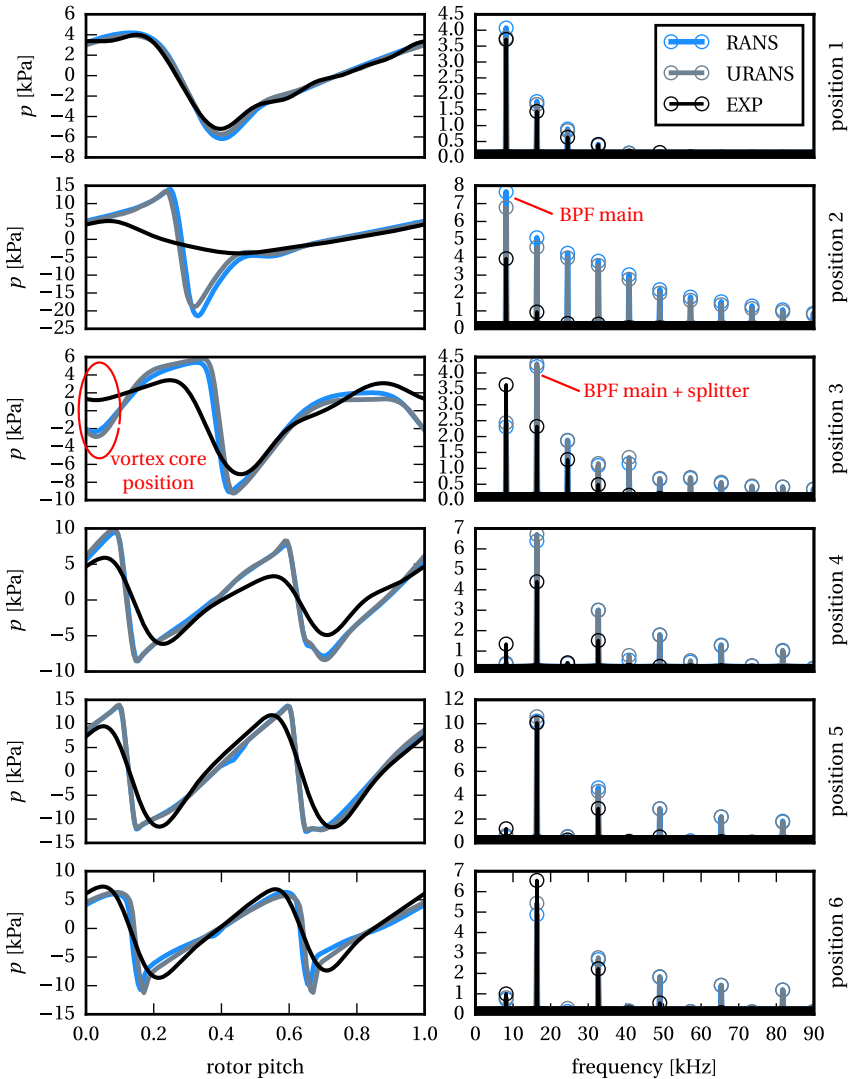


Figure 4.17 – Comparison of pressure amplitudes in the time (left) and frequency domain (right) for the different sensor positions at the impeller shroud at $n = 70000$ rpm and $\dot{m}_{\text{red}} = 0.4$ kg/s, the experimental values represent ensemble averaged data

4.4.2 Vaneless Diffuser Configuration

This section presents the validation for the vaneless diffuser case. It has to be noted that the vaneless diffuser design is based on the vaned diffuser by removing the blades and thus is not adjusted to the impeller outflow. Furthermore, the volute does not match the resulting stage design as it is designed for the vaned diffuser outflow angle. The aim here is to validate the models of this configuration for further studies with the vaneless diffuser on the one hand and to further examine if the vaned diffuser is responsible for the discrepancies observed in section 4.4.1 on the other. Figure 4.18 summarizes the results for the global compressor characteristics and some distinguished operating points.

The prediction of the total pressure ratio π_{tt} in figure 4.18a is in good agreement with the measured data. The steady-state numerical results over-predict the pressure rise by 4% to 5% but the trends are captured well. The choke massflow is predicted accurately with a difference of about 1%. The normalization of the results in figure 4.18b shows that the over-prediction of the pressure rise is systematic and that the slope of the speedlines matches well for the complete operating range. Moreover, the URANS results are very close to the RANS calculations for all considered operating points. This is in contrast to the vaned diffuser configuration for which the differences increased with rising speed. Consequently, this further confirms the conclusions drawn for the vaned diffuser flow being responsible for the discrepancies at high speeds in section 4.4.1.

Figure 4.18c compares the isentropic efficiencies. The computations again predict larger efficiencies compared to the experimental results. Again, the general trends are captured by the computations, except for the lowest speed at 50 000 rpm. The experiments show a decline for this speedline, whereas the calculations predict the highest efficiencies at this speed. Moreover, the discrepancies of the absolute values increase for lower speeds. Presumably this is related to heat transfer issues at the test rig. At low speeds, heat is transferred from the gearbox to the flow, which increases the flow temperature and thus deteriorates the efficiency. The gearbox is located directly behind the diffuser hub, where most heat transfer takes place. As the flow paths in the vaneless diffuser increase significantly compared to the vaned diffuser, a larger temperature rise is obtained, which explains the increased discrepancies.

Moreover, the non-matching of the diffuser and the volute may result in in flow separations near the endwalls, which could be problematic at low speeds,

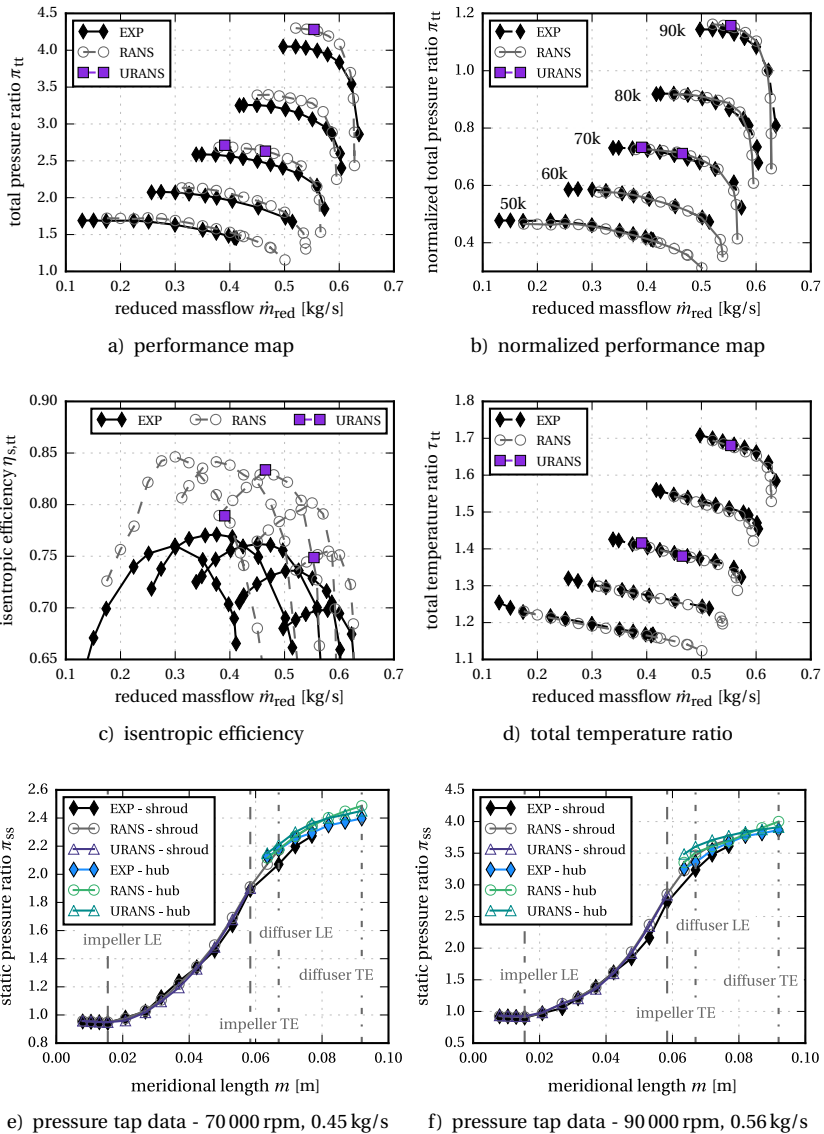


Figure 4.18 – CFD validation with experimental data for the smooth casing and the vaneless diffuser setup

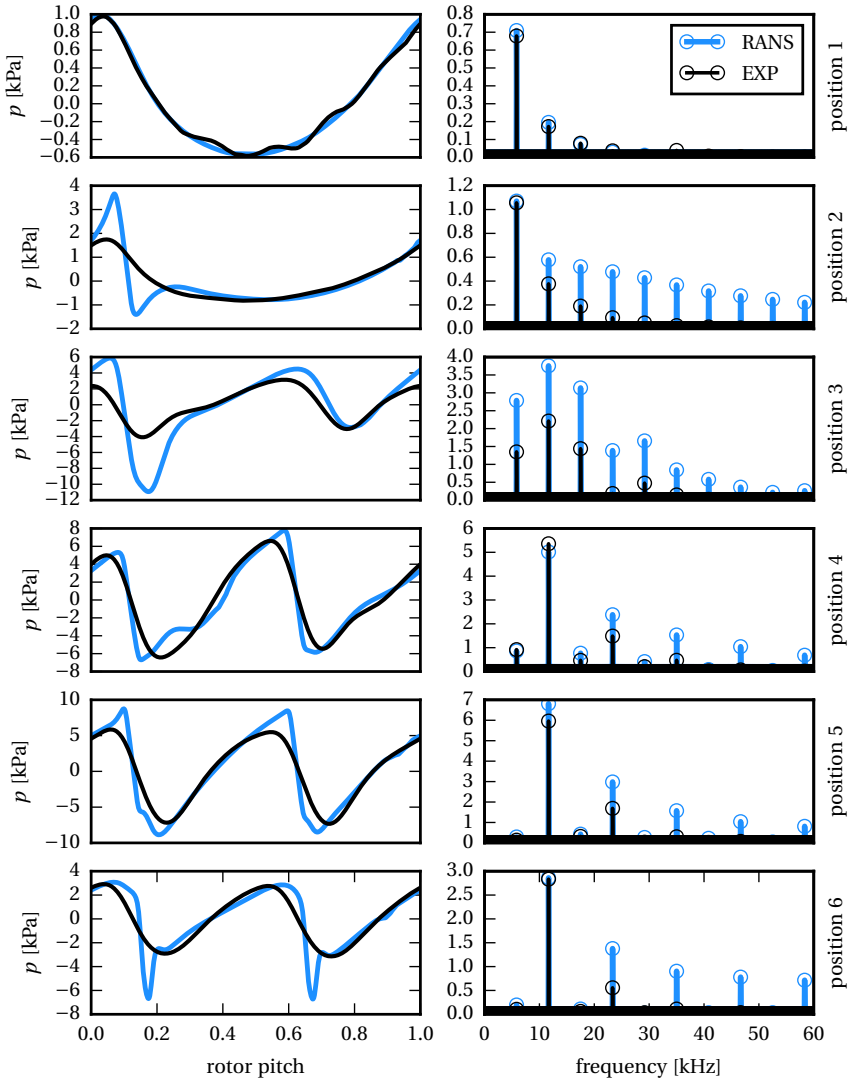


Figure 4.19 – Comparison of pressure amplitudes in the time (left) and frequency domain (right) for the different sensor positions at the impeller shroud at $n = 50000$ rpm and $\dot{m}_{\text{red}} = 0.4$ kg/s, the experimental values represent ensemble averaged data

in particular as the flow velocities are decreased. As seen for the vaned diffuser, the steady-state model struggles to predict those regions and thus to predict the efficiency accurately. The total temperature ratios τ_{tt} in figure 4.18d again match well for all speedlines. However, the temperature rise is somewhat lower in the computations due to the assumption of adiabatic conditions and smooth surfaces.

The static pressure rise characteristics for two different operating points are given in figures 4.18e and 4.18f. Once more, the impeller casing pressures match well. The pressure rise characteristic in the diffuser is reflected much better than in the vaned diffuser. However, the pressure rise is still exceeded by the RANS model in the rear diffuser part. The URANS model once more captures the pressure rise more accurately.

The ensemble averaged circumferential pressure signals are again similarly calculated by the RANS simulations. A comparison for a low speed operating point is given in figure 4.19. As expected, no impact of the diffuser change is observed in the impeller pressure signals. As for the 70 000 rpm speedline in figure 4.17, the positions 1, 2, 5 and 6 are captured with good agreement, except for the sharper pressure gradients at the blades. Again, some discrepancies are observed at positions 3 and 4. These are presumably caused by the heavily unsteady flow field at those locations caused by the tip vortex fluctuations and its interaction with the splitter blade. This is supported by the significantly increased standard deviations of the pressure signals, which indicate strong fluctuations, see figure A.1 in the appendix, where an example of a high speed operating point is given additionally.

4.4.3 Discussion

The comparison of the simulations to measured data shows a good agreement regarding the general characteristics of the compressor stage for the URANS and also the RANS models. Increased discrepancies arise for the upper speedlines of the vaned diffuser, where the overall pressure ratio is significantly over-predicted by the steady-state simulations. It is shown that this is due to flow separations and blockage in the diffuser channels, which are not sufficiently captured. However, the results suggest that the flow in the impeller is predicted with sufficient accuracy. Both models (RANS and URANS) show similar results that represent the general impeller characteristics (pressure rise) and flow features (circumferential pressure distributions) well. This is also supported in the vaned diffuser case.

As expected, the overall performance characteristics like pressure ratio and efficiency are over-predicted by the simulations. This is strongly depending on the fidelity and the quality of the numerical models. However, a tradeoff has to be made to reduce numerical costs. Thus, simplifications and assumptions are used and subordinate physical mechanisms are neglected. A short overview emphasizing on the most influential shares that contribute to the corresponding uncertainties is given below.

- *surface roughness*: The models use smooth, no slip walls, whereas the actual parts are rough, in particular the casted volute. This leads to increased surface friction at the endwalls and hence an increased boundary layer thickness. This significantly affects the efficiency and the pressure rise in the compressor stage. As the roughness values have not been determined, these are not included in the models, which therefore tend to over-predict the measured results.
- *heat transfer*: Depending on the operating point which defines the specific flow temperatures, heat is transferred to the surrounding and the oil in the gearbox, or from the gearbox to the flow. The heat transfer to the surrounding air is minimized by the usage of insulation but this is not possible for the gearbox, which is directly attached to the compressor stage. Therefore, this directly affects the flow temperature which is used of the evaluation of the efficiency. This effect is of particular relevance at low speeds, where the oil temperature (80° at gearbox inlet) is significantly higher than the flow temperature. Nevertheless, the models assume adiabatic conditions as the actual heat flows are unknown and very difficult to determine during experimental investigations.
- *turbulence modeling*: The well established SST-k- ω two-equation model is selected for the present study. Generally speaking, this model yields good results compared to the rather small computational effort that is required for the approximation of the turbulent fluctuations. However, turbulence is highly involved in the flow effects that occur in centrifugal compressors, in particular when it comes to flow separations and towards instability. Hence, this surly contributes to the discrepancies as there is obviously room for improvement here.

Further points besides the selected turbulence model are boundary condition specifications, geometric simplifications, the assumption of periodicity, the usage of mixing planes in the RANS models and manufacturing and assembly

tolerances. However, all these effects are believed to have only minor impact on the observed discrepancies.

All in all, it is concluded that the selected numerical models are capable of predicting the compressor characteristics and general trends. Moreover, they offer a good cost-to-benefit ratio, which allows for a sufficient number of simulations. Despite some discrepancies in the absolute values this is sufficient, as the present study is focused on the demonstration of relative trends and the understanding of the underlying flow mechanisms.

5 Numerical Groove Design Study

This chapter investigates the design parameters of circumferential grooves in the presented radial compressor. The available design suggestions for axial compressors are somewhat inconsistent and furthermore it is unclear if these can be applied to the centrifugal compressor flow field, see section 2.3.2. Therefore, this study aims at understanding the underlying mechanisms of the design parameters and deriving guidelines for an effective design. Furthermore, the potentially most effective designs are identified to test, validate and further evaluate the corresponding effects. The essential parts of this study are also published in [7].

The following investigation comprises a numerical study to provide guidelines for an effective groove design in terms of pressure rise and efficiency of the compressor. Moreover, the groove mechanisms and their influence on the near tip flow field are evaluated to understand the underlying flow mechanisms. The impact on the tip vortex development and its interaction with the impeller core flow is analyzed in particular to assess beneficial effects that affect the compressor work input and the formation of losses due to mixing processes.

Additionally, these mechanisms are used to find indications for a possible stall margin improvement (*SMI*) by evaluating the flow fields of near stall operating points. An optimization towards maximum *SMI* is not performed within the design study, as various researchers have shown that steady-state CFD models are not capable of predicting the stall points nor the mechanisms of stall inception correctly. Houghton [83] for example performed tests and numerical calculations on optimized groove locations in an axial compressor and found that his simulations predict a maximum in *SMI* where the experiments show a minimum. Therefore, he concluded that it is more informative to analyze the impacts on the near casing flow field, rather than to calculate the actual stall points.

Following this, the changes in the near tip flow field induced by the different groove designs are considered in the selection of the final configurations. These are defined at the end of this chapter for further experimental and more detailed numerical investigations. Based on the results, guidelines for an effective design are derived, which include the general trends of the study as well as insights from the available open literature.

5.1 Investigation Approach

This section introduces the approach of the numerical groove design study. Firstly, the different groove parameters and the respective nomenclature is introduced. Thereafter, the methodology of the investigations is presented.

5.1.1 Parametrization of the Groove Geometry

The rotational symmetry of the grooves leads to a two-dimensional definition in the axial-radial plane. The groove shape is defined by four different parameters in the present study. The definition of these parameters is depicted in figure 5.1. The figure shows a sketch of a single rectangular groove. Other geometric shapes like rounded grooves or non-rectangular shapes are not considered in this study. Houghton [83] however showed for an axial compressor that rounded groove shapes have a detrimental effect on the efficiency and no impact on the *SMI* compared to rectangular ones.

All geometric parameters are defined with respect to a basepoint. This point is located on the shroud casing line of the compressor which remains unchanged. Its location is given by the parameter m' , which represents the dimensionless meridional location in the impeller. This parameter becomes zero at the leading edge of the impeller main blade and one at the trailing edge. Accordingly, it is defined on a percentage basis. The groove inclination angle γ is defined with respect to the shroud normal vector. Therefore, the inclination remains comparable for different meridional groove locations. Positive angles are defined as an inclination towards the compressor inducer, whereas a negative angle indicates an inclination towards the TE. The width of the groove b is defined in normal direction to the resulting groove direction vector depicted in the sketch and is equally divided to both sides. The depth t defines the length of the groove direction vector and is also measured with respect to the basepoint.

The groove number g describes the amount of grooves in multiple groove configurations but is omitted for single groove cases. If more than one groove is present in a certain configuration, a consecutive numbering of the grooves starting with the groove closest to the leading edge is performed. If the individual parameters of multiple grooves are identical, these are omitted in the designation of the configuration.

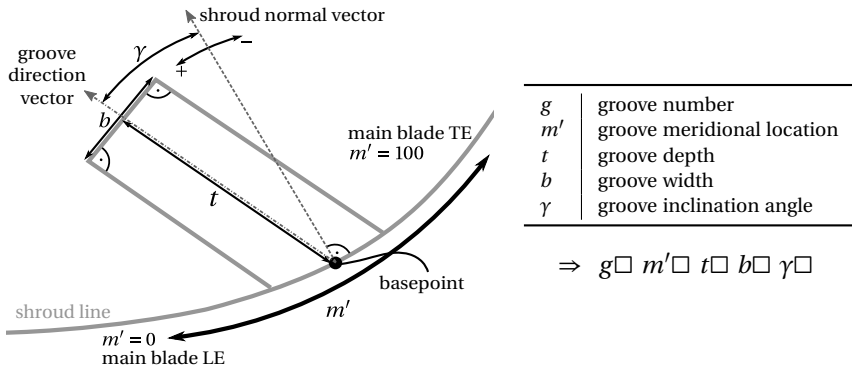


Figure 5.1 – Circumferential groove shape parametrization and nomenclature of groove parameters

This results in the following nomenclature to identify different casing groove configurations. The single parameters are connected in the same sequence as listed below the table in figure 5.1. The squares are replaced with the respective values. If there are different values for any parameter these are listed and separated with a slash. For example a configuration named – $g2 \ m'50/80 \ t3 \ b1.5 \ \gamma45$ – has two circumferential grooves at meridional locations of 50 % and 80 %, which both are inclined by 45° with respect to the shroud normal vector. The groove depth is 3 mm and the width is 1.5 mm.

5.1.2 Methodology of the Design Study

In order to assess the impact of the groove design independently from restrictions imposed by the diffuser, only the impeller performance is evaluated in this study. Therefore, the evaluation of the overall quantities, namely efficiency and pressure ratio is performed at the outlet of the impeller just in front of the interface, see figure 4.1. The reduced stage model, see section 4.2.1, that neglects the volute and the piping systems, is used to minimize the computational effort.

In order to keep the computational costs down, only a single speed is considered in this study. Moreover, it is expected, that the respective trends and mechanisms can be transferred to different speeds, provided that the effects are not based on shocks or other speed connected phenomena. Due to the highest blade loadings and thus strongest leakage flows, the design speed of

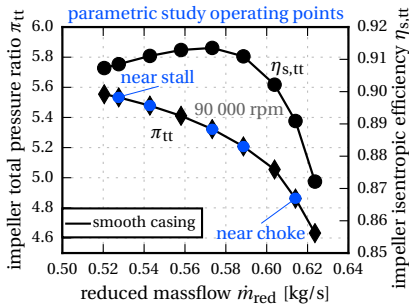


Figure 5.2 – Operating points of the groove design study

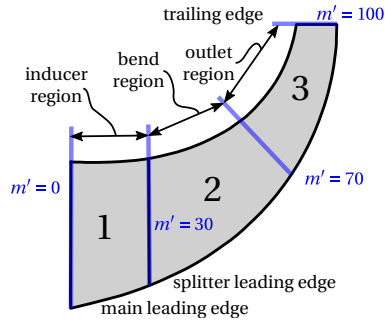


Figure 5.3 – Definition of impeller subregions

90 000 rpm, which also represents the maximum speed of the compressor, is chosen for the investigations. Five different operating points are considered and evaluated for each configuration, representing the whole speedline from near choke to near stall. Figure 5.2 shows these operating points marked on the considered speedline for the smooth casing (*sc*) configuration. Values for the impeller isentropic efficiencies and the total pressure ratio are given, which form the reference for the following study.

The impeller is divided into three distinct regions to identify and distinguish potential local optima for the groove design parameters. Moreover, different flow phenomena are expected to be affected by an application in the different regions. The inducer region, where the tip vortex development is most prominent, extends up to the splitter blade leading edge (m' from 0% to 30%). It is followed by the bend region (30% to 70%), which is characterized by the subdivision of the flow channel, additional splitter blade leakage flow and the start of the flow turning in radial direction. Thereafter, the radial directed outlet region (m' from 70% to 100%), where typically large regions of low momentum fluid are present near the shroud, is defined.

To assess the effects and the mechanisms of the different geometrical parameters in an isolated manner, each of them is varied one after the other whilst fixing the remaining parameters. This aims mainly at finding trends and understanding the underlying effects to derive guidelines, rather than finding the optimized best configuration possible. A baseline groove shape is defined, following the experience of axial compressor studies that are introduced in section 2.3. The suggested values are transferred to the dimensions of the

radial compressor used in this study. A groove aspect ratio of $t/b = 2$ is selected and an approximate groove opening at the casing of about 7% of the unwrapped meridional blade length led to a initial groove width of $b = 1.5$ mm. Thus, the depth is set to $t = 3$ mm. An initial inclination angle of $\gamma = 45^\circ$ is used, following the observations of Bareiss et al. [6].

Firstly, this baseline groove is used for the investigation on the groove location. Subsequently the remaining parameters are varied. Figure 5.4 gives an overview of the order of the parametrized studies and the respective parameter ranges. Eight different locations are considered in the first study, stretching from the inducer up to the outlet region. Grooves located directly above either the main or the splitter blade leading edges are not considered here, as previously conducted studies showed that this leads to a significant deterioration of work input and efficiency [101, 118]. Thereafter, the inclination angle γ is varied separately within the range of -60° to 60° for the distinct regions, represented by the locations $m' = 15, 50$ and 85% . Even higher inclination angles were not considered as these would not be manufacturable due to the groove edges becoming too thin. Based on the results, the subsequent studies of aspect ratio and size are performed with a constant inclination angle of $\gamma = 60^\circ$.

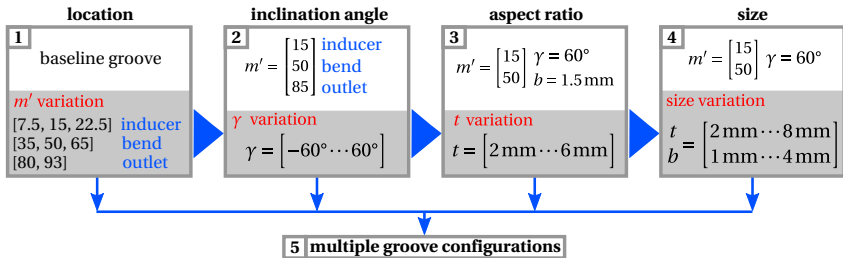


Figure 5.4 – Approach and ranges of the parametrized study on single groove location and shape

Once again, different locations are studied to ensure that the flow mechanisms, which possibly differ in each region are captured. The aspect ratio is varied by changing the groove depth in the range of 2 mm to 6 mm. Building on the results, the size of the grooves is changed by scaling the grooves in width and depth with a constant aspect ratio of 2. Finally, multiple groove configurations are defined to investigate the interaction of the single groove effects based on the previously obtained findings.

5.2 Performance Impact of Groove Parameters

The results of the design study for the different parameters are presented in this section. Overall results in terms of pressure rise and efficiency are evaluated with respect to the *sc* configuration. Thus, averaged values for the five considered operating points, represented by n , are defined according to the equations 5.1 to obtain a single value that includes the overall performance of the respective configuration.

$$\overline{\Delta\pi_{tt}} = \sum_{n=1}^5 \left(\frac{\pi_{tt, \text{grooved}}}{\pi_{tt, \text{sc}}} - 1 \right) / 5 \quad \overline{\Delta\eta_{s,tt}} = \sum_{n=1}^5 \left(\frac{\eta_{s,tt, \text{grooved}}}{\eta_{s,tt, \text{sc}}} - 1 \right) / 5 \quad (5.1)$$

5.2.1 Groove Location

Figure 5.5 summarizes the overall results for the groove location study. Eight different locations from $m' = 7.5\%$ near main blade leading edge in the inducer up to $m' = 93\%$ near the trailing edge are considered. Both locations are chosen to be close to the LE and TE respectively, whilst keeping the opening completely above the blades.

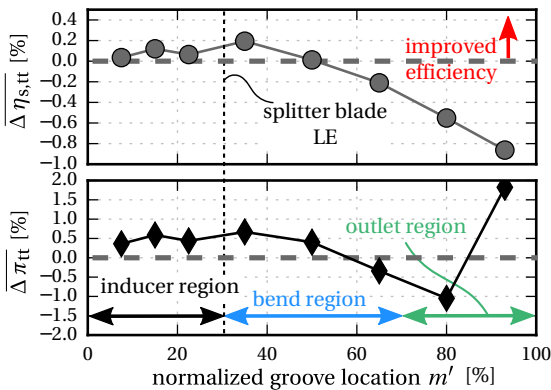


Figure 5.5 – Averaged impact of single groove location on the impeller total pressure ratio and isentropic efficiency for the baseline groove shape with respect to the smooth casing configuration - 90 krpm, $t/b = 2$

The results show an improvement compared to the *sc* configuration up to locations of $m' \leq 50\%$. Both, averaged efficiency and pressure ratio are improved for groove locations in the inducer and the front part of the bend region. The highest efficiency increase of 0.2% is found directly after the splitter blade LE at $m' = 37\%$. All considered grooves in the inducer slightly increase efficiency and total pressure ratio.

A contrary trend is observed for a placement of the baseline groove towards the rear part of the impeller. Efficiency decreases by up to -0.84% near the TE. The results show a similar trend for the pressure ratio but an exception is present for the near TE groove, where the pressure rise is considerably improved. The corresponding flow mechanisms, which strongly depend on the groove location, are presented in section 5.3.

The detailed results for the dependency on the operating points are given in the appendix (see B.1). In general, the shape of the speedline is not affected and the averaged results represent the overall trends very well. Some exceptions are present near choke due to marginal changes in the choking massflow rate resulting from the different near tip flow fields. This is further discussed for the final configurations in section 5.4.2. However, these changes are small and of minor interest for the general design study. Therefore, averaged values are used to represent the trends. Nevertheless, the operating point dependency is discussed if required.

5.2.2 Groove Inclination

The impact of the groove inclination within a range of -60° to 60° is studied for the baseline groove shape for the three different groove locations representing the specific impeller regions. In particular, $m' = 15\%$, 50% and 85% have been selected to represent the inducer, the bend region and the radially directed outlet region.

Figure 5.6 presents the mean overall results with respect to the *sc* configuration. Again, a clear trend is observed independently of the groove location. Both efficiency and pressure ratio increase towards higher inclination angles with an almost linear slope. Nevertheless, only highly inclined grooves at $m' = 15\%$ and 50% increase the compressor efficiency and the total pressure rise. Despite showing the same trend for the inclination, the groove at $m' = 85\%$ performs worse than the *sc* configuration for all investigated angles. The trend for the groove inclination is resulting from the different flow patterns that

develop inside the grooves. This is exemplified in figure 5.7, which presents a comparison of three differently inclined grooves of $\gamma = -60^\circ$, 0° and 60° at a meridional location of $m' = 50\%$.

In and outflow zones into the groove are highlighted by a spanwise momentum contour at the groove interface to the impeller core domain. Additionally, streamtubes originating from this interface are shown to visualize the groove outflow directions. The positive inclination ($\gamma = 60^\circ$) imposes a vortex flow pattern that enables a circumferential transport of the leakage flow and an outflow in streamwise direction of the core flow. This is illustrated by the streamtubes, which indicate that most of the flow leaving the groove is directed towards the outlet. An exemplary sketch of the corresponding pattern is given in figure 5.8.

The leakage flow over the tip enters the groove at the blade pressure sides and near the downstream edge of the groove on the suction sides. The vortex that forms in the groove transports the flow in circumferential direction and to the upstream edge of the groove. Due to the positive inclination, the groove outflow is more aligned with the core flow when reentering the impeller domain. Therefore mixing losses are reduced. These findings are similar to the work of Sakuma et al. [136] who stressed that a vortex flow inside the groove is crucial for the transport of the tip leakage flow, which they attributed to result in an improved *SMI* and pressure ratio.

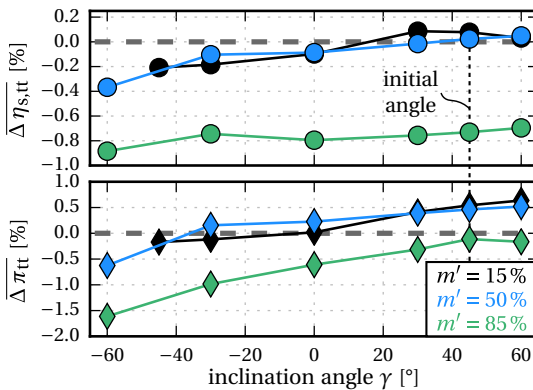


Figure 5.6 – Impact of the inclination angle γ on the averaged impeller pressure ratio and efficiency for different groove locations with respect to the smooth casing configuration - 90 krpm, $t/b = 2$

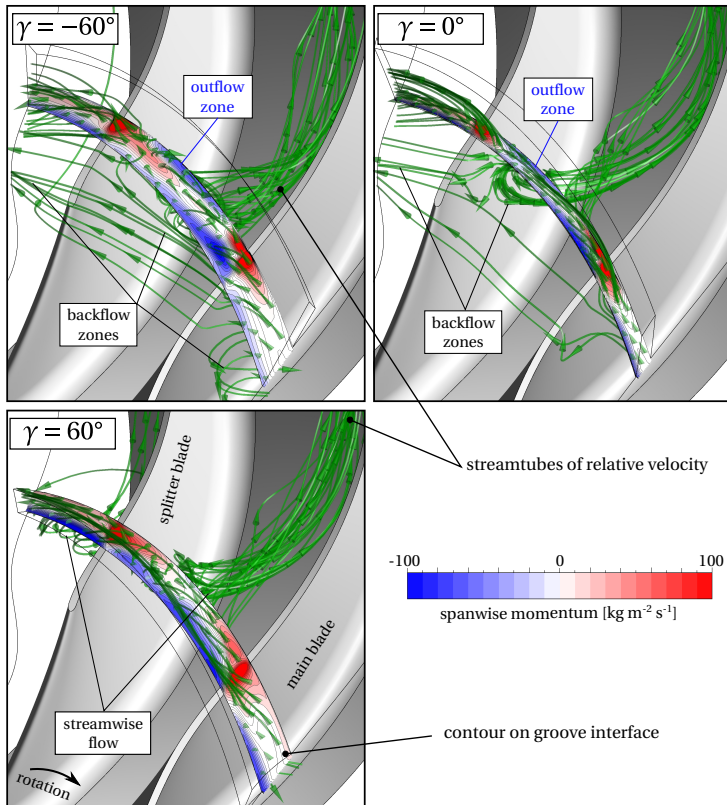


Figure 5.7 – Interaction of differently inclined grooves at $m' = 50\%$ with the near casing flow field, represented by a contour of spanwise momentum and additional streamtubes starting at the groove interface in the relative frame of reference for $\dot{m}_{\text{red}} = 0.54 \text{ kg/s}$

This is in contrast to the negatively ($\gamma = -60^\circ$) and also the non inclined groove ($\gamma = 0^\circ$). Both show outflow zones in the rear parts of the grooves in figure 5.7. This obstructs the development of the vortical flow structure and thus the circumferential transport. As a result, large shares of the groove flow are directed upstream, where the incoming flow is blocked due to backflow zones that emerge. Accordingly, losses are increased due to the flow mixing, which explains the overall results for the inclination.

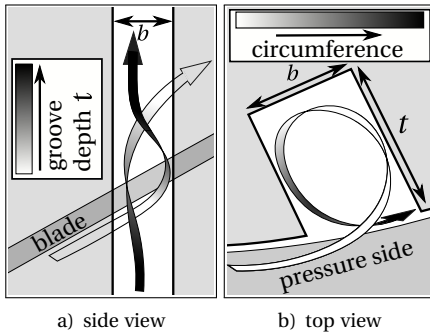


Figure 5.8 – Schematic vortex flow pattern inside of a positively inclined circumferential groove

Similar impacts on the flow structures are also found for the inducer and the outlet regions. Consequently, all further studies use the highest inclination of 60° , which is also suggested as a general guideline. Higher angles might be even more advantageous in terms of reducing the mixing losses but these are not investigated here for reasons of manufacturability.

in contrast to axial ones, where, according to the published research, this parameter is found to be of minor significance. Certainly, this is connected to the smaller relative blade heights, the bend from axial to radial direction and the therefore increased extent and importance of the near casing flow fields.

However, the groove inclination seems to be of significant importance in centrifugal compressors

5.2.3 Groove Dimension

To find optimized geometric dimensions of the circumferential grooves, the width b and the depth t are varied for different groove locations. A constant inclination angle of 60° is maintained, based on the results of section 5.2.2. The groove aspect ratio, defined by t/b , is used as a dimensionless parameter describing the shape of the groove. Firstly, the depth of baseline groove is varied while the width is kept constant at $b = 1.5\text{mm}$.

Figure 5.9 plots the results for aspect ratios ranging from 1.33 to 4, which is similar to the ranges that are found in previous studies for axial compressor grooves. The impact of the groove aspect ratio, synonymous to the depth in this study, is small in comparison to the effects of location and inclination. The impact on both pressure rise and impeller efficiency is below 0.1 % for the investigated locations in the inducer and the bend region. The outlet region is not considered here as the previous results showed only detrimental effects. However, the variation of the groove size for the outlet region showed that the general impact is independent of the location, see figure B.9.

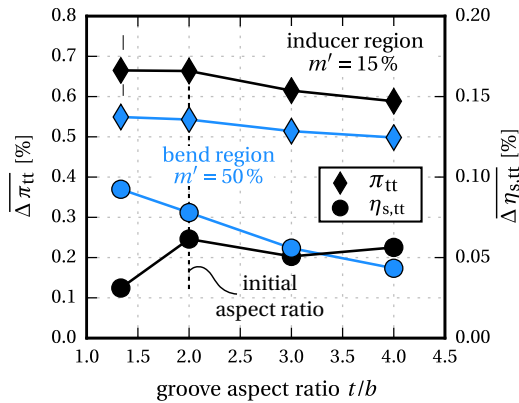


Figure 5.9 – Impact of the groove shape in terms of aspect ratio on the averaged impeller pressure ratio and efficiency for different groove locations with respect to the smooth casing configuration and a constant groove width of $b = 1.5$ mm

Despite the marginal overall impact, a trend of increased performance towards smaller aspect ratios and thus more shallow grooves is observed. This is consistent to the findings of Rabe and Hah [133] for a transonic axial compressor. Endwall losses due to surface friction increase as more wetted area is provided with the application of deeper grooves. However, the overall impact remains small as no fundamental changes in the flow structures are caused.

Different researchers tested various aspect ratios for axial compressors and observed the same trends. Müller et al. [123] additionally reported that aspect ratios below 1.5 deteriorate the *SMI* that was found for higher values, whereas Shabbir and Adamczyk [143] found no differences for aspect ratios bigger than 2. This can be attributed to the required flow pattern inside the grooves that enables a circumferential transport of the local leakage flows. If the grooves are too shallow, the pattern shown in figure 5.8 can not develop as the flow inside the groove is dominated by the interaction with the core flow. A very deep groove however allows for an unhindered groove flow but an additional circumferential flow near the groove bottom develops. This part of the flow does not contribute to the general effect but increases losses due to viscous friction.

A groove aspect ratio in the range of 2 is suggested for an optimized design as no information on the actual *SMI* is present, based on the results of the study and the published literature (see section 2.3.2).

Consequently, the groove size is investigated with a constant aspect ratio of 2. Therefore, the width of the groove is varied in the range of $b = 1$ mm to 4 mm with the corresponding depth. Figure 5.10 presents the mean results of the groove size variation based on the smooth casing configuration. Once more, a clear trend is observed for both locations.

The results deteriorate significantly for large grooves at both locations. A groove width of 4 mm leads to a drop in mean efficiency of over 1 % in the inducer, whereas groove widths of $b \leq 2$ mm improve or maintain the mean impeller efficiency. Moreover, the convergence criteria are not fulfilled anymore for the near stall operating points for very large grooves of $b = 4$ mm. Similar results are observed for the mean total pressure rise which is coupled to the efficiency.

For small widths of $b \leq 2$ mm, the differences between the configurations are very small. This equals dimensionless groove openings at the casing between approximately 4 % to 10 % of the unwrapped meridional chord length of the main blade, which can be calculated based on the groove opening

$$b_{\text{casing}} = b / \cos(\gamma). \quad (5.2)$$

These values are again consistent to the findings in axial compressors, see Du et al. [34], Sakuma et al. [136] or chapter 2.3.2 for instance. Moreover, the general trend is again independent of the groove location. This is supported by the results for an outlet region groove, despite showing a deterioration compared to the *sc*, see figure B.9 in the appendix. In fact, this applies for all investigated geometrical parameters. Accordingly, a constant groove width of $b = 1.5$ mm and a corresponding depth of $t = 3$ mm is selected for the present study, being exactly the initially defined groove size. This equals an opening of 7 % of the unwrapped chord length, which is therefore suggested as a rough design parameter. In addition, this is supported by the knowledge gained in axial compressor research.

It has to be noted that the final selection in this study is not only based on the aerodynamic performance. The selection of the chosen size over even smaller ones is also driven by sensor applicability and prototype manufacturing issues, which both become much easier and less costly for larger groove sizes.

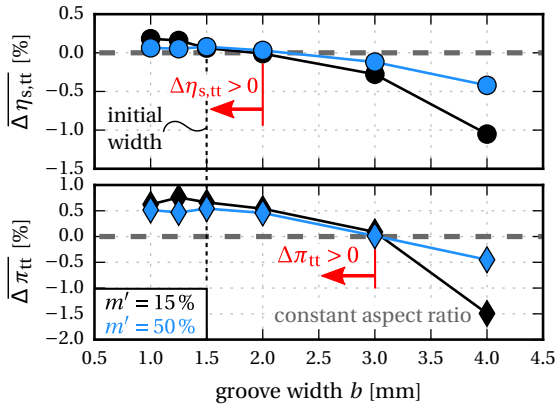


Figure 5.10 – Impact of the groove size in terms of impeller pressure ratio and efficiency for different groove locations with respect to the smooth casing configuration for a constant aspect ratio of $t/b = 2$

5.2.4 Multiple Groove Interaction

This section presents the results of multiple groove investigations with the aim of exploring the interaction of differently located grooves. Based on the previous findings, an optimized groove shape of $\gamma = 60^\circ$, $b = 1.5\text{ mm}$ and $t = 3\text{ mm}$ is used. A constant shape is suggested due to identical trends of the different geometric parameters for all locations. Consequently, the specifications for the shape are omitted in the following descriptions.

Promising single groove configurations are combined to find out whether the single groove effects can be enhanced or if the interference of the effects limits the function of specific grooves. Figure 5.11 plots the averaged results in terms of impeller efficiency and pressure ratio for configurations with up to 4 grooves applied. The grooves are located in the inducer and the bend section up to a position of $m' = 50\%$ based on the location study in 5.2.1. The groove number is increasing towards the right. In addition, two single groove configurations are included as references.

Each multiple groove configuration exceeds the overall improvements of the single groove cases for both efficiency and pressure ratio. This suggests that the single groove trends add up and in conclusion that the respective effects can be superimposed. Moreover, the results imply that the single groove mechanisms are not decisively influenced by an interference with

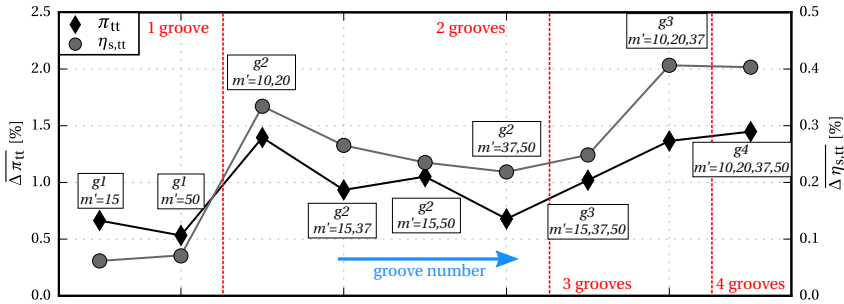


Figure 5.11 – Performance of multiple groove configurations based on combinations of effective single groove locations with the optimized groove shape of $\gamma = 60^\circ$, $b = 1.5$ mm and $t = 3$ mm

other grooves, as improvements occur for any combination. Multiple inducer grooves (g^2 , $m' = 10,20$) show a higher potential compared to other configurations with 2 grooves. This is further exceeded if additional bend region grooves are added, resulting in mean improvements of up to 1.45 % in pressure ratio and 0.41 % in efficiency (g^4 , $m' = 10,20,37,50$).

Additional configurations including an outlet region groove at $m' = 92\%$ are investigated to check if this location provides different results in a multiple groove arrangement. The single groove showed a significantly increased total pressure ratio but a large drop in efficiency. The results for two configurations are summarized in table 5.1. These further support the conclusions of a superposition of the single groove effects. Adding an outlet region groove to inducer and bend region grooves significantly increases the pressure rise but deteriorates the efficiency, just like its individual effect.

Table 5.1 – Multiple groove performance with outlet region grooves

| groove locations | $\overline{\Delta \pi_{tt}}$ | $\overline{\Delta \eta_{s,tt}}$ |
|--------------------|------------------------------|---------------------------------|
| $m' = 37,50,92$ | 1.69 % | -0.617 % |
| $m' = 10,20,37,92$ | 2.98 % | -0.445 % |

5.3 Flow Mechanisms

This section addresses the underlying flow mechanisms for the parametric study findings to further examine how the performance is affected in dependence of the groove location. The overall findings indicate that this is by far the most influential of the studied parameters. Therefore, the flow mechanisms are evaluated for the different impeller regions, which have been previously defined, see figure 5.3.

The parametrized study also revealed that the impact of the inclination angle and the groove dimensions is independent of the location. The corresponding flow mechanisms have therefore been discussed in the previous sections. In addition, the different designs are analyzed in terms of their impact on the flow structures that are typically associated with the onset of unstable operation. This includes the near tip flow field evolution in terms of impeller stall (see section 2.2.1) as well as the impeller outlet flow fields, in particular the flow angle distribution, in terms of diffuser stall (see section 2.2.2).

Figure 5.12 presents the circumferential averaged flow angles α for several different groove configurations, evaluated directly after the impeller outlet at a radius of $r = 58\text{ mm}$. The optimized groove shape is used for all considered locations. The single groove results in figure 5.12a demonstrate that a

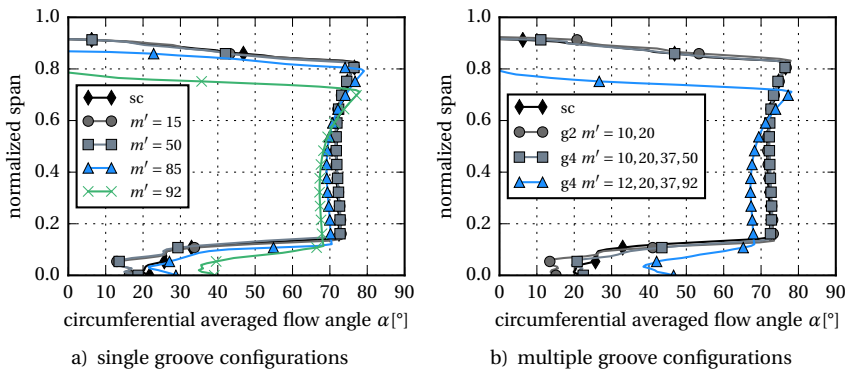


Figure 5.12 – Circumferential averaged impeller outlet flow angle distribution for different groove configurations at $r = 58\text{ mm}$ with the optimized groove shape for the near stall operating point $\dot{m}_{\text{red}} = 0.525\text{ kg/s}$

groove placement in the inducer ($m' = 15$) and in the bend region ($m' = 50$) has no influence on the averaged impeller outlet flow angle distribution. The same applies for multiple grooves in these regions as shown in figure 5.12b. This indicates that the diffuser performance and stability are most likely not decisively affected, neither for the vaned nor the vaneless diffuser configuration. Consequently, the evaluation focuses on the impact on the impeller near casing flow for those locations. However, these conclusions are drawn from simplified models and thus still have to be validated.

In contrast to that, a groove placement farther downstream significantly affects the flow angle distribution. The separated flow region near the tip extends and affects the core flow distribution. The comparison of multiple groove configurations in figure 5.12b shows that this effect is solely induced by the outlet region groove. A recirculation region develops at the shroud near the TE as a result of such a groove application. This leads to a locally increased massflow rate that reduces the flow turning and increases the flow losses. The respective mechanisms are further discussed in section 5.3.3, which introduces the general groove mechanisms in the outlet region.

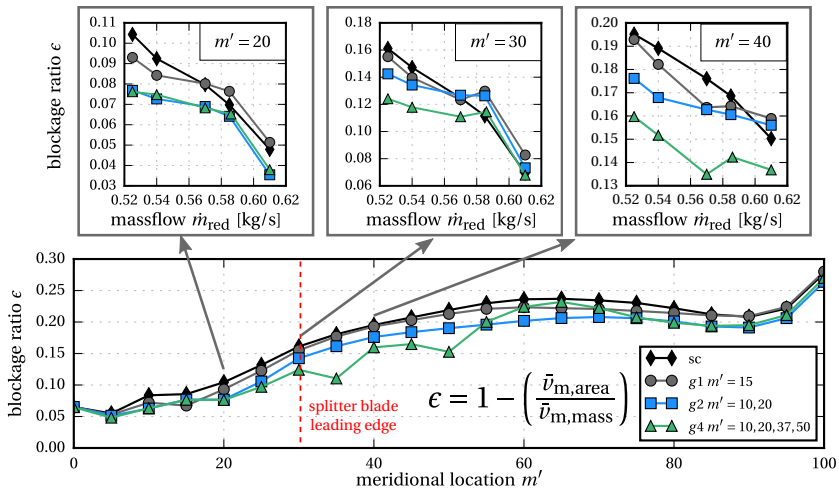


Figure 5.13 – Blockage ratio distribution for selected groove configurations depending on the meridional location (bottom) for $\dot{m}_{red} = 0.525$ kg/s and depending on the flow rate at specific meridional locations (top)

The stall in the impeller is often linked to the evolution of blockage in the inducer tip region, or alternatively the presence of low momentum fluid regions (section 2.2.1). The increasing extent of those regions, accompanied by rising blockage levels, is commonly considered as one of the main precursors for the onset of flow instabilities. Moreover, these strongly affect the impeller performance as the flow turning contribution of the blade tips in those regions is reduced and flow losses due to incidence and mixing processes are increased. In general, those regions increase with decreasing flow rates as a result of the shifting tip vortex trajectory and the reduced throughflow velocities. Ultimately, this can lead to a spillage of local flow shares at both the main or the splitter blades, which is connected to a further rise of blockage and often initiates unstable operation. According to that, a reduction of blockage in these regions can positively affect the performance and moreover result in a more evenly distributed flow fields.

The lower part of figure 5.13 depicts the blockage ratio ϵ along the meridional coordinate m' for selected groove configurations at the near stall operating point. For reasons of simplicity and ease of implementation, this study uses the ratio of mass and area averaged meridional velocities v_m that is also used by Hazby and Xu [77] for example.

$$\epsilon = 1 - \left(\frac{\bar{v}_{m,\text{area}}}{\bar{v}_{m,\text{mass}}} \right) \quad (5.3)$$

The results show that all considered groove configurations lead to a significant reduction of blockage at the respective groove locations. In general, this effect is maintained for the remaining flowpath through the impeller up to the TE. The effects add up for the multi-grooved cases, which therefore reach even lower levels and once more confirm the superposition of single groove effects. In particular the inducer and the bend region in the immediate vicinity of to the specific groove locations are relieved. Significant blockage reductions compared to the *sc* configuration are observed.

Additionally, the blockage development as a function of the flow rate is presented in the upper part of figure 5.13 for selected meridional positions. All locations indicate that the effects are not only present for near stall operating points, but for the complete speedline. A nearly linear growth towards decreasing flow rates is observed for the *sc* configuration, due to increasing incidence and the shift of the tip vortex trajectory, which is well known from the fundamental centrifugal compressor flow described in section 2.1.

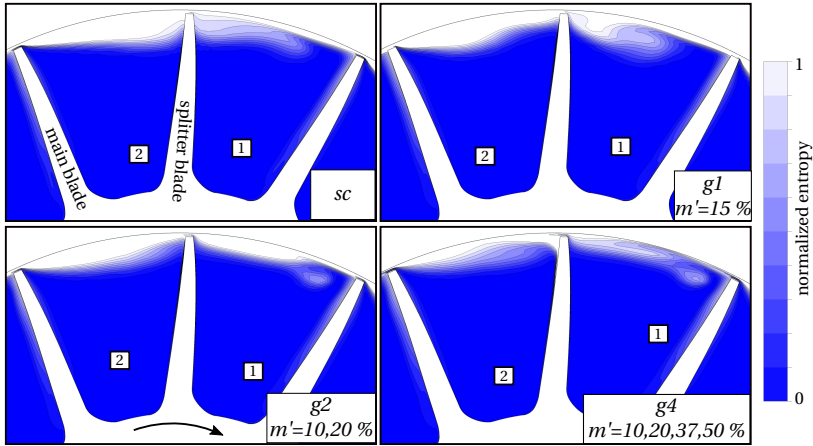


Figure 5.14 – Normalized entropy distribution directly downstream of the splitter blade LE at $m' = 31\%$ for different configurations at $\dot{m}_{\text{red}} = 0.525 \text{ kg/s}$

The application of grooves leads to a flatter characteristic towards low flow rates at all meridional positions. As a result, the maximum reductions of blockage are observed for the operating point near stall, which possibly indicates a delay of flow instabilities originating in the inducer or the bend region. However, the blockage values behind the splitter blade LE are increased for the $g1$ and $g2$ configurations for the operating points near choke. This is due to the redistributed inducer groove flow that interacts with the splitter blade at these flow rates.

The application of further bend region grooves ($g4$) reduces this effect and results in reduced values for almost all operating points and locations. The corresponding entropy contours in figure 5.14, taken directly downstream of the splitter blade LE ($m' = 31\%$), underline this effect. The flow channels are subdivided, whereby 1 is assigned to the main blade suction side channel and 2 is used for the splitter blade suction side. Entropy is chosen for the visualization as a clear distinction between the different flow regions is possible, despite the lack of any information on the flow direction. As the flow to the compressor is undisturbed, the entropy generation can be accounted to the losses in the impeller.

Large regions of high entropy fluid, resulting from the interaction of tip leakage, boundary layer and secondary flows, are present in the sc case. In partic-

ular channel 2 is affected, where most of the near casing area is blocked by the accumulation of these highly distorted flows. The application of grooves in the inducer ($g1$ and $g2$) leads to a more even distribution of these regions between the two channels. Moreover, the reduced extent of those regions and the lower levels of entropy suggest that the accumulated losses up to this plane are reduced.

Adding additional grooves in the bend region, downstream of the splitter blade LE ($g4$), further reduces the blocked high entropy regions and thus further reduces the so far generated losses. This indicates that the application of grooves in the inducer and in the bend region could positively affect the compressor stability, provided that impeller stall is being responsible for the overall instability. The respective effects that contribute to the reduction of blockage are described in the following sections, in order to understand the respective flow mechanisms.

5.3.1 Inducer Grooves

The reduction of blockage due to inducer groove application is caused by a weakening and deflection of the tip vortex. This vortex, for the most part, originates from the main blade tip leakage flow. Its deflection results from a circumferential transport of the leakage flow in the inducer groove.

The general effect is visualized in figure 5.15. For improved visibility and simplicity, only an exemplary single groove configuration at $m' = 15$ is shown here. Streamlines originating from the first and the second 10% of the tip gap represent the different shares of the leakage flow. In the baseline case (sc) the leakage flow along the blade tip gap (partly shown in green) wraps around the already existing part of the tip vortex that originates near the main blade leading edge (orange). In combination, the typical structure of the tip vortex is formed.

This development and the resulting structure are significantly affected by an inducer groove application. The leakage share near the groove (green) is sucked into the groove and transported in circumferential direction. As a result, the described rollup is hindered and the development is weakened, as less kinetic energy is fed into the already existing vortex. Consequently, the early share of the tip vortex (orange) is deflected in streamwise direction (black arrows) and becomes more aligned with the core flow.

The reduced levels of relative total pressure indicate a reduction of mixing losses, especially in the near vortex regions. Moreover, the flow to the splitter blade is improved as the otherwise impinging vortex, leading to spillage and backflows at the splitter blade, is deflected.

The corresponding surface shear strain rates of the splitter blade alongside streamlines from the first 10 % of the tip gap in figure 5.16 further demonstrate this effect. In the *sc* case, the vortex impinges onto the splitter blade near the casing. A backflow region forms and a part of the distorted near casing flow spills around the splitter blade leading edge.

This results in a separation on the near tip suction side, indicated by very low levels of the shear strain rate. Introducing a single groove in the inducer ($g1\ m' = 15$) significantly reduces this separation due to the reduced interaction of splitter blade and tip vortex. Adding a second groove in configuration $g2\ m' = 10,20$ intensifies this effect.

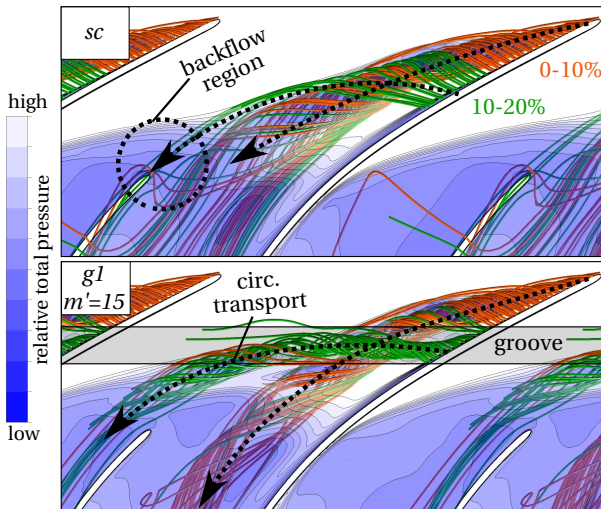


Figure 5.15 – Impact of an exemplary single inducer groove at $m' = 15\%$ on the tip vortex development and the near tip flow field (95 % span) for a flow rate of $\dot{m}_{\text{red}} = 0.525\text{ kg/s}$ and a speed of 90 krpm

The tip vortex becomes more evenly distributed and consequently the flow separation near the leading edge vanishes completely. Moreover, the extend of the downstream separation is also remarkably reduced. Consequently, the loading near the LE is increased for the inducer groove configurations, which contributes to the increased pressure rise of the grooved configurations. This is further supported by figure 5.17 which presents the corresponding normalized blade loading at 90% span for the splitter blade front part. Almost no loading is present for the *sc* case near the leading edge due to the low inflow velocities. In accordance with figure 5.16, the blade loading near the leading edge is significantly improved by the introduction of grooves. The increased loading of two inducer grooves also complies with the mechanism described in the previous figure, as the suction side separation is reduced and pushed farther downstream.

In summary, this explains why blockage and losses are reduced and additionally indicates that the application of inducer grooves can provide a more evenly distributed flow field near the tip. Moreover, a stabilizing effect on the near tip flow field is expected which could extend the range of stable operation, depending on the actual stall mechanisms of the compressor.

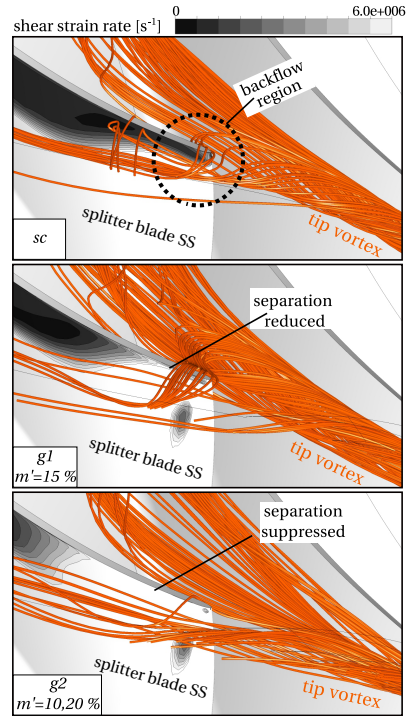


Figure 5.16 – Tip vortex flow interaction with the splitter blade for a flow rate of $\dot{m}_{red} = 0.525 \text{ kg/s}$

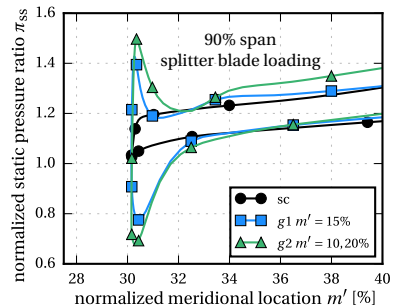


Figure 5.17 – Splitter blade loading at 90% span and $\dot{m}_{red} = 0.525 \text{ kg/s}$

5.3.2 Bend Region Grooves

The application of bend region grooves near the splitter LE further strengthens these phenomena as indicated by the entropy contour evaluation in figure 5.14. The negative streamwise velocity component of the tip leakage flow in the bend region contributes to the accumulation of distorted high entropy fluid near the tip and on the blade suction sides.

A comparison of the leakage flow evolution of the *sc* case and the single optimized groove at a representative location of $m' = 50$ is given in figure 5.18. Streamlines in the relative frame of reference, originating from the splitter blade tip gap, are shown to assess the groove flow mechanism. Significant differences are observed for the flowpaths of the leakage flows when comparing both configurations. The *sc* leakage flow remains near the casing and moves upstream due to the adverse pressure gradient. There it partially spills around the splitter blade leading edge of the adjacent passage, mixes with the core flow and is transported towards the outlet. Consequently, the presented streamlines in the *sc* case (left) are subject to high losses on their path as indicated by the increasing entropy levels. These levels are reduced for the bend region groove configuration and the development of backflow regions is suppressed. The major part of the leakage share below the groove is captured inside the groove and is then transported to the adjacent impeller channel. There it mostly reenters the core flow without flowing towards the inducer.

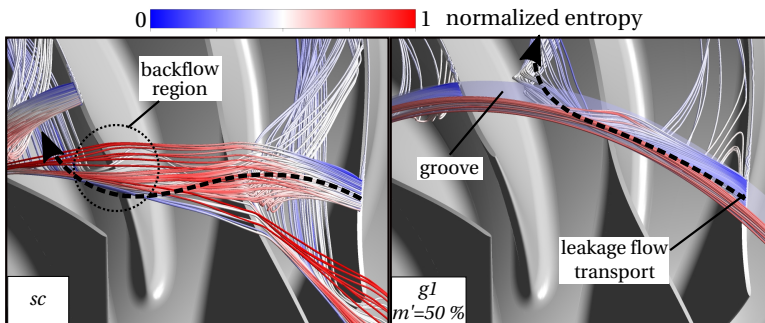


Figure 5.18 – Impact of an exemplary bend region groove at $m' = 50$ on the leakage flow originating in the splitter blade tip gap below the groove for a flow rate of $\dot{m}_{\text{red}} = 0.525 \text{ kg/s}$

Thus, the major effect of the bend region grooves is characterized by a redistribution of local leakage flows which prevents backflows and reduces the accumulation of low momentum fluid near the tip. This effect is also present when the groove is moved towards the splitter blade LE as seen in the previous results. On the contrary, moving the groove downstream deteriorates the performance. The responsible mechanisms are discussed in the following section.

5.3.3 Outlet Region Grooves

The results of the groove location study suggest that placing grooves in the outlet region ($m' \geq 70$) has a negative impact on both efficiency and also the total pressure rise of the compressor, see section 5.2.1. However, an exception is found for a near TE groove, which significantly increases the total pressure ratio while efficiency further deteriorates.

The trend of decreasing efficiency with increased m' is linked to the increase in radius and thus rotational speed. In contrast to axial compressors, the blade loading increases when moving towards the compressor TE, which results in higher leakage flow velocities and thus higher shear stresses in the boundary layers. As a result, the additional endwall losses that are introduced by the grooves inner surface increase for higher m' as the circumferential velocities in the groove increase as well. The resulting torque on the groove surface for different locations in figure 5.19 exemplifies this. The increasing endwall losses for higher m' are not compensated by the distribution of the leakage flow anymore and thus overall efficiency decreases, see figure 5.5.

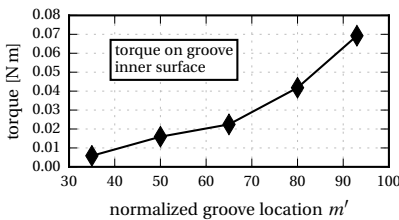


Figure 5.19 – Torque resulting from the shear stresses acting on the groove inner surfaces for different groove locations at $\dot{m}_{red} = 0.57 \text{ kg/s}$

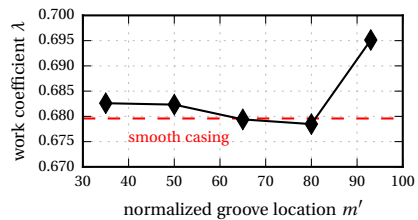


Figure 5.20 – Impeller work coefficient for different groove locations at the maximum efficiency operating point of $\dot{m}_{red} = 0.57 \text{ kg/s}$

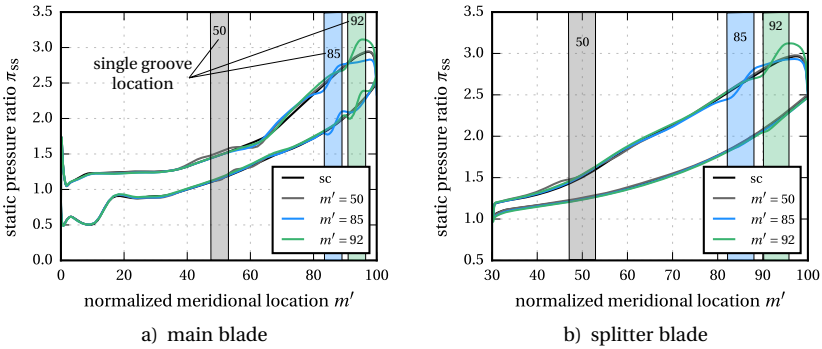


Figure 5.21 – Impeller blade loading at 90% span for different single groove locations with the optimized groove shape for $\dot{m}_{red} = 0.525 \text{ kg/s}$

The same, decreasing trend is found for the total pressure ratio (figure 5.5), which is mostly resulting from the reduced efficiency. In addition, the work input and thus the blade loading is affected. The impeller work coefficient λ for differently located grooves is given in figure 5.20, following the same trend. Figure 5.21 plots the near tip blade loading for two outlet groove configurations near the TE in comparison to the *sc* configuration and a bend region groove at $m' = 50\%$. The work coefficient λ increases for the bend region groove ($m' = 50\%$) and accordingly the loading is increased near the groove. This results from the redistribution of the low momentum fluid regions that start to accumulate in the bend region allowing for an improved flow turning.

These regions grow in meridional direction due to the accumulation of leakage and secondary flows and cover large parts of the impeller volume near the casing, see figure 2.2. In the outlet region ($m' \geq 70\%$), the whole circumference is covered, see for example figure 5.25 - 1.

Consequently the application of grooves is ineffective here, as the redistribution of the leakage flow does not result in an improved flow turning. Even detrimental effects are observed towards the TE, resulting in a lower work coefficient compared to the smooth casing. This is also demonstrated by the blade loading in figure 5.21 for the near TE configuration $m' = 85\%$. The interaction of the groove outflow with the near casing flow field leads to a decrease of the loading downstream of the groove. This impact becomes more severe when moving to higher radii, resulting in a drop of the loading that causes the reduced work input.

As mentioned earlier, an exception is found for $m' = 92$. The work coefficient increases significantly while the efficiency further decreases. Accordingly, an increase of the blade loading near the TE is observed for the main and the splitter blade in figure 5.21 a) and b).

The responsible mechanism becomes apparent from figure 5.22, which depicts the radial velocity distribution at the impeller outlet for the maximum efficiency operating point. Small backflow areas near the casing are present for the baseline case (left), indicated by the negative radial velocities. The strength and extent of these areas is significantly increased for the outlet groove configuration (right). The groove outflow pushes the core flow towards the hub, resulting in the formation of an extended recirculation zone. This explains the increased overall work input as the recirculating fluid artificially increases the positive share of the local massflow rate in streamwise direction.

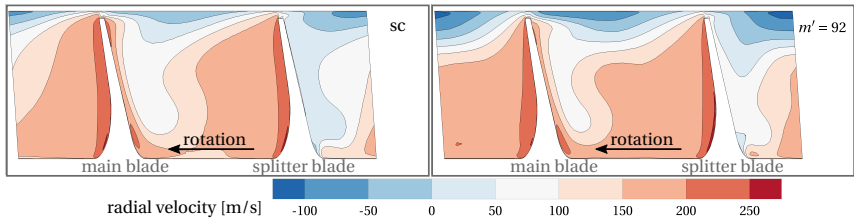


Figure 5.22 – Radial velocity distribution at the impeller outlet for the *sc* configuration and a near TE groove at the maximum efficiency operating point of $\dot{m}_{red} = 0.57 \text{ kg/s}$

The same mechanism is observed towards stall as well, as indicated by the flow angle profiles in figure 5.12 a). The increased recirculation area acts as blockage for the core flow, which therefore is accelerated. This results in a decrease of the core flow impeller outlet angle α . However, the maximum flow angles remain unchanged and the spanwise stretch of healthy core flow is reduced. This indicates that the diffuser stability and performance might deteriorate for a groove at this position, in particular for a vaned diffuser, where near tip flow separations are often involved in the stall process, see Everitt and Spakovszky [41] for example.

Summarizing, the results suggest that placing grooves in the outlet region provides no beneficial effects. The additionally introduced endwall surface has a detrimental effect on the efficiency. Furthermore, the outlet flow field is

affected in such a way that the stability and effectiveness of a vaned diffuser is presumably reduced.

5.4 Findings and Discussion

This section summarizes the findings of the numerical design study and on that basis derives some guidelines for an effective groove design in the studied compressor. Furthermore, these insights are used to select the most promising configurations for detailed experimental testing and further numerical investigations.

5.4.1 Design Guidelines

A numerical design study to analyze the impact of various design parameters on the impeller overall performance is performed. Additionally, the impact on the near tip flow field is evaluated to understand the associated mechanisms and to elaborate if these can possibly improve the stability of the near casing flow. The results are summarized in figure 5.23 and remarks on each parameter including trends and reference values or ranges are given below.

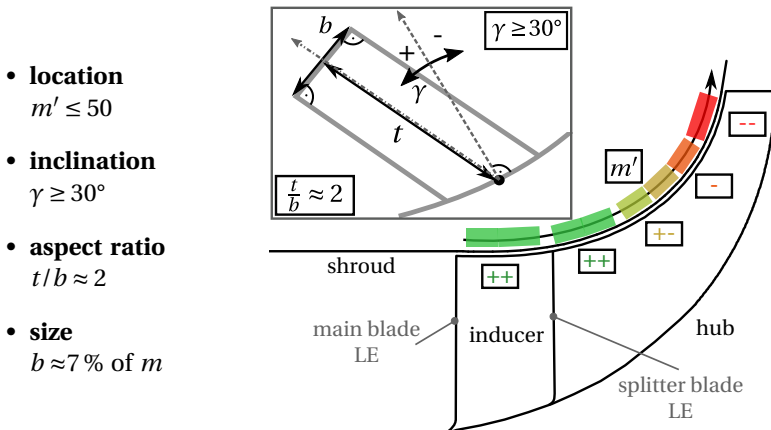


Figure 5.23 – Groove design guidelines including optimized parameters for single grooves based on the results of the numerical studies

- **groove location m'**

⇒ near LE in inducer and bend region ⇒ $m' \leq 50$

A clear trend is observed for the location, being the most influential parameter. Based on the results, a placement near the leading edges of the main and the splitter blade is suggested to reduce blockage and to smoothen the near tip flow field.

- **groove inclination γ**

⇒ high inclination ⇒ $\gamma \geq 30^\circ$

Ideally, high inclination angles should be used to enable a specific vortex flow pattern inside the grooves, similarly described by Sakuma et al. [136]. This reduces mixing losses and stabilizes the near tip flow field as the groove outflow is guided in streamwise direction and thus prevents local backflows. However, the maximum realizable angle has to be checked with manufacturing restrictions.

- **groove aspect ratio t/b**

⇒ aspect ratio in the range of $t/b = 2$

The results suggest an aspect ratio of about 2 to be most efficient. Larger depths or aspect ratios deteriorate the efficiency as the surface friction areas are increased. However, the impact of this parameter is rather small which complies with several studies from axial compressors where various groove depths proved to be efficient.

- **groove size / width b**

⇒ groove opening of about 7 % of the meridional chord length

Small groove widths of about 1 mm to 2 mm are found to be effective for the present compressor, which determines the size of the groove. This equals a dimensionless groove opening at the shroud of 4 % to 10 % of the meridional chord length.

- **groove number g**

⇒ multiple grooves favorable – complying with single groove parameters

In general, the results suggest that high groove numbers are preferable as the single groove effects are partially superimposed without interference. Therefore, multi-groove configurations should be used according to the single groove findings.

It has to be noted that these recommendations are based on the presented compressor and only refer to the maximum speedline. Nevertheless, it is assumed that the effects and the observed trends can be transferred to similar compressor designs and to other speedlines as well. A validation and further investigations on selected configurations is presented in the following chapters.

5.4.2 Selection of Final Groove Configurations

This section discusses the selection of the final groove configurations that are used for further numerical investigations and experimental testing. The CFD results suggest that a multiple groove configuration with the optimized groove shape offers the highest increase in efficiency and total pressure ratio. Moreover, they indicate that a placement in the inducer and the front bend region has a stabilizing effect on the near tip flow field as the tip vortex is weakened and deflected. Thus the interaction with the splitter blade is reduced which results in reduced blockage and mixing losses, in particular towards lower flow rates.

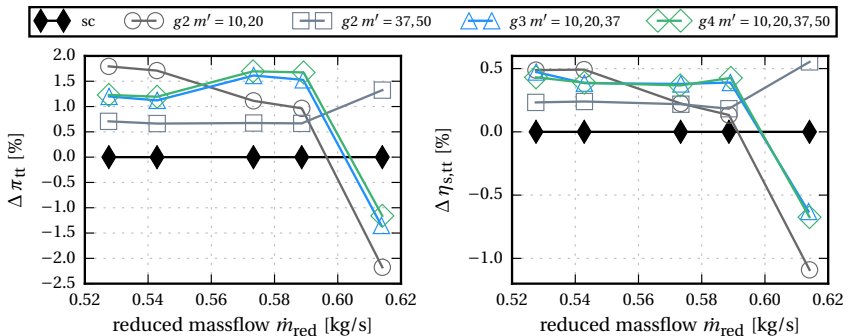


Figure 5.24 – Operating point dependency of selected multiple groove configurations

The full characteristics of promising multi-groove configurations are depicted in figure 5.24. The comparison suggests that grooves exclusively placed in the bend region ($g2\ m'37,50$) result in a different slope than inducer grooves ($g2\ m'10,20$). These show reduced values for the near choke point. This

results from a slight change in the flow to the throat which reduces the choke massflow that dominates the slope of the speedline near choke. However, an increased pressure rise is observed towards lower flow rates which could be beneficial for the stability.

Based on the characteristics, the inducer groove configuration $g2$ $m'_{10,20}$ and configuration $g4$ $m'_{10,20,37,50}$ with additional bend region grooves is selected for further studies, as they show the most promising results. Figure 5.25 depicts the Mach number distributions near the tip for these cases in comparison to the smooth casing and a single inducer groove. Both configurations show a significant improvement of the flow to the splitter blade. Moreover the interaction of the passage shock with the tip vortex is reduced which is indicated by the reduced Mach number gradients. Additionally, low momentum fluid regions in the inducer are removed which reduces blockage.

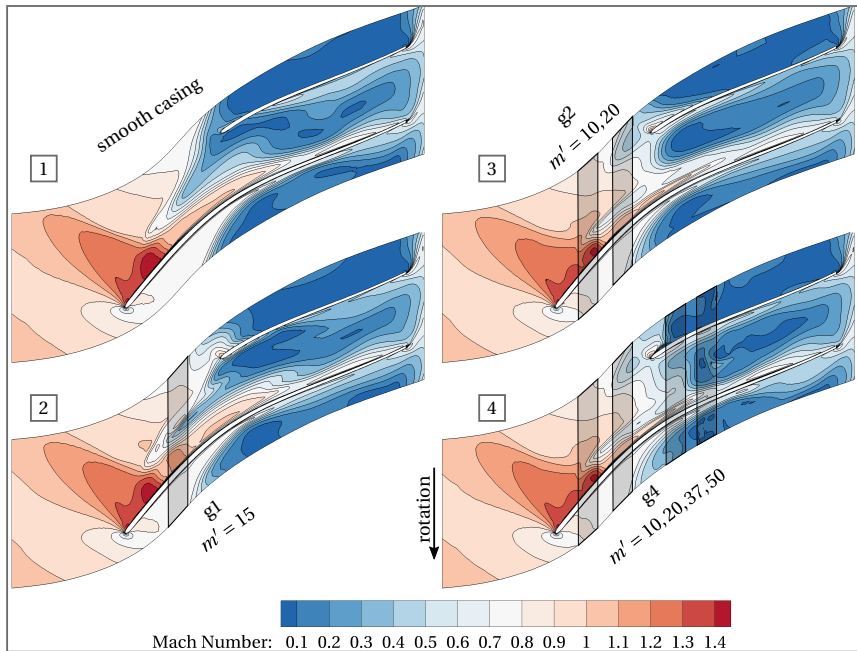


Figure 5.25 – Relative Mach number distribution at 90% span for different groove configurations and a flow rate of $\dot{m}_{red} = 0.525 \text{ kg/s}$

The published literature (see chapter 2) indicates that these effects should result in improved stability of the flow, which is investigated in the following chapters. A meridional cross section of the final optimized groove configurations that are used for testing and further, more sophisticated numerical studies are given in figure 5.26.

From this point on, the locations of the single grooves are omitted in the labeling of the different configurations for reasons of simplicity. Hence, only *sc*, *g2* and *g4* are used in the remaining part of the work.

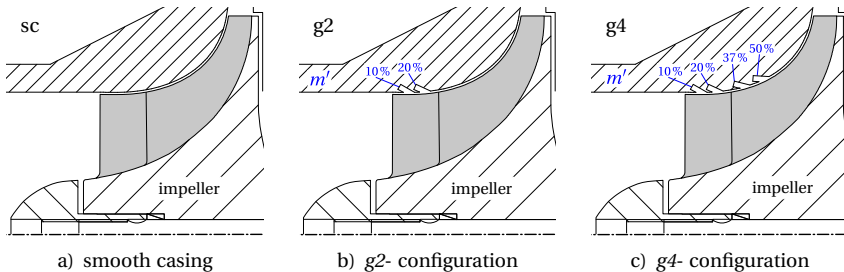


Figure 5.26 – Final configurations that are selected for experimental testing and further numerical studies

The measurement locations of the casing pressure taps need to be adjusted to account for the different casing geometries. Therefore, some rearrangements are made, as the maximum number of measurement channels is fixed. The respective adjustments for the *g2* and the *g4* casing parts are depicted in figure 5.27.

One Kulite sensor from the diffuser (sensor number 7) is shifted to the first inducer groove for both cases (*g2* and *g4*). Additionally, each groove is equipped with static pressure taps to retain the resolution of the casing pressure characteristics, whereby the taps that could not be used anymore are relocated. Moreover, the number of taps in front of the blades is reduced to account for the increasing number of grooves. Nevertheless, most measuring locations could be retained, except for the location at $m' = 50\%$, which has to be moved to $m' = 55\%$ in the *g4* configuration.

However, all comparisons in the following analysis of the measured data are performed for equal measuring locations, if not specifically stated otherwise.

The evaluation of the experimental as well as the numerical results is accordingly adjusted.

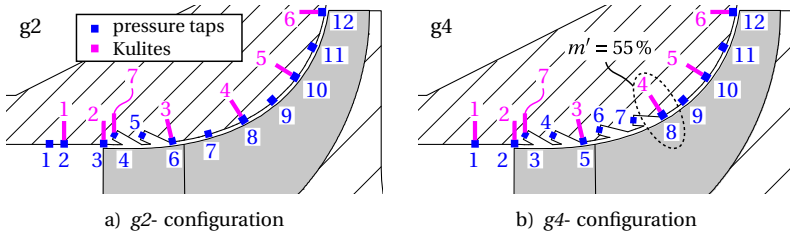


Figure 5.27 – Measuring point adjustments for the grooved casings

6 Stability with Casing Grooves

The impact of the finally selected groove configurations ($g2$ and $g4$) on the compressor stability is evaluated in this chapter. Therefore, the results of the investigations that are focused on the stall margin improvements (SMI) are presented. The impact on efficiency and pressure rise is not discussed here, but it is analyzed in the following chapter 7.

Firstly, the general stability characteristic is evaluated to understand how the present compressor becomes unstable at different operating speeds. Thereafter, the experimental results for the grooved configurations ($g2$ and $g4$) are shown and evaluated with respect to the baseline design (sc) for both the vaned and the vaneless diffuser configuration. Subsequently, the results are discussed and conclusions are drawn upon the main findings. Detailed studies involving experimental data and numerical studies are then used to further analyze the governing mechanisms that are responsible for the improvements observed in the measurements.

6.1 Stability of the Baseline Compressor Stage

This section introduces the general stability behavior of the baseline compressor stage with the smooth casing, which acts as a reference for the grooved configurations. Based on the methodology presented in section 3.2.3, clear regions of operating conditions can be defined in the performance map. Figure 6.1 presents the measured operating map of the baseline compressor stage with the vaned diffuser. The instability line separates the different zones of operation towards low flow rates. The stable operating range is indicated by 1). At high flow rates, the operation is limited by choke occurring in the vaned diffuser at all speeds except for 50 krpm, where the system resistance limits the range of operation.

Towards low flow rates, two different routes to compressor instability are observed. At high speeds of 80 krpm and 90 krpm the compressor enters the surge zone 3) abruptly, whereby deep surge is observed. No prior indications on stall are found for the stable operating points in the Kulite sensor data. This means that the throttle condition at which the initial instability is triggered directly initiates a deep surge with violent pressure fluctuations and flow

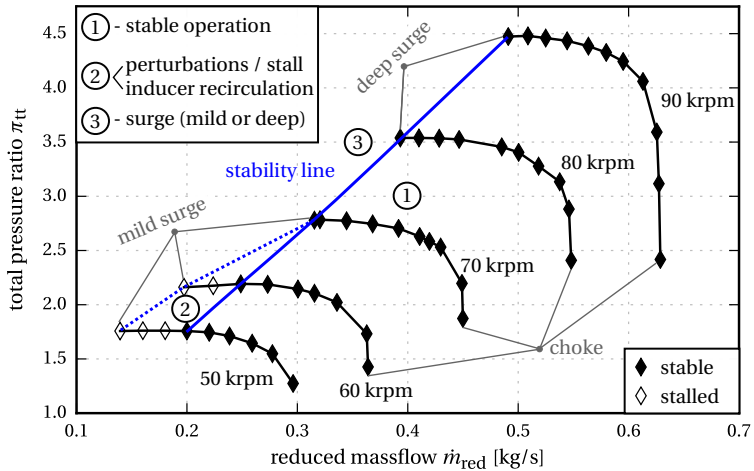


Figure 6.1 – Operating map of the compressor stage with the vaned diffuser

reversal. For low rotational speeds of 50 krpm and 60 krpm, progressive stall behavior is found, which is indicated by region 2). Firstly, distinct pressure perturbations are observed that then increase in amplitude and extend to an inducer recirculation zone, which ultimately develops into a mild surge with further throttling, see figure 3.9. This is also confirmed by the numerical results. A transitional region exists between those two. At 70 krpm, abrupt mild surge is observed, whereby the pressure amplitudes are much lower than for higher speeds and no flow reversal takes place. Further throttling eventually leads to deep surge. The corresponding pressure signals during surge are given in figure 6.2, showing the evolution from the initially mild to a deep surge at 70 krpm and the abrupt deep surge at 90 krpm. The mild surge has a frequency of approximately 21 Hz, whereas deep surge occurs with about 4 Hz. These frequencies are defined by the specific test rig geometry and may change if the system is modified. The instability line then connects the last stable operating points, where no instabilities are observed. This matches the basic stability theory as the last stable points coincide with the turning points of the total pressure characteristics in figure 6.1.

A very similar behavior towards unstable operation is found for the vaneless diffuser configuration. Again, abrupt mild surge is observed beginning at

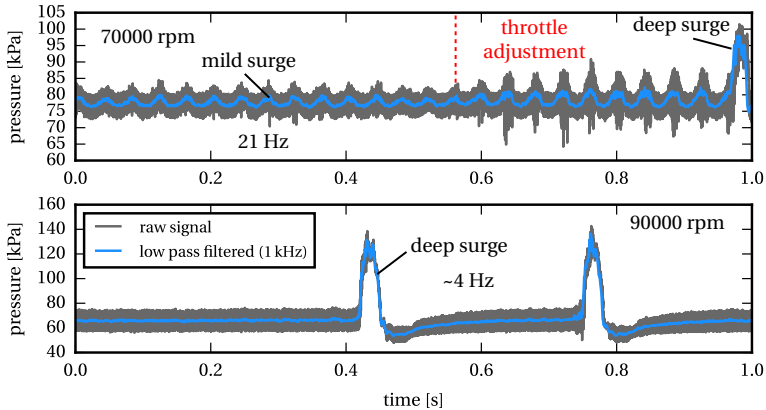


Figure 6.2 – Pressure signals (position 1, upstream of LE) during surge at different rotational speeds for the vaned diffuser configuration

70 krpm, whereas it is preceded by diffuser rotating stall or inducer instabilities at lower speeds. Very similar observations are reported by Zheng and Liu [177]. As expected, a wider operating range is achieved as the choke limit is shifted to higher flow rates by removing the diffuser blades. The respective operating map is presented in the next section together with the grooved casing results.

The different routes to instability are closely connected to the respective near casing flow fields in the impeller, which are significantly different for the considered speeds. Figure 6.3 presents the near casing Mach number distributions in the inducer, obtained from steady-state RANS calculations at the last converging operating point, to exemplify the general context. At low speeds, the inducer flow is subsonic and completely detached from the casing, forming a recirculation zone just like observed in the experiments. The onset of this zone and thus instability is caused by an initial spillage at the main blade leading edges, after the tip vortex has become completely tangential. However, the compressor is still operable with a fully detached inducer, even in the simulations. This changes when moving to higher rotational speeds. At 70 krpm, the inflow becomes partially transonic near the blade suction side and the vortex interface, which divides the healthy flow from the low momentum fluid regions, is not yet fully tangential.

With increasing blade speed, the inducer flow becomes more and more transonic and a passage shock develops which ends on the main blade suction

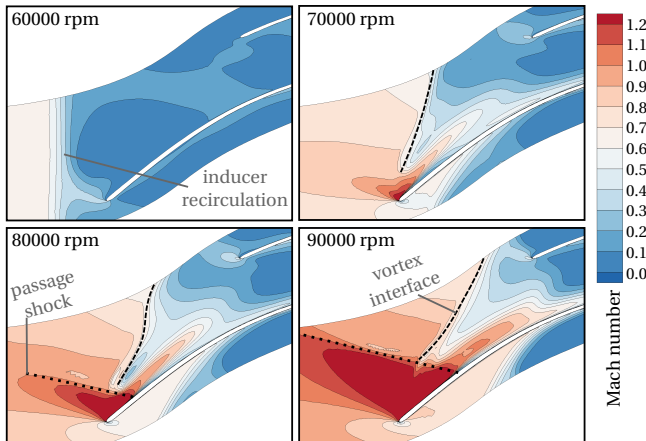


Figure 6.3 – Inducer near tip Mach number distribution (95 % span) for different rotational speeds at last stable operating conditions

side. The strength of this shock increases with speed and the endpoint on the main blade suction side moves downstream as the shock angle changes. As a result, the tip vortex and especially its interface are pushed in meridional direction, which leads to enhanced interaction with the splitter blade. Unstable operation is then likely to be triggered by a breakdown of the near tip flow field due to increasing flow resistance and blockage in the vicinity of the splitter blade, for example similarly reported by Hazby and Xu [77]. The results from the design study also suggest that this process is coupled to blockage and flow separations at the near tip leading edge of the splitter blade, whereby the blockage is also strongly affected by the flow turning in radial direction in the bend region, see also figure 2.2.

Summing this up, the data and the available literature indicates that the different routes to instability are closely linked to the flow state in the inducer. For subsonic conditions a rather progressive route to instability is observed, which involves perturbations in the inducer and a recirculation zone prior to mild surge. In contrast to that, abrupt surge is found at transonic operating conditions at high blade speeds. The 70 krpm speedline seems to be somewhat in-between, as an abrupt mild surge is observed before entering deep surge. Nevertheless, it is associated with the transonic regime as the near casing flow fields near stall seem comparable and abrupt surge behavior is found. Moreover, no destabilizing modes are observed prior to surge, which leads to the conclusion that spike-type stall inception is present at these conditions.

6.2 Influence on Operating Range

This section presents the impact of the two different groove configurations on the operating range of the compressor. For this purpose, the operating map of each variant is measured. Subsequently, the stability line is derived according to the methodology presented in section 3.2.3. Each diffuser configuration, namely the vaned and the vaneless type, is discussed individually. A comparison of both respective performance maps is given in the appendix in figure C.1.

6.2.1 Vaned Diffuser Measurements

The measured operating map for the different groove configurations with the vaned diffuser is shown in figure 6.4. Additionally, the respective stability lines are marked in the map. Diamond shaped markers are used for the stable operating points, whereas circles denote an unstable operation. For these points either rotating stall or an inducer recirculation is detected. The related calculation of the stall margin (SM) and its improvement (SMI) with respect to the sc configuration is presented in figure 6.5, whereby

$$SM = 1 - \left(\frac{\dot{m}_{\text{stall}}}{\dot{m}_{\text{choke}}} \right) \quad \text{and} \quad SMI = SM_{gc} - SM_{sc}.$$

The measured results show a clear and significant impact of the groove application on the stable operating range with the vaned diffuser. Both grooved configurations show a similar SMI of approximately 6% for the subsonic operating speeds of 50 krpm and 60 krpm. At 70 krpm the improvement of $g2$ declines to 3%, whereas $g4$ still reaches over 6%.

For transonic conditions at 80 krpm and 90 krpm the SMI of $g4$ decreases to values around 2%, but is still clearly detectable in the measurements. The $g2$ configuration however shows a small deterioration of the SMI , whereby this is mostly caused by a lower choke massflow rate. The flow rate of the last stable operating point remains almost equal to the smooth casing, indicating that $g2$ has only very limited impact at these transonic conditions.

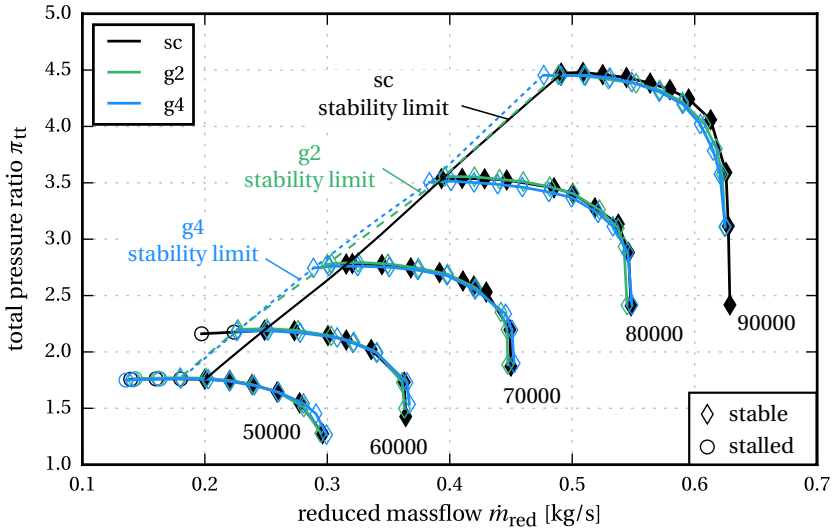


Figure 6.4 – Measured operating map for the *sc*, *g2* and *g4* configurations including stability lines – vaned diffuser setup

| <i>n</i> [rpm] | | <i>sc</i> | <i>g2</i> | <i>g4</i> |
|----------------|------------|-----------|---------------|--------------|
| 90 000 | <i>SM</i> | 21.91 % | 21.76 % | 23.69 % |
| | <i>SMI</i> | - | -0.1 % | 1.8 % |
| 80 000 | <i>SM</i> | 28.24 % | 27.33 % | 30.14 % |
| | <i>SMI</i> | - | -0.9 % | 1.9 % |
| 70 000 | <i>SM</i> | 29.89 % | 32.93 % | 36.21 % |
| | <i>SMI</i> | - | 3.0 % | 6.3 % |
| 60 000 | <i>SM</i> | 31.66 % | 37.47 % | 38.40 % |
| | <i>SMI</i> | - | 5.8 % | 6.7 % |
| 50 000 | <i>SM</i> | 32.47 % | 38.95 % | 39.81 % |
| | <i>SMI</i> | - | 6.5 % | 7.3 % |

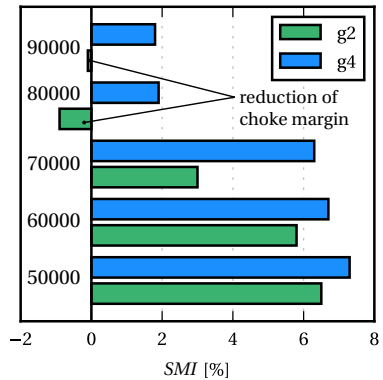


Figure 6.5 – *SMI* evaluation of the grooved configurations for the different speedlines with the vaned diffuser

6.2.2 Vaneless Diffuser Measurements

Equivalent measurements are performed with the vaneless diffuser, whereby the data is analyzed accordingly. The respective operating map and the corresponding analysis is given in figures 6.6 and 6.7. In general, the operating range becomes wider due to the different characteristic of the vaneless diffuser, which shifts the choke margin to higher massflows.

Comparable trends as for the vaned diffuser are found towards unstable operation for all speedlines. Again, the *g4* configuration offers a significant *SMI* for the complete operating map, whereas the improvements of *g2* are somewhat limited to low speed operation. At 50 krpm and 60 krpm both configurations offer a *SMI* of approximately 11 % and 6 % respectively. At higher speeds, a significant *SMI* is only observed for *g4*, with similar values as for the vaned diffuser. Again, small changes in the choke margin affect the *SMI* results. In general, a moderate increase in the maximum flow rate is observed for the higher speeds ≥ 70 krpm. This coincides with the occurrence of choke which is indicated by the speedlines becoming vertical. Further discussion of these results is provided in the next sections.

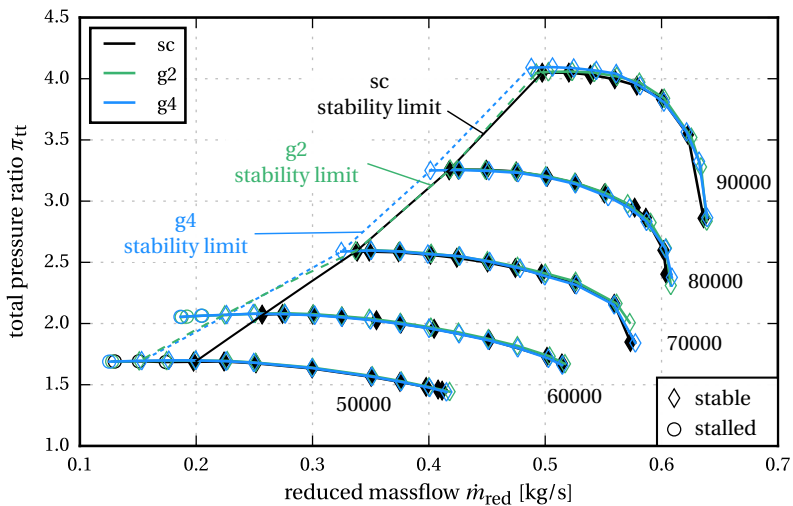


Figure 6.6 – Measured operating map for the *sc*, *g2* and *g4* configurations including stability lines – vaneless diffuser setup

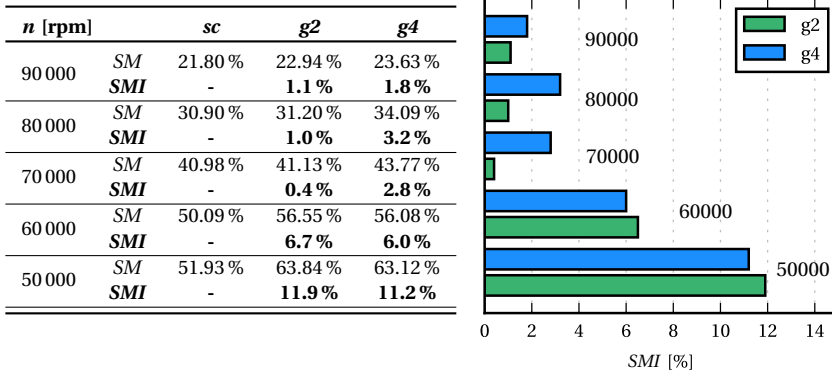


Figure 6.7 – *SMI* evaluation of the grooved configurations for the different speedlines with the vaneless diffuser

6.3 Discussion of Measured Results

The main findings of the experimental study on the *SMI* of circumferential groove application are discussed within this section. Thereupon, several conclusions can be drawn, which allow for hypothesis on the responsible flow mechanisms. These are investigated in detail using experimental and numerical data to further validate the findings and to understand the governing flow mechanisms, which lead to the *SMIs* that are found in the experiments. The respective mechanisms are investigated separately, as clear differences for subsonic and transonic operating conditions have been observed in previous sections.

The following main conclusions can be drawn, based on the experimental results. First of all, the results provide experimental proof of concept for the assumptions that were made in the design study regarding the stability of the compressor stage at 90 krpm. A stall margin improvement is achieved for the considered speedline, which can therefore be linked to the previously described mechanisms. Moreover, significant improvements are found for the complete operating map. Secondly, two different routes to instability are identified. The numerical simulations suggest that the formation of a recirculation zone is involved in the process for an operation up to 60 krpm. At higher speeds, the inducer flow gets unstable way before the tip vortex inter-

face and its trajectory become perpendicular. This indicates that effects like shock-vortex interaction and the interaction with the splitter blade initiate the increase of blockage. This eventually leads to a breakdown of the near tip flow field that triggers spike-type stall inception. These points are further supported by the experimentally obtained *SMI* trends. Those are independent from the specific diffuser, as both grooved casing configurations show very similar trends for the different speedlines. This indicates that the effects that cause the improvements can be associated to the impeller flow field. Hence, the root of instability in the present compressor can be linked to the impeller flow field, which reinforces the validity of the different mechanisms indicated in section 6.1. Nonetheless, the diffusers and the volute still influence the stability of the system. For example, the non-matching vaneless diffuser system leads to a general shift of the surge margin to higher flow rates compared to the vaned diffuser stage, compare figures 6.4 and 6.6.

Thirdly, a fundamental difference between the two groove configurations and the respective groove locations exists. The results suggest that the grooves in the inducer (present in *g2* and *g4*) are responsible for the *SMI* at subsonic conditions, by stabilizing the near tip flow field and hence delaying the initial spillage of the flow. In contrast to that, the bend region grooves downstream of the splitter blade LE (*g4* only) seem to facilitate the *SMI* at transonic conditions, as only the *g4* configuration offers improvements at those speeds. Again, the 70 krpm speedline seems not to fit perfectly in this scheme as it is somewhat in-between, where the mechanism switches. The isolated inducer grooves (*g2*) provide an improvement for the vaned diffuser, but remain almost ineffective for the vaneless one.

Based on the measured overall data, the following hypothesis can be made for the different groove configurations.

- **inducer grooves** — $m' = 10$ and 20
The inducer grooves are, for the most part, responsible for the facilitation of a *SMI* at subsonic inducer flow conditions by delaying the spillage at the main blades due to a deflection and redistribution of the tip vortex.
- **bend region grooves** — $m' = 37$ and 50
The bend region grooves additionally reduce the upstream blockage by a redistribution of local leakage flows in the bend region. In combination with the inducer grooves this leads to a delay of a flow breakdown near the casing at transonic operating conditions, which ultimately leads to flow spillage as well.

Moreover, it is interesting to note that similar trends in terms of *SMI* are observed in the steady-state performance map calculations, which are based on convergence criteria to estimate the last stable operating point. The *g4* configuration converges to lower massflows at transonic conditions, whereas *g2* remains similar to the smooth casing. At 70 krpm both grooved configurations show an increase in range. Again, this is independent from the diffuser and therefore provides further validation for the numerical models in terms of capturing the relevant mechanisms in the near tip flow field towards unstable operation. The respective operating maps are depicted in figures C.2 and C.3 in the appendix.

The following sections provide some more detailed analysis of the available data to validate these hypothesis. On the one hand, the measured data is analyzed in detail. On the other, numerical simulations are used to gain further insight in the physical mechanisms of the *SMI*.

6.4 Analysis at Transonic Operating Conditions

This section analyzes the flow mechanisms that lead to the *SMI* to corroborate the presented hypothesis. Moreover, it is assessed if the numerical models are capable of predicting comparable trends, which could be useful for future design approaches. A rotational speed of 70 krpm is selected for the investigations, as the greatest impact is observed here. In addition, dynamically throttled URANS calculations were performed for this speedline.

The measured overall data suggests that the *SMI* is generated by a stabilization of the impeller flow field, which is therefore evaluated in detail. Firstly, the influence of the grooves at a stable near-stall operating point is analyzed. Thereafter, numerical simulations of the stall inception process are presented.

6.4.1 Influence at Near-Stall Operation

The plots in figure 6.8 show the measured and calculated speedline for the different groove cases and the different diffuser configurations. The near-stall operating points that are selected for detailed comparisons are marked with red squares. Different operating points are used for the experiments and the calculations, representing the last stable flow rate that is achieved by all casing configurations.

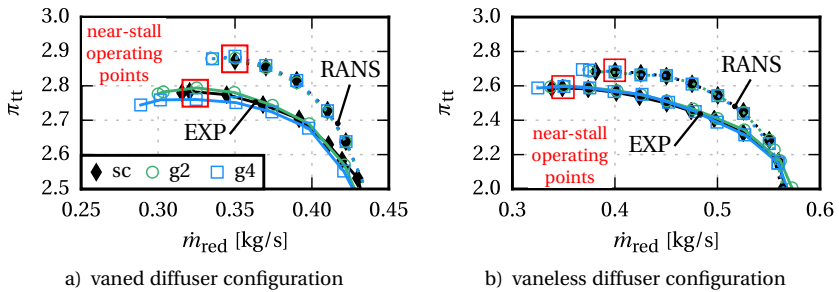


Figure 6.8 – Closeup of experimental and numerical speedline at 70 krpm for the different cases near stall

In terms of *SMI*, the measured and calculated speedlines show a remarkable resemblance. Despite predicting earlier instability, the RANS models yield very similar trends on the basis of convergence criteria, compared to the experiments. This suggests that the major mechanisms, that lead to instability and unsteadiness, are reproduced in the steady-state models. Thus, the RANS results are used to examine the groove influence on the near tip flow field to initially understand the mechanisms of the *SMI*. Thereupon, experimental results are analyzed to support the findings. The following RANS evaluations are presented for the vaned diffuser. However, the mechanisms are assumed to be transferable to the vaneless one, as these seem to be almost completely independent from the diffuser.

Figure 6.9 depicts the inducer near tip flow field, showing the extent of the total pressure deficit that is produced by the tip leakage vortex and its interaction with the passage shock, the casing boundary layer and other secondary flows. Based upon that, different tip vortex characteristics are marked in the plots to compare the different cases. As already found for the design study at 90 krpm, the vortex trajectory, which describes the direction of the vortex center, is again deflected in streamwise direction for the grooved configurations. This can be attributed to the inducer groove mechanism described in section 5.3.1. In addition, the expansion angle φ of the vortex cone decreases significantly from 35° for the smooth casing to around 26° and 24° for *g2* and *g4*. This expansion angle describes the extent of the vortex cone in a certain span plane and is used here to roughly quantify the change of the vortex and its interface to the incoming flow (vortex interface). Consequently, the vortex interface is also shifted in streamwise direction. This suggests that the smooth

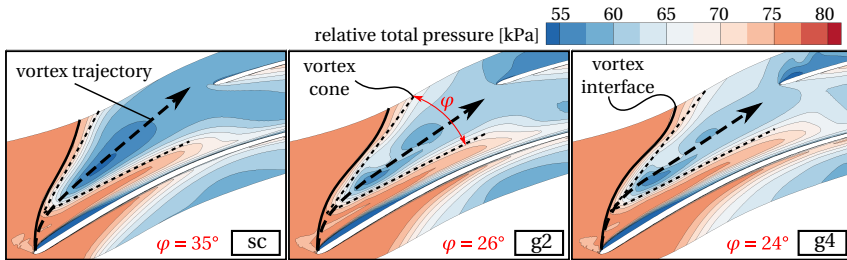


Figure 6.9 – Inducer total pressure contour (RANS) at 90 % span for 70 krpm at a near-stall flow rate of 0.35 kg/s for the vaned diffuser

casing is much closer to a flow breakdown and that the grooved cases hold additional reserves to fall back on.

The widening of the vortex and the eventual spillage of the interface are primarily linked to the flow resistance that is imposed onto it near the splitter blade. This resistance is equivalent to flow blockage. Figure 6.10 visualizes the extent of these regions based on the entropy distribution on a corresponding plane. Moreover, the blockage values according to equation (5.3) are given. It becomes clear that the blocked areas, and henceforth the flow resistance, are much less pronounced for the grooved cases. The blockage reduces from 18 % to 15.5 % for *g2* and 13.5 % for the *g4* configuration.

One part is caused by the inducer grooves, but another major share of the reduction is stemming from the bend region grooves present in *g4*. The actual cause for the reduction is pointed out in figure 6.11. Backward oriented

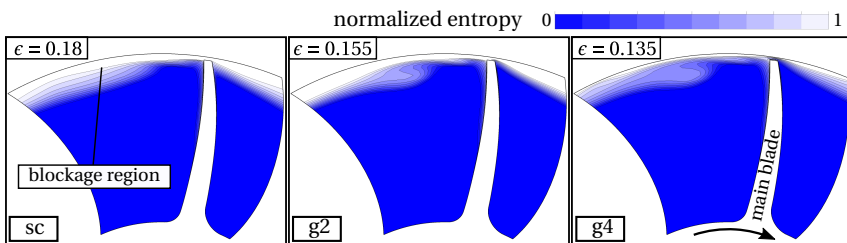


Figure 6.10 – Entropy distribution and blockage values on an axial plane upstream of the splitter blade (Kulite position 3) for the 70 krpm near-stall point

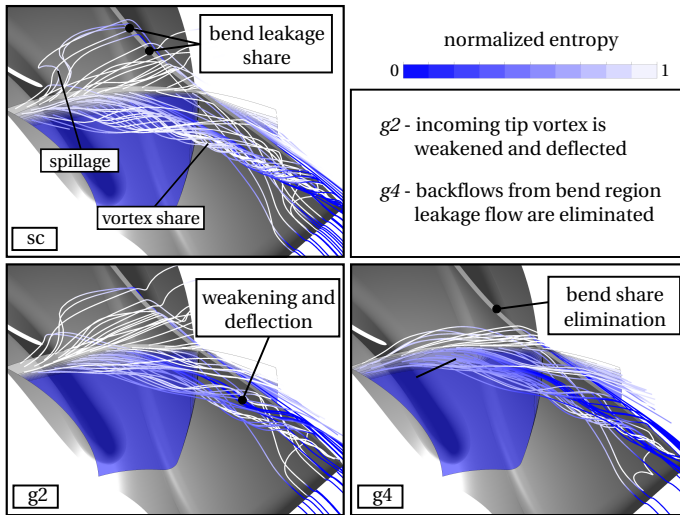


Figure 6.11 – Impact of grooved variants on the flow shares that contribute to the blockage in the inducer for the 70 krpm near-stall point – plot shows incoming streamlines that form the blocked area on the evaluation plane from figure 6.10

streamlines that originate in the respective blockage regions, which represent the incoming flow, are used to visualize the contributing flow shares.

Two major effects can be identified that dominate this process. Firstly, leakage flows from the bend region flow towards the inducer, where they spill around the splitter blade LE. Secondly, these flows interact with the incoming flow shares involved in the typical tip leakage vortex. As a result, blockage or rather flow resistance is generated, that ultimately leads to a breakdown of the orderly flow near the tip.

The application of inducer grooves (*g2*) improves only one part of the interacting effects. The deflection and the weakening of the incoming tip vortex hinders the interaction and therefore reduces the blockage. The bend region grooves in configuration *g4* however additionally eliminate large parts of the bend leakage shares, leading to a further reduction in blockage. This is achieved by a redistribution of the leakage flows, which is in general described in section 5.3.2.

This could explain why the *g4* configuration leads to a significant *SMI* at transonic speeds, whereas the *g2* configuration offers only marginal improvements here. Moreover, the measured *SMI* results suggest that the bend groove mechanism is much more important at clearly transonic operating conditions (80 krpm and 90 krpm), compared to inducer grooves.

Figure 6.12 plots the measured, ensemble averaged pressure signals for the sensor position 3 in the inducer alongside the corresponding standard deviations (same meridional location as the evaluation plane in figures 6.10 and 6.11). As expected, the characteristics of the signals show a clear resemblance. The courses agree well, in particular near the main blade location that is characterized by the pressure drop from PS to SS. However, differences between the cases are observed in the tip vortex affected region at about 0.6 to 0.1 rotor pitch. Whereas the grooved configurations show a distinct pressure drop at 0.9 rotor pitch, the *sc* case seems to have a much flatter characteristic in this region. This indicates a wider, less concentrated tip leakage vortex, which resembles the steady-state RANS simulation results. The corresponding CFD pressure courses are not included in figure 6.12 as the near stall flow rate of the experiment was not reached in the simulations (see speedlines in figure 6.8a). However, the validation in section 4.4 showed that similar distributions can be expected.

Moreover, this is also supported by the measured standard deviations in the plot on the right. Again, very similar fluctuations are measured in the vicinity

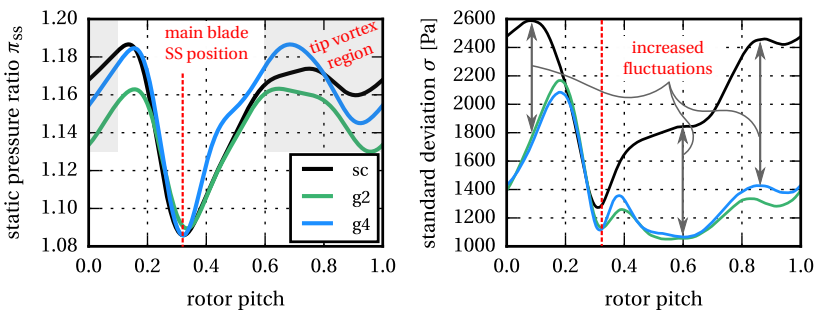


Figure 6.12 – Ensemble averaged circumferential pressure distribution and RMS standard deviation σ — measured at sensor position 3 in the inducer for the vaned diffuser near-stall operating point at 70 krpm

of the blade. In contrast to that, significantly different values are recorded for the remaining pitch. The standard deviation remains on much lower levels for the grooved cases, whereby almost equal values are measured for $g2$ and $g4$. Significantly increased fluctuations are observed for the baseline casing with almost doubled values in the vortex region. This shows that the sc flowfield is less steady around the circumference compared to the grooved cases. Therefore, it can be concluded that the inducer grooves lead to a significant reduction of unsteadiness in the near tip region. This was also similarly observed by Van de Wyer et al. [156] in his detailed measurements of the near tip flow field in an axial compressor. Moreover, this confirms the link between rising unsteadiness and the onset of instability proposed in the literature (e.g. [167, 168]), as both configurations lead to a SMI . Similar results in terms of unsteadiness reduction in the inducer are obtained for the vaneless diffuser near-stall point, see figure C.4 in the appendix, despite no clear SMI is observed for the $g2$ configuration here.

The corresponding DFT spectra for both diffuser configurations are depicted in figure 6.13, additionally including position 2 which is located directly above the leading edges. At position 3, significantly higher low frequency shares are present in a broadband manner below the BPF for sc . However, notable amplitudes are also present in the grooved cases but generally on a lower level. Again, this reduction seems to be independent of the diffuser. More distinct differences are observed at position 2. Only very low amplitudes other than for the BPF are observed for the grooved cases $g2$ and $g4$ in figure 6.13a. The sc configuration however, again experiences broadband pressure fluctuations below and also above the BPF. At this position, this indicates that the tip leakage interface is almost tangential and thus close to spillage. Once more, this matches the SMI trends and further supports the proposed mechanism.

The measurements of the vaneless diffuser configuration in figure 6.13b show a similar trend, but a clear difference between $g2$ and $g4$ exists at position 2. Again $g4$ shows the lowest level of unsteadiness, followed by $g2$ and sc . This again indicates a less tangential vortex interface for the grooved cases. However, the amplitudes are much lower as for the vaned diffuser near-stall point. This stems from the higher near stall flow rates and the therefore less tangential tip vortex, which results from the non-matching vaneless diffuser application.

Summing this up, the unsteady measurements generally support the proposed theory of the SMI mechanism. The evaluations indicate a reduction in unsteadiness and a reduced extent of the low momentum fluid region in the

inducer as a result of groove application. Nevertheless, much more extensive and sophisticated measurements would be required to further resolve the flow mechanisms in the measurements, which are not available in the present work. As an alternative, additional numerical studies on the stall inception process are presented in the following section.

6.4.2 Numerical Simulation of Stall Inception

Six different stall simulations (all configurations with both diffusers) are performed to assess the impact of the grooves on the onset of aerodynamic flow instabilities. The compressor is throttled transiently until a breakdown of the flow occurs and a surge cycle is initiated. The approach of the simulations is presented in section 4.2.2. Several numerical probes are used to record the respective signals during the throttled transient, whereby most positions are taken from the experimental setup, such as the Kulite sensor locations 1 to 8. Additionally, the complete flow field is stored for every full revolution for further evaluation.

Figure 6.14 presents the global evolution of the massflow at the impeller outlet during the transient throttling process for the different simulations.

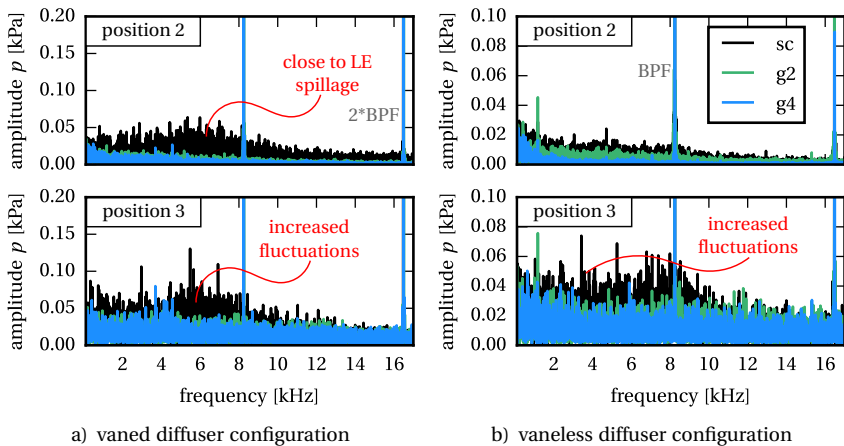


Figure 6.13 – Near-stall (see figure 6.8) DFT spectrum of the Kulite pressure signals at the main blade leading edge and in the inducer for the different cases – 70 krpm

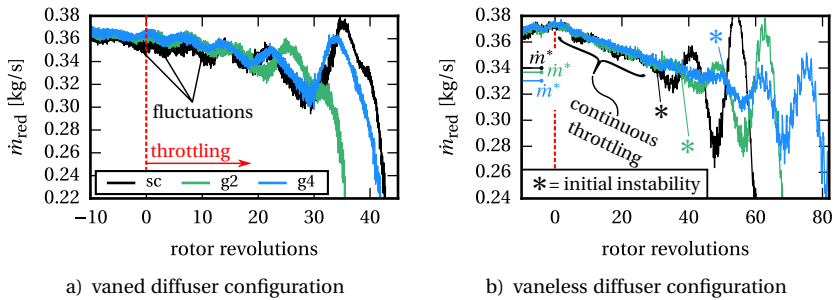


Figure 6.14 – Massflow evolution at the impeller outlet for the different cases extracted from the throttled simulations - throttling starts at 0 revolutions

The throttle condition is adjusted from 0 revolutions forward. In general, a similar development is found for all cases. The flow rate decreases until a first instability seems to occur, that initiates strong massflow fluctuations. Thereby, the onset of unstable operation is marked by an initial breakdown of the massflow. The flow rate then recovers briefly and enters a phase of cyclic fluctuations, whereby the amplitude increases until the stop criterion of the simulations is met.

Nevertheless, significant differences are found for the different diffusers. The vaneless diffuser in figure 6.14b shows a phase of continuous throttling until the *sc* configuration first gets unstable. Thereby, the initial instability is marked with a star (*) that represents the first spillage of the flow at the main blades, which is further explained in the following sections. The *g2* and *g4* configurations remain stable at higher throttle values and thus delay the stall onset to lower flow rates. The specific points and massflows are marked with a star.

The vaned diffuser simulations, see figure 6.14a, are strongly dominated by massflow fluctuations that start even before the throttle boundary condition is modified. These seem stronger for the *sc* configuration, which could hint a similar improvement as for the vaneless diffuser case. However, no clear onset of instability can be determined from these characteristics. Moreover, the number of rotor of revolutions until the stop criterion is reached contradicts this indication. This is due to a rotating stall that emerges in the vaned diffuser and affects the global flow rates. The pressure signal of 17 circumferentially distributed numerical probes at the casing in the vaneless space is shown in

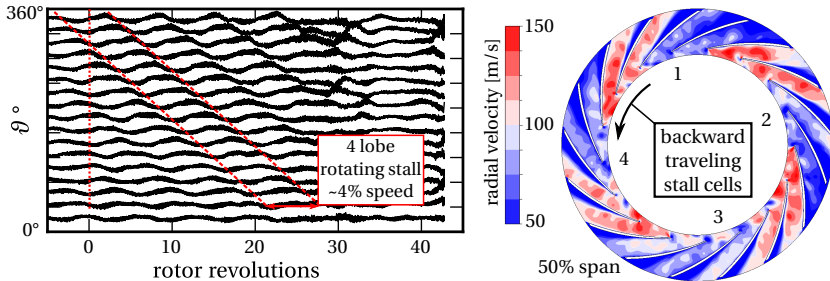


Figure 6.15 – Vaned diffuser pressure signal during the throttled simulation with the smooth casing, extracted in the vaneless space at the shroud (left) — instantaneous radial velocity field at 50 % span after 9 rotor revolutions (right)

figure 6.15. The evaluation of the signals yields a 4 lobe stall that rotates with $\approx 4\%$ of the impeller speed in backward direction. The plot on the right clearly visualizes this pattern by means of the radial velocity field at an instantaneous rotor position.

The pattern develops well before the throttling process starts and is not found in any of the corresponding measurements, where no rotating structures have been detected in the vaned diffuser. Thus it is assumed, that this is again connected to the numerical problems with the vaned diffuser, which were already observed in the steady-state simulations, see section 4.4.1. However, this is not of particular interest for the present study and subsequently this is not further evaluated in detail. Nevertheless, this rotating stall for certain affects the impeller flow field and thus it is hard to isolate the specific groove impact. Therefore, the following evaluations on the effect of the casing grooves are presented for the vaneless diffuser. Still, very similar mechanisms and effects are also found for the vaned diffuser, which are not shown here for the sake of clarity.

Figure 6.16 plots the evolution of the static pressure at sensor position 1, just upstream of the impeller LE. Both, the raw signal as well as the low pass filtered signal are shown. These clearly indicate the onset of unstable flow phenomena that affect the inducer during the throttling process.

In general, the amplitude of the raw signal increases until the initial breakdown occurs, which starts the phase of cyclic fluctuations. Additional fluctuations in the filtered signal become evident at this point. The simulations suggest that the baseline configuration becomes unstable after approximately 31 rotor

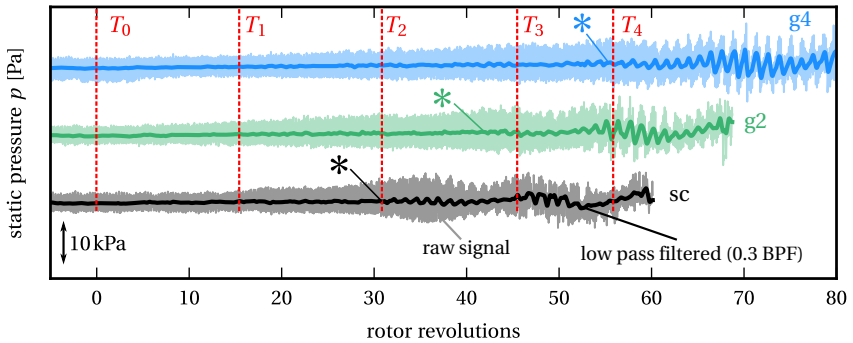


Figure 6.16 – Evolution of the static pressure at the sensor position 1 extracted from the throttled simulations towards unstable operation for the different cases with the vaneless diffuser

revolutions, whereas $g2$ remains stable for another 10 revolutions and $g4$ for another 25. This equals 5% and 12% increased throttle parameters, see equation (4.2). Remarkably, this trend corresponds well with the experimental *SMI* results, where $g4$ is superior to $g2$ and the baseline casing as well. Additionally, very similar stall flow rates are observed, compare CFD in figure 6.14b and EXP in figure 6.6. The smooth casing reaches approximately 0.34 kg/s, whereas the $g4$ configuration remains stable up until 0.33 kg/s, just like in the experiments.

Suitable timesteps (T_0 to T_4) are selected to analyze the flow mechanisms leading to instability and to compare the different cases in detail. Figure 6.17 presents an evaluation of the blockage ratio on the previously used plane at sensor position 3 in the inducer. The corresponding inducer flow fields are depicted in figures 6.19 to 6.23 by means of total pressure contours at 90% span. The evaluation of the flow clearly connects the onset of the flow breakdown with the first occurrence of spillage at the main blade LE. This provides further support for the previously proposed hypothesis and moreover complies with the criterion of Vo et al. [158] for spike-type stall inception. Moreover, a clear connection to the increasing blockage can be drawn.

The results in figure 6.17 show that the blockage rises almost linearly until the initial spillage occurs. For the present study a critical blockage level is found that – if exceeded – triggers the spillage. However, this criterion is no hard limit and will most certainly differ for other compressors and operating points. Nevertheless, the concurrence of instability and a certain blockage

value might be transferable. As the blockage ratio is reduced for the grooved configurations, the onset of instability is delayed. It is interesting to note, that the reduction is already present for the non-throttled condition at T_0 . This corresponds to the steady-state calculations, which on the one hand explains the predicted *SMI* and on the other hand confirms the validity of the approach that was used in the design study.

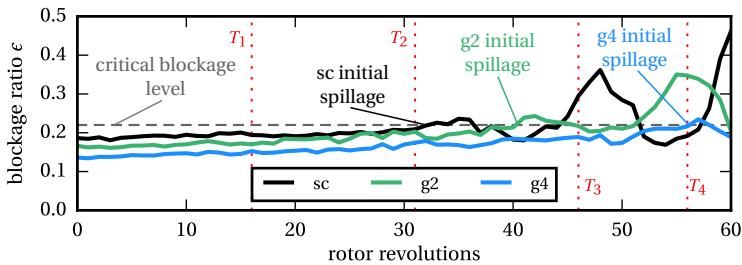


Figure 6.17 – Evolution of the blockage ratio ϵ during the throttling - evaluated at the sensor position 3 plane for the different cases with the vaneless diffuser

The blockage gradient remains constant for the grooved cases, which means that the general mechanism is rather delayed than altered. Figure 6.19 shows that this corresponds with the already introduced deflection of the tip vortex, whereby the vortex interface is pushed in streamwise direction.

Flow Field Evaluation

The evolution of the inducer flow field for the selected timesteps is visualized in the figures 6.19 to 6.23. Firstly, some general observations are elucidated, which are followed by a comparison of the grooved cases to the *sc* flow fields.

A significant circumferential inhomogeneity is observed for all cases. The non-matching volute and diffuser clearly impose an asymmetrical pressure field that strongly influences the different impeller channels. As a result, one specific channel can be identified, which initially becomes unstable. Its location is defined by the position of the narrowest part of the volute ($\vartheta \approx 75^\circ$ to 125° , just after the tongue, which is located at about 60° , see figure 3.5). This is most probably the cause for the reduced stall flow rates compared to the vaned diffuser configuration, that are observed in the measurements. Accordingly, a more homogeneous distribution is observed for the vaned

diffuser configurations. Nonetheless, the CFD results suggest that the stall mechanism and the effect of the grooves remain unchanged and thus support the independency from the diffuser that is found in the measurements.

In general, the following process towards stall is observed. The increasing blockage combined with the increasing inflow incidence during the throttling moves the vortex interface towards a more circumferential direction. At T_0 all configurations are still stable and the vortex interface is not yet perpendicular, whereby $g2$ and $g4$ show the previously described improvement, as the interface is deflected. At timestep T_1 , the vortex interface in the respective blade channel of sc is almost tangential, whereas $g2$ and $g4$ still show a more stable inducer flow field. Additionally, a shedding of vortical structures from the main blade suction sides of the affected channels is observed. Figure 6.18 exemplarily visualizes the shedding, the transportation and the spillage of these vortices in a top and a front-side view. They originate from suction-side flow separations due to a local transgression of the critical incidence and have been similarly reported by various researchers to occur prior to spillage towards spike-type stall [12, 79, 91, 131, 167].

A tornado shaped structure that stretches from the main blade SS to the shroud is observed, which is similarly reported by Yamada et al. [170], compare figure 2.6. However, these structures are convected downstream at still stable operating conditions. Upon further throttling, these detached, vortical structures move in tangential direction and finally spill around the adjacent leading edge. Figure 6.18, taken at T_2 , clearly shows the participation of the vortical structures in this process. This initial spillage acts as the first spike disturbance that triggers the global stage instability for the baseline design, also shown in figure 6.21. This process is accordingly delayed for $g2$ and $g4$, where the interface becomes more and more

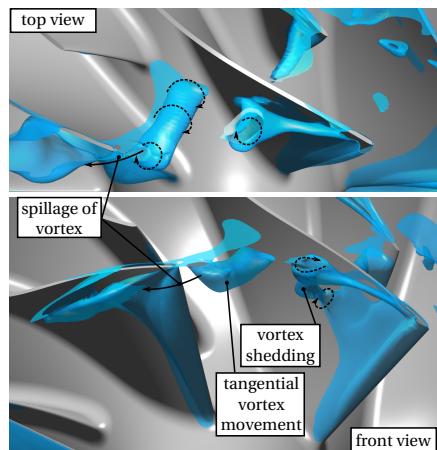


Figure 6.18 – Instantaneous isosurface of the density for the sc configuration at T_2 showing a 3-dimensional visualization of the vortex shedding and the spillage process – compare to figure 6.21

tangential and vortex shedding emerges as well. However, spillage is not yet imminent with the grooves at this timestep.

Accordingly, the vortices still move downstream along the trajectory of the leakage flow. Subsequently, the flow in the *sc* configuration temporarily recovers after the initial spike and then enters a cyclic phase of violent instability and recovery. The second, much more violent spillage of the *sc* configuration is underway after 46 full rotor revolutions at T_3 . The circumferential extent is drastically increased and almost all channels are close to spillage as well. Configuration *g2* experiences the initial spillage at this throttle condition, whereas the interface for *g4* becomes almost tangential as well, but no spillage occurs yet.

The next timestep at T_4 in figure 6.23 is characterized by the initial spike disturbance of *g4*, whereas *g2* is in the phase of the second, more violent instability. The baseline casing is temporarily recovered, before the final breakdown starts, which is characterized by spillage around the whole circumference. This leads to a severe increase in blockage and a drop of the flow rate – compare to figure 6.14b.

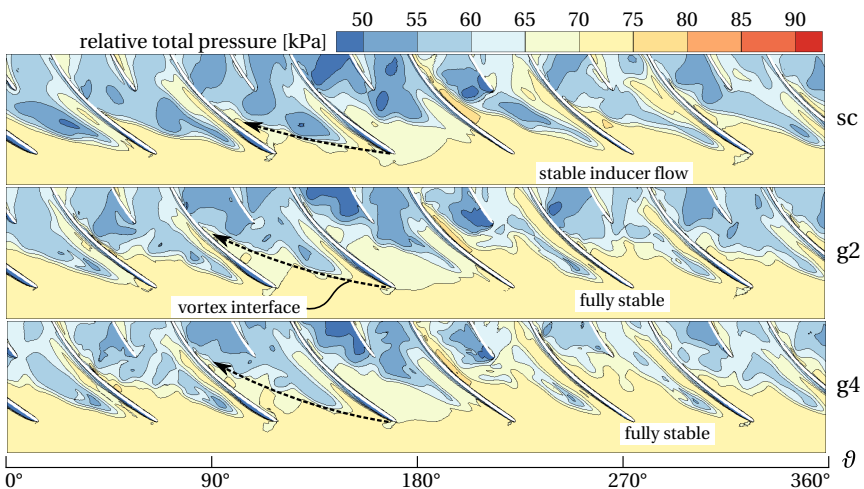


Figure 6.19 – T_0 inducer flow field at 90% span - throttle not yet modified

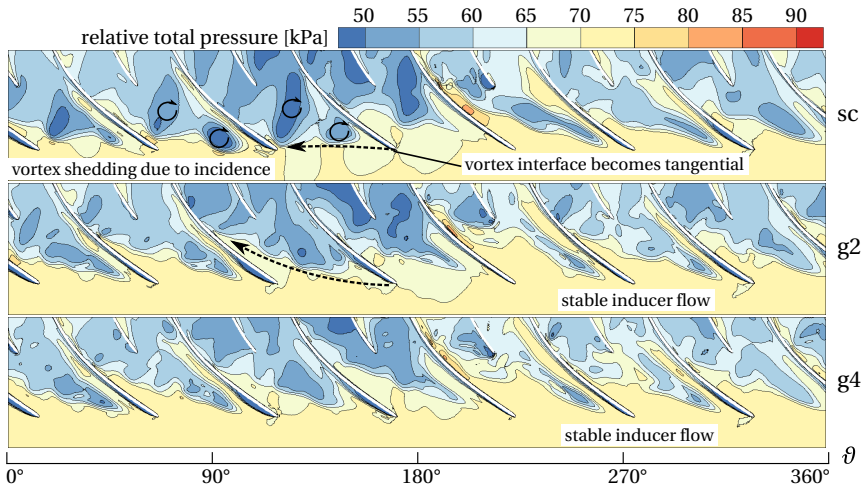


Figure 6.20 – T_1 inducer flow field at 90% span - throttle parameter Δ : +8%

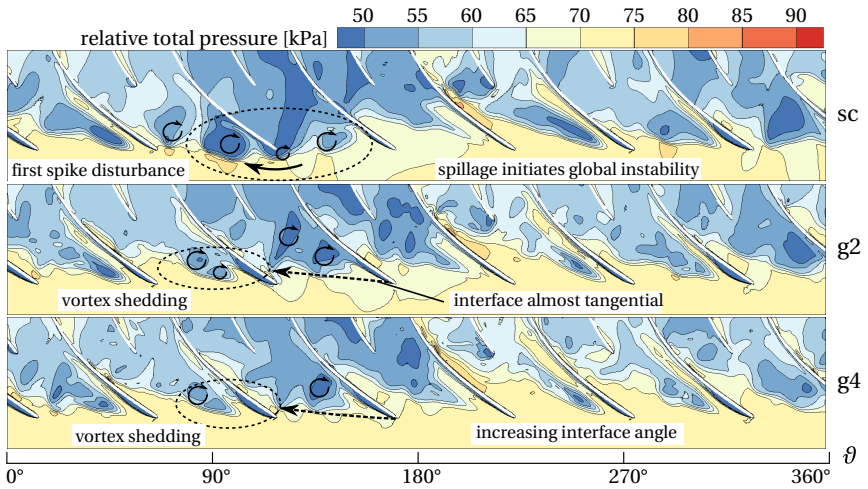


Figure 6.21 – T_2 inducer flow field at 90% span - throttle parameter Δ : +15%

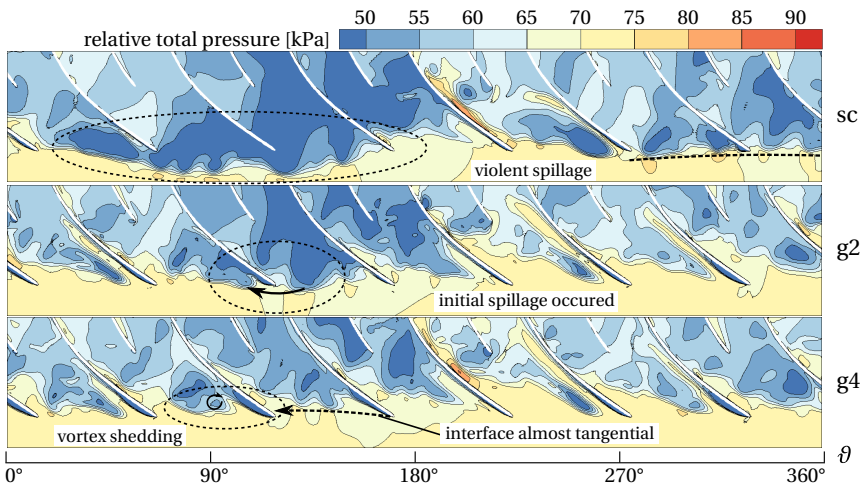


Figure 6.22 – T_3 inducer flow field at 90% span - throttle parameter Δ : +23%

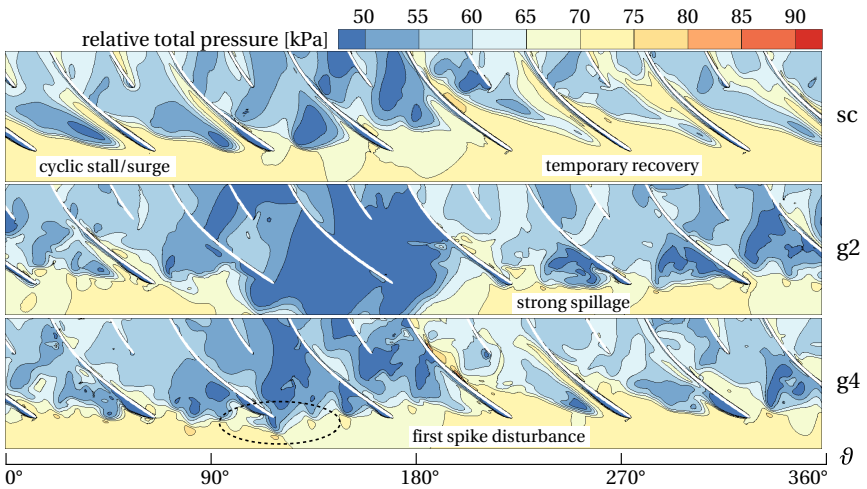


Figure 6.23 – T_4 inducer flow field at 90% span - throttle parameter Δ : +28%

6.4.3 Discussion

The evaluation of the mechanisms leading to instability at a transonic rotational speed of 70 krpm clearly supports the hypothesis that are drawn from the *SMI* measurements. Spike-type stall inception by means of LE spillage is found to be resulting from the flow breakdown in the throttled simulations, whereby this process is strongly coupled to leakage flows, blockage and vortex shedding. This is also supported by the measured data at near stall operating conditions.

The results show that the *SMI* of the grooves is generated by a delay of the spillage and not by a substantial change of the process itself. Moreover, the inception can be located to a specific circumferential location due to the asymmetric shape of the volute, which is similarly reported by other researchers as well [172, 174]. The main cause for the delay of the spillage is the reduction of the blockage in the inducer near the splitter blades. This blockage acts as a flow resistance and pushes the vortex interface in circumferential direction and therefore closer to spillage.

Inducer grooves (*g2*) redistribute the local leakage flows and thus weaken and deflect the tip vortex. As a result, they reduce the blockage and delay the spillage at this speed. Additional bend region grooves (*g4*) lead to a significant blockage reduction near the splitter blade LE by a suppression of local leakage backflows. Hence, the spillage is further delayed and a higher *SMI* reached. This effect becomes more and more important towards even higher rotational speeds, as the strength and amount of these backflows increases due to an increasing adverse pressure gradient and stronger secondary flows. Subsequently, this explains why only the *g4* configuration leads to a significant *SMI* at these transonic conditions.

Additionally, grooves in general introduce a circumferential connection between the different impeller channels. The transient simulations show that this leads to increased circumferential mixing and thus reduces the effect of any geometric nonuniformity, such as induced by the volute.

6.5 Analysis at Subsonic Operating Conditions

This section analyzes the mechanisms of the *SMI* at low rotational speeds, whereby experimental data and RANS calculations at 60 krpm are used. The experiments suggest that both grooved configurations delay the onset of the instabilities, whereby similar *SMIs* are observed for *g2* and *g4*. However, this might be due to the rather low resolution of the flow rate, as only a limited number of operating points were measured.

The major difference compared to higher speeds, is the lower adverse pressure gradient and therefore a decreased flow resistance. As a result, a gradually evolving, progressive path to instability is found for the present compressor. The instability starts with the development and growth of distinct frequency perturbations, which then extend to a fully detached recirculation zone. This zone grows with further throttling until mild surge occurs, see figure 3.9 for example. Consequently, the exact determination of the last stable operating point is difficult. Therefore, only trends are demonstrated to assess the impact of the grooves, whereby flow spillage and the formation of a recirculation zone is roughly defined as the onset of instability in this study. The general trends for the different diffusers are found to be transferable. Hence, only the vaned configuration is presented here.

Figure 6.24 shows the measured and calculated speedlines at 60 krpm for the different cases. The last shown point in the simulations is defined by convergence, whereas the onset of mild surge is used in the experiments. Interestingly, a similar trend is observed for these points in both experiment

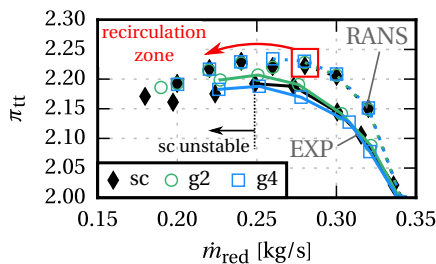


Figure 6.24 – Closeup of the RANS and experimental speedline at 60 krpm for the different casing configurations with the vaned diffuser – Stable operating points are indicated with lines between the markers

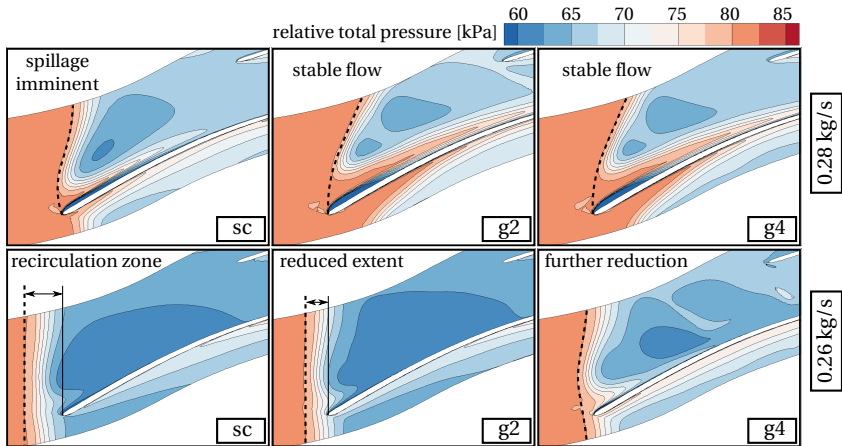


Figure 6.25 – Recirculation zone development by means of an inducer total pressure contour (RANS) at 90% span with the vaned diffuser at 60 krpm and flow rates of 0.28 kg/s and 0.26 kg/s

and computation. Both groove configurations shift these points to higher flow rates, compared to the baseline case (*sc*). This means that the progression from the first spillage to surge occurs faster with grooves. In contrast to that, the onset of instability by means of the used criterion is delayed. In a physical sense, this criterion represents the initial spillage and the formation of the recirculation zone, whereby the low momentum flow near the tip extends upstream of the impeller leading edges.

This is observed in the simulations as well. Figure 6.25 shows that this spillage of the flow is delayed with the grooved configurations. It is imminent for the baseline case at 0.28 kg/s, whereas the leakage interface is not yet tangential for the grooved cases. The initial spillage has occurred for all configurations at 0.26 kg/s. Nevertheless, clear differences are observed as the extent of the recirculation region is reduced for *g2* and even more for *g4*.

This is further confirmed in figure 6.26, which presents the corresponding meridional view on the periodic interface. Furthermore, the total pressure contour shows that the spanwise extent of the affected zone near the tip is not increased. On the contrary, it rather decreases as well.

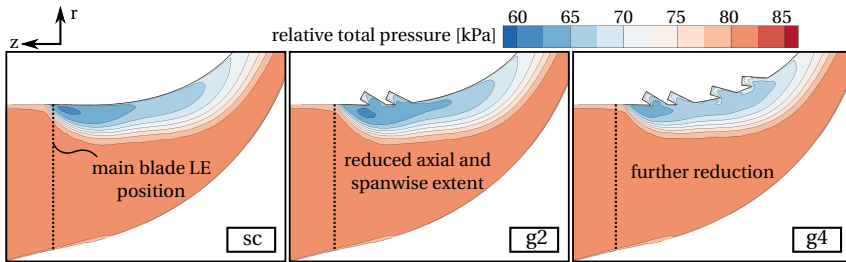


Figure 6.26 – Meridional view of the near tip flow separation at 60 krpm and a flow rate of 0.26 kg/s – meridional projection of the periodic interface

The experimental results clearly support this delay. Moreover, the flow rates at which the initial spillage occurs match very well. Figure 6.27 shows the ensemble averaged pressure signals and RMS-values at the blade leading edges for 0.275 kg/s. The drastically increased fluctuations for the smooth casing indicate that flow spillage has occurred and that the detached recirculation zone extends at least up to the measurement location. No significant differences are observed in the mean pressure ratios but the low RMS levels of the grooved cases indicate that the flow is still stable. Comparable to the simulations, *g4* shows even lower values than *g2*.

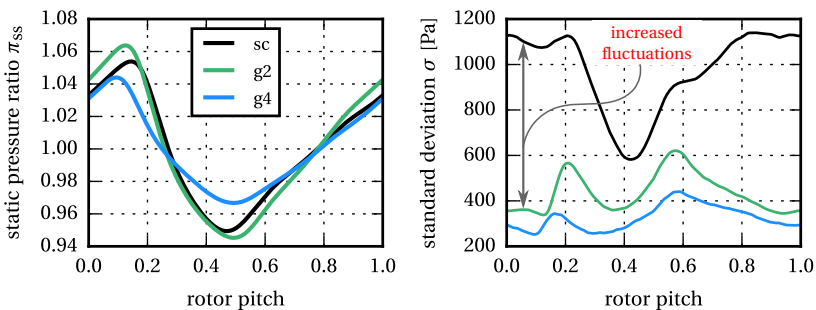


Figure 6.27 – Measured ensemble averaged pressure signals and standard deviations (RMS) for the different cases for 0.275 kg/s at sensor position 2 above the LE

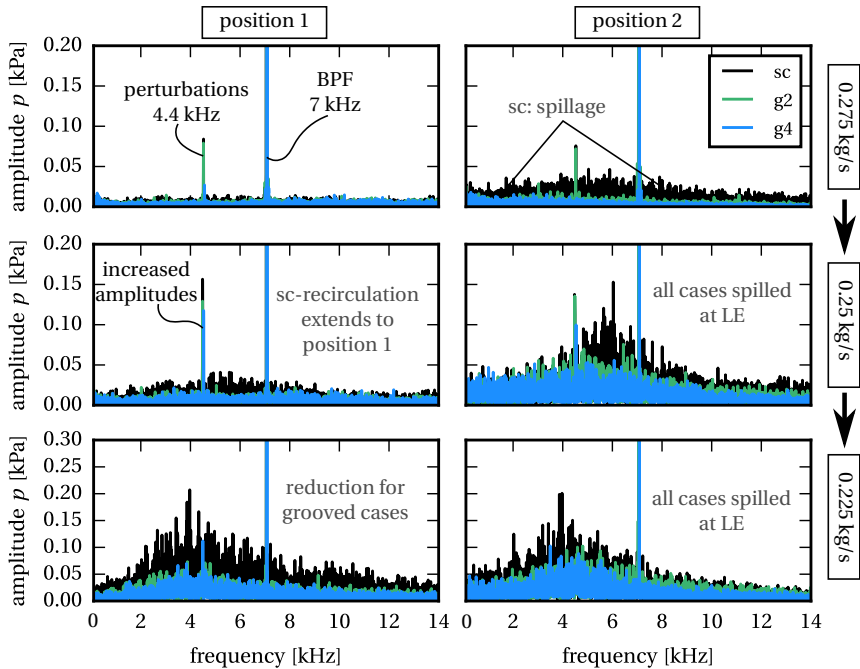


Figure 6.28 – Measured spectra of the pressure amplitudes at position 1 and 2 for different flow rates at 60 krpm

The corresponding spectra of the pressure amplitudes in figure 6.28 demonstrate the development of the spillage process towards lower flow rates. Initially, a distinct frequency of 4.4 kHz is present, that then develops into a broadband hump. This indicates the presence of a modal perturbation, that could for example comprise a small sized separation bubble near the casing, that extends around the whole circumference after the spillage. At 0.275 kg/s, the increased broadband amplitudes again indicate that spillage has already occurred at position 2 for *sc*, whereby the extent not yet affects position 1. The recirculation zone then extends to the front sensor as clearly higher amplitudes are observed here for the baseline casing at 0.25 kg/s. Meanwhile, the grooved cases are becoming unstable as well, as increased amplitudes and the shift towards the hump are observed at position 2 at this massflow rate.

The zone then further extends and unsteadiness further increases. Thereby, a similar hump-shaped distribution is developing for all cases at position 1 at 0.225 kg/s. However, a significant reduction is still present for the grooved cases, which again indicates the delay of this process. Nevertheless, further data would be required to further confirm and understand the detailed mechanisms of these indications.

All in all, it is shown that the rising unsteadiness and the resulting development of a recirculation zone can be delayed with the application of the grooves. However, the determination of the *SMI* is not as clear as for the transonic speedlines as the criterion is somewhat arbitrary and only limited operating points are evaluated. Again, the results suggest that the deflection of the tip vortex causes this effect. Additionally, it is expected that the grooves reduce circumferential inhomogeneities, which contribute to the results. However, this could not be resolved from the measurements or the RANS data.

6.6 Summary on Stability

The grooved configurations *g2* and *g4* are investigated with respect to the extension of the stable operating range. The measured performance maps show that both configurations lead to a *SMI*, independently of the diffuser that is used. The *g4* casing achieves significant improvements for the complete operating range, whereas *g2* only shows a *SMI* for speeds up to 70 000 rpm. The respective mechanisms are evaluated using the measured data as well as additional numerical simulations.

It is found that these differences are closely coupled to the flow state in the impeller inducer, where the onset of instability is triggered in the present compressor. The corresponding mechanisms are schematically sketched in figure 6.29. The flow breakdown at transonic speeds is dominated by blockage in the bend region, which acts as a resistance for the incoming near tip flow. This flow resistance increases with higher speed and loading. Consequently, the interface direction near stall moves in a more streamwise direction for higher speeds.

The breakdown is then initiated by excessive flow blockage in the blade passage near the tip that pushes the leakage flow towards spillage, see figure 6.29a. This is similar to the mechanisms in axial compressors, described by Vo et al. [158], Pullan et al. [131], Hewkin-Smith et al. [79] and others. However, the cause for the rising blockage is different and can be replaced with the flow

turning in radial direction and the splitter blade interaction in the present centrifugal compressor. The calculation of the stall inception supports this mechanism and furthermore indicates that a critical blockage level has to be exceeded to trigger the inception. Moreover, tornado-like vortex shedding from the main blade suction side is involved in the process.

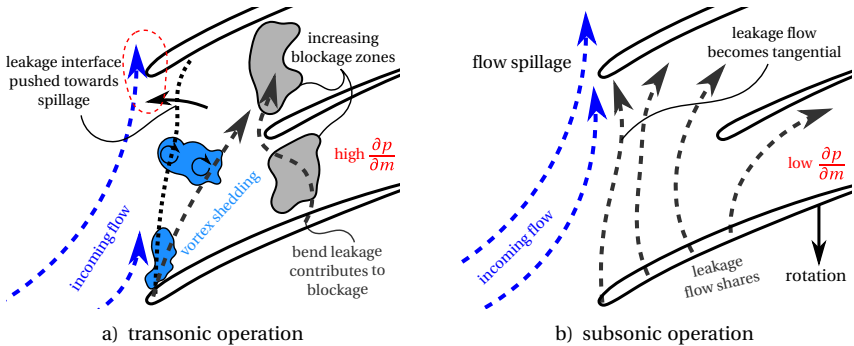


Figure 6.29 – Schematic of the flow mechanisms leading to flow spillage and unstable operation at different operating conditions

The adverse pressure gradient reduces for lower speeds at subsonic conditions. As a result, the stability is not dominated by blockage, but rather by the leakage flow that is directed tangentially. Moreover, the flow near the casing is close to separation due to the flow turning in radial direction. At some point, the incoming flow is deflected and spillage occurs, see figure 6.29b. Subsequently, the flow detaches from the casing and a recirculation zone forms that is quasi-stable, depending on the pressure rise characteristics.

The numerical studies show that both groove locations, inducer and bend region grooves, reduce the blockage in the inducer. However, the bend region grooves used in *g4* lead to an additional reduction of the blockage in their vicinity and upstream near the splitter blade leading edges. This region becomes more and more important towards higher rotational speeds and thus explains the superiority of *g4* at these conditions.

The inducer grooves lead to a weakening and a deflection of the tip vortex and thus shift the vortex interface in streamwise direction. Consequently, the *g2* configuration achieves significant improvements at subsonic conditions, similar to *g4*. Nevertheless, the simulations suggest that the additional block-

age reduction with additional bend region grooves seems to be even more effective.

In summary, the respective grooves are most effective if they can directly influence the governing stall mechanisms. Consequently, the groove placement has to be selected accordingly. Tip vortex deflection, leakage flow redistribution and the reduction of blockage are identified to be the main mechanisms that enable a *SMI* with circumferential grooves. Using a combination of inducer and bend region grooves proved to be most effective in this study as the whole considered operating range is improved. Moreover, the author is convinced that these findings on the delay of the specific stall mechanisms are transferable to different compressor designs as well. However, the results confirm once again that a profound knowledge on the specific stalling mechanisms is indispensable for the useful application of casing treatments, just like suggested by Greitzer et al. [65].

7 Performance with Casing Grooves

This chapter analyzes the impact of the casing groove application on the performance of the centrifugal compressor stage in terms of overall efficiency, work input and the resulting total pressure rise. Firstly, the experimental results of the investigated groove configurations are presented and evaluated in comparison to the baseline casing. This is once more subdivided into the different diffuser cases. Thereafter, the results are discussed and compared to the equivalent numerical simulations. Thereupon, conclusions are drawn and – if possible – the respective aerodynamic mechanisms that are responsible for the findings are discussed.

7.1 Vaned Diffuser Measurements

This section presents the measured results for the vaned diffuser configuration. Figure 7.1 depicts the isentropic efficiency for the different configurations within the tested operating range. A general increase in efficiency for the grooved configurations is observed for all speeds. A more detailed evaluation relative to the *sc* variant is given in figure 7.2, presenting the maximum and the mean differences in absolute efficiency points.

To calculate those values, the speedlines are clipped to joint ranges which neglect the values near choke that would falsify the results. The respective mass-flow ranges are given in the corresponding table. Then, a linear interpolation is performed to obtain comparable speedlines, whereby $\max \Delta\eta$ represents the maximum absolute difference in efficiency of those speedlines. The mean difference is then calculated by a least square approach, which searches for the shift in efficiency that yields the best fit to the *sc* configuration, considering the given range.

The mean results show an improved efficiency for both configurations at every speedline. The *g2* configuration offers an almost constant mean increase of 0.5%, except for the maximum speed, where no significant change is observed. Contrary to this, a mean improvement of 0.4% is measured at this speedline for *g4*. However, the *g4* improvements at lower speeds do not reach the values of *g2*. The maximum values for both configurations are even higher, reaching over 1.0% at some points.

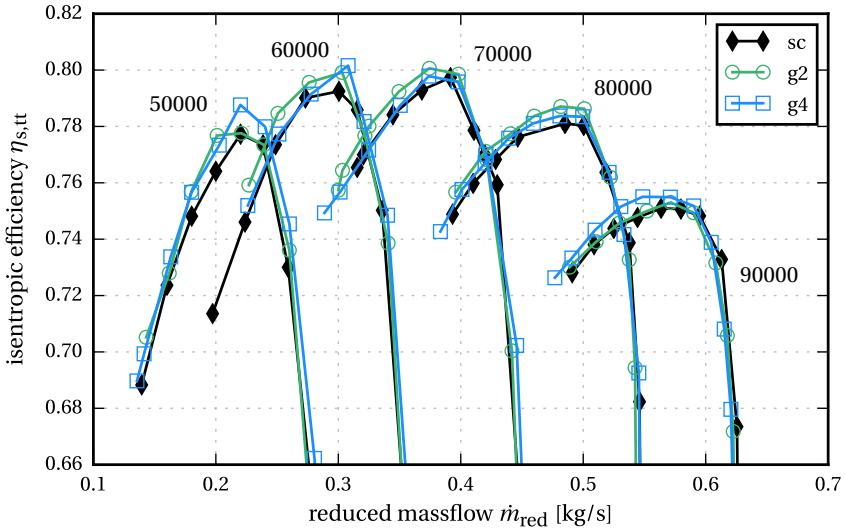


Figure 7.1 – Measured isentropic efficiency with the vaned diffuser for the different operating speeds

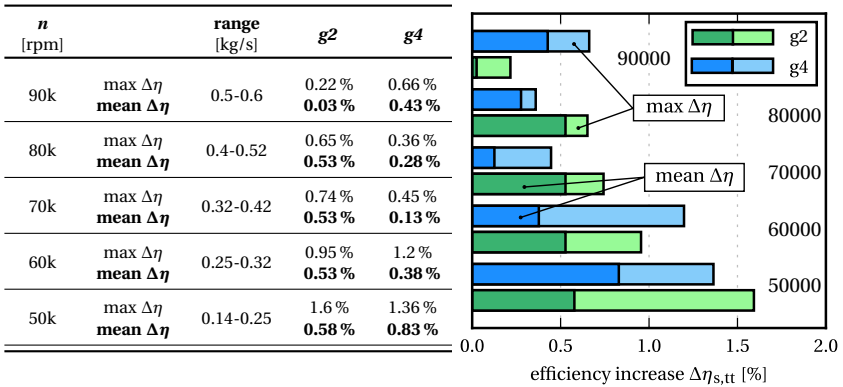


Figure 7.2 – Mean and maximum efficiency change of $g2$ and $g4$ for the different speedlines with the vaned diffuser – absolute percentage points given with respect to sc

The measured performance map has already been introduced in the previous chapter in figure 6.4. At low speeds the total pressure rise remains almost unaffected by the groove application. No significant changes are observed for the overall measurements. Towards higher speeds, the pressure rise deteriorates for the *g4* configuration and at 90 krpm also for *g2*. This is contradictory to the design study results, which predict an increase, particularly at high speeds. This may be due to the fact, that only static pressures are measured

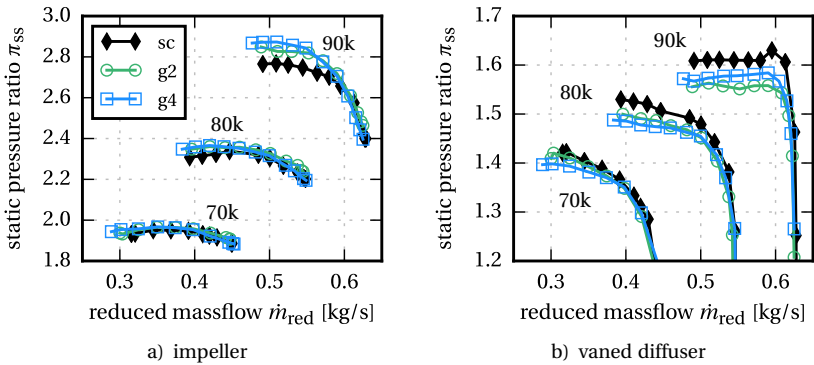


Figure 7.3 – Component static pressure ratios for the vaned diffuser configuration – impeller: p_{12}/p_{in} ; diffuser: p_{22}/p_{12}

at the test rig. Effectively, this reduces the experimental information to static pressure comparisons, as the total pressures are calculated on the basis of the conservation of mass. Moreover, the validation (section 4.4) showed that large scale flow separations occur in the vaned diffuser at these operating conditions. Figure 7.3 introduces the static pressure rise for the individual components, based on the circumferentially averaged pressure taps, for the transonic speedlines. Both groove variants show a significantly increased static pressure rise within the impeller, in comparison to the smooth casing, see figure 7.3a.

However, these benefits are lost in the diffuser, where the diffusion is significantly reduced. This suggests that the flow to the diffuser is changed for the grooved cases, as its pressure rise characteristic clearly changes. A plausible theory, which is supported by the RANS design study results in section 5.3, is that the work input and thus the flow turning in the impeller near tip region is increased. Furthermore, the blockage is reduced, which in combination leads

to increased diffusion and thus higher static pressures at the impeller outlet. Consequently, the outflow angles increase, which results in an increased incidence to the diffuser blades and thus explains the decline of the pressure rise in figure 7.3b.

However, the specific cause could not be identified from the measured data. Nevertheless, this shows that the vaned diffuser dominates the overall results and that the grooves may actually increase the overall pressure rise, if the diffuser is adapted accordingly to the flow conditions.

In addition, a reduction of the choke flow rates is observed for the transonic speedlines. More precisely, the reduced massflows are 0.7% lower for the grooved configurations at 90 krpm. The limit is imposed by the vaned diffuser, which is choking at this operating condition. Therefore, this supports the aforementioned theory, as the choke flow rate depends on the effective flow area, which in turn depends on the diffuser inflow angles. Again, this could be adjusted in the design if the diffuser is matched to the respective outflow conditions. Further discussion on the mechanisms is given in the following sections.

7.2 Vaneless Diffuser Measurements

The measured efficiencies with the vaneless diffuser and the corresponding evaluation are shown in the figures 7.4 and 7.5. The evaluation is performed according to the vaned diffuser results. In general, very similar results are obtained. Again, both groove configurations do not deteriorate the efficiency but lead to improvements for the whole map. Just as for the vaned case, $g2$ shows higher values than $g4$ for most speedlines except for 90 krpm.

The improvements are mainly observed around the peak efficiency flow rates, whereas the impact towards lower flow rates is negligible. This becomes also apparent from the maximum improvements in figure 7.5, which are significantly higher than the calculated mean values. The $g2$ configuration again reaches well above 1%, whereas around 0.5% are detected for $g4$.

The overall performance map for the vaneless case is shown in figure 6.7 in the previous chapter. In contrast to the vaned diffuser case, the overall pressure ratio is improved or at least maintained for all speeds. Again, the differences become most prominent at the maximum speed, where a clear improvement is observed for the $g4$ configuration and also, but less pronounced, for $g2$. This

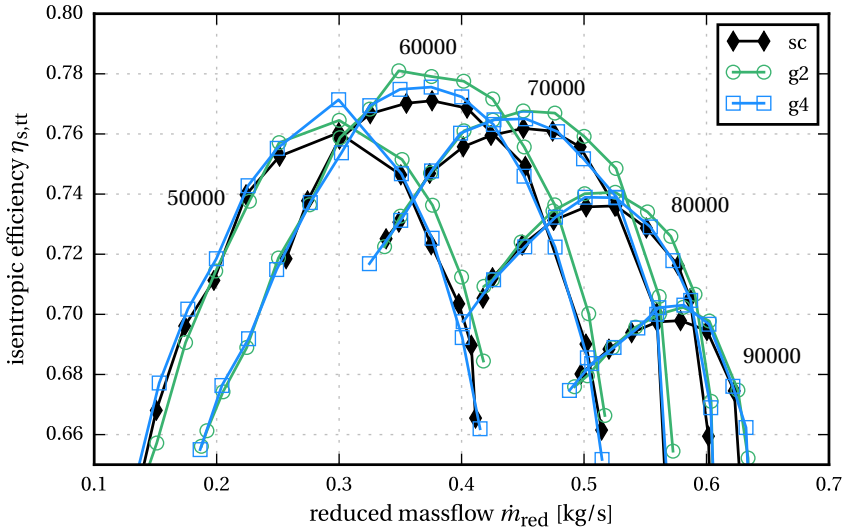


Figure 7.4 – Measured isentropic efficiency with the vaneless diffuser for the different operating speeds

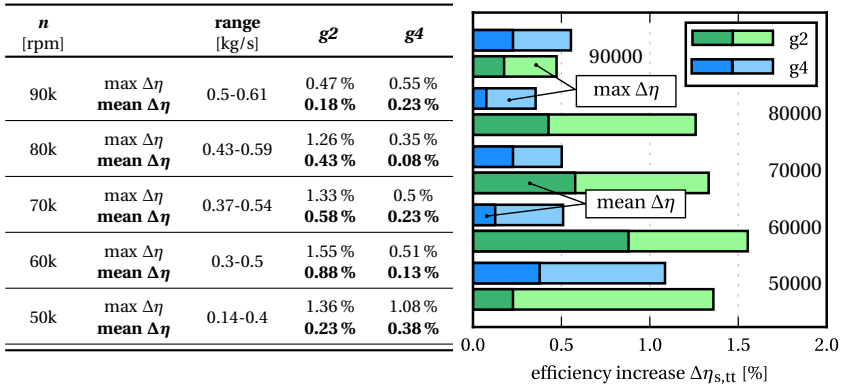


Figure 7.5 – Mean and maximum efficiency change of *g2* and *g4* for the different speedlines with the vaneless diffuser – absolute percentage points given with respect to *sc*

matches the expectations from the design study, where comparable improvements are found.

Figure 7.6 depicts the static pressure rise curves broken down to the individual components, based on the pressure tap measurements. The vaneless diffuser pressure ratio declines for the grooved cases, whereas increased values are observed for the impeller, just like for the vaned diffuser case. This supports the assumption of increased flow turning and reduced blockage in the impeller. For the vaneless diffuser, this results in longer flow paths that in turn lead to thicker boundary layers. This reduces the effective flow area in the diffuser and accordingly its diffusion capability.

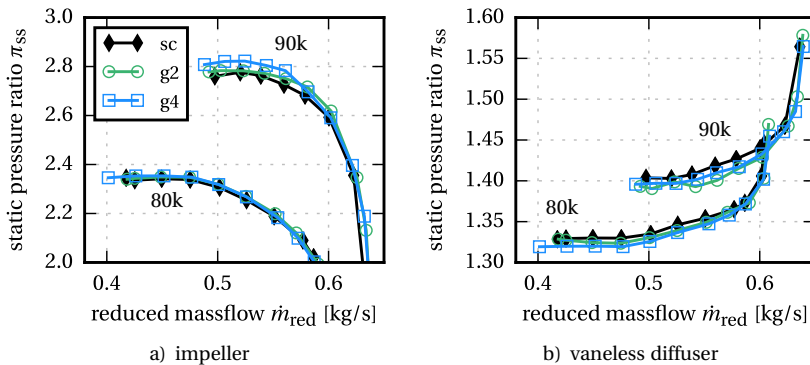


Figure 7.6 – Component static pressure ratios for the vaneless diffuser configuration – impeller: p_{12}/p_{in} ; diffuser: p_{22}/p_{12}

In contrast to the vaned diffuser, an increase in the choke margin is observed for the vaneless case from 70 krpm to 90 krpm. As the vaneless configuration provides a higher cross section area for the flow, the choke location is shifted to the impeller, whereby it has to be noted that the vaneless diffuser is not matched to the stage design. This reversed trend shows that the groove application leads to an increase of the effective flow area, which once again suggests a reduction of blockage in the near tip region. Further analysis on this topic is provided in section 7.3.2.

7.3 Mechanisms and Discussion

This section discusses the measured results and provides further analysis by means of the corresponding numerical simulations. On the one hand, the agreement of the simulations and the mechanisms identified in the design study are assessed. On the other, the available data is used to narrow down and to further evaluate these mechanisms.

7.3.1 Influence on Efficiency and Work Input

The measurements show that both groove configurations lead to an increase in efficiency for almost the complete operating map, whereby this is independent of the diffuser that is used. The measured improvements are well above the uncertainty ranges found in the reproducibility study in section 3.2.4. Moreover, clear trends are found for all respective speedlines. Both points strongly support the credibility of the measured results, at least on a relative scale compared to the baseline design. Besides that, no clear trend that would correlate the efficiency to the operating speed is observed. Furthermore, an increase in total pressure ratio is found in the experiments towards high rotational speeds — at least directly for the vaneless diffuser configuration. The total pressure rise is directly depending on the work input and the efficiency of the change of state. As the overall efficiency is improved for almost the complete map, both of them seem to be affected by the application of the grooves.

In general, the implementation of grooves introduces additional wetted surfaces on the inner groove sides, compared to the smooth casing. This increases the friction losses at the shroud, due to the higher shroud surface area. These losses scale with the compressor speed, as the casing flow speed and thus the groove flow speed are mainly defined by the local tip blade speed.

Figure 7.7 depicts the averaged torque that acts on the impeller cas-

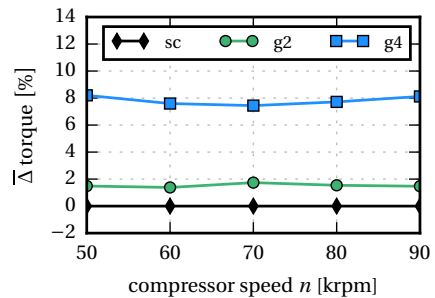


Figure 7.7 – Speedline averaged relative casing torque extracted from the RANS calculations with the vaned diffuser – includes shroud and groove surfaces

ing with respect to the smooth casing. The averaging is performed for each speedline by linear interpolation on a standardized vector that represents the specific operating range. This is equivalent to the shroud friction losses, as the torque on the casing results purely from the aerodynamic shear stresses due to the boundary layers.

Both grooved configurations show a nearly constant relative increase for the different rotational speeds. Thereby, much higher values are reached by $g4$ due to the additional grooves and the increased blade speeds at the bend groove locations.

From this it can be concluded that the positive effects on the flow need to overcompensate these increased friction losses to achieve an overall efficiency improvement. The previously presented CFD results suggest that the tip vortex weakening and its deflection lead to a reduction of mixing losses near the tip. The blockage is reduced and thus a more even flow distribution is generated.

As a result, the entropy production in the near tip region, that mainly results from the mixing of the tip vortex with the core flow, is significantly reduced. This is indicated in the previously depicted figures 5.14 and 6.10. Moreover, an improved flow to the splitter blade is found at high speeds, see section 5.3.

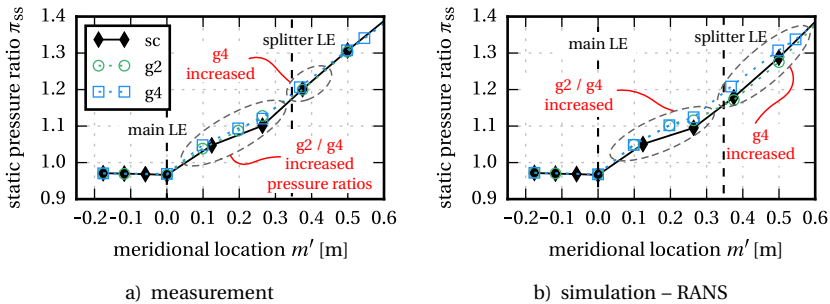


Figure 7.8 – Impeller casing pressure ratios for the different configurations at 70 000 rpm and 0.375 kg/s

This reduction of blockage in the vicinity of the grooves (inducer and bend) is clearly perceptible in the measured casing pressures in this region. These are depicted in figure 7.8a, whereas the corresponding CFD results are plotted in figure 7.8b. An exemplary operating point at 70 krpm and 0.375 kg/s is selected but similar results are found for the whole map, independently of the

diffuser. Both groove configurations show an increase of the static pressure in the inducer up to the splitter blade, whereas only *g4* shows increased values in the bend region. This trend is also very similarly found in the calculations. This once more indicates that the blockage in the measurements is reduced, just as in the calculations. Moreover, it confirms the aforementioned key mechanisms that are identified in the design study in section 5.3.

In contrast to the measurements, the RANS calculations predict a scaling of the groove impact on the impeller efficiency with the compressor speed. This becomes particularly evident in figure 7.9b, which shows the averaged efficiency change for each speedline with respect to the smooth casing for the vaneless diffuser. The averaging is again performed linearly for each speedline in the specific range. The full RANS based efficiency maps are given in figures D.1 and D.2 in the appendix. Only the high speeds offer an

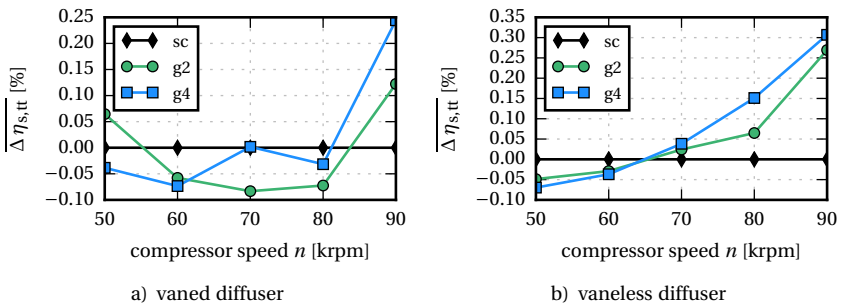


Figure 7.9 – Averaged impact on impeller efficiency for the different operating speeds – extracted from the full stage RANS calculations

overall increase in efficiency with a similar magnitude as the measurements. The calculations with the vaned diffuser in figure 7.9a however, only show an improvement for 90 krpm, whereas small reductions are predicted for the other speeds. It is assumed that this different trend is due to the interaction with the vaned diffuser, but no clear mechanism was found.

Assessing the vaneless case that is not obstructed by the diffuser, somewhat opposing trends are found for simulation and experiment. The simulations reveal only small changes at lower speeds, whereas the measurements provide significant improvements, in particular for the *g2* case (compare to mean values in figure 7.5).

To further assess the numerical model, figure 7.10 plots additional URANS results for operating points near stall and near peak efficiency at 70krpm, whereby an averaged value of one full rotor revolution is used. The discrepancies in efficiency are below 0.2% for the different configurations, again indicating that the efficiency remains almost constant at this speed. Moreover, only marginal differences are found in comparison to the RANS results. Therefore, it can be deduced that the simplifications, which are made in the RANS models compared to the URANS models, are not the cause for the discrepancies in efficiency compared to the experiments.

The measurements furthermore show an increase of the impeller static pressure rise for *g2* and *g4* towards high rotational speeds, independently of the diffuser that is applied. This increased diffusion supports the findings of blockage reduction in the impeller passages. Additionally, this suggests that the work input and thus the flow turning could be affected, just as indicated in the design study.

Figure 7.11 presents the impeller static pressure rise characteristics based on the RANS simulations, corresponding to the experimental results in figure 7.6a. The same trends as for the experiments are found here, as both grooved configurations show an increase in the impeller, in particular at maximum speed. Moreover, *g4* mostly shows higher values than *g2*, which also complies with the experiments.

The CFD simulations suggest that this is not only caused by the improved efficiency but that the work input is also increased. This is demonstrated by the averaged changes in the work coefficient λ displayed in figure 7.12.

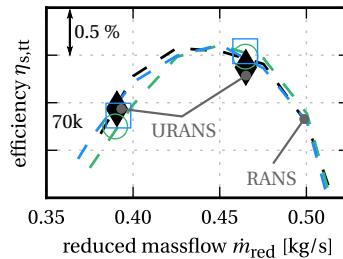


Figure 7.10 – URANS and RANS impeller efficiencies for the different configurations with the vaneless diffuser at 70 000 rpm

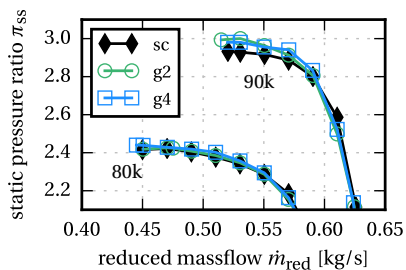


Figure 7.11 – RANS based impeller static pressure ratio with the vaneless diffuser

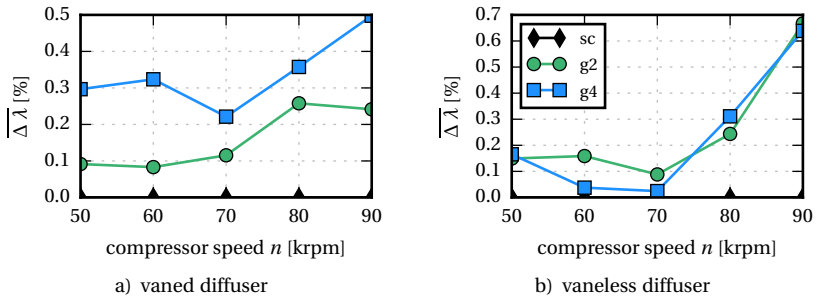


Figure 7.12 – Averaged impact on the impeller work coefficient λ for the different operating speeds based on the *sc* configuration – results extracted from the full stage RANS calculations

Consistent with the efficiency, each data point represents the average change compared to the smooth casing variant for a whole speedline. Just as before, the increase scales roughly with the rotational speed for the higher speeds, with the maximum values being present at top speed. Moreover, enhanced values are found for all speeds in comparison to the baseline design. This in turn means that the flow turning in the impeller has to be increased for the whole operating range.

Figure 7.13 presents the radial velocity at the impeller outlet, which is an adequate measure for the flow rate distribution, alongside the corresponding massflow averaged flow angles. An exemplary operating point at 90 krpm and peak effi-

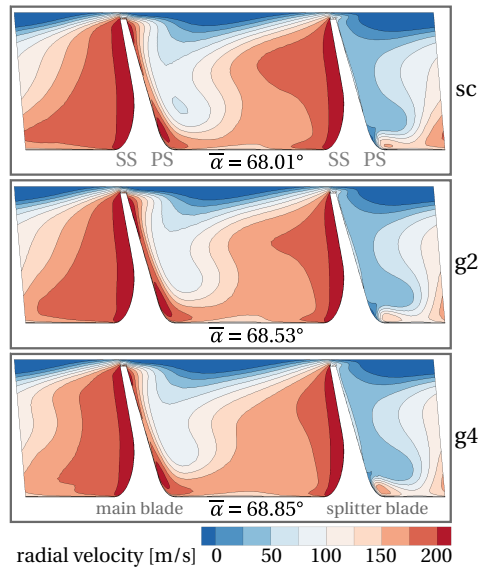


Figure 7.13 – Radial velocity distribution and massflow-averaged absolute flow angles α at the impeller outlet for the vaneless diffuser at 90 000 rpm and peak efficiency (0.57 kg/s)

ciency is selected. Significantly increased mean flow angles are found for both grooved cases, whereby $g4$ ($+0.85^\circ$) yields an even higher outflow angle than $g2$ ($+0.52^\circ$). This can also be traced back to the general groove mechanisms that are described in section 5.3, which mainly affect the flow in the vicinity of the grooves but also lead to a more homogenous flow field at the impeller outlet. The typical jet-wake characteristic (see section 2.1) remains, but its markedness is significantly alleviated by the blockage reduction and the flow redistribution. The regions of high velocity on the blade suction sides, where most flow is concentrated, are clearly reduced in figure 7.13. Moreover, the gradients are less strong, which is indicated by the increased distances of the selected isolines. Thus, a more homogeneous flow distribution is achieved, which enables reduced throughflow velocities and thus increased flow turning.

This effect also explains the λ -scaling with the compressor speed, as the strength and extend of the jet-wake flow and its underlying effects (secondary and leakage flows) also scale with the speed. Naturally, the impeller loading which provides the work input for the increased flow turning and diffusion is affected as well.

The corresponding pressure distribution around the blades, based on the inlet pressure at 85 % span, is plotted in figure 7.14. Whereas only minor changes are observed for the main blade in figure 7.14a, substantial differences are found for the splitter blade, see figure 7.14b. A significant increase of the loading in the front part up to $m' = 60\%$ is observed, whereby $g4$ again is improved in comparison to $g2$. In particular, the pressure side and the near LE

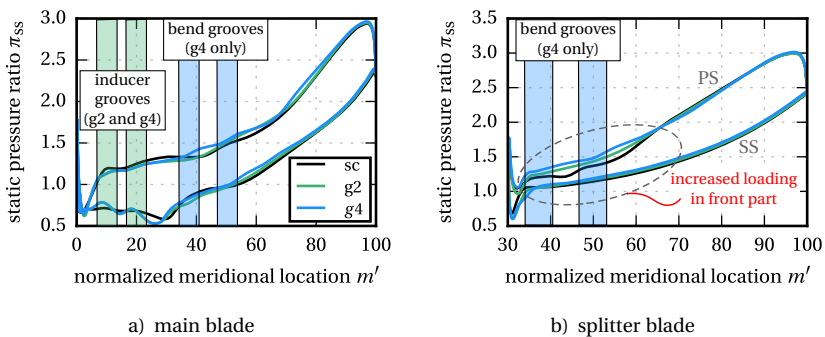


Figure 7.14 – Impeller blade loading at 85 % span for the peak efficiency operating point at at 90 000 rpm and 0.57 kg/s with the vaneless diffuser

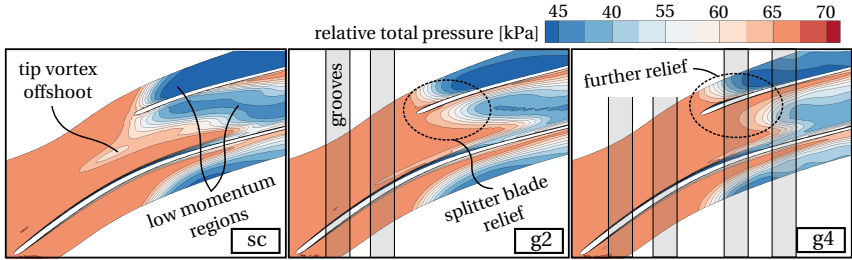


Figure 7.15 – Near tip relative total pressure field at 85 % span for the different cases with the vaneless diffuser at 90 000 rpm and peak efficiency (0.57 kg/s)

suction side distributions are affected. The responsible flow mechanisms are the same as discussed in the previous chapters. The suppression of backflows and splitter blade LE separations lead to a reduction of blockage and thus improved work input in this region, see flow mechanisms in section 5.3.

This is additionally depicted in figures 7.15 and 7.16, which demonstrate the flow changes near the splitter blade. Whereas the low momentum regions at this spanwise position still stretch up to the splitter blade LE for the baseline case, the front part is clearly less affected for the grooved cases. This is apparent in figure 7.15, showing the relative total pressure distribution on the corresponding constant span plane. Again, the inducer grooves weaken and redistribute the tip vortex and thus remove the vortex offshoots that are still present for *sc*. The bend region grooves in *g4* further reduce and push back the low momentum regions, which explains the increased loading in the front part, especially at the PS.

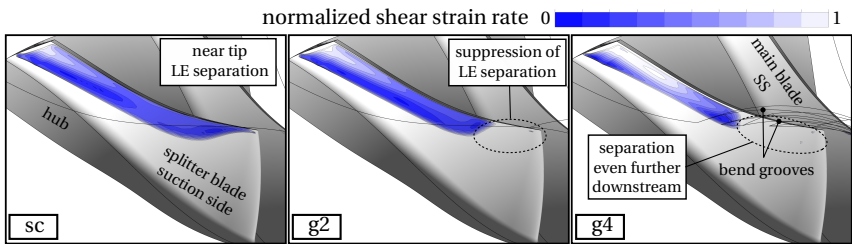


Figure 7.16 – Shear strain rate on the splitter blade suction side for the different cases with the vaneless diffuser at 90 000 rpm and peak efficiency (0.57 kg/s)

Furthermore, the splitter SS is also less affected, as the flow spillage at the LE is suppressed. As a result, the detachment of the flow from the suction side, which forms a major part of the wake region (see figure 7.13), is shifted further downstream. This becomes clear from the normalized shear strain rate contour in figure 7.16, whereby values close to zero correspond to a flow separation from the respective surfaces. For the smooth casing, the separation starts directly at the LE near the tip, whereas this is considerably delayed for the grooved cases. This again emphasizes the importance of the altered flow interaction with the splitter blade, which is responsible for major parts of the work input and efficiency improvements.

Based on the simulations, the following conclusions can be drawn for the groove impact on work input and efficiency. The increase in pressure rise, that is found in the experiments towards high speeds, is accordingly predicted by the simulations. These suggest that the flow mechanisms that are enabled by the grooves increase the work input to the fluid and also the efficiency of the change of state. This is connected to the reduction of blockage, which is accordingly found in the static pressure tap values of the experiments. The simulations moreover indicate that both effects scale with the compressor speed, which physically makes sense given that the strength of the leakage and secondary flows reduce with reducing speed as well.

However, these trends are not found in the efficiency measurements, where clear improvements for all speeds are observed. It is therefore assumed that the simulations do not fully capture the groove impact on the complex loss generation mechanisms in the near tip region. Surely, the effects already discussed in the validation section 4.4 are involved, as well as the turbulence modeling, the surface roughness and the boundary layer development.

Apart from that, the measured results indicate that the g_2 configuration is somewhat superior to g_4 in terms of efficiency. It is likely that this is connected to the higher friction losses in the bend region grooves. This could mean that the positive effects on the flow field are captured in the simulations, but the additional losses associated with the groove surface friction might be overestimated in comparison to the experiments. However, the specific cause could not be identified in this study, which would require much more detailed measurements to resolve the actual flow fields and mechanisms.

All in all, the results show that the application of circumferential grooves, if done correctly, does not deteriorate the compressor performance. On the contrary, the selected cases yield considerable improvements for the efficiency

and the pressure rise for large parts of the operating map. Furthermore, the available data indicates that the already introduced mechanisms of blockage reduction, leakage flow redistribution and tip vortex weakening are once more responsible for these improvements.

7.3.2 Influence on Choke Margin

The measured performance maps indicate that the choke margin is affected by the groove application. A slight decrease is observed for the vaneless diffuser configuration. The maximum flow rate is defined by the effective flow area in the diffuser for these cases. This becomes apparent from figure 4.14e for example, where the pressure drop occurring at the throat is clearly located in the diffuser. Similar results are obtained in the calculations, which also predict a slight reduction at maximum speed, see figure C.2 in the appendix. This can be traced back to a change of the diffuser inlet flow conditions, which reduce the effective flow area. More precisely, the inflow angle resulting of the impeller discharge flow is increased, which is discussed in the previous section, see also figure 7.13. Consequently, the negative influence on the choke margin could be avoided if the diffuser design is adjusted accordingly. Moreover, this once more validates the grooved CFD results with respect to the measurements.

A contrary behavior is observed for the measured data with the vaneless diffuser. The key difference here is that the throat area, which limits the flow rate, is shifted to the impeller. As a result, increased choke flow rates are observed for both, the measurements and the simulations.

Figure 7.17 plots the differences with respect to the baseline casing for the different operating speeds, where the compressor could be driven into clear choke (≥ 70 krpm). The $g2$ value for 70 krpm is missing as the recorded operating point is flawed and does not represent a comparable condition. Nevertheless, the general trends of experiment and CFD match well, despite that lower relative improvements are found for the latter. The $g4$ configuration shows

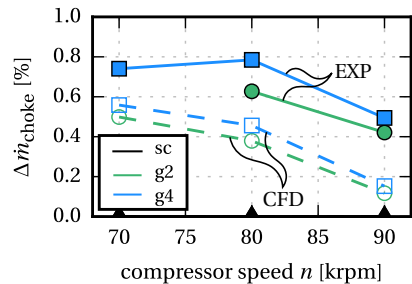


Figure 7.17 – Speed dependent changes of the choke massflow rates for the different cases with the vaneless diffuser

slightly higher choke flow rates than $g2$ for both methods at all speeds. Moreover, a decrease towards maximum speed is observed as well. Again the measured trends for the grooved cases are very well captured in the RANS simulations.

This improvement in the choke margin can again be traced back to the mechanism of blockage reduction in the inducer and bend regions. Moreover, the grooves also increase the geometrical cross section area of the impeller at their respective locations. As the impeller throat is located here, both effects directly affect the effective flow area and therefore increase the maximum flow rate. The simulations indicate that the actual throat, where $M = 1$ is reached, is for the most part located in the inducer. This explains why $g4$ is only marginal superior to $g2$ for the present compressor. However, this clearly depends on the specific compressor and may change for different designs.

In consequence, the results show that circumferential grooves can impact the choke margin up to a certain extent. If choke occurs in the area of influence of the grooves, a slight increase of the maximum flow rate can be achieved for a certain speed. Relative improvements in the range of 0.5 % to 0.8 % were found in the present study with the vaneless diffuser. If choke occurs somewhere else, no interference or even a deterioration has to be expected, depending on the location and the specific groove effects.

8 Summary and Conclusion

The present work investigates the application of circumferential groove casing treatments, which were already known to be effective in axial compressors, to centrifugal compressors. Preferably such grooves would extend the stable operating range without deteriorating the performance or the efficiency of the compressor. Consequently, the main objectives were to show if a stall margin improvement (*SMI*) is achievable and what impact on the compressor characteristics can be expected. Moreover, the related issues of an optimized, effective design and the understanding of the underlying mechanisms were of key interest.

To shed light upon these points a thorough investigation including CFD simulations and experimental studies was performed. Therefore, a state-of-the-art centrifugal compressor and the corresponding test rig, which enabled the investigation of different casing designs, have been built at the ITSM, whereby steady-state as well as time resolved measurement techniques were employed. The modular approach of the test rig furthermore allowed for two different diffuser setups of a vaned and a vaneless type. Additionally, different numerical models were developed to study the corresponding flow fields in detail. These have been validated for the baseline *sc* case, whereby a sufficient accuracy was obtained that qualified the models for further usage.

A preliminary design study using CFD calculations has then been applied to identify the impact of the different design parameters and to obtain optimized configurations for further testing and more detailed investigations. The location, the inclination, and the size of a single groove was varied. Clear trends for all parameters were found, whereby the location had by far the highest impact. An application in the inducer or the bend region proved to be effective in terms of overall efficiency and pressure ratio, whereas locations near the outlet deteriorated the performance. A reduction of the total pressure deficit near the casing was found to be the corresponding flow effect, which moreover indicated a potential *SMI*.

The trends and working mechanisms of the inclination and the size of the groove were found to be independent of the location. Based on the results, high inclination angles of $\gamma \geq 30^\circ$ are suggested. Additionally, a groove width of $b \approx 7\%$ of the unwrapped meridional casing length and an aspect ratio of $t/b \approx 2$ were found to work best. However, the sensitivity of these parameters

was rather low and small adjustments seem to be permissible. Nevertheless, care has to be taken in the design of the grooves as a specific vortex flow pattern inside the grooves should be enabled. The subsequent multiple groove studies revealed that the single groove effects can be superimposed, which confirms the suggestions of various researchers [53, 81, 129, 135] for axial compressors. Design guidelines were derived based on these results and two specific configurations, namely *g2* featuring two inducer grooves and *g4* with two additional grooves in the bend region, were selected for experimental testing, further numerical investigations and a more detailed analysis.

The measured performance maps generally support the findings of the numerical design study. An increase in pressure rise and efficiency was observed for both cases. The *g4* configuration showed improvements in efficiency of up to approximately 0.5 %, independently of the diffuser setup. Even higher values are measured for the *g2* case where maximum values above 1 % and an averaged improvement of about 0.5 % was reached. More importantly, these improvements were obtained in a similar way for the complete operating range, improving the overall efficiency of the compressor. In addition, the investigations showed that the work input and consequently the compressor pressure rise is increased, in particular for high rotational speeds.

In terms of operating range, a considerable *SMI* was observed for both grooved configurations, again independently of the diffuser setup that was used. However, the effectiveness was found to be depending on the compressor speed. Similar results were obtained for subsonic flow conditions, whereas only *g4* achieved improvements at transonic speeds. Typically, the range was extended by about 3 % for these transonic conditions, whereby even higher values were observed at lower speeds. It was shown that this is connected to the general stall mechanisms of the compressor stage, while the near casing flow in the impeller was identified to initiate the instabilities at all speeds. At low speeds, the tip vortex trajectory becomes perpendicular, whereby spillage occurs at the main blades and starts the development of an unstable recirculation zone. At high speeds a flow breakdown due to excessive blockage leads to the spillage that is followed by abrupt surge.

Detailed analyses were then performed to identify and assess the flow mechanisms of the groove application, which confirmed the general findings of the design study. Additionally, CFD simulations towards unstable operation were conducted to understand and further substantiate the experimentally obtained results. In general, the grooves lead to a redistribution of local near tip leakage flows. These mainly enter the specific groove on the blade pressure

sides and are then transported in circumferential direction, whereby the otherwise strong tip leakage flow is weakened. Consequently, grooves placed in the inducer ($g2$) directly affect the evolution of the tip vortex, which is weakened and thus deflected in streamwise direction. In contrast to that, grooves in the bend region (additionally applied in $g4$) reduce the accumulation of low momentum fluid by suppressing local leakage backflows and spillage at the splitter blade. Both effects significantly reduce the near casing blockage that is resulting from these total pressure deficit regions. This has been identified as the major mechanism that is responsible for the improvements.

For the present compressor it was found that the *SMI* at subsonic speeds is achieved by a delay of the spillage due to the deflection of the tip vortex. The blockage reduction in the vicinity of the splitter blade tip delays the flow breakdown and thus the onset of instability at transonic speeds. The simulations towards stall have clearly related this to the reduction in blockage, which thus explains the observed superiority of $g4$ in terms of *SMI*.

The reduction of blockage was also found to be connected to the performance map improvements. The increased efficiencies were caused by a reduction of flow mixing losses that overcompensate the additionally induced surface friction losses in the grooves. This also explained the superiority of $g2$, as the groove friction losses in the inducer are relatively small due to the low blade tip speeds. Furthermore, the near tip splitter blade loading at high speeds is increased as the flow to the blade was not blocked anymore. This increased the work input and thus the pressure ratio.

Conclusion

Based on the objectives of the present work, some main conclusions can be drawn. First of all, the results show that circumferential grooves can effectively be applied in a centrifugal compressor to extend the stable operating range while also improving the overall efficiency. Additionally, the pressure ratio remains unchanged or can even be improved. Moreover, circumferential grooves offer several other benefits compared to currently employed casing treatments (CT), such as reduced size requirements and cheaper production.

Secondly, the effectiveness in terms of *SMI* and also efficiency depends strongly on the groove design, in particular the specific locations. These need to be selected in such a way that the respective stall mechanisms can be influenced by the CT. Therefore, profound knowledge on the stall mechanisms

is required to assess potential benefits, in particular for future applications. In terms of efficiency, the ratio of tip vortex mixing-loss reduction to the increase in surface friction is of key importance. Thus, groove locations towards the inducer seem preferable, as the surface friction losses are strongly depending on the local blade tip speed that increases towards the impeller outlet.

Thirdly, substantial evidence is presented that links the *SMI* and the performance improvements to a reduction of the near casing blockage. Consequently, the groove design should aim at a reduction of this blockage, which is similarly suggested by Houghton [83] for axial compressors. Accordingly, the author is convinced that the presented design guidelines can be similarly applied to other compressors to improve the above-mentioned points, at least for comparable designs. In addition, the results of the present work suggest that the use of steady-state simulations is sufficient for the initial groove design. However, further validation is required at this point.

Significant differences are found for an optimized design in comparison to previous studies in axial compressors, mainly due to the flow turning in radial direction and the presence of splitter blades. Nevertheless, the presented results suggest that the general concepts and working mechanisms of the *SMI* can be transferred for the inducer flow field, which is similar to axial compressors.

Future Work

However, further testing of different groove configurations and far more extensive measurement techniques would be required to further understand and validate the presented mechanisms. Optical, time-resolved measurements, such as PIV (particle image velocimetry), could be an effective method to analyze the governing mechanisms in the near tip regions in detail. In general, testing with larger compressors also would be highly beneficial in this context, due to the improved measurement accuracy and resolution as a result of the much easier accessibility and lower rotational speed. In addition, more advanced, non-rectangular groove shapes could be investigated to further exploit the potential of this kind of casing treatment.

Moreover, the applicability of the casing treatment and the presented design guidelines to other centrifugal compressors should be addressed. Particularly the transferability to similar as well as highly different designs (wide range of design flow coefficients) should be checked and validated. This also involves

the validation of the measured efficiencies. Testing at different facilities, where the compressor is decoupled from heat sources or sinks, such as the oil loop and gearbox in the present work, could yield further improved confidence of the measured values.

Another interesting topic is the matching of the diffuser to the impeller with circumferential grooves. The studies showed that the impeller discharge flow changes, which could potentially yield further efficiency improvements if the diffuser design is adjusted. Consequently, the casing grooves should be included during the design process to achieve the desired component matching.

Bibliography

- [1] Abdelhamid, A.: Effects of Vaneless Diffuser Geometry on Flow Instability in Centrifugal Compression Systems, 81-GT-10, in: Proceedings of ASME 1981 International Gas Turbine Conference and Products Show
- [2] Abdelhamid, A. N.: Analysis of Rotating Stall in Vaneless Diffusers of Centrifugal Compressors, 80-GT-184, in: Proceedings of ASME 1980 International Gas Turbine Conference and Products Show
- [3] Adamczyk, J. J.; Celestina, M. L.; Greitzer, E. M.: The Role of Tip Clearance in High-Speed Fan Stall, *Trans. ASME, J. Turbomach.*, Vol. 115, pp. 28–39, 1993
- [4] Amann, C.; Nordenson, G.; Skellenger, G.: Casing Modification for Increasing the Surge Margin of a Centrifugal Compressor in an Automotive Turbine Engine, *Trans. ASME, J. Eng. Power*, Vol. 97(3), pp. 329–335, 1975
- [5] Bailey, E. E.: Effect of Grooved Casing Treatment on the Flow Range Capability of a Single-Stage Axial-Flow Compressor, Technical Report NASA-TM-X-2459, National Aeronautics and Space Administration, 1972
- [6] Bareiss, S.; Chebli, E.; Vogt, D. M.: Investigation on the Impact of Circumferential Grooves on Aerodynamic Centrifugal Compressor Performance, GT2015-42211, in: Proceedings of ASME Turbo Expo 2015
- [7] Bareiss, S.; Vogt, D. M.: Numerical Investigation on the Design of Circumferential Groove Casing Treatments in a Radial Compressor, ETC2019-038, in: Proceedings of 13th European Conference on Turbomachinery Fluid Dynamics & Thermodynamics, ETC13, 2019
- [8] Beheshti, B. H.; Teixeira, J. A.; Ivey, P. C.; Ghorbanian, K.; Farhanieh, B.: Parametric Study of Tip Clearance – Casing Treatment on Performance and Stability of a Transonic Axial Compressor, *Trans. ASME, J. Turbomach.*, Vol. 126, p. 527-535, 2004
- [9] Berdanier, R. A.; Smith, N. R.; Fabian, J. C.; Key, N. L.: Humidity Effects on Experimental Compressor Performance – Corrected Conditions for Real Gases, *Trans. ASME, J. Turbomach.*, Vol. 137(3), p. 031011, 2015
- [10] Blazek, J.: *Computational Fluid Dynamics: Principles and Applications*, Butterworth-Heinemann, 2015
- [11] Bourgeois, J.; Martinuzzi, R.; Savory, E.; Zhang, C.; Roberts, D.: Assessment of Turbulence Model Predictions for an Aero-Engine Centrifugal Compressor, *Trans. ASME, J. Turbomach.*, Vol. 133, p. 011025, 2011

- [12] Bousquet, Y.; Binder, N.; Dufour, G.; Carbonneau, X.; Roumeas, M.; Trebinjac, I.: Numerical Simulation of Stall Inception Mechanisms in a Centrifugal Compressor with Vaned Diffuser, *Trans. ASME, J. Turbomach.*, Vol. 138(12), p. 121005, 2016
- [13] Bousquet, Y.; Carbonneau, X.; Dufour, G.; Binder, N.; Trebinjac, I.: Analysis of the Unsteady Flow Field in a Centrifugal Compressor from Peak Efficiency to Near Stall with Full-Annulus Simulations, *Int. J. Rotating Machinery*, Vol. 2014, 2014
- [14] Buffaz, N.; Trébinjac, I.: Detailed Analysis of the Flow in the Inducer of a Transonic Centrifugal Compressor, *J. Thermal Science*, Vol. 21(1), pp. 1–12, 2012
- [15] Camp, T. R.; Day, I. J.: A Study of Spike and Modal Stall Phenomena in a Low-Speed Axial Compressor, *Trans. ASME, J. Turbomach.*, Vol. 120, pp. 393–401, 1998
- [16] Carnie, G.; Wang, Y.; Qin, N.; Shahpar, S.: Design Optimisation of Casing Grooves Using the Zipper Layer Meshing Method, GT2011-45483, in: *Proceedings of ASME Turbo Expo 2011*, ASME
- [17] Casey, M. V.: The Effect of Reynolds Number on the Efficiency of Centrifugal Compressor Stages, *Trans. ASME, J. Turbomach.*, Vol. 107, pp. 541–548, 1985
- [18] Casey, M. V.; Dalbert, P.; Roth, P.: The Use of 3D Viscous Flow Calculations in the Design and Analysis of Industrial Centrifugal Compressors, *Trans. ASME, J. Turbomach.*, Vol. 114, pp. 27–37, 1992
- [19] Chen, H.; Lei, V.-M.: Casing Treatment and Inlet Swirl of Centrifugal Compressors, *Trans. ASME, J. Turbomach.*, Vol. 135, 2013
- [20] Chen, X.; Ai, Z.; Ji, Y.; Qin, G.: Numerical Investigation of a Centrifugal Compressor with a Single Circumferential Groove in Different Types of Diffusers, GT2017-63151, in: *Proceedings of ASME Turbo Expo 2017*
- [21] Chen, X.; Qin, G.; Ai, Z.; Ji, Y.: Numerical Analysis of Flow in a Centrifugal Compressor with Circumferential Grooves: Influence of Groove Location and Number on Flow Instability, *IOP Conference Series: Materials Science and Engineering*, Vol. 232, 2017
- [22] Choi, K.-J.; Kim, J.-H.; Kim, K.-Y.: Design Optimization of Circumferential Casing Grooves for a Transonic Axial Compressor to Enhance Stall Margin, GT2010-22396, in: *Proceedings of ASME Turbo Expo 2010*
- [23] Cumpsty, N. A.: *Compressor Aerodynamics*, Krieger Publishing Company, 2004
- [24] Day, I.: Stall Inception in Axial Flow Compressors, *Trans. ASME, J. Turbomach.*, Vol. 115, pp. 1–9, 1993
- [25] Day, I.: Axial Compressor Performance During Surge, *AIAA Journal of Propulsion and Power*, Vol. 10(3), pp. 329–336, 1994

-
- [26] Day, I. J.: Active Suppression of Rotating Stall and Surge in Axial Compressors, *Trans. ASME, J. Turbomach.*, Vol. 115, pp. 40–47, 1993
- [27] Day, I. J.: Stall, Surge, and 75 Years of Research, *Trans. ASME, J. Turbomach.*, Vol. 138(1), p. 011001, 2016
- [28] Dean, R. C.; Senoo, Y.: Rotating Wakes in Vaneless Diffusers, *Trans. ASME, J. Basic Eng.*, Vol. 82, pp. 563–574, 1960
- [29] Deniz, S.; Greitzer, E. M.; Cumpsty, N. A.: Effects of Inlet Flow Field Conditions on the Performance of Centrifugal Compressor Diffusers: Part 2 – Straight-Channel Diffuser, *Trans. ASME, J. Turbomach.*, Vol. 122(1), pp. 11–21, 2000
- [30] Denton, J. D.: Loss Mechanisms in Turbomachines, *Trans. ASME, J. Turbomach.*, Vol. 115(4), pp. 621–656, 1993
- [31] Deppe, A.; Saathoff, H.; Stark, U.: Spike-Type Stall Inception in Axial-Flow Compressors, ETC6 145, in: 6th European Turbomachinery Conference, Fluid Dynamics and Thermodynamics
- [32] Dodds, J.; Vahdati, M.: Rotating Stall Observations in a High Speed Compressor – Part I: Experimental Study, *Trans. ASME, J. Turbomach.*, Vol. 137(5), p. 051002, 2015
- [33] Dodds, J.; Vahdati, M.: Rotating Stall Observations in a High Speed Compressor – Part II: Numerical Study, *Trans. ASME, J. Turbomach.*, Vol. 137(5), p. 051003, 2015
- [34] Du, J.; Li, J.; Gao, L.; Lin, F.; Chen, J.: The Impact of Casing Groove Location on Stall Margin and Tip Clearance Flow in a Low-Speed Axial Compressor, *Trans. ASME, J. Turbomach.*, Vol. 138(12), pp. 121007-1–121007-11, 2016
- [35] Du, J.; Seume, J. R.: Design of Casing Treatment on a Mixed-Flow Compressor, GT2017-65226, in: *Proceedings of ASME Turbo Expo 2017*
- [36] Eckardt, D.: Instantaneous Measurements in the Jet-Wake Discharge Flow of a Centrifugal Compressor Impeller, *Trans. ASME, J. Eng. Power*, Vol. 97(3), pp. 337–345, 1975
- [37] Eckardt, D.: Detailed Flow Investigations Within a High-Speed Centrifugal Compressor Impeller, *Trans. ASME, J. Fluids Eng.*, pp. 390–402, 1976
- [38] Eisenlohr, G.; Dalbert, P.; Krain, H.; Pröll, H.; Richter, F. A.; Rohne, K. H.: Analysis of the Transonic Flow at the Inlet of a High Pressure Ratio Centrifugal Impeller, ASME Paper 98-GT-24, 1998
- [39] Emmons, H. W.; Pearson, C. E.; Grant, H. P.: Compressor Surge and Stall Propagation, *Trans. ASME*, Vol. 77(4), pp. 455–469, 1955
- [40] Everitt, J.; Spakovszky, Z.; Rusch, D.; Schiffmann, J.: The Role of Impeller Outflow Conditions on the Performance of Vaned Diffusers, GT2016-56168, in: *Proceedings of ASME Turbo Expo 2016*

- [41] Everitt, J. N.; Spakovszky, Z. S.: An Investigation of Stall Inception in Centrifugal Compressor Vaned Diffuser, *Trans. ASME, J. Turbomach.*, Vol. 135, 2013
- [42] Eynon, P.; Whitfield, A.; Firth, M.; Parkes, A.; Saxton, R.: A Study of the Flow Characteristics in the Inducer Bleed Slot of a Centrifugal Compressor, 96-GT-262, in: ASME 1996 International Gas Turbine and Aeroengine Congress and Exhibition, American Society of Mechanical Engineers
- [43] Farge, T.; Johnson, M.; Maksoud, T.: Tip Leakage in a Centrifugal Impeller, *Trans. ASME, J. Turbomach.*, Vol. 111(3), pp. 244–249, 1989
- [44] Ferziger, J. H.; Peric, M.: *Computational Methods for Fluid Dynamics*, Springer Science & Business Media, 2012
- [45] Filipenco, V. G.; Deniz, S.; Johnston, J. M.; Greitzer, E. M.; Cumpsty, N. A.: Effects of Inlet Flow Field Conditions on the Performance of Centrifugal Compressor Diffusers: Part 1 – Discrete-Passage Diffuser, *Trans. ASME, J. Turbomach.*, Vol. 122(1), pp. 1–10, 2000
- [46] Fischer, K.; Thoma, D.: Investigation of the Flow Conditions in a Centrifugal Pump, *Trans. ASME*, Vol. 54, pp. 141–155, 1932
- [47] Fisher, E.: Application of Map Width Enhancement Devices to Turbocharger Compressor Stages, *SAE Transactions*, Vol. 97, pp. 1303–1310, 1988
- [48] Frigne, P.; Van Den Braembussche, R.: Distinction Between Different Types of Impeller and Diffuser Rotating Stall in a Centrifugal Compressor with Vaneless Diffuser, *Trans. ASME, J. Eng. Gas Turb. Power*, Vol. 106(2), pp. 468–474, 1984
- [49] Frigne, P.; Van den Braembussche, R.: A Theoretical Model for Rotating Stall in the Vaneless Diffuser of a Centrifugal Compressor, *Trans. ASME, J. Eng. Gas Turb. Power*, Vol. 107(2), pp. 507–513, 1985
- [50] Fujisawa, N.; Ema, D.; Ohta, Y.: Unsteady Behavior of Diffuser Stall in a Centrifugal Compressor With Vaned Diffuser, GT2017-63400, in: *Proceedings of ASME Turbo Expo 2017*
- [51] Fujisawa, N.; Hara, S.; Ohta, Y.: Unsteady Behavior of Leading-Edge Vortex and Diffuser Stall in a Centrifugal Compressor with Vaned Diffuser, *J. Thermal Science*, Vol. 25(1), pp. 13–21, 2016
- [52] Fujisawa, N.; Inui, T.; Ohta, Y.: Evolution Process of Diffuser Stall in a Centrifugal Compressor With Vaned Diffuser, GT2018-75462, in: *Proceedings of ASME Turbo Expo 2018*
- [53] Fujita, H.; Takata, H.: A Study on Configurations of Casing Treatments for Axial Flow Compressors, *Bulletin of JSME*, Vol. 27(230), pp. 1675–1681, 1984
- [54] Furukawa, M.; Inoue, M.; Saiki, K.; Yamada, K.: The Role of Tip Leakage Vortex Breakdown in Compressor Rotor Aerodynamics, *ASME Paper 98-GT-239*, 1998

-
- [55] Furukawa, M.; Saiki, K.; Yamada, K.; Inoue, M.: Unsteady Flow Behavior Due to Breakdown of Tip Leakage Vortex in an Axial Compressor Rotor at Near-Stall Condition, 2000-GT-666, in: Proceedings of ASME Turbo Expo 2000
- [56] Galloway, L.; Rusch, D.; Spence, S.; Vogel, K.; Hunziker, R.; Kim, S. I.: An Investigation of Centrifugal Compressor Stability Enhancement Using a Novel Vaned Diffuser Recirculation Technique, Trans. ASME, J. Turbomach., Vol. 140(12), p. 121009, 2018
- [57] Galloway, L.; Spence, S.; Kim, S. I.; Rusch, D.; Vogel, K.; Hunziker, R.: An Investigation of the Stability Enhancement of a Centrifugal Compressor Stage Using a Porous Throat Diffuser, Trans. ASME, J. Turbomach., Vol. 140(1), p. 011008, 2018
- [58] Gao, P.; Chu, W.; Wu, Y.: The Mechanism of Stall Margin Improvement in a Centrifugal Compressor with the Air Bleeding Circumferential Grooves Casing Treatment, in: New Trends in Fluid Mechanics Research, pp. 482–485, Springer, 2007
- [59] Gao, P.; Zhang, Y.; Zhang, S.: Numerical Investigation of the Different Casing Treatment in a Centrifugal Compressor, in: 2010 Asia-Pacific Conference on Wearable Computing Systems, Shenzhen, China
- [60] Garnier, V. H.; Epstein, A. H.; Greitzer, E. M.: Rotating Waves as a Stall Inception Indication in Axial Compressors, Trans. ASME, J. Turbomach., Vol. 113, pp. 290–302, 1991
- [61] Gibson, L.; Galloway, L.; Kim, S.; Spence, S.: Assessment of Turbulence Model Predictions for a Centrifugal Compressor Simulation, GPPF-2017-0138, in: Proceedings of the 1st Global Power and Propulsion Forum: GPPF 2017, Vol. 1
- [62] Greitzer, E. M.: Surge and Rotating Stall in Axial Flow Compressors – Part I: Theoretical Compression System Model, Trans. ASME, J. Eng. Power, Vol. 98(2), pp. 190–198, 1976
- [63] Greitzer, E. M.: Surge and Rotating Stall in Axial Flow Compressors – Part II: Experimental Results and Comparison with Theory, Trans. ASME, J. Eng. Power, Vol. 98(2), pp. 199–211, 1976
- [64] Greitzer, E. M.: The Stability of Pumping Systems - The 1980 Freeman Scholar Lecture, Journal of Fluids Engineering, Vol. 103(2), pp. 193–242, 1981
- [65] Greitzer, E. M.; Nikkanen, J. P.; Haddad, D. H.; Joslyn, H. D.; Mazzawy, R. S.: A Fundamental Criterion for the Application of Rotor Casing Treatment, Trans. ASME, J. Fluids Eng., Vol. 101, pp. 237–243, 1979
- [66] Greitzer, E. M.; Tan, C. S.; Graf, M. B.: Internal Flow: Concepts and Applications, Cambridge University Press, 2004
- [67] Grieb, H.: Verdichter für Turbo-Flugtriebwerke, Springer, 2009
- [68] Guo, Q.; Chen, H.; Zhu, X.; Du, Z.; Zhao, Y.: Numerical Simulations of Stall inside a Centrifugal Compressor, Proc. Instn. Mech. Engrs., Bd. 221(5), S. 683–693, 2007

- [69] Hah, C.; Bergner, J.; Schiffer, H.-P.: Short Length-Scale Rotating Stall Inception in a Transonic Axial Compressor - Criteria and Mechanisms, GT2006-90045, in: Proceedings of ASME Turbo Expo 2006
- [70] Hah, C.; Krain, H.: Secondary Flows and Vortex Motion in a High-Efficiency Backswept Impeller at Design and Off-Design Conditions, Trans. ASME, J. Turbomach., Vol. 112, pp. 7–13, 1990
- [71] Hah, C.; Mueller, M.; Schiffer, H.-P.: Study of Convective Flow Effects in Endwall Casing Treatments in Transonic Compressor Rotors, GT2012-68411, in: Proceedings of ASME Turbo Expo 2012
- [72] Halawa, T.; Alqaradawi, M.; Gadala, M. S.; Shahin, I.; Badr, O.: Numerical Investigation of Rotating Stall in Centrifugal Compressor with Vaned and Vaneless Diffuser, J. Thermal Science, Vol. 24(4), pp. 323–333, 2015
- [73] Harley, P.; Starke, A.; Bamba, T.; Filsinger, D.: Axial Groove Casing Treatment in an Automotive Turbocharger Centrifugal Compressor, Proc. IMechE, Part C: J. Mech. Engrg. Sci., p. 1-13, 2016
- [74] Hathaway, M. D.: Passive Endwall Treatments for Enhancing Stability, NASA Technical Memorandum, Vol. 214409, 2007
- [75] Haupt, U.; Abdelhamid, A.; Kaemmer, N.; Rautenberg, M.: Excitation of Blade Vibration by Flow Instability in Centrifugal Compressors, 86-GT-283, in: Proceedings of ASME 1986 International Gas Turbine Conference and Exhibit
- [76] Haynes, J. M.; Hendricks, G. J.; Epstein, A. H.: Active Stabilizations of Rotating Stall in a Three-Stage Axial Compressor, Trans. ASME, J. Turbomach., Vol. 116(2), 1994
- [77] Hazby, H. R.; Xu, L.: Role of Tip Leakage in Stall of a Transonic Centrifugal Impeller, GT2009-59372, in: Proceedings of ASME Turbo Expo 2009
- [78] Hembera, M.; Kau, H.-P.; Johann, E.: Simulation of Casing Treatments of a Transonic Compressor Stage, Int. J. Rotating Machinery, 2008
- [79] Hewkin-Smith, M.; Pullan, G.; Grimshaw, S.; Greitzer, E.; Spakovszky, Z.: The Role of Tip Leakage Flow in Spike-Type Rotating Stall Inception, GT2017-63655, in: Proceedings of ASME Turbo Expo 2017
- [80] High-Performance Computing Center Stuttgart: CRAY XC40 - HAZEL HEN System Description, <https://www.hlrs.de/systems/cray-xc40-hazel-hen/>, Accessed: 2019-04-17
- [81] Houghton, T.; Day, I.: Enhancing the Stability of Subsonic Compressors Using Casing Grooves, Trans. ASME, J. Turbomach., Vol. 133(021007), 2011
- [82] Houghton, T.; Day, I.: Stability Enhancement by Casing Grooves: The Importance of Stall Inception Mechanism and Solidity, Trans. ASME, J. Turbomach., Vol. 134(021003), 2012

-
- [83] Houghton, T. O.: Axial Compressor Stability Enhancement, Ph.D. thesis, University of Cambridge, Feb. 2010
- [84] Hoying, D. A.; Tan, C. S.; Vo, H. D.; Greitzer, E. M.: Role of Blade Passage Flow Structures in Axial Compressor Rotating Stall Inception, *Trans. ASME, J. Turbomach.*, Vol. 121(4), pp. 735–742, 1999
- [85] Huang, X.; Chen, H.; Fu, S.: CFD Investigation on the Circumferential Grooves Casing Treatment of Transonic Compressor, GT2008-51107, in: *Proceedings of ASME Turbo Expo 2008*
- [86] Hunziker, R.; Dickmann, H.-P.; Emmrich, R.: Numerical and Experimental Investigation of a Centrifugal Compressor with an Inducer Casing Bleed System, *Proc. Instn. Mech. Engrs.*, Vol. 215(6), p. 783-791, 2001
- [87] Hunziker, R.; Gyarmathy, G.: The Operational Stability of a Centrifugal Compressor and its Dependence on the Characteristics of the Subcomponents, *Trans. ASME, J. Turbomach.*, Vol. 116(2), pp. 250–259, 1994
- [88] Ibaraki, S.; Iwakiri, K.: Vortical Flow Structure and Loss Generation Process in a Transonic Centrifugal Compressor Impeller, GT2007-27791, in: *Proceedings of ASME Turbo Expo 2007*
- [89] Ibaraki, S.; Matsuo, T.; Kuma, H.; Sumida, K.; Suita, T.: Aerodynamics of a Transonic Centrifugal Compressor Impeller, GT2002-30374, in: *Proceedings of ASME Turbo Expo 2002*
- [90] Inoue, M.; Cumpsty, N. A.: Experimental Study of Centrifugal Impeller Discharge Flow in Vaneless and Vaned Diffusers, *Trans. ASME, J. Eng. Gas Turb. Power*, Vol. 106, pp. 455–467, 1984
- [91] Inoue, M.; Kuroumaru, M.; Tanino, T.; Yoshida, S.; Furukawa, M.: Comparative Studies on Short and Long Length-Scale Stall Cell Propagating in an Axial Compressor Rotor, *Trans. ASME, J. Turbomach.*, Vol. 123(1), pp. 24–30, 2001
- [92] Ishida, M.; Sakaguchi, D.; Ueki, H.: Optimization of Inlet Ring Groove Arrangement for Suppression of Unstable Flow in a Centrifugal Impeller, GT2005-68675, in: *Proceedings of ASME Turbo Expo 2005*
- [93] Ishida, M.; Surana, T.; Ueki, H.; Sakaguchi, D.: Suppression of Unstable Flow at Small Flow Rates in a Centrifugal Blower by Controlling Tip Leakage Flow and Reverse Flow, GT2004-53400, in: *Proceedings of ASME Turbo Expo 2004*
- [94] Jansen, W.: Rotating Stall in a Radial Vaneless Diffuser, in: *Trans. ASME*, Vol. 86 of D, pp. 750–758, ASME, Dec. 1964
- [95] Jansen, W.; Carter, A.; Swarden, M.: Improvements in Surge Margin for Centrifugal Compressors, *Centrifugal Compressors, Flow Phenomena and Performance in AGARD Conference Proceedings*, Vol. 282(19), 1980

-
- [96] Japikse, D.: Centrifugal Compressor Design and Performance, Concepts ETI Press, 1996
- [97] Johnson, M. W.; Moore, J.: The Development of Wake Flow in a Centrifugal Impeller, Trans. ASME, J. Eng. Power, Vol. 106, pp. 382–389, 1980
- [98] Johnson, M. W.; Moore, J.: The Influence of Flow Rate on the Wake in a Centrifugal Impeller, Trans. ASME, J. Eng. Power, Vol. 105, pp. 33–39, 1983
- [99] Kämmer, N.; Rautenberg, M.: A Distinction Between Different Types of Stall in a Centrifugal Compressor Stage, Trans. ASME, J. Eng. Gas Turb. Power, Vol. 108(1), pp. 83–92, 1986
- [100] Kempter, D.: Numerische Untersuchung zum Einfluss von Vereinfachungen von Geometrie und Modellierung eines Radialverdichters mit Umfangsnuten, Studienarbeit, Institute of Thermal Turbomachinery and Machinery Laboratory (ITSM), University of Stuttgart, Sept. 2015
- [101] Kim, J.; Choi, K.; Kim, K.: Performance Evaluation of a Transonic Axial Compressor with Circumferential Casing Grooves, Proc. IMechE, Part A: J. Power and Energy, Bd. 226(2), S. 218–230, 2012
- [102] Kim, J.-H.; Choi, K.-J.; Kim, K.-Y.: Aerodynamic Analysis and Optimization of a Transonic Axial Compressor with Casing Grooves to Improve Operating Stability, Aerospace Science and Technology, Bd. 29(1), S. 81–91, 2013
- [103] Kim, S.; Pullan, G.; Hall, C.; Grewe, R.; Wilson, M.; Gunn, E.: Stall Inception in Low Pressure Ratio Fans, GT2018-75153, in: Proceedings of ASME Turbo Expo 2018
- [104] Koyyalamudi, V.; Nagpurwala, Q.: Stall Margin Improvement in a Centrifugal Compressor through Inducer Casing Treatment, Int. J. Rotating Machinery, Bd. 2016, S. 1-19, 2016
- [105] Krain, H.: Secondary Flow Measurements with L2F-Technique in Centrifugal Compressors, AGARD CP-421, pp. (34-1)–(34-10), 1987
- [106] Lawless, P.; Fleeter, S.: Rotating Stall Acoustic Signature in a Low-Speed Centrifugal Compressor: Part 1 – Vaneless Diffuser, Trans. ASME, J. Turbomach., Vol. 117(1), pp. 87–96, 1995
- [107] Lawless, P. B.; Fleeter, S.: Rotating Stall Acoustic Signature in a Low Speed Centrifugal Compressor: Part 2 – Vaned Diffuser, 93-GT-254, in: Proceedings of ASME 1993 International Gas Turbine Conference and Exhibit
- [108] Legras, G.; Gourdain, N.; Trébinjac, I.; Ottavy, X.: Analysis of Unsteadiness on Casing Treatment Mechanisms in an Axial Compressor, GT2011-45806, in: Proceedings of ASME Turbo Expo 2011
- [109] Legras, G.; Trébinjac, I.; Gourdain, N.; Ottavy, X.; Castillon, L.: A Novel Approach to Evaluate the Benefits of Casing Treatment in Axial Compressors, Int. J. Rotating Machinery, Vol. 2012, 2012

-
- [110] Lemmon, E. W.; Huber, M. L.; McLinden, M. O.: NIST Standard Reference Database 23: Reference Fluid Thermodynamic and Transport Properties-REFPROP, Version 9.1, National Institute of Standards and Technology, 2013
- [111] Lou, E.; Fabian, J. C.; Key, N. L.: Stall Inception in a High-Speed Centrifugal Compressor During Speed Transients, *Trans. ASME, J. Turbomach.*, Vol. 139(12), p. 121004, 2017
- [112] Lu, X.; Chu, W.; Zhu, J.: Mechanism of the Interaction between Casing Treatment and Tip Leakage Flow in a Subsonic Axial Compressor, GT2006-90077, in: *Proceedings of ASME Turbo Expo 2006*
- [113] Mao, X.; Liu, B.; Zhao, H.: Numerical Analysis of the Circumferential Grooves Casing Treatment in a Counter-Rotating Axial Flow Compressor, *Applied Thermal Engineering*, Vol. 130, pp. 29–39, 2018
- [114] Marble, F. E.: Propagation of Stall in a Compressor Blade Row, *Journal of the Aeronautical Science*, Vol. 22, pp. 541–554, 1955
- [115] McDougall, N. M.; Cumpsty, N. A.; Hynes, T. P.: Stall Inception in Axial Compressors, *Trans. ASME, J. Turbomach.*, Vol. 112, pp. 116–125, 1990
- [116] Menter, F. R.; Kuntz, M.; Langtry, R.: Ten Years of Industrial Experience with the SST Turbulence Model, *Int. Communications in Heat and Mass Transfer*, Vol. 4, 2003
- [117] Mileshin, V.; Brailko, I.; Startsev, A.: Application of Casing Circumferential Grooves to Counteract the Influence of Tip Clearance, GT2008-51147, in: *Proceedings of ASME Turbo Expo 2008*
- [118] Mirzabozorg, M. A. S.; Bazazzadeh, M.; Hamzezhade, M.: Numerical Study on the Effect of Single Shallow Circumferential Groove Casing Treatment on the Flow Field and the Stability of a Transonic Compressor, *Journal of Applied Fluid Mechanics*, Vol. 10(1), pp. 257–265, 2017
- [119] Mizuki, S.; Oosawa, Y.: Unsteady Flow within Centrifugal Compressor Channels under Rotating Stall and Surge, *Trans. ASME, J. Turbomach.*, Vol. 114(2), pp. 312–320, 1992
- [120] Moore, F. K.; Greitzer, E. M.: A Theory of Post-Stall Transients in Axial Compression Systems: Part I - Development of Equations, *Trans. ASME, J. Eng. Gas Turb. Power*, Vol. 108(1), 1986
- [121] Müller, M. W.: Untersuchungen zum Einfluss von Gehäusestrukturierungen auf die Stabilität und die Leistungsdaten eines transsonischen Axialverdichters, *Dissertation, Technische Universität Darmstadt*, 2011
- [122] Müller, M. W.; Biela, C.; Schiffer, H.-P.; Hah, C.: Interaction of Rotor and Casing Treatment Flow in an Axial Single-Stage Transonic Compressor with Circumferential Grooves, GT2008-50135, in: *Proceedings of ASME Turbo Expo 2008*

-
- [123] Müller, M. W.; Schiffer, H.-P.; Hah, C.: Effect of Circumferential Grooves on the Aerodynamic Performance of an Axial Single-Stage Transonic Compressor, GT2007-27365, in: Proceedings of ASME Turbo Expo 2007
- [124] Nan, X.; Lin, F.; Wang, S.; Liu, L.; Ma, N.; Chen, J.: The Analysis of Axial Momentum of the Rotor Tip Flows for Axial Compressors With Circumferential Grooves, GT2014-26495, in: Proceedings of ASME Turbo Expo 2014
- [125] Nezym, V. Y.: Development of New Casing Treatment Configuration, JSME Int. J., Vol. 47(4), pp. 804–812, 2004
- [126] Nitsche, W.; Brunn, A.: Strömungsmesstechnik, Springer, 2006
- [127] Paduano, J.; Epstein, A.; Valavani, L.; Longley, J.; Greitzer, E.; Guenette, G.: Active Control of Rotating Stall in a Low Speed Axial Compressor, 91-GT-088, in: Proceedings of ASME 1991 International Gas Turbine Conference and Exhibit
- [128] Paduano, J.; Greitzer, E.; Epstein, A.: Compression System Stability and Active Control, Annual Review of Fluid Mechanics, Bd. 33(1), S. 491–517, 2001
- [129] Perrot, V.; Touyeras, A.; Lucien, G.: Detailed CFD Analysis of a Grooved Casing Treatment on an Axial Subsonic Compressor, ETC7 16, in: 7th European Turbomachinery Conference
- [130] Prince, D. C. J.; Wisler, D. C.; Hilvers, D. E.: Study of Casing Treatment: Stall Margin Improvement Phenomena, Tech. Rep. CR-134552, GE R73AEG326, NASA, March 1974
- [131] Pullan, G.; Young, A.; Day, I.; Greitzer, E.; Spakovszky, Z.: Origins and Structure of Spike-Type Rotating Stall, Trans. ASME, J. Turbomach., Vol. 137, 2015
- [132] Qiang, X.-Q.; Zhu, M.-M.; Teng, J.-F.: Effect of Circumferential Grooves Casing Treatment on Tip Leakage Flow and Loss in a Transonic Mixed-Flow Compressor, Journal of Theoretical and Applied Mechanics, Vol. 51, 2013
- [133] Rabe, D. C.; Hah, C.: Application of Casing Circumferential Grooves for Improved Stall Margin in a Transonic Axial Compressor, GT2002-30641, in: Proceedings of ASME Turbo Expo 2002
- [134] Rolfes, M.; Lange, M.; Vogeler, K.; Mailach, R.: Experimental and Numerical Investigation of a Circumferential Groove Casing Treatment in a Low-Speed Axial Research Compressor at Different Tip Clearances, Trans. ASME, J. Turbomach., Vol. 139(12), p. 121009, 2017
- [135] Ross, M. H.; Cameron, J. D.; Morris, S. C.; Chen, H.; Shi, K.: Axial Compressor Stall, Circumferential Groove Casing Treatment, and the Tip-Clearance Momentum Flux, AIAA Journal of Propulsion and Power, Vol. 34(1), pp. 146–152, 2018
- [136] Sakuma, Y.; Watanabe, T.; Himeno, T.; Kato, D.; Murooka, T.; Shuto, Y.: Numerical Analysis of Flow in a Transonic Compressor With a Single Circumferential Casing Groove: Influence of Groove Location and Depth on Flow Instability, Trans. ASME, J. Turbomach., Vol. 136(3), pp. 031017–031017-9, 2014

-
- [137] Schaefer, S.: Numerische Untersuchung der Betriebsgrenzen eines Radialverdichters mit Casing Grooves, Masterarbeit, Institute of Thermal Turbomachinery and Machinery Laboratory (ITSM), University of Stuttgart, Jan. 2018
- [138] Schlechtriem, S.; Lötzerich, M.: Breakdown of Tip Leakage Vortices in Compressor at Flow Conditions Close to Stall, ASME Paper 97-GT-41, 1997
- [139] Schleer, M.; Abhari, R. S.: Clearance Effects on the Evolution of the Flow in the Vaneless Diffuser of a Centrifugal Compressor at Part Load Condition, Trans. ASME, J. Turbomach., Vol. 130(3), p. 031009, 2008
- [140] Schleer, M.; Song, S. J.; Abhari, R. S.: Clearance Effects on the Onset of Instability in a Centrifugal Compressor, Trans. ASME, J. Turbomach., Vol. 130(3), p. 031002, 2008
- [141] Senoo, Y.; Kinoshita, Y.: Limits of Rotating Stall and Stall in Vaneless Diffuser of Centrifugal Compressors, 78-GT-19, in: Proceedings of ASME 1978 International Gas Turbine Conference and Products Show
- [142] Senoo, Y.; Kinoshita, Y.; Ishida, M.: Asymmetric Flow in Vaneless Diffusers of Centrifugal Blowers, Trans. ASME, J. Fluids Eng., Vol. 99(1), pp. 104–111, 1977
- [143] Shabbir, A.; Adamczyk, J. J.: Flow Mechanism for Stall Margin Improvement due to Circumferential Casing Grooves on Axial Compressors, Trans. ASME, J. Turbomach., Vol. 127, pp. 709–717, 2005
- [144] Sivagnanasundaram, S.; Spence, S.; Early, J.: Map Width Enhancement Technique for a Turbocharger Compressor, Trans. ASME, J. Turbomach., Vol. 136, pp. 061002-1–061002-10, 2014
- [145] Skoch, G. J.: Experimental Investigation of Centrifugal Compressor Stabilization Techniques, Trans. ASME, J. Turbomach., Vol. 125, pp. 704–713, 2003
- [146] Smith, G.; Cumpsty, N.: Flow Phenomena in Compressor Casing Treatment, Trans. ASME, J. Eng. Gas Turb. Power, Vol. 106(3), pp. 532–541, 1984
- [147] Spakovszky, Z. S.; Roduner, C. H.: Spike and Modal Stall Inception in an Advanced Turbocharger Centrifugal Compressor, Trans. ASME, J. Turbomach., Vol. 131, 2009
- [148] Sun, H.; Hu, L.; Zhang, J.; Hanna, D.; Krivitzky, E.; Larosiliere, L.; Lai, M.; Yang, C.: Switchable Dual-Port Casing Treatment Scheme for an Enhanced Turbocharger Compressor Operating Range, Proceedings of the Institution of Mechanical Engineers, Part D: Journal of Automobile Engineering, Vol. 228(3), pp. 235–244, 2014
- [149] Sundström, E.; Mihăescu, M.; Giachi, M.; Belardini, E.; Michelassi, V.: Analysis of Vaneless Diffuser Stall Instability in a Centrifugal Compressor, International Journal of Turbomachinery, Propulsion and Power, Vol. 2(4), p. 19, 2017

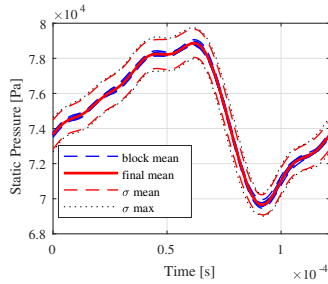
-
- [150] Sutherland, W.: LII. The Viscosity of Gases and Molecular Force, The London, Edinburgh, and Dublin Philosophical Magazine and Journal of Science, Vol. 36(223), pp. 507–531, 1893
- [151] Taghavi-Zenouz, R.; Solki, E.; Afshari, H.: Stall Margin Improvement of a Centrifugal Compressor Utilizing Various Stepped Tip Gap Configurations, Proc. IMechE, Part A: J. Power and Energy, Vol. 228, pp. 772–781, 2014
- [152] Takata, H.; Tsukuda, Y.: Stall Margin Improvement by Casing Treatment - Its Mechanism and Effectiveness, Trans. ASME, J. Eng. Power, Vol. 99(1), pp. 121–133, 1977
- [153] Tamaki, H.: Effect of Recirculation Device on Performance of High Pressure Ratio Centrifugal Compressor, GT2010-22570, in: Proceedings of ASME Turbo Expo 2010
- [154] Tan, C.; Day, I.; Morris, S.; Wadia, A.: Spike-type Compressor Stall Inception, Detection, and Control, Annual Review of Fluid Mechanics, Vol. 42, pp. 275–300, 2010
- [155] Thompson, D. W.; King, P. I.; Hah, C.; Rabe, D. C.: Experimental and Computational Investigation of Stepped Tip Gap Effects on the Flowfield of a Transonic Axial-Flow Compressor Rotor, 98-GT-090, in: ASME 1998 International Gas Turbine and Aeroengine Congress and Exhibition
- [156] Van de Wyer, N.; Farkas, B.; Desset, J.; Brouckaert, J.; Thomas, J.-F.; Hiernaux, S.: Experimental Investigation of the Steady and Unsteady Flow Field in a Single Stage Low Pressure Axial Compressor with a Circumferential Groove Casing Treatment, GT2010-23474, in: Proceedings of ASME Turbo Expo 2010
- [157] Versteeg, H. K.; Malalasekera, W.: An Introduction to Computational Fluid Dynamics: The Finite Volume Method, Pearson education, 2007
- [158] Vo, H. D.; Tan, C. S.; Greitzer, E. M.: Criteria for Spike Initiated Rotating Stall, Trans. ASME, J. Turbomach., Vol. 130, pp. 1–9, 2008
- [159] Weichert, S.; Day, I.: Detailed Measurements of Spike Formation in an Axial Compressor, Trans. ASME, J. Turbomach., Vol. 136(5), p. 051006, 2014
- [160] Wernet, M. P.; Bright, M. M.; Skoch, G. J.: An Investigation of Surge in a High-Speed Centrifugal Compressor using Digital PIV, Trans. ASME, J. Turbomach., Vol. 123(2), pp. 418–428, 2001
- [161] Wilke, I.; Kau, H.-P.: A Numerical Investigation of the Influence of Casing Treatments on the Tip Leakage Flow in a HPC Front Stage, GT2002-30642, in: Proceedings of ASME Turbo Expo 2002
- [162] Wisler, D.; Hilvers, D.: Stator Hub Treatment Study, Tech. Rep. CR-134729, GE R74AEG410, NASA, Dec. 1973

-
- [163] Wu, Y.; Chu, W.; Zhang, H.; Li, Q.: Parametric Investigation of Circumferential Grooves on Compressor Rotor Performance, *Trans. ASME, J. Fluids Eng.*, Vol. 132(12), p. 121103, 2010
- [164] Wu, Y.; Li, Q.; Tian, J.; Chu, W.: Investigation of Pre-Stall Behavior in an Axial Compressor Rotor—Part I: Unsteadiness of Tip Clearance Flow, *Trans. ASME, J. Turbomach.*, Vol. 134(5), pp. 051027-1–051027-12, 2012
- [165] Wu, Y.; Li, Q.; Tian, J.; Chu, W.: Investigation of Pre-Stall Behavior in an Axial Compressor Rotor—Part II: Flow Mechanism of Spike Emergence, *Trans. ASME, J. Turbomach.*, Vol. 134(5), pp. 051028-1–051028-10, 2012
- [166] Yamada, K.; Funazaki, K.; Furukawa, M.: The Behavior of Tip Clearance Flow at Near-Stall Condition in a Transonic Axial Compressor Rotor, GT2007-27725, in: *Proceedings of ASME Turbo Expo 2007*
- [167] Yamada, K.; Furukawa, M.; Fukushima, H.; Ibaraki, S.; Tomita, I.: The Role of Tip Leakage Vortex Breakdown in Flow Fields and Aerodynamic Characteristics of Transonic Centrifugal Compressor Impellers, GT2011-46253, in: *Proceedings of ASME Turbo Expo 2011*
- [168] Yamada, K.; Furukawa, M.; Nakano, T.; Inoue, M.; Funazaki, K.: Unsteady Three-Dimensional Flow Phenomena Due to Breakdown of Tip Leakage Vortex in a Transonic Axial Compressor Rotor, GT2004-53745, in: *Proceedings of ASME Turbo Expo 2004*
- [169] Yamada, K.; Furukawa, M.; Tamura, Y.; Saito, S.; Matsuoka, A.; Nakayama, K.: Large-Scale Detached-Eddy Simulation Analysis of Stall Inception Process in a Multistage Axial Flow Compressor, *Trans. ASME, J. Turbomach.*, Vol. 139(7), p. 071002, 2017
- [170] Yamada, K.; Kikuta, H.; Iwakiri, K.; Furukawa, M.; Gunjishima, S.: An Explanation for Flow Features of Spike-Type Stall Inception in an Axial Compressor Rotor, *Trans. ASME, J. Turbomach.*, Vol. 135(2), p. 021023, 2013
- [171] Yang, C.; Wang, Y.; Lao, D.; Zhang, H.; Qi, M.; Tong, D.: Investigation of the Coupling Mechanism Between Bent Pipes and Volute on the Stall Inception at the Centrifugal Compressor Inlet, GT2017-63356, in: *Proceedings of ASME Turbo Expo 2017*
- [172] Yang, C.; Wang, Y.; Tong, D.; Yang, C.; Li, Y.: Stall Inception Induced by the Volute Tongue at Centrifugal Compressor Inlet, *Proc. IMechE, Part G: J. Aerospace and Engineering*, Vol. 231(5), pp. 931–940, 2017
- [173] Yang, M.; Martinez-Botas, R.; Zhang, Y.: Inlet Duct Treatment for Stability Improvement on a High Pressure Ratio Centrifugal Compressor, in: *Proceedings of ASME Turbo Expo 2013*
- [174] Zhang, H.; Yang, C.; Yang, D.; Wang, W.; Yang, C.; Qi, M.: Investigation on the Stall Inception Circumferential Position and Stall Process Behavior in a Centrifugal

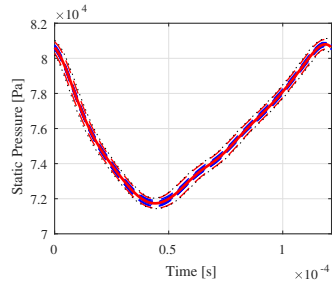
Compressor with Volute, GT2018-75765, in: Proceedings of ASME Turbo Expo 2018

- [175] Zhao, J.; Xi, G.; Wang, Z.; Zhao, Y.: The Unsteady Pre-Stall Behavior of the Spike-Type Rotating Stall within an Airfoil Vaned-Diffuser, GT2018-76145, in: Proceedings of ASME Turbo Expo 2018
- [176] Zhao, S.; Lu, X.; Zhu, J.; Zhang, H.: Investigation for the Effects of Circumferential Grooves on the Unsteadiness of Tip Clearance Flow to Enhance Compressor Flow Instability, GT2010-22652, in: Proceedings of ASME Turbo Expo 2010
- [177] Zheng, X.; Liu, A.: Phenomenon and Mechanism of Two-Regime-Surge in a Centrifugal Compressor, Trans. ASME, J. Turbomach., Vol. 137(8), p. 081007, 2015
- [178] Zheng, X.; Sun, Z.; Kawakubo, T.; Tamaki, H.: Experimental Investigation of Surge and Stall in a Turbocharger Centrifugal Compressor with a Vaned Diffuser, Experimental Thermal and Fluid Science, Vol. 82, pp. 493–506, 2017

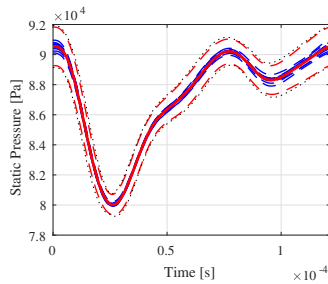
A Validation Data



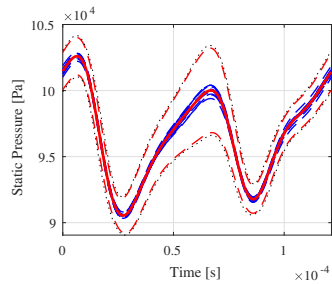
a) position 1



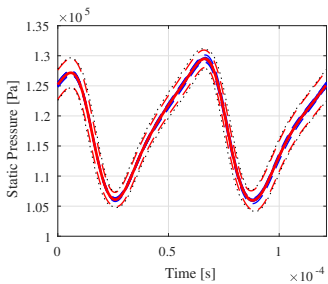
b) position 2



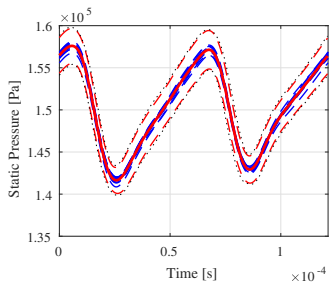
c) position 3



d) position 4



e) position 5



f) position 6

Figure A.1 – Ensemble averaged signals based on raw pressure signals for the smooth casing vaned diffuser configuration at $n = 70000$ rpm and $\dot{m}_{red} = 0.4$ kg/s

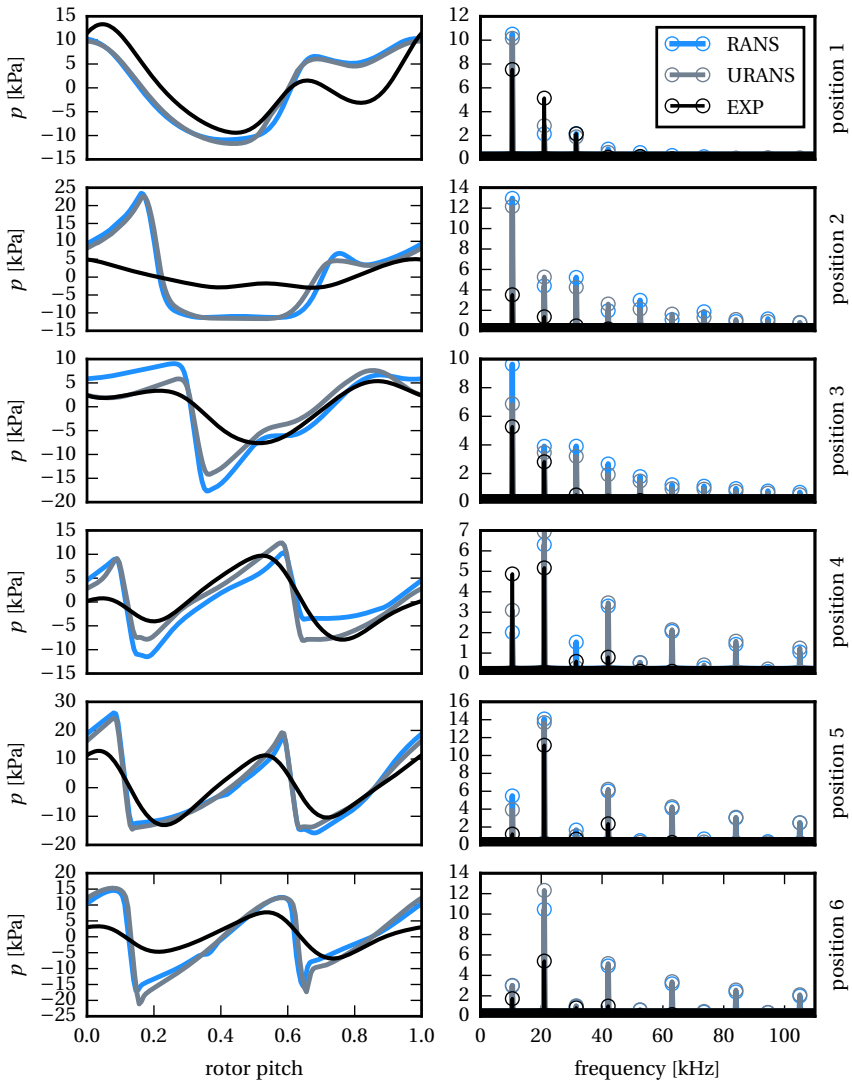


Figure A.2 – Comparison of pressure amplitudes in the time (left) and frequency domain (right) for the different impeller sensor positions at $n = 90000$ rpm and $\dot{m}_{\text{red}} = 0.54$ kg/s, the experimental values represent ensemble averaged data, vaneless diffuser configuration

B Parametric design study

B.1 Groove Location

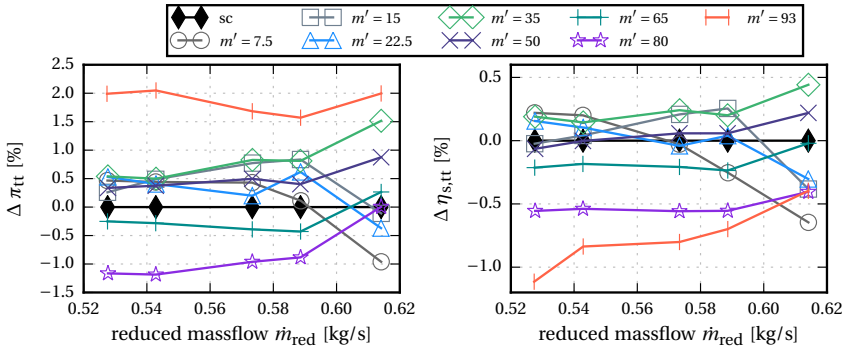


Figure B.1 – Groove location variation with the initial groove shape of $\gamma = 45^\circ$, $t = 3$ mm and $b = 1.5$ mm - results based on the sc configuration

B.2 Groove Inclination

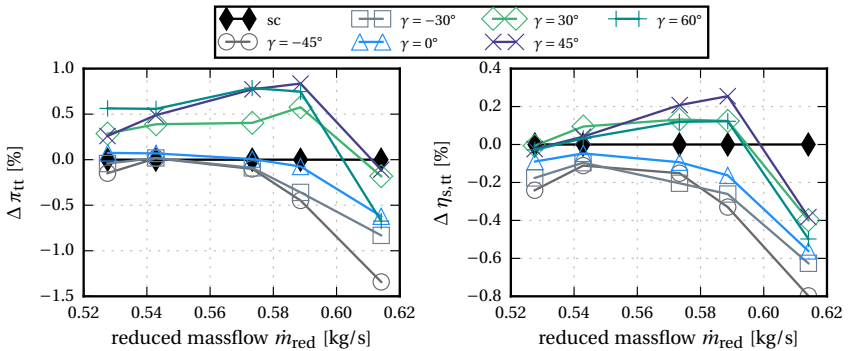


Figure B.2 – Operating point dependency for the single groove inclination study at a meridional location of $m' = 15$ with the initial groove shape of $\gamma = 60^\circ$, $t = 3$ mm and $b = 1.5$ mm

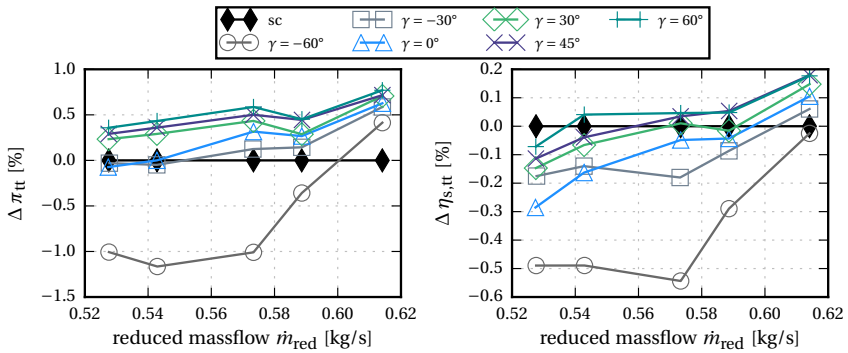


Figure B.3 – Operating point dependency for the single groove inclination study at a meridional location of $m' = 50$ with the initial groove shape of $\gamma = 60^\circ$, $t = 3\text{ mm}$ and $b = 1.5\text{ mm}$

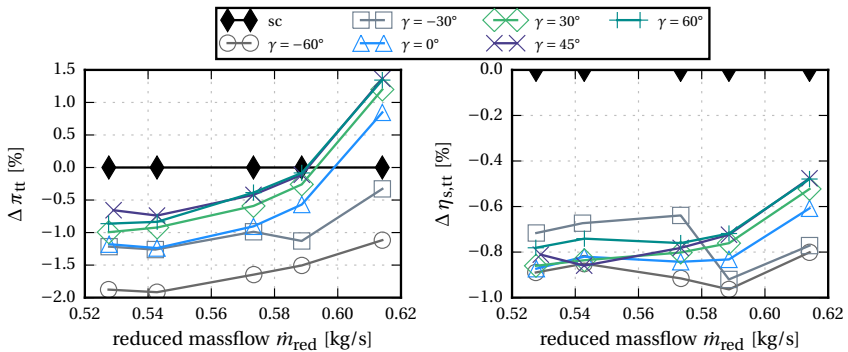


Figure B.4 – Operating point dependency for the single groove inclination study at a meridional location of $m' = 85$ with the initial groove shape of $\gamma = 60^\circ$, $t = 3\text{ mm}$ and $b = 1.5\text{ mm}$

B.3 Groove Dimension

Aspect Ratio

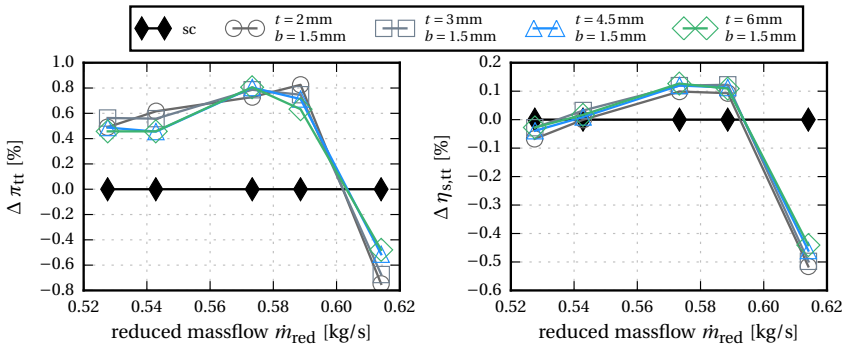


Figure B.5 – Variation of the groove aspect ratio for a single groove at $m' = 15$, $\gamma = 60^\circ$ inclination and a constant groove width of $t = 3$ mm

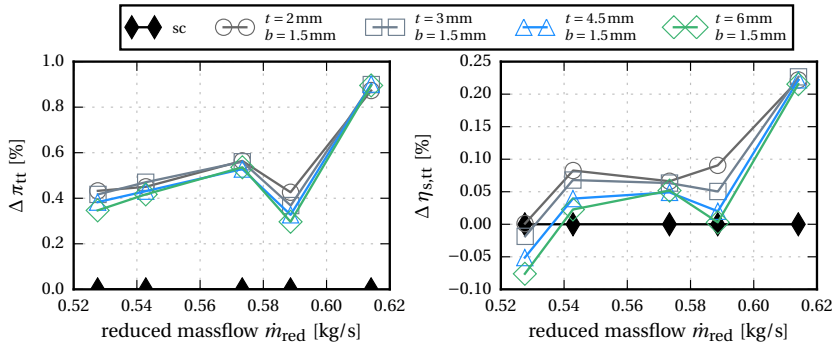


Figure B.6 – Variation of the groove aspect ratio for a single groove at $m' = 50$, $\gamma = 60^\circ$ inclination and a constant groove width of $t = 3$ mm

Groove Size

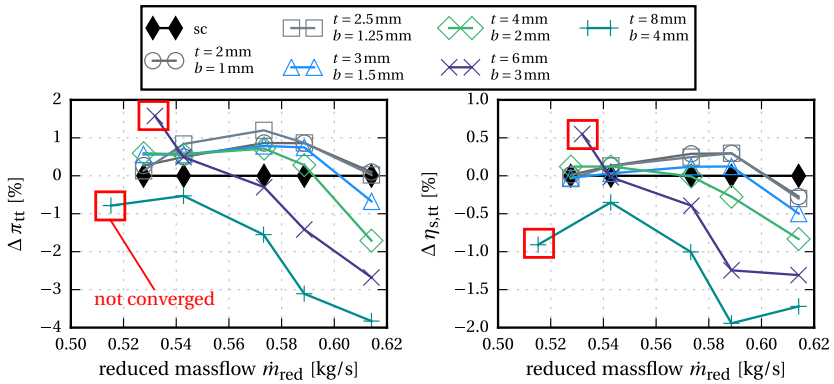


Figure B.7 – Variation of the groove size for a single groove at $m' = 15$, $\gamma = 60^\circ$ inclination and a constant aspect ratio of 2

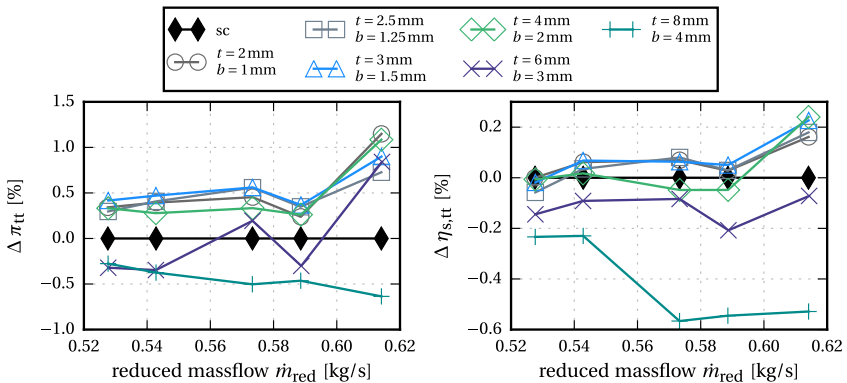


Figure B.8 – Variation of the groove size for a single groove at $m' = 50$, $\gamma = 60^\circ$ inclination and a constant aspect ratio of 2

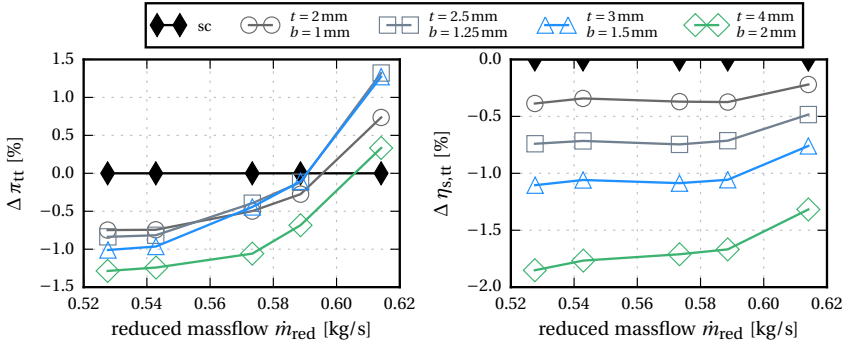


Figure B.9 – Variation of the groove size for a single groove at $m' = 85$, $\gamma = 60^\circ$ inclination and a constant aspect ratio of 2

C Stability with Casing Grooves

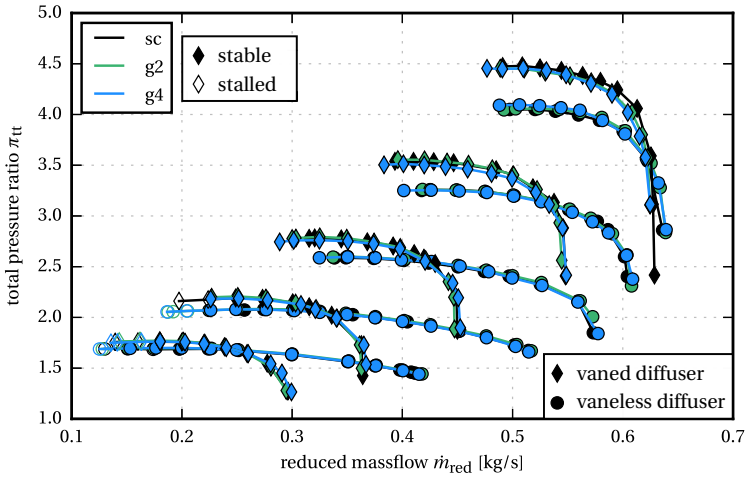


Figure C.1 – Comparison of the measured operating maps of *sc*, *g2* and *g4* with the vane and the vaneless diffuser

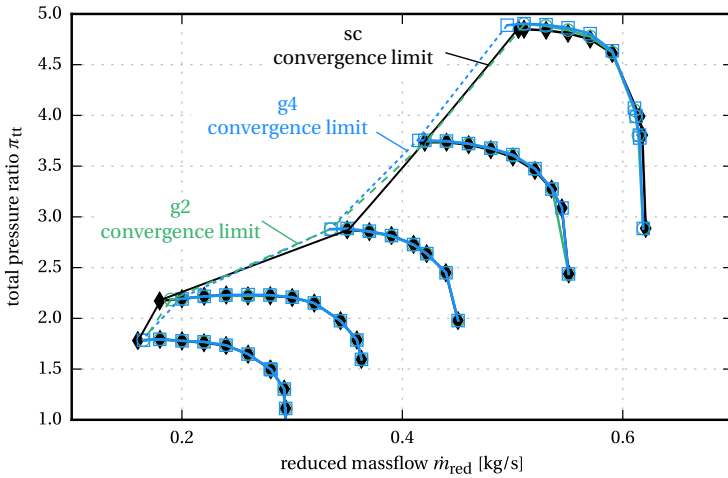


Figure C.2 – RANS operating map for the full stage model with the vaned diffuser including stability lines based on the last converged points

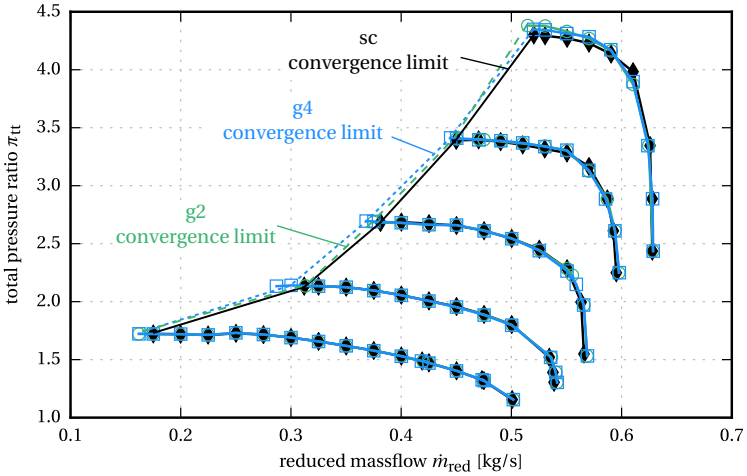


Figure C.3 – RANS operating map for the full stage model with the vaneless diffuser including stability lines based on the last converged points

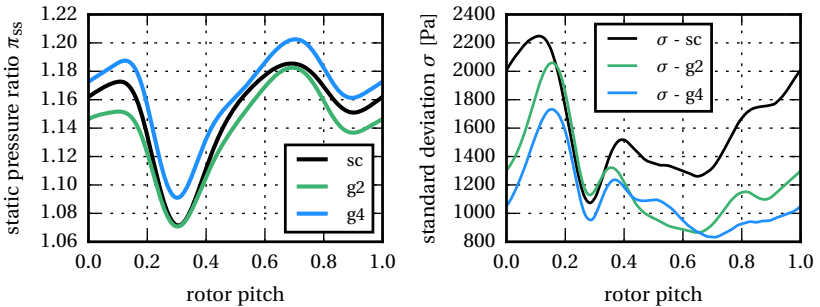


Figure C.4 – Ensemble averaged circumferential pressure distribution and standard deviation σ — measured at sensor position 3 in the inducer for the vaneless diffuser near-stall operating point at 70 krpm

D Performance with Casing Grooves

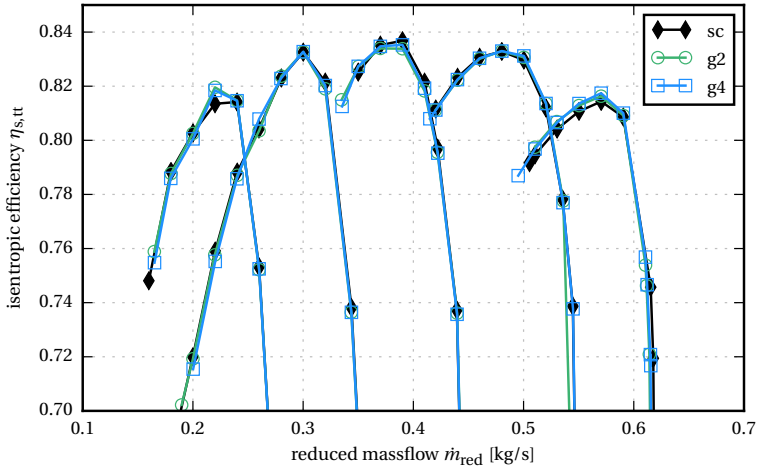


Figure D.1 – Full stage RANS efficiency map with the vaned diffuser

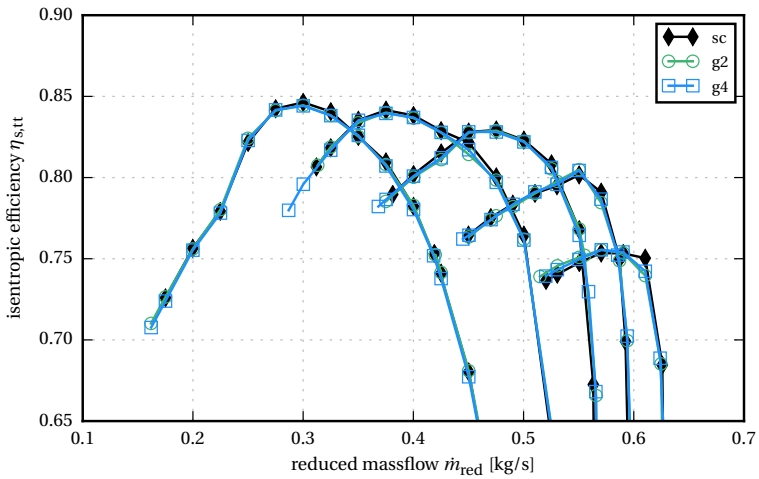


Figure D.2 – Full stage RANS efficiency map with the vaneless diffuser